SOME ASPECTS OF HIGGS PHYSICS AND WIMP DARK MATTER

by

Xing Wang

B.S. in Physics, Tsinghua University, 2013

Submitted to the Graduate Faculty of

the Kenneth P. Dietrich School of Arts and Sciences in partial

fulfillment

of the requirements for the degree of

Doctor of Philosophy

University of Pittsburgh

2019

UNIVERSITY OF PITTSBURGH

KENNETH P. DIETRICH SCHOOL OF ARTS AND SCIENCES

This dissertation was presented

by

Xing Wang

It was defended on

May 1st 2019

and approved by

Tao Han, Distinguished Professor, University of Pittsburgh

Tae Min Hong, Assistant Professor, University of Pittsburgh

Arthur Kosowsky, Professor, University of Pittsburgh

Adam Leibovich, Professor, University of Pittsburgh

Ira Rothstein, Professor, Carnegie Mellon University

Dissertation Director: Tao Han, Distinguished Professor, University of Pittsburgh

SOME ASPECTS OF HIGGS PHYSICS AND WIMP DARK MATTER

Xing Wang, PhD

University of Pittsburgh, 2019

The discovery of the Higgs boson at the CERN Large Hadron Collider (LHC) in 2012 has filled in the last missing piece of the Standard Model (SM). Yet we would like to know where the next physics scale above the electroweak scale lies. In this thesis, I focus on two directions to search for possible new physics beyond the SM: the Higgs boson and the dark matter. As the recently discovered Higgs boson may serve as a lamppost for new physics search, it is of great importance to scrutinize its properties and look for possible deviations from the SM. In particular, we study the Higgs boson rare decays to a pair of fermions associated with a photon and its observability at the LHC, and exploit $h \to c\bar{c}\gamma$ to probe the charm-quark Yukawa coupling. On the other hand, the existence of the dark matter has been well-established via many astronomical observations, in spite of its unknown particle origin. The TeV scale naturally appears if we assume that the correct dark matter abundance is achieved via thermal freeze-out with interaction strength of electroweak force, which is known as the "WIMP miracle". It is crucial to search for such dark matter particles at the colliders. Future high-energy colliders provide excellent environments not only for discovering such particles but also for examining its properties such as spin and coupling structure. We study the search strategies and the observability of weakly interacting massive particles (WIMP) with compressed spectra at the future colliders, and exploit single-photon processes and antler-topology processes to determine not only the spins but also the coupling structures at future high-energy e^+e^- colliders.

TABLE OF CONTENTS

LIST OF TABLES

LIST OF FIGURES

LIST OF EQUATIONS

PREFACE

This preface is dedicated to acknowledge the countless help I have received during my Ph.D. program.

First and foremost, I would like to thank my advisor, Professor Tao Han, who has been a tremendous mentor for me. I could not have accomplished this Ph.D. without his patience, motivation, immense knowledge, and most importantly, his continuous guidance and support. The joy and enthusiasm he has for his research is contagious and motivational, and will be a life-long inspiration for me. Forever shall I remain indebted to him.

There are many people who have played crucial roles in my graduate study: Brian Batell, Joshua Berger, Joseph Boudreau, Tae Min Hong, Cindy Cercone, Neil Christensen, Ayres Freitas, Dorival Goncalves, Leyla Hirschfeld, Ahmed Ismail, Adam Leibovich, Zhen Liu, Satyanarayan Mukhopadhyay, Jim Mueller, Josh Sayre, Brock Tweedie, Cedric Weiland, Sussane Westhoff, Zixin Yang, Rongpu Zhou. I would like to express special gratitude to Professor Seong Youl Choi, who held my hands through my early projects and passed on knowledge that would benefit me throughout the career. I also want to thank my officemates, including Junmou Chen, Lin Dai, Wai Kin Lai, Hongkai Liu, Zhuoni Qian, Richard Ruiz, Barmak Shams Es Haghi, and Daniel Wiegand, for not only the helpful and constructive discussions on wide ranges of topics, but also the fun and joy we had together.

I would also like to thank the support from Dietrich School of Art & Sciences Fellowship, Andrew Mellon Predoctoral Fellowship, and PITT-PACC.

Lastly I thank my parents for their unfailing support, unconditional trust, timely encouragement, and endless patience. It was their love that raised me up again when I got weary.

1.0 INTRODUCTION

With the recent triumph of the Higgs boson discovery in 2012 at the CERN Large Hadron Collider (LHC) [1, 2], there have been uninterrupted successes in particle physics for the last half century, and we have completed the Standard Model to great precisions. While the Standard Model could be valid all the way up to the Planck scale, however, many profound puzzles of nature still need to be answered. For example, there is a huge hierarchy between the electroweak (EW) scale and the Planck scale. Since the radiative corrections to the Higgs boson mass is quadratically sensitive to the new physics scale, a 125 GeV Higgs boson requires huge cancellations, which makes our theory seem highly fine-tuned. Also, the particle nature of the dark matter still remains unknown, in spite of the evidence from various astronomical observations. The existence of nonzero neutrino masses is a clear indication of physics beyond the Standard Model (BSM), but we still have no clue regarding to the origin of such masses. As this list continues, new physics should be expected to appear at some point to address these fundamental questions. However, despite of many plausible arguments, there is no clear sign of where the next physics scales are or should be, which posts an intriguing challenge for particle physics. This thesis attempts to tackle a few phenomenological issues in the hope to shed light on some of these questions.

1.1 HIGGS BOSON AND YUKAWA COUPLINGS

Although all the studies indicate that the recently discovered particle is consistent with the Standard Model (SM) Higgs boson [3], there are only a handful leading channels observed at the LHC and accuracies on the branching fraction measurements, even assuming it is the

SM Higgs boson, are still no better than about 10%. There are compelling motivations that the SM needs to be extended, including the particle dark matter, the origin of the neutrino mass, and perhaps the most puzzling related to the electroweak scale, the "naturalness" for the Higgs boson mass in the SM. Therefore, more detailed studies regarding the properties of the Higgs boson are necessary to test the SM and to look for possible new physics beyond the Standard Model.

With a large amount of data being accumulated at the LHC Run-2 and the higher luminosity expectation of 3 ab^{-1} (HL-LHC), one would expect to produce a large sample, eventually reaching about 50 pb$\times$ 3 $ab^{-1} \approx$ 150 million Higgs bosons. As thus, searching for rare decays of the Higgs boson becomes feasible and thus increasingly important to test the Higgs sector in the Standard Model and to seek for new physics beyond the SM. Therefore, it is of fundamental importance to establish the pattern of the Higgs boson Yukawa couplings to fermions in order to verify the Standard Model (SM) and seek hints of physics beyond the SM (BSM). The couplings to third generation fermions have all been observed with over 5σ significance. For top quarks, there is a large indirect contribution to the gluon-gluon fusion production mode and the photon-photon decay mode. However, direct observation is important to ensure there are no BSM quantum corrections to Higgs boson production or decay. Both the ATLAS and CMS collaborations have recently observed the production of top quark pairs in association to the Higgs boson [4, 5] as well as Higgs boson decays to bottom quark pairs [6, 7]. For leptons, the challenging decay channel $h \to \tau^+\tau^-$ reached 5σ already from the LHC Run 1 data [3] and now ATLAS and CMS have both individually observed this decay mode [8, 9]. With the upgrade of the LHC to its high-luminosity phase (HL-LHC), the Higgs boson coupling measurements to the heaviest generation of fermions will reach an accuracy of about or better than 20% [10] and will extend to kinematic regions with high transverse momenta of the Higgs boson (p_T^h) [11, 12].

Direct observations of the Higgs couplings to the second-generation of fermions will be critically important to confirm the pattern of non-universal Yukawa couplings and search for deviations from the SM as predicted in theories with an extended Higgs sector [13]. The channel $h \to \mu^+\mu^-$ is the cleanest Higgs boson signal of all decay modes [14, 15]. Even with a branching fraction as small as 2×10^{-4}, ATLAS and CMS almost have the sensitivity to

the SM rate [16, 17] and a measurement with an accuracy of 13% is expected at the HL-LHC [18]. In contrast to $h \to \mu^+\mu^-$, the second generation hadronic decay modes of the Higgs boson are very difficult to distinguish from SM backgrounds, including other Higgs boson decays. While b-jet tagging is a powerful tool for rejecting backgrounds, c-jets are harder to distinguish from b and light jets [19–21] and strange-jets are nearly identical to up- and down-quark jets [22, 23]. The $h \to c\bar{c}$ branching ratio is expected to be about 3%, so the challenge is background rejection and triggering, not statistics. The Higgs boson rare decays to a light fermion pair are usually very difficult to observe because of the suppression by the small Yukawa couplings. For instance, the branching fraction of $h \to e^+e^-$ is $\mathcal{O}(10^{-8})$, and thus hopeless to detect this decay channel at colliders.

In this thesis, we studied the Higgs boson rare decay channels $h \to f\bar{f}\gamma$ where $f = \tau, \mu, e$ and b, c and their observability at the LHC, in Chapter 2. In Chapter 3, we examine the feasibility of a Higgs-charm Yukawa coupling measurement in the $h \to c\bar{c}\gamma$ channel at the HL-LHC. By proposing an optimal triggering strategy and simulating realistic detector effects, we show that a coupling of about 8 times the SM value may be reached at 95% confidence after the HL-LHC. This approach is complementary and competitive with other methods.

1.2 DARK MATTER AT FUTURE COLLIDERS

Many models beyond the SM [24–36] have been proposed and studied not only to resolve several conceptual issues like the gauge hierarchy problem but also to explain the dark matter (DM) composition of the Universe with new stable weakly interacting massive particles [37–39]. As a plausible candidate for the dark matter (DM) in the Universe, such weakly interacting massive particles (WIMP) are being intensely searched for both in laboratory experiments and through a broad range of astrophysical probes [38, 40].

Among the multitude of possibilities for particle DM, WIMPs remain a highly motivated candidate due to the predictable nature of the thermal relic abundance, and the correlated predictions for their experimental and observational probes. WIMP dark matter particles that belong to a multiplet of the standard model weak interactions are one of the best

representatives, but are often challenging to probe in direct detection experiments due to loop-suppressed scattering cross-sections. Searches at hadron colliders are thus crucial for testing such a scenario, and depending upon the gauge representation, can be complementary to indirect detection probes in different mass windows. Moreover, since the relic abundance of electroweak DM is uniquely determined by its mass value, they represent a well-defined target in the collider search for DM in general. In Chapter 4, we studied collider probes of two representative scenarios for electroweak DM, namely a wino-like $\mathrm{SU}(2)_{\mathrm{L}}$ triplet and a Higgsino-like $\mathrm{SU}(2)_{\mathrm{L}}$ doublet at three at three different future hadron colliders: the high-luminosity HL-LHC, the proposed 27-TeV LHC upgrade (HE-LHC) and the 100-TeV FCC-hh/SppC.

Once any new particle indicating new physics beyond the SM is discovered at the LHC or high energy e^+e^- colliders, one of the first crucial steps is to experimentally determine its spin as well as its mass because spin is one of the canonical characteristics of all particles required for defining a new theoretical framework as a Lorentz-invariant quantum field theory [41]. However, a (discrete) symmetry such as R parity in supersymmetric (SUSY) models and Kaluza-Klein (KK) parity in universal extra-dimension (UED) models is generally introduced to guarantee the stability of the particles and thus to explain the DM relic density quantitatively. As a consequence, the new particles can be produced only in pairs at high energy hadron or lepton colliders, leading to challenging signatures with at least two invisible final-state particles.

At hadron colliders like the LHC such a signal with invisible particles is usually insufficiently constrained for full kinematic reconstructions, rendering the unambiguous and precise determination of the masses, spins and couplings of (new) particles produced in the intermediate or final stages challenging, even if conceptually possible, as demonstrated in many previous works on mass measurements [42–60] and on spin determination [61–86].

In contrast to hadron colliders, an e^+e^- collider [87–93] has a fixed center-of-mass (c.m.) energy and c.m. frame and the collider can be equipped with longitudinally and/or transversely polarized beams. These characteristic features allow us to exploit several complementary techniques at e^+e^- colliders for unambiguously determining the spins as well as the masses of new pairwise-produced particles, the invisible particles from the decays of the

parent particles and the particles exchanged as intermediate states, with good precision.

In Chapter 5 and 6, we provide systematic and detailed methods not only for determining the spins of the (nearly) invisible particles unambiguously, but also for characterizing each of the three benchmark scenarios through single-photon processes and antler-topology processes at e^+e^- colliders by exploiting electron and positron beam polarizations. We find that, if kinematically accessible, the spins and coupling strengths of the invisible particles to γ/Z in such single-photon processes can be determined clearly by exploiting the initial electron (and positron) beam polarization and investigating the threshold excitation patterns of the processes.

The thesis is arranged in the following structure. After an introduction, in Chapter 2, we studied the Higgs boson rare decay channels $h \to f\bar{f}\gamma$ where $f = \tau, \mu, e$ and b, c and their observability at the LHC. In Chapter 3, we examine the feasibility of a Higgs-charm Yukawa coupling measurement in the $h \to c\bar{c}\gamma$ channel at the HL-LHC, by proposing an optimal triggering strategy and simulating realistic detector effects. In Chapter 4, we studied collider probes of two representative scenarios for electroweak DM, namely an wino-like $\mathrm{SU}(2)_\mathrm{L}$ triplet and a Higgsino-like $\mathrm{SU}(2)_\mathrm{L}$ doublet at three at three different future hadron colliders: the high-luminosity HL-LHC, the proposed 27-TeV LHC upgrade (HE-LHC) and the 100-TeV FCC-hh/SppC. In Chapter 5, we study the pair production in association with a hard photon radiation in high energy e^+e^- collisions, to explore three characteristic scenarios, each of which has a nearly degenerate pair of a charged state and a neutral state with a small mass difference. In Chapter 6, we carry out a systematic study of kinematic observables connected with the antler-topology process $e^+e^- \to \mathcal{P}^+\mathcal{P}^- \to \ell^+\ell^-\mathcal{D}^0\bar{\mathcal{D}}^0$ which could serve as model-independent tests for determining the spins of the charged particles $\mathcal{P}^\pm$ and the invisible neutral particles $\mathcal{D}^0$ and $\bar{\mathcal{D}}^0$ as well as the intermediate virtual particles participating in the production process.

As of this writing, the relevant publications can be found in Refs. [94–99].

2.0 RADIATIVE HIGGS DECAY TO A FERMION PAIR

In this chapter, we study other rare decay channels: the Higgs radiative decay to a fermion pair $h \to f\bar{f}\gamma$. Firstly, this decay channel receives contribution that is proportional to the Higgs-fermion interaction strength, which may provide a complementary way to measure certain Yukawa couplings. Secondly, as it also receives contributions from electroweak (EW) one-loop diagrams [100], this channel is not necessarily governed by the Yukawa coupling for light fermions, leading to violation of the Yukawa scaling. Due to this enhancement, the Higgs transitions to light fermions may be observable via the radiative decays despite the smallness of fermion masses. The searches for those Higgs decays are not only to test the consistency of the SM, but also to seek for potential new physics in either the Yukawa or the electroweak sector [101–104]. We present our systematical treatment to such channels from the observational points of view at the LHC. We lay out the kinematical features for the leptonic channels $h \to \mu^+\mu^-\gamma, e^+e^-\gamma$ near γ^*, Z poles and the interplay in between, and propose new cuts based on the kinematical features to optimize the on-going searches. We also motivate a new search for $h \to \tau^+\tau^-\gamma$ which should be within the scope of observability for a Higgs rare decay at the LHC. Furthermore, we propose another new channel $h \to c\bar{c}\gamma$ to be searched for at the LHC, which could complement the existing proposals on probing the charm-quark Yukawa coupling at the LHC. In the due course, we point out the numerical significance of the QED running mass concerning the future precision Higgs measurements of the Yukawa couplings.

The rest of the chapter is organized as follows. We present the full one-loop electroweak corrections to the decay $h \to f\bar{f}$ in Sec. 2.1 and show the kinematical features by some differential distributions. We then discuss the observability of the leptonic channels at the LHC in Sec. 2.2. We finally study the difficult channel $h \to c\bar{c}\gamma$ in Sec. 2.3. We summarize

our results in Sec. 2.4.

2.1 $h \to f\bar{f}(\gamma)$ AT ONE-LOOP

It is well known that the tree-level decay width for $h \to f\bar{f}$ as shown in Fig. 2.1a is

$$\Gamma^0_{h\to f\bar{f}} = \frac{y_f^2 N_c}{16\pi}\, m_h\, \beta_f^3, \qquad \beta_f = \sqrt{1-\frac{4m_f^2}{m_h^2}}. \tag{2.1}$$

where, in the SM, the Yukawa coupling is $y_f = \sqrt{2}\, m_f/v$, and the color factor $N_c = 3$ (1) for a color triplet (singlet) fermion. Quantum chromodynamics (QCD) corrections to the decay of the Higgs to a quark pair have been known up to N^{4}LO at $\mathcal{O}(\alpha_s^4)$ [105–107]. To serve as a comparison with the current work, we write the expression as

$$\Gamma_{\text{NLO QCD}} = \Gamma^0\left(1 + C_F\frac{\bar{\alpha}_s}{\pi}\,\frac{17}{4} + \mathcal{O}(\alpha_s^2)\right), \quad \Gamma^0 = \frac{N_c}{8\pi}\, m_h\, \frac{\bar{m}_f^2}{v^2}\, \beta_f^3, \tag{2.2}$$

where $\bar{\alpha}_s^2$ and $\bar{m}_f^2$ are the renormalized QCD running coupling and quark mass, respectively, to the scale m_h^2 in the $\overline{\text{MS}}$ subtraction scheme, and the color factor $C_F = (N_c^2-1)/2N_c = 4/3$. The most significant effect is due to the running of the quark mass from $\mu_0 = m_f$ to $\mu = m_h$ [108–112]. For the sake of illustration and comparison, we only give the one-loop QCD running mass expression as

$$\bar{m}(\mu) = \bar{m}(\mu_0)\left(\frac{\bar{\alpha}_s(\mu)}{\bar{\alpha}_s(\mu_0)}\right)^{\frac{\gamma_0}{b_0}} = \bar{m}(\mu_0)\left(1+\frac{b_0}{4\pi}\bar{\alpha}_s(\mu_0)\ln\frac{\mu^2}{\mu_0^2}\right)^{-\frac{\gamma_0}{b_0}} \tag{2.3}$$

where $\gamma_0 = 4$ and $b_0 = 11 - 2n_f/3$ in QCD.

2.1.1 $\mathcal{O}(y_f^2\alpha)$ corrections

Similar to the above, QED corrections to the Higgs radiative decay at $\mathcal{O}(y_f^2\alpha)$, depicted in Figs. 2.1b–2.1d, have the same form except for the color factor and the electric charge of the fermions [113],

$$\Gamma_{\text{NLO QED}} = \Gamma^0 \left(1 + Q_f^2 \frac{\bar{\alpha}}{\pi} \frac{17}{4} + \mathcal{O}(\alpha^2)\right). \tag{2.4}$$

Therefore, the QED corrections to the partial width at the next-to-leading order (NLO) contribute about $Q_f^2 \times \mathcal{O}(1\%)$ to the Higgs partial width to a fermion pair. Analogous to QCD, we should also take into account the effect of QED running mass, which can be calculated using Eq. (2.3) with $\gamma_0 = 3Q_f^2$ and $b_0 = -4\sum_f Q_f^2/3$ in QED. This 1-loop running from m_f to m_h will change the fermion mass by about 4% for the electron and about 0.1% (0.8%) for the b-quark (c-quark), comparable to the fix-oder QED correction as above. The running mass effect from N^{4}LO QCD [114,115] and NLO QED are summarized in Table 2.1. The difference between the QED resummed running mass in Eq. (2.3) and its $\mathcal{O}(\alpha)$ expansion is relatively small due to the weakly-coupled nature of QED, and contributes to the NLO QED corrections at percentage level, as shown in the parentheses in Table 2.1. The entries in the last column of Table 2.1 are evaluated with the running Yukawa coupling effects, using the LO partial width formula of Eq. (2.1). We note that the full SM prediction for the Higgs total width is 4.1 MeV [116].

The complete EW corrections to $h \to f\bar{f}$ partial width at $\mathcal{O}(y_f^2\alpha)$ is

$$\delta\Gamma_{\text{EW}} = \Gamma^0 \left(\frac{2\delta m_f^{\text{QED}}}{\bar{m}_f} + Q_f^2 \frac{\bar{\alpha}}{\pi} \frac{17}{4} + \Delta_{\text{weak}} + \mathcal{O}(\alpha^2)\right), \tag{2.5}$$

where $\delta m_f^{\text{QED}} = \bar{m}(m_h) - \bar{m}(m_f)$ as listed in Table 2.1, and Δ_{weak} follows the on-shell definition in [117]. The two terms of QED are for mass and vertex corrections and they have opposite signs. The 1-loop EW diagrams as shown in Figs. 2.1b–2.1g are all proportional to m_f, and thus we will refer this section as "Yukawa corrections". We also refer the exclusive real photon emission represented by Fig. 2.1d as "QED radiation" in later sections. EW corrections with higher-order loops up to $\mathcal{O}(\alpha\alpha_s)$ [118] and $\mathcal{O}(\alpha_s^2 G_F m_t^2)$ [119,120] have also been calculated, that we will not include in the current study.

As the precision of the Higgs measurements improves in the future, it will become necessary to take these corrections into account. In particular, the projected precision of the $hb\bar{b}$ coupling determination was estimated to be 0.3% at the International Linear Collider [121].

2.1.2 $\mathcal{O}(y_t^2\alpha^3, \alpha^4)$ corrections

Besides the $\mathcal{O}(y_f^2\alpha)$ corrections from the chirality-flipping diagrams governed by the Yukawa couplings, the decay of a Higgs boson to a pair of fermions plus a photon can also be induced by electroweak loops of top quark and gauge bosons. Figure 2.2 shows some representative electroweak one-loop diagrams. According to their distinctive kinematics and couplings, they can be cast into five classes:

I. $h \to \gamma Z^* \to f\bar{f}\gamma$ (Figs. 2.2a, 2.2b)

II. $h \to \gamma\gamma^* \to f\bar{f}\gamma$ (Figs. 2.2a, 2.2b)

III. Z-boson box or triangle with final state radiation (Figs. 2.2c, 2.2d)

IV. W-boson box or triangle with final state radiation (Figs. 2.2c, 2.2d, 2.2e)

V. top-quark box or triangle with final state radiation (Figs. 2.2f, 2.2g, 2.2h, only for $h \to b\bar{b}\gamma$)

We will call them collectively the "EW+γ" contributions, distinctive from the chirality-flipping Yukawa corrections in Sec. 2.1.1. The interference between the QED radiation in Fig. 2.1d and the EW+γ processes in Fig. 2.2 is suppressed by m_f/M_W, as they have different chiral structures for the final state fermions. The EW+γ loops are finite at the ultra-violet (UV) so that there is no need for renormalization, as pointed out in Ref. [122].

In the infrared (IR) limit, the amplitude in Fig. 2.2 is proportional to the fermion mass m_f due to the chiral structure and the QED Ward-Takahashi identity. This is also true in the collinear region for diagrams in Figs. 2.2c and 2.2f, where the amplitude factorizes into that of $h \to f\bar{f}$ convolved with a collinear splitting. Therefore, the IR/collinear singularities do not show up in the massless limit $m_f \to 0$. This behavior of Fig. 2.2 remains to be valid to all orders in perturbation theory because of the chiral symmetry. In the limit $m_f \to 0$, however, the diagrams in Figs. 2.2a and 2.2b diverge as the invariant mass of the fermion

pair approaches the photon pole $M_{f\bar{f}} \to 0$. Therefore, a finite fermion mass needs to be kept for Figs. 2.2a and 2.2b so that $M^2_{f\bar{f}} > 4m^2_f$, to regularize the divergent behavior.

We perform the calculation in the Feynman gauge. As a cross check, the analytic results have been calculated and given in [100], where a non-linear R_ξ gauge was used. All the diagrams are generated by *FeynArts* [123], and *FeynCalc* [124] is used to simplify the amplitudes further. The numerical evaluation of all Passarino-Veltman loop integrals [125] are performed by LoopTools [126]. And we use *Vegas* [127] as the phase space integrator.

2.1.3 Partial decay widths

The Yukawa corrections as in Figs. 2.1b−2.1g are of the order $y_f^2\alpha$, governed by the Yukawa couplings, while the EW+γ loops in Figs. 2.2a, 2.2f−2.2h involve $t\bar{t}h$ coupling and are thus of the order $y_t^2\alpha^3$, and the order of α^4 for Figs. 2.2b−2.2e. We present our results for these two decay mechanisms in Table 2.2. The first column shows the NLO EW corrections to the Yukawa interactions as given in Eq. (2.5). The inclusive corrections are small and negative. The second column gives the one-loop EW+γ contributions at the order of $y_t^2\alpha^3$ and the order of α^4, including their interference. The dominant EW+γ contributions are from diagrams in Figs. 2.2a and 2.2b, featured by $\gamma^*, Z \to f\bar{f}$. The rest of the diagrams is sub-leading and contributing about a few percent. As seen, those contributions from EW+γ loops are essentially independent of the light fermion masses and thus independent of the Yukawa couplings. The moderate dependence on the mass is due to the kinematical enhancement from the photon splitting near $M_{f\bar{f}} \sim 2m_f$. In comparison with these two decay mechanisms of the Yukawa corrections and EW+γ contributions, we see that the orders of magnitudes are comparable for the $c\bar{c}$ case. The Yukawa corrections dominate over the EW+γ contributions for the decays to $b\bar{b}$ and $\tau^+\tau^-$, while it becomes the other way around for $\mu^+\mu^-$ and e^+e^-, due to their much smaller Yukawa couplings.

From the observational point of view with the $f\bar{f}\gamma$ events, we require a photon in the final state to satisfy the minimal acceptance cuts[1]

$$E_\gamma > 5 \text{ or } 15 \text{ GeV} \quad \text{and} \quad \Delta R_{\gamma f},\ \Delta R_{\gamma \bar{f}} > 0.4, \tag{2.6}$$

[1]The kinematical variables here are in the Higgs boson rest-frame. In realistic simulations, one may need to evaluate them in the lab frame.

with the separation defined in the pseudo rapidity-azimuthal angle space $\Delta R_{\gamma f} = (\Delta\eta^2 + \Delta\phi^2)^{1/2}$. In Table 2.2, we list the partial widths and the branching fractions (BR) in the last two columns with a photon satisfying the cuts in Eq. (2.6). We note that the exclusive partial widths of $f\bar{f}\gamma$ can be sizable. The branching fractions of $b\bar{b}\gamma$, $\tau^+\tau^-\gamma$ are of the order of 0.2%, largely from the QED radiation and thus quite sensitive to the photon energy threshold. The branching fraction of $c\bar{c}\gamma$, on the other hand, is about 6×10^{-4}, with comparable contributions from the QED radiation and EW+γ processes, and thus also rather sensitive to the photon energy cut. Those for $e^+e^-\gamma$ and $\mu^+\mu^-\gamma$ are about 10^{-4}, dominantly from the EW+γ processes and thus insensitive to the photon energy threshold, to be further discussed below. It is interesting to note that it would be totally conceivable for observation of those clean leptonic channels at the HL-LHC. We also show the Higgs decay branching fractions to fermions in Fig. 2.3. It is quite informative to compare our results for the exclusive radiative decays $h \to f\bar{f}\gamma$ with those from $h \to f\bar{f}$.

It is interesting to explore some kinematical distributions to appreciate the underlying decay mechanisms and to guide future experimental searches. In Fig. 2.4, we show the photon energy distributions in the Higgs boson rest frame for the individual fermionic channels for the QED radiation (solid blue curves) and for the EW+γ processes (solid red curves) and the total (upper curves). The E_γ spectrum of the QED radiation exhibits the common infrared behavior: the observable photon energy spectrum diverges like dE_γ/E_γ, although the inclusive integrated rate is finite due to the cancelation from the virtual loop diagrams. The energy spectrum of the EW+γ processes, on the other hand, exhibits a double-hump structure as seen from the red curves in Fig. 2.4, characterizing the two dominant underlying processes

$$E_\gamma = \frac{m_h}{2}(1-\frac{m_Z^2}{m_h^2}) \approx 30 \text{ GeV, for } \gamma Z \text{ production,} \tag{2.7}$$

$$E_\gamma = \frac{m_h}{2}(1-\frac{m_{\gamma^*}^2}{m_h^2}) \approx 63 \text{ GeV, for } \gamma\gamma^* \text{ production.} \tag{2.8}$$

The diagrams of Figs. 2.2c and 2.2e have a spurious divergence in the infrared (soft) and collinear region. However, in the soft/collinear limit, the amplitude has to be proportional to the fermion mass due to conservation of angular momentum, and thus vanishes in the massless limit, as confirmed by the plots here.

We also show the invariant mass distributions of the fermion pairs in Fig. 2.5. Generally speaking, there is a correlation between the invariant mass and the energy as $M_{ff}^2 = m_h^2 - 2m_h E_\gamma$. While the invariant mass spectrum of the QED radiation has a rather smooth distribution, those from EW+γ processes are again seen with the double-humps, one near the Z-pole and another near $m_{\gamma^*} \sim 2m_f$, which becomes more pronounced for a smaller fermion mass. This is the reason why the decay rate for $e^+e^-\gamma$ is larger than that for $\mu^+\mu^-\gamma$.

Finally, we show in Fig. 2.6 the distributions of the photon separation from the fermions, defined in Eq. (2.6). As expected, the QED radiation exhibit a collinear divergence near $\Delta R_{\gamma f} \to 0$, and the EW+$\gamma$ processes lead to a back-to-back structure $\Delta R_{\gamma f} \to \pi$.

2.2 LHC SEARCH FOR $\ell^+\ell^-\gamma$

In the upcoming and future LHC programs, it is of fundamental importance to observe the Higgs boson rare decays to check the consistency of the SM and seek for hints for new physics. Given the anticipated large yield at the HL-LHC, reaching about 150 million Higgs bosons, the very clean final states $\ell^+\ell^-\gamma$ ($\ell = \mu, e$) should be among the first to look for. We now discuss their observability at the LHC.

As mentioned in Sec. 2.1.3, the radiative decays $h \to \mu^+\mu^-\gamma$ and $h \to e^+e^-\gamma$ are mainly from the chirality-conserving EW+γ loop diagrams. As seen from Figs. 2.5d and 2.5e, the leading contributions are from $h \to \gamma^*\gamma, Z\gamma \to \ell^+\ell^-\gamma$ [128–133]. It is thus a good search strategy to focus on the γ-pole and the Z-pole. Some searches have been carried out by ATLAS [134] and CMS [135, 136] at the $7-8$ TeV LHC. We present our analyses below in the hope to serve as a theoretical guidance for the future experimental searches at the LHC. We focus on the leading production for the Higgs boson via the gluon fusion. The QCD corrections are taken into account by multiplying a flat NNLO QCD K-factor of $K = 2.7$ for the gluon fusion [137]. The dominant SM background is the Drell-Yan production of the lepton pair $\ell^+\ell^-$ with an initial/final state photon radiation. We calculate the background processes at LO using *MadGraph* [138], and then multiplied by flat QCD K-factors $K = 1.4$

for $pp \to Z\gamma \to \ell^+\ell^-\gamma$ [139], and $K = 6.2$ for $pp \to \gamma^*\gamma \to \ell^+\ell^-\gamma$ [140].

2.2.1 $h \to \gamma^*\gamma \to \ell^+\ell^-\gamma$

To make the close connection with the LHC searches, we first follow the event selection cuts adopted by the CMS collaboration [136]. As the invariant mass of the lepton pair approaches to $2m_f$, the lepton pair tends to be collimated. This becomes particularly challenging for the electron channel, because the electron pair merges into one supercluster. Therefore, a single muon plus a photon trigger for the muon channel and a di-photon trigger for the electron channel are implemented. To select the signal events near the γ-pole from the Higgs decay and effectively suppress the backgrounds, we require the invariant masses to be

$$M_{\mu\mu} < 20 \text{ GeV}, \quad M_{ee} < 1.5 \text{ GeV}, \quad 120 \text{ GeV} < M_{\ell\ell\gamma} < 130 \text{ GeV}. \tag{2.9}$$

The leading (sub-leading) muon must satisfy the acceptance of the transverse momentum and pseudo-rapidity

$$p_T^\mu > 23 \text{ (4) GeV}, \quad |\eta_\mu| < 2.4. \tag{2.10}$$

The electrons must satisfy

$$|p_{Te^+}| + |p_{Te^-}| > 44 \text{ GeV}, \quad |\eta_e| < 1.44. \tag{2.11}$$

so that a multivariate discriminator can be used to separate $\gamma^* \to e^+e^-$ from jets or single electrons [136].[2] The photon must satisfy the following acceptance and be well-separated from leptons

$$p_T^\gamma > 0.3 M_{\ell\ell\gamma}, \quad |\eta_\gamma| < 1.44, \quad \Delta R_{\gamma\ell} > 1. \tag{2.12}$$

We would like to point out that, given the well-predicted kinematical properties of a fully reconstructable decay of the Higgs boson, the analyses may be improved by further utilizing the signal kinematical features. One of striking features is the mono-chromatic nature of the photon as given in Eqs. (2.7) and (2.8). We thus propose to tighten the Higgs mass cut in

[2] CMS trained a discriminator to identify electron pairs, which they claim to have an efficiency around 40%. We did not include this treatment in our simulations due to the lack of details on the discriminator. But it would not change our conclusion even if such an efficiency is included.

Eq. (2.9) as much as experimentally feasible, then boost the system to the Higgs boson rest frame, and impose the following cuts

$$60 < E_\gamma < 63 \text{ GeV in the rest frame of } \ell\ell\gamma, \tag{2.13}$$

Another alternative option is to tighten the transverse momentum cut on the photon,

$$p_T^\gamma > 55 \text{ GeV}. \tag{2.14}$$

The comparison of different cuts are demonstrated in Table 2.3, where the cross sections of signals and backgrounds, as well as the statistical significances are listed. The first row in each block in Table 2.3 is calculated using the CMS acceptance cuts in Eqs. (2.15)−(2.17), and therefore serves as the reference to illustrate possible improvements by imposing our addtional cuts based on kinematical features. Due to the stronger enhancement near the photon pole $\gamma^* \to e^+e^-$, one would be able to reach a $4.5\sigma/14\sigma$ sensitivity for the channel $h \to e^+e^-\gamma$ at the LHC with an integrated luminosity 0.3 ab^{-1}/3 ab^{-1}, and a $3.1\sigma/9.9\sigma$ for the channel $h \to \mu^+\mu^-\gamma$. It is interesting to compare our results for the radiative decay $h \to \mu^+\mu^-\gamma$ with the ATLAS projection [141] for the direct decay $h \to \mu^+\mu^-$ with the sensitivity reach of $2.3\sigma/7.0\sigma$ for 0.3 ab^{-1}/3 ab^{-1}. Similar results have also been obtained by the CMS collaboration [142].

2.2.2 $h \to Z\gamma \to \ell^+\ell^-\gamma$

To select the signal events near the Z-pole from the Higgs decay and effectively suppress the backgrounds, we first follow the CMS analysis [135] and require the invariant masses of the final state particles to be

$$M_{\ell\ell} > 50 \text{ GeV}, \quad 120 \text{ GeV} < M_{\ell\ell\gamma} < 130 \text{ GeV}. \tag{2.15}$$

The leading (sub-leading) lepton must satisfy the acceptance of the transverse momentum and pseudo-rapidity

$$p_T^\ell > 20 \text{ (10) GeV}, \quad |\eta_\mu| < 2.5, \quad |\eta_e| < 2.4. \tag{2.16}$$

The photon must satisfy the following acceptance and be well-separated from leptons[3]

$$p_T^\gamma > 15 \text{ GeV}, \quad |\eta_\gamma| < 2.5, \quad \Delta R_{\gamma\ell} > 0.4. \tag{2.17}$$

Similarily to the $h \to \gamma^*\gamma \to \ell^+\ell^-\gamma$ study, we again propose to tighten the energy and momentum cuts

$$27 < E_\gamma < 33 \text{ GeV in the rest frame of } \ell\ell\gamma, \tag{2.18}$$

$$p_T^\gamma > 25 \text{ GeV}, \tag{2.19}$$

as listed in Table 2.3. Although the tight cuts do not improve the statistical significance significantly for these channels, the signal-to-background ratios are improved by about a factor of two, reaching a 1% level. This would help to keep potential systematic errors in better control. Unlike the γ-pole feature discussed above, there is no appreciable difference between e^+e^- and $\mu^+\mu^-$ channels. One would be able to reach a $1.7\sigma/5.5\sigma$ sensitivity at the LHC with an integrated luminosity 0.3 ab^{-1}/3 ab^{-1}. Although weaker signals than the $\gamma^*\gamma$ channels above, these will significantly improve the overall observability for $h \to \ell^+\ell^-\gamma$ if the analyses can be combined.

2.2.3 $h \to J/\psi\ \gamma \to \ell^+\ell^-\gamma$

With respect to another similar final state from the Higgs boson decay, a comparative remark is in order. It has been pointed out that the Higgs rare decay to a photon associated with a heavy vector meson J/ψ may provide the direct access to the charm-Yukawa coupling via the clean leptonic decay channels [143]. The branching fraction in the SM is predicted [144–146] to be

$$\text{BR}_{\text{SM}}(h \to J/\psi\ \gamma) = 2.79 \times 10^{-6} \quad \text{and} \quad \text{BR}_{\text{SM}}(h \to J/\psi\ \gamma \to \mu^+\mu^-\gamma) = 2.3 \times 10^{-7}, \tag{2.20}$$

which is very small. Furthermore, the "direct contribution" involving the charm-Yukawa coupling is much smaller than that from the "indirect contribution" via $\gamma^* \to J/\psi$ [144], making the probe to the charm-Yukawa coupling in this channel extremely challenging.

[3] We also impose $1.44 < |\eta| < 1.57$ to simulate the CMS barrel-end cap transition region. Additional cuts from CMS $p_T^\gamma > (15/110)M_{\ell\ell\gamma}$ and $M_{\ell\ell\gamma} + M_{\ell\ell} > 185$ GeV have been also adopted.

Nevertheless, for comparison, this result has been marked in Figs. 2.5d and 2.5e, in units of keV and without the photon acceptance cuts. The superb muon pair mass resolution of the order 100 MeV would be needed in order to have a chance to dig out the weak signal from the continuum $h \to \gamma^*\gamma \to \ell^+\ell^-\gamma$ events, on top of the other SM background sources. We propose to start with the larger event samples of $\ell^+\ell^-\gamma$ as discussed in the last two sections, relax the J/ψ-specific cuts in the hope for an early observation of the $h \to \ell^+\ell^-\gamma$ signal, and then to extend the search to scrutinize the potential excess from $J/\psi \to \ell^+\ell^-$.

Dedicated searches for this decay channel have been performed by ATLAS [147] and CMS [136]. With 20 fb^{-1} luminosity, both ATLAS and CMS set a bound of BR($h \to J/\psi\ \gamma$) $< 1.5 \times 10^{-3}$ under the assumption of SM Higgs production. If the beyond-the-Standard-Model (BSM) physics only enhances the charm-Yukawa coupling by a factor of κ_c,

$$y_c^{\rm BSM} = \kappa_c y_c^{\rm SM}, \tag{2.21}$$

then this experimental bound can be translated into a loose bound on $\kappa_c \lesssim 220$ [148]. With 3 ab^{-1} luminosity at the HL-LHC, the expected upper limit to BR$_{\rm SM}(h \to J/\psi\ \gamma)$ is about 15 times the SM value [149], which corresponds to a upper bound of about $\kappa_c \lesssim 50$.

2.2.4 $h \to \tau^+\tau^-\gamma$

Besides the clean $e^+e^-\gamma$, $\mu^+\mu^-\gamma$ final states, the $\tau^+\tau^-\gamma$ channel is also of considerable interests from the observational point of view. The direct decay $h \to \tau^+\tau^+$ has been observed in the LHC experiments mainly via the vector-boson-fusion production mechanism [150,151]. The radiative decay channel $h \to \tau^+\tau^+\gamma$ may be searched for via the leading production channel of gluon fusion. To compare the rates, we have at the 14 TeV LHC,

$$\sigma(WW, ZZ \to h \to \tau^+\tau^-) = (4.2\ {\rm pb}) \times (6.3\%) \approx 260\ {\rm fb}; \tag{2.22}$$

$$\sigma(gg \to h \to \tau^+\tau^-\gamma) = (49\ {\rm pb}) \times (0.1\%) \approx 50\ {\rm fb}. \tag{2.23}$$

Thus, it is quite conceivable to observe this radiative decay mode in the future searches. The kinematical features of this decay will be rather different from those presented in the last sections due to the dominance of the QED radiation. Because of the complexity of the tau

decay final states, the signal observation and the background suppression will need to be carefully analyzed [152]. We will leave this to a future analysis.

2.3 LHC SEARCH FOR $c\bar{c}\gamma$ AND THE CHARM-YUKAWA COUPLING

It is crucially important to search for the decay $h \to c\bar{c}$, since it is the largest mode for the Higgs boson to couple to the second generation of fermions, which would be sensitive to the physics beyond the Standard Model. It has been pointed out that the charm-Yukawa coupling could be significantly modified in various BSM models [153–163]. Given the difficulty as seen above in searching for $h \to J/\psi\ \gamma \to \ell^+\ell^-\gamma$, other methods have also been explored to probe the charm-Yukawa coupling [164–170]. In this section, we discuss the possibility of constraining the charm-Yukawa coupling using the open-flavor channel $pp \to c\bar{c}\gamma$, which has a much larger branching fraction about 4×10^{-4}, as seen in Fig. 2.3. The additional photon radiation may serve as the trigger and is in favor of picking out the $c\bar{c}$ events over $b\bar{b}$ due to the larger charm electric charge.

The signal events are characterized by a high-p_T photon recoiling against a pair of charm-jets. To identify such events, an efficient charm-tagging technique is required. Although currently there is no dedicated charm-tagging being implemented at the LHC, the discrimination of a c-jet from a b-jet has been studied and used in the calibration of the b-tagging efficiency [171, 172]. ATLAS also proposed a c-tagging algorithm [20] based on the neural network that could achieve about 20% (90%) tagging efficiency with a medium (loose) cut criteria in the search for $pp \to \tilde{t}\tilde{t}^* \to (c\tilde{\chi}_1^0)(c\tilde{\chi}_1^0)$. In the current study, we choose three representative operating points listed in Table 3.1, for the c-tagging efficiency ϵ_c, and b and light jets contamination rates, ϵ_b and ϵ_j, respectively. When increasing the c-tagging efficiency from I to III, we must accept higher contaminations from a heavier quark and light jets.

The dominant background is the QCD di-jet plus a direct photon production, with the jets to be mis-tagged as c-jets. Another major background is the QCD 3-jet production, leading to two mis-tagged c-jets associated with a fake photon radiation. Following an ATLAS analysis [173], we take the photon fake rate from a light-quark jet and from a gluon

jet to be

$$\epsilon_{q\to\gamma} = 0.06\%, \quad \epsilon_{g\to\gamma} = 0.006\%, \tag{2.24}$$

respectively. We note that the fake photon contamination contributes about $(10-30)\%$ to the total background. Another potentially large background is from jet fragmentation into a real photon. We assume that the stringent photon isolation requirement will be sufficient to suppressed this QCD background, as pointed out in the prompt photon studies [174]. In our simulations, we require that both the c-jets and the photon be hard and well-isolated in the central region

$$p_T \ > \ 20 \text{ GeV}, \ \ |\eta| < 2.5, \ \text{ and } \ \Delta R > 0.4. \tag{2.25}$$

The ultimate sensitivity for the signal $h \to c\bar{c}\gamma$ depends on the invariant mass reconstruction $M_{jj\gamma} = m_h$, and thus the energy resolution of the charm-jets. In this study, we assume that the Higgs resonance peak can be reconstructed within 20% and thus we require

$$100 \text{ GeV} < M_{jj\gamma} < 150 \text{ GeV}. \tag{2.26}$$

Tightening this mass cut would linearly improve the signal-to-background ratio. We also apply $p_T^{\max} > 40$ GeV to further increase the signal-to-background ratio S/B. With these cuts applied, the background rate at the HL-LHC would be controlled below 1 kHz, within the detector's trigger ability. A fully implementable trigger scheme and the cut optimization are under investigation. After the above cuts applied, we list the numbers of events in Table 2.5 for an integrated luminosity of 3000 fb^{-1}. We note that, within the SM, the signal events from the QED radiation and the EW+γ processes are comparable, unlike the situation in $h \to J/\psi\ \gamma$ where the dominant contribution is from the "indirect contribution" via $\gamma^* \to J/\psi$. Unfortunately, with the Standard Model predictions for the signal and backgrounds being $S/B < 10^{-4}$, it would not be promising to observe this channel at the HL-LHC.

If the BSM physics significantly modifies the charm-Yukawa coupling as parameterized in Eq. (2.21), then the QED radiation will be scaled by a factor of κ_c^2. In principle, such a deviation would also change to rate through the Higgs total width. However, since the SM branching fraction is of $\mathcal{O}(10^{-4})$, we approximate the Higgs total width to be unchanged.

Although both the QED radiation and EW+γ processes contribute to the signal, it would be dominated by the QED radiation if the charm-Yukawa coupling significantly deviates from the SM value. Therefore, considering only the statistical significance by the Gaussian standard deviation

$$\sigma_{\rm SD} = \frac{N_{\rm S}^{\rm BSM}}{\sqrt{N_{\rm B}}} \simeq \frac{\kappa_c^2\, N_{\rm S}^{\rm QED}}{\sqrt{N_{\rm B}}}, \tag{2.27}$$

the 2σ-bounds on the charm-Yukawa coupling are obtained as

$$\kappa_c < 12.5\ (7.0),\ \ 11.1\ (6.3),\ \ 11.2\ (6.3). \tag{2.28}$$

for operating points I, II, III with a luminosity of 3000 fb^{-1}. Those results with the Higgs radiative decay, although still rather weak, could be comparable to the recent studies on the charm-Yukawa coupling [166–168, 170] and seem to be more advantageous to $h \to J/\psi\ \gamma$. We have complied the existing results in Table 2.6. The first three methods listed here rely on different production mechanisms and certain charm-tagging techniques with various assumptions of c-tagging efficiencies.[4] Nevertheless, they tend to have better performances than the $h \to J/\psi\ \gamma$ channel, mainly because of the larger signal rates for the open c-flavor production. Those channels should thus be complementary in the future explorations.

Before closing this section, we would like to comment on the $h \to b\bar{b}\gamma$ channel at the LHC. The current measurement on the $h \to b\bar{b}$ channel is mainly through $q\bar{q} \to Vh$ production and already of about 3σ significance with current data at the LHC [175, 176]. Although dominated by the QED radiation, the $h \to b\bar{b}\gamma$ channel is scaled down further by the bottom-quark electric charge squared, a factor of 4, compared to $h \to c\bar{c}\gamma$. As listed in Table 2.2, the braching fraction of $h \to b\bar{b}$ with $E_\gamma > 15$ GeV is about 500 times less than that of $h \to b\bar{b}$. Therefore, it would be less promising for the $h \to b\bar{b}\gamma$ channel to compete with $h \to b\bar{b}$, in contrast to our analysis above for $h \to c\bar{c}\gamma$.

[4]The authors in [166] used an integrated luminosity of 2×3000 fb^{-1} (combining both the ATLAS and CMS data), and the tagging efficiencies $\epsilon_c = 0.5$, $\epsilon_b = 0.2$, and $\epsilon_j = 0.005$; while the authors in [167] adopted the tagging efficiencies $\epsilon_c = 0.4$, $\epsilon_b = 0.3$, and $\epsilon_j = 0.01$. If using their choices for our analysis, we would have gotten a slightly stronger bound with $\kappa_c < 4.2$ and 4.9, respectively.

2.4 SUMMARY

With a large data sample of the Higgs boson being accumulated at the LHC or anticipated at the HL-LHC, it is strongly motivated to search for rare decays of the Higgs boson to test the Higgs sector in the SM and to seek for hints of BSM physics. In this work, we studied the Higgs rare decay channels $h \to f\bar{f}\gamma$ where $f = \tau, \mu, e$ and b, c and their observability at the LHC. Our results can be summarized as follows.

- This radiative decay channel receives contributions from QED corrections to the Yukawa interactions at $\mathcal{O}(y_f^2\alpha)$ and EW+γ processes at $\mathcal{O}(y_t^2\alpha^3, \alpha^4)$, as we discussed in Sec. 2.1.1 and 2.1.2. The QED corrections constitute about $Q_f^2 \times \mathcal{O}(1\%)$ to the partial widths of fermionic Higgs decays in particular through the running mass, and therefore should be taken into account for future precision Higgs physics. The difference between the QED resummed running mass in Eq. (2.3) and its $\mathcal{O}(\alpha)$ approximation only contributes to the NLO QED corrections at percentage level, due to the weakly-coupled nature of QED, as shown in Table 2.1.
- As showed in Sec. 2.1.3, the contributions from the Yukawa corrections (Fig. 2.1) and the EW+γ contributions (Fig. 2.2) exhibit quite different patterns for different fermions in the final state: While they are comparable for $c\bar{c}\gamma$, the Yukawa corrections dominate for $b\bar{b}\gamma$, $\tau^+\tau^-\gamma$. The EW+γ loops overwhelm for $\mu^+\mu^-\gamma$, $e^+e^-\gamma$, which results in the branching fractions of the order $\mathcal{O}(10^{-4})$ despite their tiny Yukawa couplings (see Fig. 2.3). The main contributions in the EW+γ loops are around the Z-pole, as well as the γ-pole near $m_{\gamma^*} \approx 2m_f$. The kinematic distributions, especially the photon energy distributions in Fig. 2.4 and the invariant mass distributions in Fig. 2.5 are quite informative to reveal the underlying decay mechanisms, and to guide the experimental searches.
- As the $e^+e^-\gamma$ and $\mu^+\mu^-\gamma$ channels exhibit the violation of the Yukawa scaling, we studied their observability at the LHC in Sec. 2.2, taking into account the signal characteristics and the SM background. We proposed new cuts based on the kinematical features in Eqs. (2.13), (2.14), (2.18), and (2.19) in addition to the selection cuts by CMS. For $pp \to \gamma\gamma^* \to \ell^+\ell^-\gamma$ channels, the statistical significances and the siginal-to-background ratios are improved by about 25% and 60%, respectively. For $pp \to Z\gamma \to \ell^+\ell^-\gamma$ chan-

nels, the siginal-to-background ratios are enhanced by about 80% while the statistical significances stay about the same. We conclude that, with an integrated luminosity 0.3 ab^{-1}/3 ab^{-1}, the channels $h \to \gamma^*\gamma \to e^+e^-\gamma$ ($\mu^+\mu^-\gamma$) should be observable at the level of $4.5\sigma/14\sigma$ ($3.1\sigma/9.9\sigma$), and the channels $h \to Z\gamma \to e^+e^-\gamma,\ \mu^+\mu^-\gamma$ should be observable at the level of $1.5\sigma/5.5\sigma$. The sensitivity could be comparable to the direct search of the two-body decay $h \to \mu^+\mu^-$.

- The decay $h \to J/\psi\ \gamma \to \ell^+\ell^-\gamma$ has the same final state but much smaller rate. The searches for the above channels will serve as the necessary early discovery and will shed light on the potential observation for $h \to J/\psi\ \gamma$.
- In Sec. 2.2.4, we pointed out a potentially observable decay $h \to \tau^+\tau^-\gamma$. We proposed the search via the leading production mechanism from gluon fusion with the help of the additional photon.
- In Sec. 2.3, we proposed to probe the charm-Yukawa coupling via the decay channel $h \to c\bar{c}\gamma$. With the help of future c-tagging techniques, we demonstrated that the charm-Yukawa coupling y_c can be bounded as $y_c^{\text{BSM}} \lesssim 6y_c^{\text{SM}}$ at 2σ level at the HL-LHC. We find it potentially comparable to the other related studies in the literature, and better than the $J/\psi\ \gamma$ channel in constraining the charm-Yukawa coupling. A more comprehensive analysis with realistic simulations is under way.

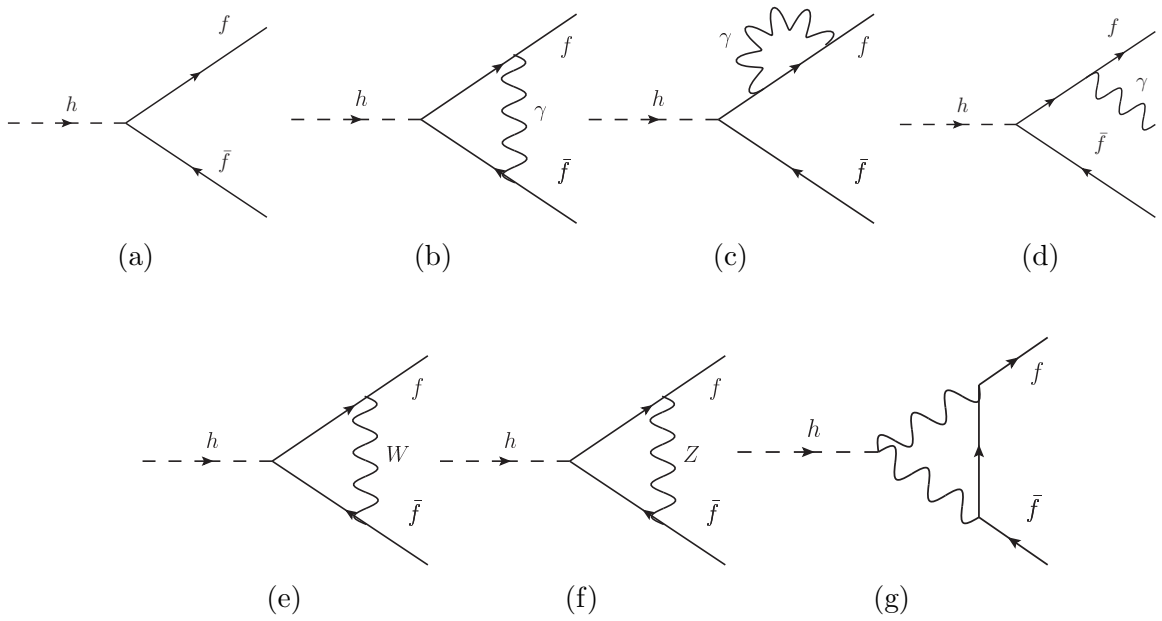

Figure 2.1: Representative Feynman diagrams of $h \to f\bar{f}$ and its EW radiative corrections up to $\mathcal{O}(y_f^2\alpha)$.

Fermion	$\bar{m}_f(m_f)$ [GeV]	$\delta\bar{m}_f^{\rm QCD}$ [GeV]	$\delta\bar{m}_f^{\rm QED}$ [MeV]	$\bar{m}_f(m_h)$ [GeV]	$\Gamma^0_{h\to f\bar{f}}$ [keV]
b	4.18	-1.39	-5.72 (1%)	2.78	1900
c	1.27	-0.657	-9.33 (0.7%)	0.604	89.7
τ	1.78	-	-27.2 (0.4%)	1.75	251
μ	0.106	-	-4.05 (0.2%)	0.102	0.852
e	0.511×10^{-3}	-	-2.20×10^{-2} (0.1%)	0.489×10^{-3}	1.96×10^{-5}

Table 2.1: The $\overline{\rm MS}$ running masses with N^{4}LO QCD and NLO QED corrections. The last column is the LO width with the running Yukawa coupling effect. The relative size of the differences between the QED resummed running mass in Eq. (2.3) and its $\mathcal{O}(\alpha)$ approximation are given in the parentheses.

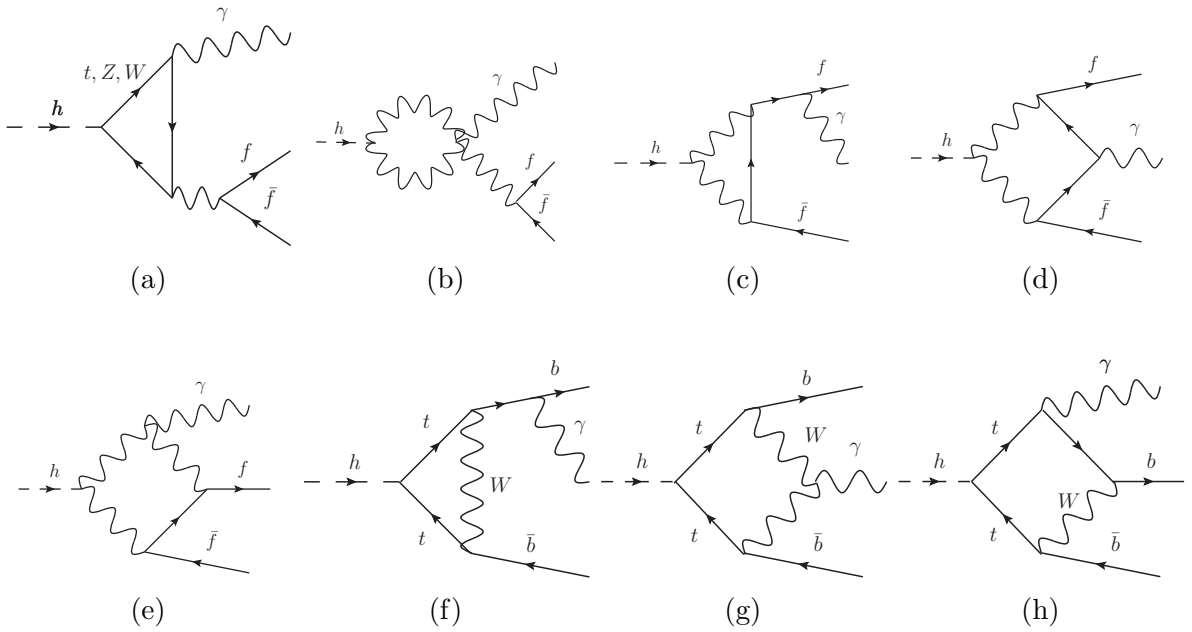

Figure 2.2: Representative Feynman diagrams of $h \to f\bar{f}\gamma$ with electroweak one-loop. (f)-(h) are present only in $h \to b\bar{b}\gamma$ channel.

	Inclusive corrections		Exclusive decay	
Decay Channels	$\delta\Gamma$ $(y_f^2\alpha)$ [keV]	$\delta\Gamma$ $(y_t^2\alpha^3, \alpha^4)$ [keV]	$\Gamma(f\bar{f}\gamma)$ [keV] $E_\gamma^{\rm cut} = 5/15$ GeV	BR$(f\bar{f}\gamma)$ $[10^{-4}]$ $E_\gamma^{\rm cut} = 5/15$ GeV
$h \to b\bar{b}(\gamma)$	-25.3	0.99	9.45/5.44	23/13
$h \to c\bar{c}(\gamma)$	-1.17	0.91	2.48/1.73	6.1/4.2
$h \to \tau^+\tau^-(\gamma)$	-1.37	0.31	10.4/5.63	25/14
$h \to \mu^+\mu^-(\gamma)$	-4.72×10^{-2}	0.41	0.436/0.420	1.1/1.0
$h \to e^+e^-(\gamma)$	-1.29×10^{-6}	0.60	0.589/0.588	1.4/1.4

Table 2.2: One-loop Yukawa and EW+γ corrections to Higgs fermionic decays. The first two columns are the inclusive corrections at the order $\mathcal{O}(y_f^2\alpha)$ and at $\mathcal{O}(y_t^2\alpha^3, \alpha^4)$, respectively. The widths and branching fractions for the exclusive decay are shown in the last two columns ($E_\gamma > 5/15$ GeV, and $\Delta R_{f\gamma} > 0.4$). The Higgs total width of 4.1 MeV is used to calculate BRs.

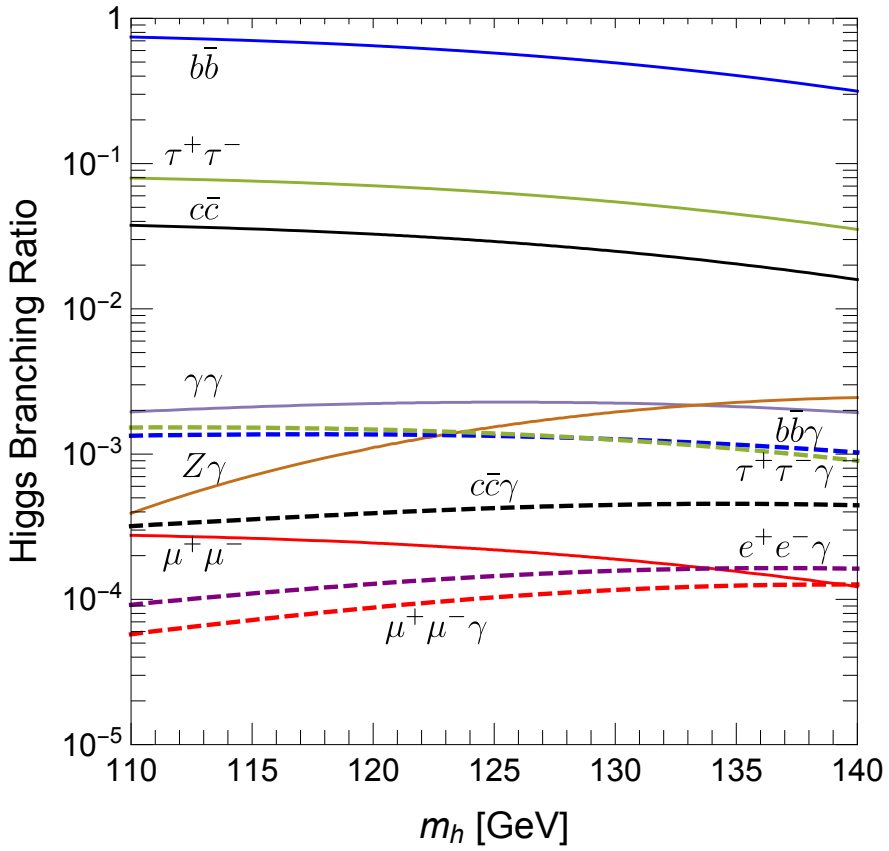

Figure 2.3: SM Higgs decay branching fractions to fermions with and without the additional photon $E_\gamma > 15$ GeV and $\Delta R > 0.4$.

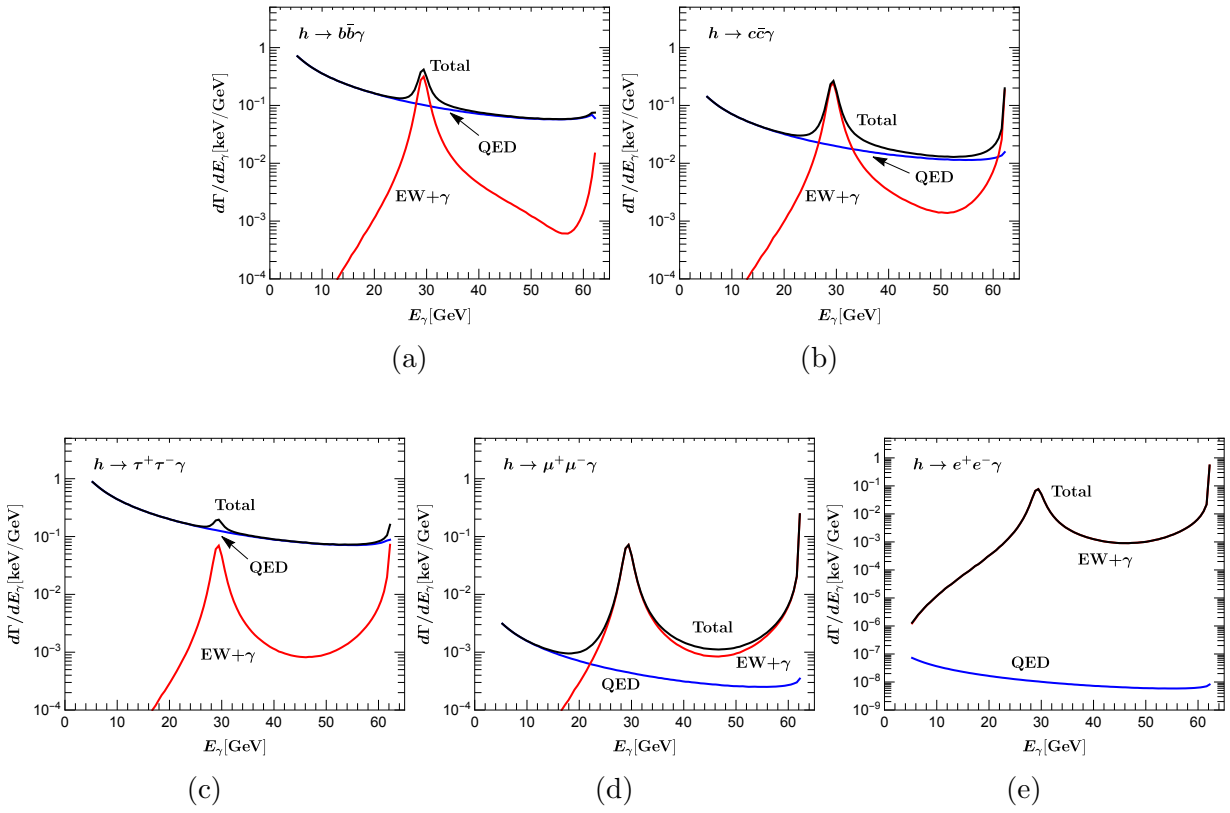

Figure 2.4: The photon energy distributions in $h \to f\bar{f}\gamma$ ($f = b, c, \tau, \mu, e$) in the Higgs boson rest frame. The blue curves are for the QED radiation (Fig. 2.1d); the red curves are for the EW+γ processes (Fig. 2.2); the upper black lines are for the total.

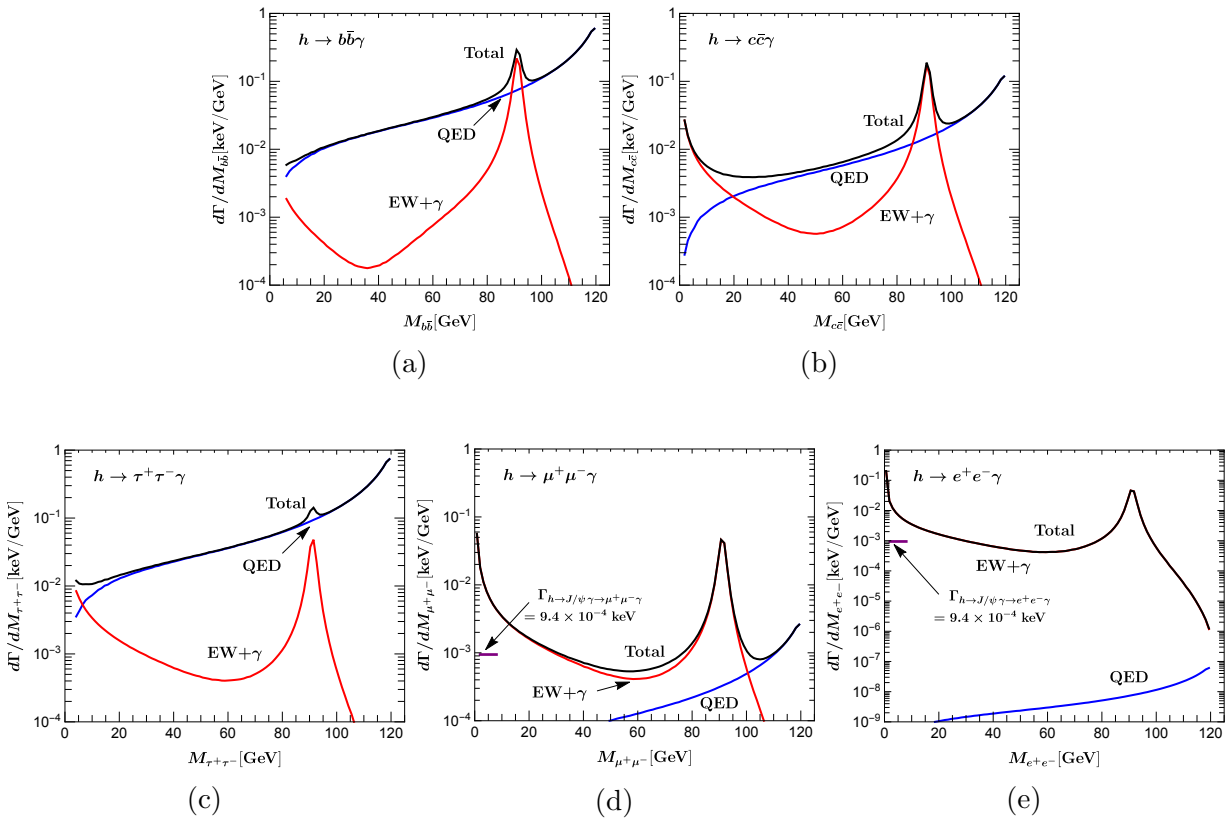

Figure 2.5: The invariant mass distributions of the fermion pair in $h \to f\bar{f}\gamma$ ($f = b, c, \tau, \mu, e$). The blue curves are for the QED radiation (Fig. 2.1d); the red curves are for the EW+γ processes (Fig. 2.2); the upper black lines are for the total. The decay widths for the channels $h \to J\psi\ \gamma \to \ell^+\ell^-\gamma$ are indicated by the horizontal bars in (d) and (e), in units of keV without the photon acceptance cuts.

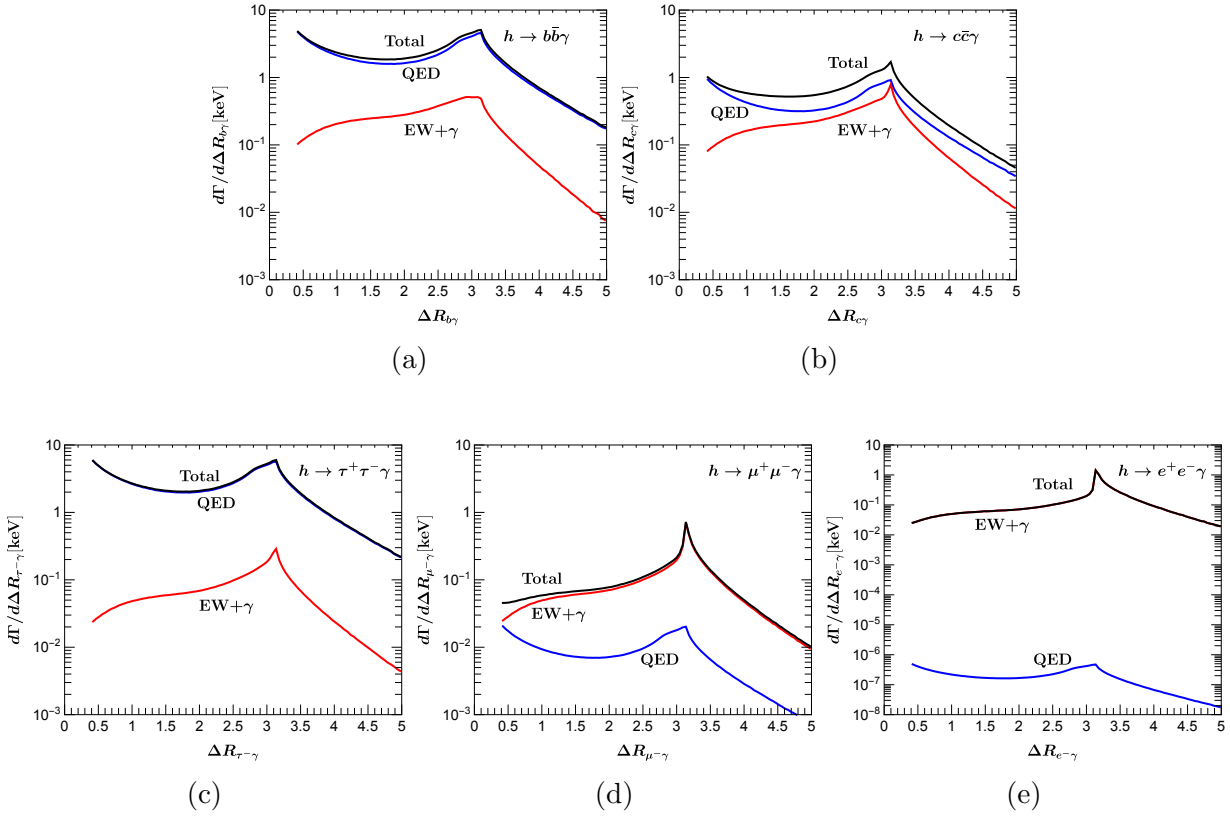

Figure 2.6: The distributions of the photon separation from the fermions in $h \to f\bar{f}\gamma$ ($f = b, c, \tau, \mu, e$) in the Higgs boson rest frame. The blue curves are for the QED radiation (Fig. 2.1d); the red curves are for the EW+γ processes (Fig. 2.2); the upper black lines are for the total.

Channel	Signal [fb]	Background [fb]	Statistical Significance with 0.3 (3) ab^{-1} luminosity
$pp \to \gamma^*\gamma \to \mu^+\mu^-\gamma$	0.69	23.5	2.47 (7.79)
$60 < E_\gamma < 63$ GeV	0.69	14.6	3.13 (9.89)
$p_{T\gamma} > 55$ GeV	0.46	11.8	2.32 (7.33)
$pp \to \gamma^*\gamma \to e^+e^-\gamma$	1.06	27.0	3.53 (11.2)
$60 < E_\gamma < 63$ GeV	1.06	17.0	4.45 (14.1)
$p_{T\gamma} > 55$ GeV	0.79	17.6	3.26 (10.3)
$pp \to Z\gamma \to \mu^+\mu^-\gamma$	1.40	214	1.66 (5.24)
$27 < E_\gamma < 33$ GeV	1.10	121	1.73 (5.48)
$p_{T\gamma} > 25$ GeV	0.91	95.9	1.61 (5.09)
$pp \to Z\gamma \to e^+e^-\gamma$	1.38	224	1.60 (5.05)
$27 < E_\gamma < 33$ GeV	1.13	126	1.74 (5.51)
$p_{T\gamma} > 25$ GeV	0.91	100	1.58 (4.98)

Table 2.3: The cross sections of signals and backgrounds, and the statistical significances of $pp \to V\gamma \to \ell^+\ell^-\gamma$, $V = Z, \gamma^*$.

Operating Point	ϵ_c	ϵ_b	ϵ_j
I	20%	10%	1%
II	30%	20%	3%
III	45%	50%	10%

Table 2.4: Representative operating points for the c-tagging efficiency (ϵ_c), b and light jets contamination rates (ϵ_b and ϵ_j).

Luminosity	Operating Point	Signal (Total)	Signal (QED)	Signal (EW+γ)	Background
3000 fb^{-1}	I	683	252	431	3.84×10^7
	II	1537	567	970	1.25×10^8
	III	3459	1275	2184	6.51×10^8

Table 2.5: Numbers of events for the signals and backgrounds with the three c-tag operating points for an integrated luminosity of 3000 fb^{-1}.

Method	κ_c upper limit projection at HL-LHC (3 ab^{-1})
$h \to c\bar{c}\gamma$ (this work)	6.3
$h \to c\bar{c}$+fit [166]	2.5
$h + c$ production [167]	2.6
Higgs kinematics [168]	4.2
$h \to J/\psi\gamma$ [149]	50

Table 2.6: Projected sensitivities for probing the $hc\bar{c}$ Yukawa coupling $\kappa_c = y_c^{\rm BSM}/y_c^{\rm SM}$ at the HL-LHC with various methods.

3.0 TESTING THE CHARM-QUARK YUKAWA COUPLING VIA $h \to c\bar{c}\gamma$ AT LHC

It is of fundamental importance to establish the pattern of the Higgs boson Yukawa couplings to fermions in order to verify the Standard Model (SM) and seek hints of physics beyond the SM (BSM). The couplings to third generation fermions have all been observed with over 5σ significance. For top quarks, there is a large indirect contribution to the gluon-gluon fusion production mode and the photon-photon decay mode. However, direct observation is important to ensure there are no BSM quantum corrections to Higgs boson production or decay. Both the ATLAS and CMS collaborations have recently observed the production of top quark pairs in association to the Higgs boson [4, 5] as well as Higgs boson decays to bottom quark pairs [6, 7]. For leptons, the challenging decay channel $h \to \tau^+\tau^-$ reached 5σ already from the LHC Run 1 data [3] and now ATLAS and CMS have both individually observed this decay mode [8, 9]. With the upgrade of the LHC to its high-luminosity phase (HL-LHC), the Higgs coupling measurements to the heaviest generation of fermions will reach an accuracy of about or better than 20% [10] and will extend to kinematic regions with high transverse momenta of the Higgs boson (p_T^h) [11, 12].

Direct observations of the Higgs couplings to the second generation of fermions will be critically important to confirm the pattern of non-universal Yukawa couplings and search for deviations from the SM as predicted in theories with an extended Higgs sector [13].

So far, there have been two experimental studies to probe the Higgs-charm Yukawa coupling (y_c). One approach is to use the clean associated production of the Higgs boson with a vector boson and exploit charm tagging [21]. A key challenge with this method is that the $h \to b\bar{b}$ contribution is large compared to the $c\bar{c}$ signal. An optimistic projection[1]

[1]This projection does not account for systematic uncertainties, nor the degradation from the extreme

for the full HL-LHC dataset suggests that 6 times the SM rate at 95% confidence level may be achievable [177]. A second approach used exclusive decays of the Higgs into a J/ψ and a photon [143]. While this final state can be well-separated from backgrounds in the $J/\psi \to \mu^+\mu^-$ channel [136, 147, 178], it suffers from a small branching ratio and modeling assumptions to extract the Higgs-charm Yukawa. In particular, the leading contribution to this process is via the *vector meson dominance* $\gamma^* \to J/\psi$, which is an order of magnitude larger than that involving the charm-quark Yukawa coupling [143–145], leading to a less sensitive upper bound on y_c of about 50 times of the SM prediction at the HL-LHC [149].

Another recent proposal for probing the Higgs-charm Yukawa coupling is to study the associated production process $gc \to ch$ [167]. This has the advantage that it is independent of the Higgs decay mode, but suffers from a low rate and significant background. Other proposals for direct or indirect probes of first- and second-generation quark-Higgs couplings [168,169,179,180] are challenging due to large SM backgrounds and contamination from other Higgs production and decay modes. A global analysis of Higgs decays can also constrain the charm-Higgs Yukawa coupling, with a projected sensitivity of about 6 times the SM expectation [148, 170].

It has been recently pointed out that the radiative decay of the Higgs boson to a pair of charm quarks could be used to constrain the charm-quark Yukawa coupling with the final state $h \to c\bar{c}\gamma$ [96]. The addition of the photon can be helpful for triggering as well as suppressing both non-Higgs and Higgs backgrounds. In particular, the electromagnetic coupling would disfavor the down-type quarks, especially the flavor-tagged $b\bar{b}\gamma$ mode. In this chapter, we examine the feasibility of a Higgs-charm Yukawa coupling measurement in the $h \to c\bar{c}\gamma$ channel at the HL-LHC. By proposing an optimal triggering strategy and simulating realistic detector effects, we show that a coupling of about 8 times the SM value may be reached at 95% confidence after the HL-LHC. This approach is complementary and competitive with other methods. We also explore the extent to which the energy upgrade of the LHC (HE-LHC) could improve the sensitivity.

The rest of the chapter is organized as follows. In Sec. 3.1, we consider the features for the signal and background processes and propose an optimal but realistic trigger. In Sec. 3.2,

pile-up at the HL-LHC, including the possible increases in lepton trigger thresholds.

we perform detailed analyses, including some basic machine learning, to obtain the optimal signal sensitivity. We extend our analyses to the HE-LHC in Sec. 3.3. The chapter ends with summary and outlook in Sec. 3.4.

3.1 TRIGGER CONSIDERATIONS AT HL-LHC

We focus on the leading Higgs production channel, gluon fusion, followed by the radiative decay

$$gg \to h \to c\bar{c}\gamma. \tag{3.1}$$

The signal is thus characterized by an isolated photon recoiling against two charm-tagged jets with a three-body invariant mass near the Higgs resonance. The energy of the two charm jets will be limited by the Higgs boson mass, and the photon tends to be soft and collinear with one of the charm quarks. Due to the large collision rate (40 MHz), enormous inelastic cross-section for $pp \to$ central activity, and limitations in hardware, most collisions at the LHC are discarded in real time. The *trigger* system is a key challenge for recording physics processes with relatively soft final states such as $h \to c\bar{c}\gamma$. The rest of this section explores the impact of triggering on the $h \to c\bar{c}\gamma$ analysis in the context of the HL-LHC.

3.1.1 Signal and background processes

Tagging jets originating from charm quarks (c-tagging) is challenging, but important for suppressing backgrounds originating from light Quantum Chromodynamic (QCD) jets and from b-quark jets. Encouragingly, a recent study from ATLAS [21] has shown very promising c-tagging results. Based on the ATLAS result, three c-tagging working points listed in Table 3.1 are studied for the $h \to c\bar{c}\gamma$ search.[2]

One of the dominant backgrounds from the $h \to c\bar{c}\gamma$ search is QCD di-jet production associated with a photon, where both jets are (mis-)tagged as c-jets. Similarly, QCD 3-jet production also contributes to the background if one of the jets is mis-identified as a photon.

[2]We choose the c-tagging working points aiming at the rejection for the largest background of the QCD light-jets production for given c-tagging efficiencies.

Operating Point	ϵ_c	ϵ_b	ϵ_j
I	20%	33%	0.13%
II	30%	33%	1%
III	41%	50%	3.3%

Table 3.1: Representative operating points for the c-tagging efficiency (ϵ_c), the b-jet mis-tag rate (ϵ_b), and the light jet mist-tag rate (ϵ_j).

In addition to these hard-scatter background processes, one or more of the tagged objects could come from an additional nearly simultaneous pp collision (pile-up). Many sophisticated pile-up mitigation techniques have been proposed [181–190] which can significantly reduce the contamination from pile-up both in the trigger and in offline analysis. However, no method can eliminate all of the pile-up and all methods perform worse (if even applicable) at the trigger level. Since pile-up conditions will be extreme at the HL-LHC (typically 200 pile-up collisions), their contribution to the event rate must be taken into account.

Current and future upgrades of the ATLAS and CMS trigger systems [191,192] will allow for multi-object requirements using offline-like information. In order to have a high efficiency, (relatively) low rate trigger for $h \to c\bar{c}\gamma$, we propose a new approach which requires two jets and one photon in the central region with invariant mass near the Higgs resonance.

3.1.2 Simulation Setup

Since the cross section for Higgs bosons is much smaller than for multijet production, the trigger rate is dominated by background. In order to estimate the trigger rate, the following background processes are simulated using `MG5aMCNLO` [138], including up to one additional

jet matched using the MLM prescription [193]:

$$pp \to j\gamma \quad \text{and} \quad pp \to jj. \tag{3.2}$$

The parton shower and hadronization are simulated with `PYTHIA6.4.28` [194], and a fast detector simulation is implemented using `DELPHES3` [195] with the detector card `delphes_card_ATLAS_PilUp.tcl`. Pile-up is modeled by mixing $\mu = 200$ minimum bias events simulated using `PYTHIA` with the hard-scatter processes.

The ATLAS and CMS trigger systems consist of a hardware trigger (L1) and a software-based high-level trigger (HLT). While the HLT jet resolution is very similar to offline, at L1, the momentum resolution for jets is much worse than offline due to the coarser detector granularity and reduced information available for the reconstruction algorithms. The event rate will have a significant contribution from events with low transverse momenta that fluctuate high, since the p_T spectrum is steeply falling. In order to model the L1 jet resolution, a normal random number is added to each jet energy with a mean of zero and a standard deviation of 13 GeV. This additional resolution is estimated from the trigger turn-on curves in Ref. [196] as follows. Consider a jet trigger that requires a L1 $p_T^{\text{L1}} > X$ GeV. The distribution of L1 jet p_T given the offline jet p_T should be approximately Gaussian (ignoring effects from the prior) with a mean μ and standard deviation σ. Suppose that $\Pr(p_T^{\text{L1}} > X | p_T^{\text{offline}} = Y) = 50\%$. Since the mean and median of a Gaussian are the same, it must be that for $p_T^{\text{offline}} = Y$, $\mu = X$. From Fig. 31a in Ref. [196], this procedure gives the relationship $p_T^{\text{offline}} \sim 2.5 \times \mu$ that is nearly independent of p_T. Now, suppose that the same L1 trigger $p_T^{\text{L1}} > X$ GeV is 99% efficient at $p_T^{\text{offline}} = Y$ GeV. This means that the 3σ tail of the Gaussian with $\mu \sim Y/2.5$ is at X. Therefore, $\sigma \sim (Y/2.5 - X)/3$. Once again using Fig. 31a in Ref. [196], this procedure gives $\sigma \sim 5$ GeV, approximately independent of p_T. Translating this 5 GeV back to an offline-scale results in $5 \times 2.5 \sim 13$ GeV. Some degradation in this resolution will occur between the LHC and the HL-LHC, but a significant amount of the loss from pile-up will be compensated by gains in performance due to detector upgrades.

In addition to degrading the resolution of reconstructed jets, pile-up is also a source of jets from additional hard multijet events and random combinations of radiation from multiple soft collisions. Offline, the most effective method for tagging these pile-up jets is

to identify the hard-scatter collision vertex and then record the contribution of momentum from tracks originating from other vertices. Full-scan tracking and vertexing is not currently available at L1, but both ATLAS and CMS will implement some form of tracking for the HL-LHC [191, 197–202]. Using Ref. [197] as an example, we assume a L1 tracking system that has nearly 100% efficiency for central charged-particle tracks with $p_T > 3$ GeV and a z_0 resolution of 0.2 cm. We further assume that some timing information will be available at L1 so that no pile-up tracks with $p_T > 3$ GeV enter the analysis. All of these conditions are optimistic, but are useful when setting a bound on what is achievable with the HL-LHC dataset. Tracks that can be identified as originating from pile-up are removed before jet clustering so that in a particle-flow-like [203, 204] jet reconstruction algorithm, pile-up jets will be reconstructed with less energy than their true energy. To further suppress pile-up jets, a transverse momentum fraction of tracks within a jet is constructed per jet:

$$r_c = \frac{\sum p_T^{\text{track}}}{p_T^{\text{jet}}}, \tag{3.3}$$

where p_T^{track} is the transverse momenta of L1 reconstructable tracks and p_T^{jet} is the transverse momenta of the corresponding jet. Large values of r_c correspond to more hard-scatter-like jets while low values of r_c are indicative of pile-up jets. Since the sophisticated pile-up mitigation techniques mentioned earlier can be employed with nearly offline-level performance at the HLT and the pile-up challenge is most severe at L1, the impact of pile-up at the HLT and offline is ignored for the results presented in later sections.

Displaced vertex reconstruction at L1 is likely not possible with high efficiency and so we assume that no explicit c-tagging will be possible at L1. At the HLT, we assume offline-like c-tagging. Flavor tagging does degrade with pile-up, but detector upgrades are expected to compensate for pile-up (Fig. 6 in Ref. [205] and Fig. 19a in Ref. [206]).

The probability for jets faking photons depends on how well-isolated photon candidates are required to be. Very stringent isolation requirements result in a purer sample of prompt photons at a cost of signal efficiency while loose requirements result in many fragmentation photons originating from jets. In our study, we follow the performance evaluation by

ATLAS [205], and assume that the fake photon rate would be

$$\epsilon_{j\to\gamma} = 2.5\ (0.7) \times 10^{-4}, \tag{3.4}$$

for a hard-scatter (pile-up) jet.[3] This false positive rate corresponds to an isolation criterion that requires the sum of the transverse energy from the calorimeter within a cone of size $R_c = 0.2$ centered around the photon candidate $E_T^{R<R_c}$ to be

$$E_T^{R<R_c} < 6 \text{ GeV}. \tag{3.5}$$

We further assume the misidentified photons carries 75% of the jet transverse momenta.

3.1.3 Trigger Design

Currently, the L1 trigger has a maximum rate of 100 kHz, while HLT has a maximum rate of 1 kHz. After the HL-LHC upgrades [207, 208], the trigger rates at L1 and HLT are expected to be about 1 MHz and 10 kHz, respectively. Therefore, it is vital to make sure the event rates of the processes are within the capacities of both the L1 trigger and the HLT.

For the L1 trigger, we required the two jets and a photon with transverse momenta

$$p_{Tj} > 27 \text{ GeV}, \quad p_{T\gamma} > 20 \text{ GeV}, \tag{3.6}$$

and well-separated in the central region

$$|\eta| < 2.5, \quad \text{and} \quad \Delta R > 0.4. \tag{3.7}$$

Pile-up jets are rejected by requiring

$$r_c > 0.2. \tag{3.8}$$

To suppress the QCD background and put the L1 trigger rate under control, we make use of the fact that the three final state objects come from the Higgs resonance decay. Therefore, we also require the invariant mass of the three trigger objects at L1 to be

$$90 \text{ GeV} < M_{jj\gamma} < 160 \text{ GeV}. \tag{3.9}$$

[3] In our simulation, we define hard-scatter jets as jets close to a truth level jet with $\Delta R < 0.3$.

As the two jets come from the Higgs decay and do not tend to have rather high transverse momenta, they are often not the two leading jets at L1. Therefore, we require the two candidate jets must be among the 5 hardest jets in each event.

The the corresponding trigger rate is listed in the first row of Table 3.2. The trigger rate is calculated using the instantaneous luminosity

$$L = 5 \times 10^{34}\ \text{cm}^{-2}\text{s}^{-1} = 5 \times 10^{-5}\ \text{fb}^{-1}\text{s}^{-1} \tag{3.10}$$

at the HL-LHC [209]. We note that the most dominant contribution at L1 comes from the QCD multi-light-jet production with a jet-faked photon. As shown in Table 3.2, the trigger proposed above would occupy less than 1% of the total bandwidth, and thus is plausible to implement as part of the HL-LHC trigger menus of ATLAS and CMS.

3.2 ANALYSES

3.2.1 Cut-based Analysis

To gain physical intuition, we start with a simple analysis that uses only thresholds on various kinematic quantities ("cut-based"). In addition to the trigger requirements as before, we select the signal events with a basic threshold on the leading jet

$$p_{Tj}^{\text{max}} > 40\ \text{GeV}. \tag{3.11}$$

Figure 3.1a shows the normalized distribution of the smaller value of the separations between photon and jets. As the photon in the signal process comes from final-state radiation, it tends to be close in angle to one of the jets. Therefore, to optimize the signal significance, we further require the smaller one of the separations between the candidate jets and photon to be

$$\Delta R_{j\gamma}^{\text{min}} < 1.8. \tag{3.12}$$

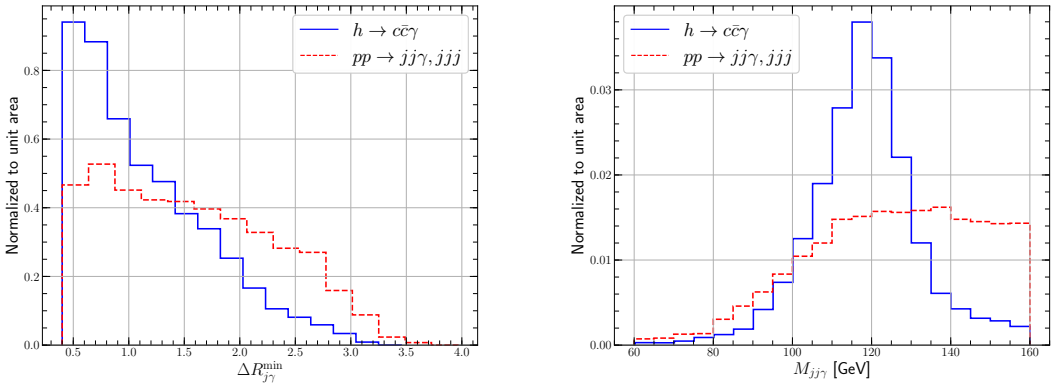

(a) (b)

Figure 3.1: Distributions of (a) the smaller value of the separations between the candidate jets and the photon; (b) the three-body invariant mass of the two candidate jets and the photon. Signal (blue solid) and background (red dashed) are both normalized to unit area.

We quantify the sensitivity using a profile likelihood fit to the three-body invariant mass in the range

$$60 \text{ GeV} < M_{jj\gamma} < 160 \text{ GeV}, \tag{3.13}$$

as shown in Fig. 3.1b, with bin widths of 5 GeV, in two event categories. The two categories are defined as having either 1 or 2 of the Higgs candidate jets c-tagged.

The expected 95% CL_s [210] upper limit (approximately at a 2σ-level) on the signal strength in the absence of systematic uncertainties is found to be[4]

$$\mu < 106, \quad 88, \quad 86, \tag{3.14}$$

for operating points I, II, III with a luminosity of 3 ab^{-1}. If the BSM physics significantly modifies the charm-Yukawa coupling, which can be parametrized using the κ-scheme,

$$y_c^{\text{BSM}} = \kappa_c \, y_c^{\text{SM}}, \tag{3.15}$$

[4]In principle, one-loop electroweak processes also contribute to $h \to c\bar{c}\gamma$, as discussed in [96]. However, it can be safely neglected given the hypothetically large Yukawa coupling y_c accessible here and the absence of interference between the QED radiation and EW contributions.

then the number of signal events would approximately scale as

$$N_{\text{sig}} \simeq \kappa_c^2 N_{\text{sig,QED}}^{\text{SM}}. \tag{3.16}$$

Then the above upper limit can be translated into

$$\kappa_c = \sqrt{\mu} < 10.4, \quad 9.4, \quad 9.3. \tag{3.17}$$

The expected numbers of events and event rates, in the range of $100 < M_{jj\gamma} < 140$ GeV, are summarized in Table 3.2, for different event categories and c-tag working points described in Table 3.1. The third column shows the numbers of events for $h \to c\bar{c}\gamma$ through QED radiation. The signal-to-background ratio S/B is between 10^{-5} to 10^{-6}. As the background is dominated by QCD multi-jet processes, it is likely that the background would be estimated using data-driven techniques. The resulting systematic uncertainties may not be small, but would likely be comparable to or smaller than the large relative statistical uncertainty on the signal. We also note that, although we aimed to optimize the light-jet rejection, the yields of the background process $h \to b\bar{b}\gamma$ due to mis-tagging is about $1.5 - 3$ times larger than those of $h \to c\bar{c}\gamma$ for different c-tagging working points, comparable to the previous studies.[5]

3.2.2 Machine Learning Analysis

In order to study the benefit from a more complex analysis approach, a boosted decision tree (BDT) is trained to distinguish the Higgs signal from the multi-jet background. The BDT is trained using `XGBoost` [211] with 5-fold cross-validation. The following 13 input features are used for training:

$$M_{j\gamma}^{\text{max}},\ M_{j\gamma}^{\text{min}},\ M_{jj},\ p_{T\gamma},\ p_{Tj}^{\text{max}},\ p_{Tj}^{\text{min}},\ \eta_\gamma,\ \eta_j^{\text{max}},\ \eta_j^{\text{min}},\ \Delta R_{j\gamma}^{\text{max}},\ \Delta R_{j\gamma}^{\text{min}},\ \Delta R_{jj},\ p_{Tjj\gamma}. \tag{3.18}$$

Even though $M_{jj\gamma}$ is the most important feature, it is not explicitly provided to the BDT in order to minimize the bias to the distribution used for the profile likelihood fit in the range of

[5] For reference, the background rates for $h \to b\bar{b}$ in the $Vh(\to c\bar{c})$ searches presented in Ref. [21] and Ref. [177] are $5 - 10$ and $1 - 5$ times higher than the signal $h \to c\bar{c}$, respectively, where different c-tagging working points are used.

Eq. (3.13) for extracting the expected upper limit.[6] The distribution of the BDT output on signal and background along with a receiver operator characteristic (ROC) curve are shown in Fig. 3.2. The two most important features used by the BDT are $p_{Tj}^{\max}$ and $\Delta R_{j\gamma}^{\min}$, which are also the features used to form the simple event selection in the previous section.

Using a selection based on the BDT, the expected 95% $\mathrm{CL_s}$ upper limit on the signal strength in the absence of systematic uncertainties is found to be

$$\mu < 91,\ \ 77,\ \ 75, \quad \Rightarrow \quad \kappa_c < 9.6,\ \ 8.8,\ \ 8.6. \tag{3.19}$$

for operating points I, II, III with a luminosity of 3 ab^{-1}. This is a modest improvement over the cut-based result by about 10%. Further gains using multivariate approaches may be possible, but will likely require advances in photon, pile-up, and c-tagging using low-level information. The distribution of $M_{jj\gamma}$ already captures most of the information available for separating signal and background given that the correct objects are identified.

3.3 HE-LHC PROJECTION

Given the recent proposal of an energy upgrade (HE-LHC) operating at $\sqrt{s} = 27$ TeV [219] after the high-luminosity phase (HL-LHC), it would be informative to estimate the potential reach for the radiative decay $h \to c\bar{c}\gamma$. However, it would be a non-trivial job to do so without knowing the high pile-up and the detector performance under the new conditions. As such, for the purpose of illustration, we can only give a crude projection by assuming a similar environment as in the above studies for HL-LHC. We consider the option with luminosity $\mathcal{L} = 3$ ab^{-1} and the same pile-up $\mu = 200$. We also assume the same L1 trigger rate.

To compensate the larger and harder background at 27 TeV, we raise the trigger threshold to

$$p_{Tj} > 40 \text{ GeV}, \quad p_{T\gamma} > 23 \text{ GeV}, \tag{3.20}$$

[6] There are many methods for performing this decorrelation using more explicit and even automated methods [212–218].

in order to maintain the same L1 event rate. As future experiments would come with significant improvements, we relax the isolation cut in Eq. (3.5) and conservatively assume that the same fake photon rate can be achieved while the photon isolation efficiency remains unchanged for photon with $p_T > 20$ GeV.

The expected 95% $\mathrm{CL_s}$ upper limit on the signal strength via cut-based analysis is found to be

$$\mu < 98,\ \ 82,\ \ 81, \quad \Rightarrow \quad \kappa_c < 9.9,\ \ 9.0,\ \ 9.0. \tag{3.21}$$

for operating points I, II, III with a luminosity of 3 ab^{-1}, in comparison with the expected 95% $\mathrm{CL_s}$ upper limit on the signal strength via BDT-based analysis to be

$$\mu < 89,\ \ 71,\ \ 70, \quad \Rightarrow \quad \kappa_c < 9.4,\ \ 8.4,\ \ 8.3. \tag{3.22}$$

We thus do not find significant improvement for probing the charm-quark Yukawa coupling at the high energy upgrade of the LHC, since the sensitivity is mostly limited by the L1 rate which in this work is assumed to stay the same at the HE-LHC. We would like to reiterate that the estimated projection here should be considered in the context of our assumptions since the results sensitively depend on the unknown pile-up and the detector performance. Given our assumptions, there is room for potential improvements should the HE-LHC experiments be constructed.

3.4 SUMMARY

While it is of fundamental importance to probe the charm-quark Yukawa coupling, it is extremely challenging at hadron colliders primarily due to the SM background and the lack of an effective trigger for the signal $h \to c\bar{c}$. We pointed out that the branching fraction for the Higgs radiative decay $h \to c\bar{c}\gamma$ is about 4×10^{-4} and thus would yield a large number of events at the HL-LHC. The existence of an additional photon in the final state may help for the signal identification and background suppression. For instance, the electromagnetic coupling would disfavor the down-type quarks, especially the flavor-tagged $b\bar{b}\gamma$ mode. We thus proposed to take advantage of the radiative decay and examine the feasibility of probing

the charm-quark Yukawa coupling. We proposed a refined triggering strategy that also included many event features combined with a boosted decision tree. Our results can be summarized as follows.

- A traditional cut-based analysis for identifying the signal $h \to c\bar{c}\gamma$ yields the sensitivity for a coupling of about 9 times of the SM value at 2σ level at the HL-LHC.
- A boosted decision tree improves the sensitivity by about 10%, reaching a coupling limit of about 8 times the SM value at 2σ.
- As a crude estimate for the sensitivity reach at the HE-LHC, assuming the same pile-up and L1 trigger rate, we found no significant improvement over the results of HL-LHC. There is room for improvement given the assumptions about the HE-LHC experiments and running conditions.

Our results with semi-realistic simulations are comparable to the other related studies [148, 167–170, 179, 180] and better than the $h \to J/\psi + \gamma$ channel [149] in constraining the charm-Yukawa coupling. Although slightly weaker than the sensitivity from the ATLAS direct search of about 3 times of the SM value [177], there are uncertainties in both analyses due to missing effects in one or the other and so more detailed experimental studies would be required to know which method will achieve the best precision. Multiple complementary approaches are needed to improve the sensitivity to test the SM prediction.

We close by making a few remarks on the possible future improvement. Since one of the limiting factors is the huge L1 event rate from QCD multi-jets background, a better photon identification would significantly improve the results. Furthermore, improved c-tagging would also enhance the sensitivity and the machine learning techniques would be more beneficial there. Finally, extending the analysis to other Higgs production modes and different kinematic regimes may help with the trigger challenge.

	Working Point	Signal (QED)	Background events	Background event rate [Hz]	$S/\sqrt{S+B}$ $[10^{-2}]$
Level-1 (L1)	No Tag	-	-	9.55×10^3	-
1 c-tag	I	269	3.37×10^8	5.62	1.47
	II	349	5.18×10^8	8.63	1.54
	III	401	8.83×10^8	14.7	1.35
2 c-tags	I	29	1.14×10^7	0.191	0.878
	II	66	2.23×10^7	0.371	1.42
	III	126	5.79×10^7	0.966	1.66

Table 3.2: Expected numbers of events of the signal and background, and event rates, in the range of $100 < M_{jj\gamma} < 140$ GeV at the HL-LHC with $\mathcal{L} = 3$ ab^{-1}. The first row gives the event rate at L1, with only the requirements in Sec. 3.1 applied. Systematic uncertainties are not accounted for in the significance calculation in the last column.

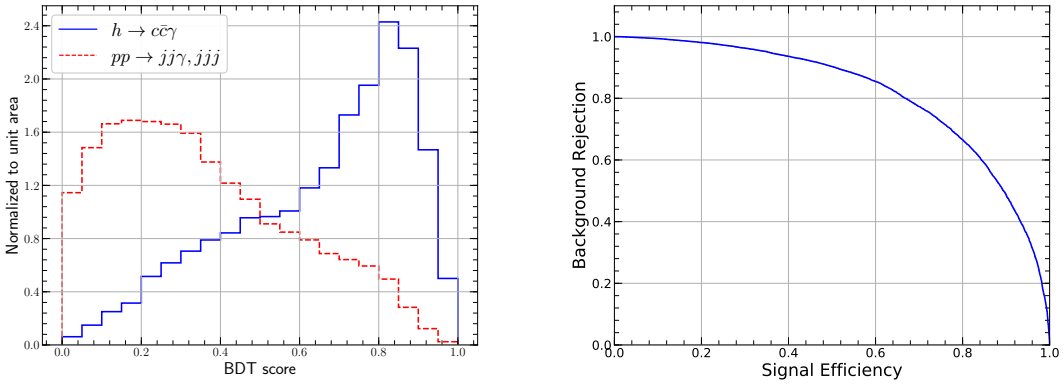

(a) (b)

Figure 3.2: (a) The distribution of the BDT score normalized to unit area. (b) Receiver operating characteristic (ROC) curve of the BDT.

4.0 ELECTROWEAK DARK MATTER AT FUTURE HADRON COLLIDERS

While the Higgs boson may serve as a lamppost to the new physics beyond the Standard Model, another important implication of new physics is the existence of the dark matter. Although its existence has been indicated by various astronomical observations, the particle nature of dark matter still remains unknown. One of the simplest realizations of weakly interacting massive particles (WIMP), that could be a natural candidate for dark matter (DM), is the electrically neutral component of a multiplet of the standard model (SM) weak interaction gauge group $\mathrm{SU}(2)_\mathrm{L}$ [220, 221]. The well-known example of such DM candidates is that of wino and Higgsino in the minimal supersymmetric SM (MSSM) with R-parity conservation [40]. For each assignment of the DM spin and the $\mathrm{SU}(2)_\mathrm{L}$ quantum numbers, the only free parameter in this model for WIMPs is the DM mass. If we further impose the requirement that a single particle species makes up the entire DM relic density through the mechanism of thermal freeze-out, we arrive at the well-known relation [222–224]

$$\Omega h^2 = 0.11 \left(\frac{2.2 \times 10^{-26}\ \mathrm{cm}^3/\mathrm{s}}{\langle \sigma_\mathrm{eff} v \rangle_\mathrm{freeze-out}} \right), \tag{4.1}$$

where, σ_eff is the effective cross-section, which includes the appropriately Boltzmann-weighted thermal averaged contribution from co-annihilating particles, important for DM belonging to electroweak multiplets [225–227]. For such electroweak DM candidates, since the annihilation rate is fixed by gauge interactions, in the limit $M_\mathrm{DM} \gg M_\mathrm{W,Z}$, it can be expressed by simple relations with only one mass-scale, M_DM. For example, for wino-like $\mathrm{SU}(2)_\mathrm{L}$ triplets, the effective annihilation rate is approximately given by [228]

$$\langle \sigma_\mathrm{eff} v \rangle_\mathrm{freeze-out} \simeq \frac{3g^4}{16\pi M_\mathrm{DM}^2}, \tag{4.2}$$

leading to the thermal relic abundance of

$$\Omega_{\tilde{W}} h^2 \simeq 0.1 \left(\frac{M_{\rm DM}}{2.2 \text{ TeV}} \right)^2 . \tag{4.3}$$

The above relation gets modified on taking into account corrections from the non-perturbative Sommerfeld enhancement in wino pair-annihilation [229–231], and $\mathrm{SU}(2)_{\rm L}$ triplets of mass around 3 TeV saturate the observed DM abundance. Similarly, for $\mathrm{SU}(2)_{\rm L}$ doublet Higgsino-like DM, the corresponding mass scale is around 1 TeV [232]. Thus, one obtains a rather robust prediction for the mass of electroweak DM making up the observed DM density. For DM lighter than the above mass scales the thermal relic density is lower, hence either making them viable candidates for a fraction of the total DM in the Universe, or requiring non-thermal production mechanisms [233].

The prospects for probing such electroweak DM at underground direct detection experiments depends on the representation of the multiplet under $\mathrm{SU}(2)_{\rm L}$ and its hypercharge. For Dirac fermions or complex scalars with non-zero hypercharge, tree-level neutral current vector interaction with the Z boson leads to a large spin-independent (SI) scattering rate with nuclei. On the other hand, for Majorana fermions and real scalars, the vector couplings vanish identically. We will focus on the detection prospects for $\mathrm{SU}(2)_{\rm L}$ triplet and doublet Majorana fermions in this study [1]. Their SI interaction rate with nuclei is suppressed, as it is generated only at the one-loop order, and suffer from accidental cancellations between different class of diagrams [236–241]. For wino-like triplet states with zero hypercharge, the SI cross-section with proton is only mildly sensitive on the DM mass, and in the limit $M_{\rm DM} \gg M_W$ is found to be around $2.3 \times 10^{-47}\text{cm}^2$, including higher order corrections at next-to-leading order in α_S [236–239]. Thus, to probe these DM candidates at the direct detection experiments, we would need multi-ton scale detectors. For Higgsino-like $\mathrm{SU}(2)_{\rm L}$

[1] $\mathrm{SU}(2)_{\rm L}$ doublet fermions with non-zero hypercharge, such as the pure Dirac Higgsino in the MSSM, have a vector interaction with the Z boson. However, effective couplings with the Higgs boson (such as those induced by integrating out the gauginos in the MSSM) generate a small mass splitting, thereby decomposing the neutral Dirac fermion into two Majorana fermions, and avoiding the vector interaction. We also need to ensure that such a mixing with the gauginos does not induce large SI scattering through the Higgs boson exchange. For mass splittings larger than $\Delta m \gtrsim \mathcal{O}(100)$ keV, inelastic up-scattering between two Majorana Higgsino mass eigenstates [234, 235] is also avoided. Such mass splittings are however typically so small that they would not affect the collider analyses in the following sections.

doublet Majorana fermions, the rate is further suppressed, and the cross-section is around 10^{-49}cm^2, which is below the irreducible neutrino floor, making a detection challenging.

Indirect detection experiments looking for gamma-ray signals from annihilating DM in low-background dwarf-spheroidal galaxies (dSphs) constitutes a more promising probe for electroweak DM candidates [221, 229–231, 242]. For wino-like DM, there is an enhancement of the annihilation rate in certain mass regions in which the exchange of multiple electroweak gauge bosons between the DM particles in the initial state gives rise to a long-range potential (Sommerfeld enhancement) [229–231]. The current constraints from the Fermi-LAT search for diffuse gamma ray signal from dSphs excludes wino DM mass below around 400 GeV, and in a small window around 2 TeV, if it makes up the whole of DM [242,243]. However, for these mass values, thermally produced winos are under-abundant. For this reason, as well as to cover the yet-unexplored window in indirect searches, collider probe becomes necessary. For Higgsino-like DM, the annihilation rate is significantly smaller, and the current dSphs constraints only probe mass values smaller than around 350 GeV, if they saturate the required DM abundance [244]. Thus for Higgsino-like states, the collider probe is crucial as well.

Directly probing heavy electroweak DM at the 14-TeV LHC is found to be very challenging − primarily because of lower Drell-Yan pair production rates for the heavy DM particle and their charged counterparts, and also for the lack of clean experimental handles which can be utilized to suppress the relevant SM backgrounds. Motivated by the supersymmetric wino and Higgsino scenarios, the ATLAS and CMS collaborations have carried out several different searches for electroweak DM at the LHC [245–249]. The main collider signatures in the framework under consideration are governed by the small mass splitting between the charged and neutral components of the EW multiplets of about a few hundred MeV. As such, there are broadly two class of searches which are mostly independent of detailed model assumptions. The first one is the classic monojet and missing transverse momentum search for a pair-produced DM particle in association with a hadronic jet originating from initial state radiation. The second one utilizes the fact that, in the absence of large additional corrections from higher-dimensional operators, the mass splitting between the charged and neutral components of the DM $\text{SU}(2)_\text{L}$ multiplets is small − of the order of a few hundred MeV. Thus, the decay length of the electrically charged state is large enough to be observed

as a disappearing charged track at the LHC detectors. This additional handle helps reduce the SM backgrounds compared to the first search category with only missing momentum requirements, though it does introduce additional systematic uncertainties in the background estimate. The current LHC lower bound using these search strategies for wino-like (Higgsino-like) states is around 460 (152) GeV at 95% C.L. [246, 247], and as we will see later, it is projected to improve to 900 (300) GeV at the end of the high-luminosity LHC run (HL-LHC) for wino (Higgsino) states.

Studies on the prospects of finding electroweak DM at future hadron colliders with the 14-TeV and 100-TeV centre of mass energies have been performed earlier with a detector design similar to that of the 8 TeV Run-1 LHC [250, 251]. Possible interesting proposals for improving the reach of Higgsino-like DM in disappearing charged track search have also been put forward [252, 253]. In particular, the latter studies investigated the impact of reducing the required number of hits in the tracking system by the candidate charged track, and found that under optimistic scenarios for the SM background estimates, the reach at a 33 TeV [253] and subsequently a 100 TeV collider [252] can be significantly improved for Higgsino states.

In this chapter, we examine the discovery potential of the electroweak DM at future high energy hadron colliders. We consider two proposals: a 27-TeV upgrade of the LHC (HE-LHC), which can be achieved within the current LHC ring with upgraded magnets [254], and the proposed 100 TeV future collider [255] at CERN (FCC-hh) [256, 257] and in China (SppC) [258]. We adopt the updated detector design with the new Insertable B-Layer (IBL) included in the ATLAS tracking system for the Run-2 13 TeV LHC [259], and model our background estimates by extrapolating the ATLAS results, using similar methods as adopted in previous studies [250, 251].

The subsequent sections are organized as follows. In Sec. 4.1 we briefly describe the relevant details of the electroweak DM model, the signal and background processes for the search channels utilized in our analysis, and the simulation framework adopted. In Sec. 4.2 we discuss the distribution of different kinematic observables used to distinguish between the signal and the background processes, the event selection criteria, and a simple optimization of the kinematic selections to improve the signal to background ratio. We then go on to present our main results, discussing the comparative reach of 14-TeV HL-LHC, 27-TeV HE-

LHC and the 100-TeV FCC-hh/SppC options, in Sec. 4.3. We conclude with a brief summary of our results and an outlook in Sec. 4.4.

4.1 ANALYSIS SETUP

4.1.1 Effective interaction Lagrangian

We begin with a brief review of the relevant effective interactions of pure wino and Higgsino states with the SM sector, as well as the radiative mass splitting between the charged and neutral components of the electroweakinos generated by SM gauge interactions. Although we will adopt the supersymmetric terminology to describe the $\mathrm{SU}(2)_\mathrm{L}$ doublet and triplet DM scenarios in the following, our discussion is valid in general for an effective theory, with the SM augmented by a stable DM multiplet.

The effective interaction Lagrangian at dimension-4 for charged ($\tilde{\chi}^\pm$) and neutral ($\tilde{\chi}^0$) winos with the SM electroweak gauge bosons is given as

$$\mathcal{L}^W_{V\chi\chi} \supseteq -g\left(\overline{\tilde{\chi}}^0\gamma^\mu\tilde{\chi}^+W^-_\mu + \mathrm{h.c.}\right) + g\overline{\tilde{\chi}}^-\gamma^\mu\tilde{\chi}^-\left(\cos\theta_W Z_\mu + \sin\theta_W A_\mu\right), \tag{4.4}$$

where g is the $\mathrm{SU}(2)_\mathrm{L}$ gauge coupling, and θ_W is the weak-mixing angle. In the absence of large corrections from couplings with the fermion and sfermion sectors of the MSSM, these gauge interactions induce a mass splitting between the charged and neutral winos ($\delta m_{\tilde{W}}$), which, at the two-loop order can be parametrized as follows [260]

$$\begin{aligned}\frac{\delta m_{\tilde{W}}}{1\ \mathrm{MeV}} = &-413.315 + 305.383\left(\log\frac{m_{\tilde{\chi}_0}}{1\ \mathrm{GeV}}\right) - 60.8831\left(\log\frac{m_{\tilde{\chi}_0}}{1\ \mathrm{GeV}}\right)^2 \\ &+ 5.41948\left(\log\frac{m_{\tilde{\chi}_0}}{1\ \mathrm{GeV}}\right)^3 - 0.181509\left(\log\frac{m_{\tilde{\chi}_0}}{1\ \mathrm{GeV}}\right)^4,\end{aligned} \tag{4.5}$$

where $m_{\tilde{\chi}_0}$ is the neutral wino mass. The corresponding decay lifetime of the charged wino to a neutral wino and a charged pion is given in terms of the $c\tau$-value by [260]

$$c\tau \simeq 3.1\ \mathrm{cm}\left[\left(\frac{\delta m_{\tilde{W}}}{164\ \mathrm{MeV}}\right)^3\sqrt{1-\frac{m_\pi^2}{\delta m_{\tilde{W}}^2}}\ \right]^{-1}, \tag{4.6}$$

with m_π being the charged pion mass. We have normalized the mass difference to 164 MeV, which is the mass splitting in the limit of heavy WIMPs, $M_{\rm DM} \gg m_W$.

Similarly, the effective interaction Lagrangian at dimension-4 for charged ($\chi_H^\pm$) and neutral (χ_H^0) Dirac Higgsinos with the SM electroweak gauge bosons is given by

$$\begin{aligned}\mathcal{L}^H_{V\chi\chi} \supseteq & -\frac{g}{\sqrt{2}}\left(\overline{\chi_H^0}\gamma^\mu\chi_H^-\, W_\mu^+ + \text{h.c.}\right) + g\overline{\chi_H^-}\gamma^\mu\chi_H^-\left(\frac{1/2-s_W^2}{c_W}\, Z_\mu + s_W A_\mu\right) \\ & - \frac{g}{2c_W}\,\overline{\chi_H^0}\gamma^\mu\chi_H^0\, Z_\mu, \end{aligned} \tag{4.7}$$

with $s_W = \sin\theta_W$ and $c_W = \cos\theta_W$. The above interactions induce a one-loop mass splitting between the charged and neutral states ($\delta m_{\tilde{H}}$) which can be written as

$$\delta m_{\tilde{H}} = \frac{g^2}{16\pi^2} m_{\tilde{H}} \sin^2\theta_W f\left(\frac{m_Z}{m_{\tilde{H}}}\right), \tag{4.8}$$

where the loop function is given by

$$f(r) = r^4 \ln r - r^2 - r\sqrt{r^2-4}(r^2+2)\ln\frac{\sqrt{r^2-4}+r}{2}. \tag{4.9}$$

The corresponding decay lifetime of the charged Higgsino to a neutral Higgsino and a charged pion can be parametrized in terms of the $c\tau$-value as [253]

$$c\tau \simeq 0.7 \text{ cm} \times \left[\left(\frac{\delta m_{\tilde{H}}}{340 \text{ MeV}}\right)^3 \sqrt{1-\frac{m_\pi^2}{\delta m_{\tilde{H}}^2}}\,\right]^{-1}. \tag{4.10}$$

As we can observe from Eqs. (4.6) and (4.10), for typical values of the mass splitting between the charged and neutral states, the charged wino has a considerably larger decay length compared to the charged Higgsino. This makes the search for winos more favorable than Higgsinos in the disappearing charged track analysis.

4.1.2 Signal and background processes

As mentioned in the introduction, we will focus on two different search strategies for electroweak DM at hadron colliders, both of which are being carried out by the ATLAS and CMS collaborations at the Run-1 and Run-2 LHC: namely, the monojet plus missing transverse momentum search and the disappearing charged track analysis. For the 27-TeV HE-LHC and 100 TeV FCC-hh/SppC upgrades, we will also discuss a simple optimization of the kinematic selection criteria in the next section. In this section, we briefly describe the signal and background processes for these search channels, as well as the Monte Carlo (MC) simulation framework adopted for them in our analysis.

For the signal process, we consider the electroweak production of chargino and neutralino pair in proton-proton collisions, where the dominant contribution to the total cross-section comes from the following three sub-processes:

$$\begin{aligned} pp &\to \tilde{\chi}_1^+ \tilde{\chi}_1^- + \text{jets}, \\ &\to \tilde{\chi}_1^\pm \tilde{\chi}_i^0 + \text{jets}, \\ &\to \tilde{\chi}_i^0 \tilde{\chi}_j^0 + \text{jets}, \text{ with } i,j = 1,2, \text{for Higgsino-like states.} \end{aligned} \tag{4.11}$$

Thus, in each event for the first two sub-processes either one or two charged states are produced, which is relevant for the disappearing track analysis. All three sub-processes contribute to the signal in the monojet search channel, since the charged pions from the chargino decay are too soft to detect at hadron colliders [2]. In the context of the MSSM, we have assumed here that all other sparticles except the DM multiplet is decoupled. Therefore, for the wino DM scenario, there is one light Majorana neutralino and one light chargino present in the low-energy spectrum. For the corresponding case of Higgsino DM, there is again one light chargino, while the number of light Majorana neutralinos is two.

For both the search channels, with the presence of missing transverse momentum as one of the criteria, the dominant SM backgrounds come from single weak boson production in association with multiple hard jets. The total background cross-section in final states without any charged leptons is thus dominated by Z+jets production, with $Z \to \bar{\nu}\nu$. A similar

[2] Future electron-proton colliders, such as the LHeC or FCC-eh, could have unique sensitivity to BSM signals with such soft final state particles, and to short lifetimes of the decaying charged states [261].

order of magnitude contribution is obtained from $W^{\pm}$+jets production, with $W^+ \to \ell^+\nu$ ($\ell = e, \mu, \tau$), where the charged lepton (except for hadronic decays of the tau) falls outside the tracker coverage of the detector. A sub-dominant component of the total background also comes from the top quark pair production process.

In our analysis, for both the signal and the background processes, we have generated MC events with matrix element (ME) and parton-shower matched using the MLM prescription [193], whereby we have included up to two additional hard jets at the ME level. All the parton level event samples have been obtained using the `MG5aMCNLO` [138, 262] event generator, followed by parton shower and hadronization with `PYTHIA6.4.28` [194], and fast detector simulation using `DELPHES3` [195, 263]. We have employed the `CTEQ6L1` [264, 265] parton distribution functions, and have used the event-by-event default choice for the factorization and renormalization scales as implemented in `MG5aMCNLO`. Jets have been defined using the `anti-`k_T algorithm [266–268], with the radius parameter $R = 0.5$.

In order to obtain a large statistics of MC events in the kinematic region of our interest, we generated our event samples after strong cuts on the transverse momentum of the leading jets at the ME level. For the dominant as well as very large Z+jets background, we have applied an additional generation level cut on the missing transverse momentum variable. This makes it difficult for us to normalize our total matched cross-sections to next-to-leading order (NLO) in QCD results, since it requires a fully differential NLO simulation to obtain the proper K-factors after the above cuts. Therefore, we abstain from adopting a normalization by such K-factors for both the signal and background processes [3].

A few more comments are in order for the disappearing charged track analysis. Since our detector simulation cannot reproduce the trigger efficiency and the charged track selection efficiency obtained by the ATLAS collaboration, we have used an overall rescaling fudge factor of 0.1 to normalize our signal event yields to those reported by ATLAS [246].

Within our simulation framework, it is also difficult to estimate the SM background rates in the disappearing charged track analysis, which ensue from fake tracklets, missing leptons, and charged hadrons. We therefore adopt an empirical formula reported by the ATLAS

[3] Since both the signal and background are electroweak processes, they have a similar NLO K-factor of about 1.4 [269,270]. Therefore, we expect the higher order corrections not to change the signal to background ratio S/B appreciably, but to slightly improve the statistical significance of the signal $S/\sqrt{B}$.

collaboration by fitting the data obtained in their LHC Run-2 analysis. The differential distribution of the disappearing charged tracks as a function of their transverse momenta (p_T) can be parametrized as follows:

$$\frac{dN_{\text{Events}}}{dp_T} = N_0 \exp\left(-p_0 \log(p_T) - p_1 \log(p_T)^2\right), \tag{4.12}$$

with $p_0 = 0.894$ and $p_1 = 0.057$, as obtained by a fit to the fake tracklet data from the 13 TeV LHC. The overall normalization factor N_0 is obtained to match the number of background events from fake tracklets obtained in the ATLAS analysis involving tracks with $p_T > 20$ GeV. For different collider energies the functional dependence on the track p_T is assumed to remain the same, while we rescale the overall normalization by the ratio of the Z+jets total cross-section, as also assumed in previous studies. Although Z+jets gives the dominant contribution to the total cross-section in the final state of interest (with a substantial missing transverse momentum and no charged lepton), there are also significant contributions from W+jets and $t\bar{t}$+jets processes. In order to take these latter contributions into account, along with the uncertainty in the background estimate using our simple methodology, we have varied the central value of the background rate by a factor of five in our subsequent analyses [4].

4.2 KINEMATIC SELECTION OF SIGNAL REGION

4.2.1 Mono-jet $+\not{E}_T$ search

The kinematic selection criteria employed in the monojet plus missing transverse momentum channel is well-established, with increasingly stronger requirements on the transverse momenta of the hadronic jets (p_{Tj}) and the missing transverse momentum ($\not{E}_T$), as the collider energy is increased. While we have optimized the above requirements for the HE-LHC and the FCC-hh/SppC analyses, for the corresponding HL-LHC scenario, our analysis

[4] As we do not perform a shape analysis, only the total number of events after the relevant cut enters our final estimate. Although the actual shape is relevant in the cut optimization, we keep the shape fixed within the scope of our study.

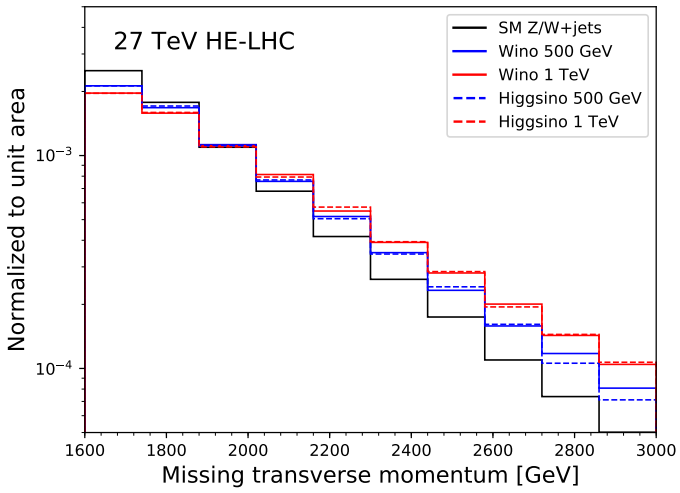

Figure 4.1: Normalized distribution for missing transverse momentum in single weak boson (W/Z) production associated with multiple hard jets, in the SM (black solid lines), and in charged and neutral wino and Higgsino pair production events at the 27-TeV HE-LHC. The results are shown for two representative mass values of the winos (solid lines) and Higgsinos (dashed lines): 500 GeV (blue) and 1 TeV (red).

closely follows the one by the CMS collaboration in Ref. [271], to facilitate comparison. In our optimization of the kinematic selections for the higher centre of mass energies, we have maximized the statistical significance of the search, at the same time ensuring a large signal event rate.

In Fig. 4.1, we show the normalized distributions for missing transverse momentum at the 27 TeV HE-LHC. The distributions are presented for both the signal process and the dominant SM background process of single weak boson (W/Z) production with multiple hard jets (black solid line). For the signal process, we show two representative mass values each for wino pair production (solid lines), and Higgsino pair production (dashed lines): namely, 500 GeV (blue) and 1 TeV (red). As we can see from this figure, for higher mass of the winos and Higgsinos, the p_T spectrum of the associated ISR (and hence the $\not{E}_T$) is also harder, as expected. A requirement of approximately $\not{E}_T > 2$ TeV can potentially enhance the signal over background ratio for the above electroweakino mass values.

For the event selection of the monojet channel, we require that all events have a hard

$\sqrt{s}$	$\not{E}_T^{\rm min}$ [GeV]	p_{T,j_1} [GeV]	p_{T,j_2} [GeV]	$p_{T,\tau}$ [GeV]
14 TeV	650	300	30	30
27 TeV	1800–2700	400	60–160	30
100 TeV	4800–7000	1200	250–450	40

Table 4.1: Threshold values of different kinematic observables, namely, $\not{E}_T^{\rm min}, p_{T,j_1}, p_{T,j_2}, p_{T,\tau}$ for different collider options in the monojet analysis, and the optimization range considered for the HE-LHC and FCC-hh/SppC colliders. See text for details.

central jet with a high threshold and also allow for a second jet with

$$p_T > p_{T,j_1}, \quad |\eta| < 2; \quad p_T > p_{T,j_2}, \quad |\eta| < 4.5; \quad \text{and} \quad \Delta R > 0.5, \tag{4.13}$$

and with an azimuthal separation $\Delta\phi_{j_1,j_2} < 2.5$, to remove back-to-back jets. Any additional jets passing the minimum threshold $p_T > p_{T,j_2}$ within $|\eta| < 4.5$ are vetoed, *i.e.,* $N_{\rm jets} \leqslant 2$. A lepton veto is applied with events with electrons (muons) with $p_T > 20$ GeV, $|\eta| < 2.5$ (2.1) are excluded. Events with hadronic taus with $p_T > p_{T,\tau}$, $|\eta| < 2.4$ are also vetoed. Finally, an optimized requirement on missing transverse momentum is applied, with $\not{E}_T > \not{E}_T{}^{\rm min}$.

We summarize the threshold values of the cuts, namely, $\not{E}_T^{\rm min}, p_{T,j_1}, p_{T,j_2}, p_{T,\tau}$, for different collider options in Table 4.1. As mentioned earlier, we vary the $\not{E}_T$ and p_{T,j_2} cuts for the 27 TeV and 100 TeV scenarios in the ranges specified in the table to optimize the signal significance.

The optimized set of kinematic cuts for the HE-LHC is given in Table 4.2, with the corresponding signal and background cross-sections. Here, basic cuts refers to the requirement of $\not{E}_T > 1600$ GeV at the matrix-element level. We also show the efficiency of each cut on the signal (ϵ_S) and background rates (ϵ_B), as well as the improvement in the signal-to-background ratio (S/B) with each cut. As we can see from Table 4.2, for the representative mass value of 500 GeV for the chargino and neutralino states, the S/B ratio that can be achieved is at most 4.59×10^{-2} for wino-like states, and 2.32×10^{-2} for Higgsino-like states.

Cuts	Bckgrnd [fb]	ϵ_B	$m_{\tilde{W}} = 500$ GeV			$m_{\tilde{H}} = 500$ GeV		
			Signal [fb]	ϵ_S	S/B [%]	Signal [fb]	ϵ_S	S/B [%]
Basic cuts	26.50	-	0.40	-	1.52	0.21	-	0.79
$p_{Tj_1} > 400$ GeV	26.12	0.99	0.40	0.99	1.52	0.21	0.99	0.79
$N_{\text{jets}} \leqslant 2$	21.13	0.81	0.33	0.83	1.55	0.17	0.83	0.81
$\Delta\phi_{j_1,j_2}$	20.13	0.95	0.32	0.98	1.60	0.17	0.98	0.83
Muon veto	16.13	0.80	0.32	1.00	1.99	0.17	1.00	1.04
Electron veto	12.78	0.79	0.32	1.00	2.52	0.17	1.00	1.31
Tau veto	10.88	0.85	0.31	0.98	2.88	0.16	0.98	1.50
$\not{E}_T > 2.2$ TeV	1.03	0.09	0.05	0.15	4.59	0.02	0.15	2.32

Table 4.2: Signal and background cross-sections in the monojet+$\not{E}_T$ channel at the 27-TeV HE-LHC after successive selection cuts on different kinematic observables; see text for details on the selection criteria. The efficiency of each cut on the signal (ϵ_S) and background rates (ϵ_B), along with the signal to background ratio (S/B) are also shown. We have shown the results for the representative mass value of 500 GeV for the wino and Higgsino states.

As such, the systematic errors could be a main concern for the monojet+$\not{E}_T$ search. However, encouragingly, the theoretical errors on the W/Z+jets background rates have been reduced to a few percent level with the recent NNLO QCD corrections and NLO electroweak corrections supplemented by Sudakov logarithms at two loops [272]. At the same time, the current uncertainties on the estimate of the background cross-sections using data-driven methods are also at the few percent level [273], which are expected to further reduce with the accumulation of higher statistics.

4.2.2 Disappearing charged track search

We have discussed the methodology adopted for our estimate of the normalization and the shape of the SM backgrounds in the disappearing charged track search analysis in Sec. 4.1.2. We also described the lifetime (expressed as $c\tau$) of the charged wino and Higgsino states in their rest frame in Sec. 4.1.1. The decay length of the charginos in the LHC detectors is determined by $c\tau$ and the transverse momentum distribution of the chargino. We show in Fig. 4.2 (left column) the transverse momentum distribution of the chargino track for both the wino-like (solid line) and the Higgsino-like (dashed line) scenarios at the 27 TeV

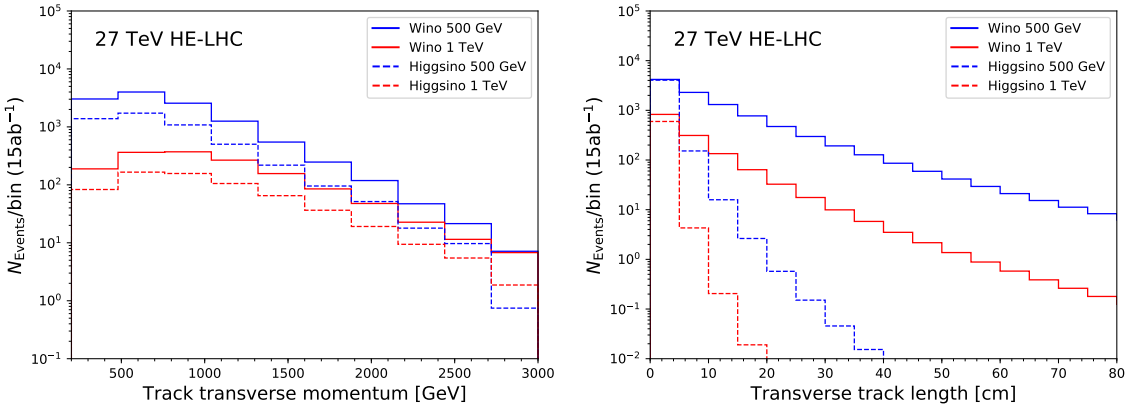

Figure 4.2: Transverse momentum (left panel) and transverse track length (right column) distribution of disappearing charged tracks in charged and neutral wino (solid lines) and Higgsino (dashed lines) pair production events (with at least one chargino in each event), for the 27-TeV HE-LHC with 15 ab^{-1} data. The results are shown for two representative mass values of the winos and Higgsinos: 500 GeV (blue) and 1 TeV (red).

HE-LHC with 15 ab^{-1} data. The distributions have been shown for the chargino mass value of 500 GeV (blue) and 1 TeV (red). As we can see from this figure, the overall shape of the distribution is similar for Higgsino and wino-like states, while the total production cross-section is a factor of two larger in the latter scenario.

Combined with the proper life-time, the transverse momentum distribution of the tracks determine the transverse charged track length in the signal events, which is the most important observable in the disappearing charged track analysis. We show this distribution in Fig. 4.2 (right column), with the parameter choice and color coding used same as for the previous figure. It is clear from this figure that in order to probe a Higgsino of mass $\mathcal{O}(1$ TeV), we need tracking coverage in the range of $10 - 20$ cm, which is now possible after the inclusion of the additional B-layer in the Run-2 upgrade of the ATALS detector.

We now briefly describe the event selection criteria used for the disappearing charged track analysis. We require one hard central jet plus large missing momentum in the events with

$$p_T > p_{T,j_1}, \quad |\eta| < 2.8, \quad \not{E}_T > \not{E}_T{}^{\text{min}}. \tag{4.14}$$

Charged lepton veto is applied as described above for the monojet channel. Furthermore,

$\sqrt{s}$	$\not{E}_T$ [GeV]	p_{T,j_1} [GeV]	p_{T,j_2} [GeV]	$p_{T,\text{track}}$ [GeV]
14 TeV	150	150	70	250
27 TeV	400 – 700	400 – 600	140	400 – 700
100 TeV	1000 – 1400	700 – 1400	500	1000 – 1400

Table 4.3: Threshold values of different kinematic observables, namely, $\not{E}_T^{\text{min}}, p_{T,j_1}, p_{T,j_2}$ and $p_{T,\text{track}}$ for different collider options in the disappearing charged track analysis, and the optimization range considered for the HE-LHC and FCC-hh/SppC colliders. See text for details.

the missing transverse momentum vector is required to have an azimuthal separation from the leading jet by

$$\Delta\phi_{j_1,\not{E}_T} > 1.5. \tag{4.15}$$

If there is a second jet with

$$p_T > p_{T,j_2}, \quad |\eta| < 2.8, \tag{4.16}$$

in addition, $\Delta\phi_{j_2,\not{E}_T} > 1.5$ is also required. A candidate charged track is required to have

$$p_T > p_{T\text{track}}, \quad 0.1 < |\eta| < 0.9, \tag{4.17}$$

with no hadronic jet within a cone of $\Delta R < 0.4$, where ΔR is the separation in the pseudo-rapidity azimuthal angle plane. Finally, we demand all events to have at least one candidate track with radial track length in the range

$$12 < d < 30 \text{ cm}. \tag{4.18}$$

We summarize the threshold values of the cuts, namely, $\not{E}_T^{\text{min}}, p_{T,j_1}, p_{T,j_2}$ and $p_{T,\text{track}}$, for different collider options in Table 4.3. As mentioned earlier, we vary the $\not{E}_T, p_{T,j_1}$ and $p_{T,\text{track}}$ cuts for the 27 TeV and 100 TeV scenarios in the ranges specified in the table to optimize the signal significance.

The optimized set of kinematic cuts for the HE-LHC is given in Table 4.4, with the corresponding signal cross-sections. Here, basic cuts refers to the requirement of $\not{E}_T >$ 150 GeV at the matrix-element level. We also show the efficiency of each cut on the signal

(ϵ_S) rates. As we can see from Table 4.2, for the representative mass value of 500 GeV for the chargino and neutralino states in the wino-like scenario, we expect a cross-section of 1.59 fb, which, after taking into account the efficiency fudge factor of 0.1 mentioned in Sec. 4.1.2, would imply 2385 signal events with 15 ab^{-1} data at the HE-LHC. Following the methodology described in the above section, we also expect around 28 background events. Thus, even if the background normalization increases by upto a factor of five, the signal to background ratio, S/B, would be in the range of $17 - 85$. Similarly, for the Higgsino-like scenario, the S/B ratio is estimated to be in the range of $1 - 7$ for the representative mass value of 300 GeV. Both these numbers are encouraging and imply that with a detector design similar to that of Run-2 LHC, the experimental uncertainties in the disappearing charged track search will be largely statistical in nature.

4.3 COMPARATIVE REACH OF DIFFERENT HADRON COLLIDER OPTIONS

We are now in a position to compare the reach of different hadron collider options in searching for wino and Higgsino dark matter and their associated charged states. We will show the results for three different scenarios of the collider energy and integrated luminosity:

$$\begin{aligned} \text{HL-LHC}: &\quad 14 \text{ TeV}, \quad 3 \text{ ab}^{-1}, \\ \text{HE-LHC}: &\quad 27 \text{ TeV}, \quad 15 \text{ ab}^{-1}, \\ \text{FCC-hh/SppC}: &\quad 100 \text{ TeV}, \quad 30 \text{ ab}^{-1}. \end{aligned} \tag{4.19}$$

To present our results on the future reach of the above collider options, we adopt a definition of significance

$$\frac{S}{\sqrt{B + (\Delta_B B)^2 + (\Delta_S S)^2}}, \tag{4.20}$$

where S and B are the total number of signal and background events as before, and Δ_S, Δ_B refer to the corresponding percentage systematic uncertainties, respectively. For the monojet channel, we have taken $\Delta_B = 1 - 2\%$ and $\Delta_S = 10\%$, while for the disappearing charged

Cuts	$m_{\tilde{W}} = 500$ GeV		$m_{\tilde{H}} = 300$ GeV	
	Signal [fb]	ϵ_S	Signal [fb]	ϵ_S
Basic cuts	102.91	-	242.53	-
Lepton veto	102.90	1.00	242.52	1.00
$p_{Tj_1} > 450$ GeV	16.42	0.16	30.86	0.13
$\not{E}_T > 550$ GeV	11.29	0.69	18.81	0.61
$\Delta\phi_{j,\not{E}_T} > 1.5$	10.61	0.94	17.54	0.93
$p_{T\text{track}} > 400$ GeV Track isolation	7.05	0.66	8.43	0.48
$12 < d < 30$ cm	1.59	0.23	0.13	0.01

Table 4.4: Signal cross-section in the disappearing charged track analysis at the 27-TeV HE-LHC after successive selection cuts on the kinematic and track-quality observables; see text for details on the selection criteria. The efficiency of each cut on the signal (ϵ_S) rates is also shown. We have presented the results for the representative mass value of 500 GeV (300 GeV) for the wino (Higgsino) states.

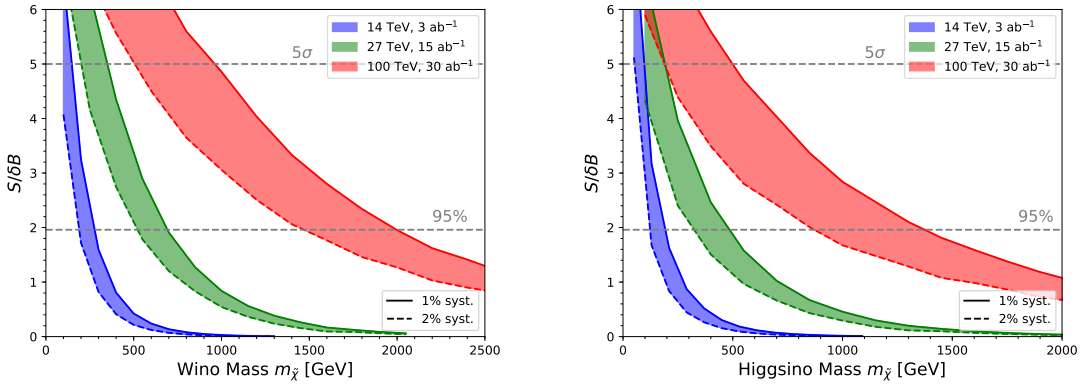

Figure 4.3: Comparative reach of the HL-LHC, HE-LHC and FCC-hh/SppC options in the monojet channel for wino-like (left panel) and Higgsino-like (right panel) DM search. The solid and dashed lines correspond to optimistic values of the systematic uncertainties on the background estimate of 1% and 2% respectively, which might be achievable using data-driven methods with the accumulation of large statistics.

track analysis, we assume $\Delta_B = 20\%$ and $\Delta_S = 10\%$. As emphasized earlier, although the systematic uncertainties in the current LHC analyses in the above channels are larger, the uncertainties in the background estimate using data-driven methods are expected to further reduce with the accumulation of higher statistics. Furthermore, since our background estimate in the disappearing track analysis is a simple extrapolation of the ATLAS results for the 13 TeV LHC, we have also varied the central value of the background yield within a factor of five (i.e., between 20% and 500%) of the number obtained using the method discussed in Sec. 4.1.2.

In Fig. 4.3 we compare the reach of the HL-LHC, HE-LHC and FCC-hh/SppC options in the monojet channel for wino-like (left panel) and Higgsino-like (right panel) DM search, where $\delta B = \sqrt{B + (\Delta_B B)^2 + (\Delta_S S)^2}$. The solid and dashed lines correspond to systematic uncertainties on the background estimate of 1% and 2% respectively. In an optimistic scenario, we can expect to probe at the 95% C.L. wino-like DM mass of upto 280, 700 and 2000 GeV, at the 14, 27 and 100 TeV colliders respectively. For the Higgsino-like scenario, these numbers are reduced to 200, 490 and 1370 GeV, primarily due to the reduced production cross-section. Clearly, a 27 TeV collider can achieve a substantially improved reach by

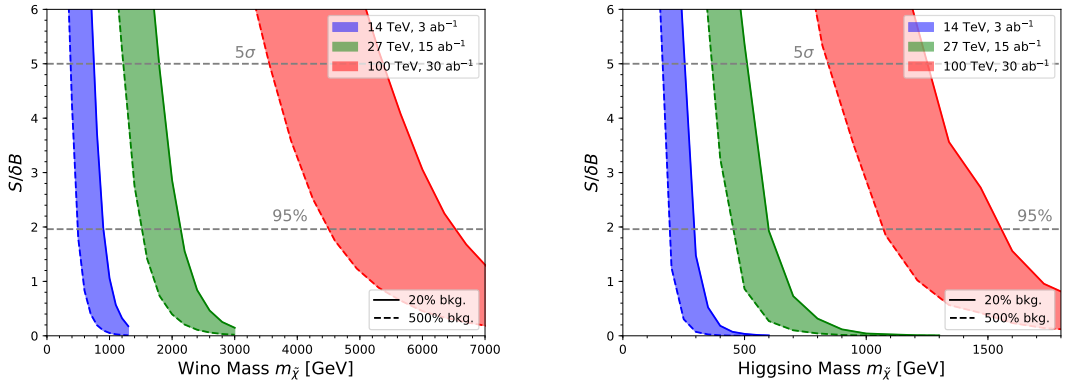

Figure 4.4: Comparative reach of the HL-LHC, HE-LHC and FCC-hh/SppC options in the disappearing charged track analysis for wino-like (left panel) and Higgsino-like (right panel) DM search. The solid and dashed lines correspond to modifying the central value of the background estimate by a factor of five, i.e., 20% and 500% of that obtained through the fit function in Eq. 4.12.

a factor of two or more compared to the HL-LHC, while the 100 TeV collider option will improve it further by another factor of three. Furthermore, a 100 TeV collider option may be able to completely cover the thermal Higgsino mass window using the monojet search, if the systematic uncertainties can be brought down to a percent level.

In Fig. 4.4 we compare the reach of the HL-LHC, HE-LHC and FCC-hh/SppC options in the disappearing charged track analysis for wino-like (left panel) and Higgsino-like (right panel) DM search. The solid and dashed lines correspond to modifying the central value of the background estimate by a factor of five, i.e., 20% and 500% of that obtained through the fit function in Eq. (4.12). With the lower value of the background estimate, the expected reach on wino-like DM mass at the 95% C.L. is 0.9, 2.1 and 6.5 TeV at the 14, 27 and 100 TeV colliders respectively. For the Higgsino-like scenario, these numbers are reduced to 300, 600 and 1550 GeV, primarily due to the smaller length of the disappearing track and the reduced production rate. For the higher value of the background estimate, the mass reach for the wino-like states are modified to 500, 1500 and 4500 GeV, respectively, at the three collider energies. Similarly, for the Higgsino-like scenario, the reach is modified to 200, 450 and 1070 GeV. We note that the signal significance in the disappearing track search is rather

sensitive to the wino and Higgsino mass values (thus making the 2σ and 5σ reach very close in mass). This is because, as the chargino lifetime in the lab frame becomes shorter for heavier masses, the signal event rate decreases exponentially.

The improvements in going from the HL-LHC to the HE-LHC, and further from the HE-LHC to the FCC-hh/SppC are very similar to those obtained for the monojet analysis above, namely, around a factor of two and three, respectively. Although we have presented the reach at the 100 TeV collider without reference to the cosmology of these DM candidates, in order for a wino heavier than around 3 TeV and a Higgsino heavier than around 1 TeV not to overclose the Universe, one would require a non-standard thermal history, with late-time entropy production [274].

4.4 SUMMARY AND OUTLOOK

Among the multitude of possibilities for particle DM, WIMPs remain a highly motivated candidate due to the predictable nature of the thermal relic abundance, and the correlated predictions for their experimental and observational probes. WIMP dark matter particles that belong to a multiplet of the standard model weak interactions are one of the best representatives, but are often challenging to probe in direct detection experiments due to loop-suppressed scattering cross-sections. Searches at hadron colliders are thus crucial for testing such a scenario, and depending upon the gauge representation, can be complementary to indirect detection probes in different mass windows. Moreover, since the relic abundance of electroweak DM is uniquely determined by its mass value, they represent a well-defined target in the collider search for DM in general.

In this chapter, we studied collider probes of two representative scenarios for electroweak DM, namely an wino-like $\mathrm{SU}(2)_\mathrm{L}$ triplet and a Higgsino-like $\mathrm{SU}(2)_\mathrm{L}$ doublet. In the absence of higher-dimensional operators, radiative corrections generate a small mass splitting between the charged and neutral components of these multiplets, of the order of a few hundred MeV, as reviewed in Sec. 4.1.1. This nearly degenerate spectrum motivates two major search channels at hadron colliders for electroweak DM and its charged counterparts, namely,

95% C.L.	Wino Monojet	Wino Disappearing Track	Higgsino Monojet	Higgsino Disappearing Track
14 TeV	280 GeV	900 GeV	200 GeV	300 GeV
27 TeV	700 GeV	2.1 TeV	490 GeV	600 GeV
100 TeV	2 TeV	6.5 TeV	1.4 TeV	1.5 TeV

Table 4.5: Summary of DM mass reach at 95% C.L. for an electroweak triplet (wino-like) and a doublet (Higgsino-like) representation, at the HL-LHC, HE-LHC and the FCC-hh/SppC colliders, in optimistic scenarios for the background systematics. See text for details.

the monojet with missing transverse momentum search and the disappearing charged track analysis. We examined the relevant signal and background processes for these search channels in proton-proton collisions in Sec. 4.1.2, along with the methodology adopted for estimating the event rates at colliders.

We presented the distributions of the important kinematic observables and the details of the kinematic selection criteria followed at different collider energies in Sec. 4.2. For our analysis, we considered three options for future hadron colliders: the high-luminosity HL-LHC, the proposed 27-TeV LHC upgrade (HE-LHC) and the 100-TeV FCC-hh/SppC. We performed an optimization of the selection criteria for the two higher centre of mass energies, maximizing the statistical significance of the particular search, at the same time ensuring a large signal event rate.

The estimates of the expected mass reach at the 27-TeV HE-LHC are discussed in Sec. 4.3. We also presented comparisons with the projected reach for the 14-TeV HL-LHC and the 100-TeV hadron collider. Our results for these three options are summarized in Table 4.5. In particular, we find that the disappearing charged track analysis at the HE-LHC can probe Higgsino-like (wino-like) DM mass of up to 600 GeV (2.1 TeV) at the 95% C.L., making it complementary to the indirect probes using gamma rays from dwarf-spheroidal galaxies. The monojet and missing transverse momentum search, on the otherhand, has a weaker reach of 490 GeV (700 GeV) at 95% C.L. for the Higgsino-like (wino-like) states. We further

see in Table 4.5 that across different collider energies, while the reach for wino-like states is improved in the disappearing track analysis by around a factor of three compared to the monojet search, for Higgsino-like states the improvement is of the order of 100 GeV. We note that the performance in the monojet search will crucially depend on how far the systematic uncertainties can be reduced using data-driven methods at future high-luminosity runs, as the signal to background ratio remains at the few percent level.

For the disappearing charged track analysis, we adopted a detector setup similar to that of the ATLAS tracking system for the Run-2 LHC upgrade, with a new Insertable B-Layer (IBL), which crucially extends the search reach for Higgsino-like states with a shorter decay length in the tracker. Since the only way to understand the backgrounds for this search is from the data, we extrapolated the 13 TeV ATLAS results to higher energies, keeping the shape of the distribution as a function of the track transverse momentum unchanged, while normalizing by the ratio of the total rates at different energies.

Although quite representative, it should be noted that our studies are limited to the case of pure electroweak doublet and triplet states. In more general scenarios, in which mixing among the electroweak multiplets, in particular, with an additional fermionic gauge singlet is non-negligible, the considerations of relic abundance and detection techniques would be substantially altered. This can also lead to rather rich physics scenarios at colliders, depending upon the other particles in the spectrum and their mass differences. For example, with a non-degenerate spectra in the chargino-neutralino sector of the MSSM, decays of the heavier states can produce electroweak gauge bosons, which would in turn lead to signals with multiple charged leptons and missing transverse momenta in the final state.

The LHC and its high-luminosity upgrade will lead the research in the energy frontier for the coming decades. The possible high-energy upgrade to 27 TeV, the HE-LHC, is an exciting option, and a potentially important step towards the 100-TeV territory at the FCC-hh/SppC colliders. As we found in this work, the proposed HE-LHC could significantly extend the scope of electroweak DM searches beyond the reach of the HL-LHC. It would thus have a fantastic potential for discovery, providing boost to the future collider programme at 100 TeV.

5.0 ELECTROWEAK DARK MATTER VIA SINGLE-PHOTON PROCESSES AT HIGH ENERGY e^+e^- COLLIDERS

Although supersymmetry [25,26] is well-motivated candidate for a natural theory which also provides a cold dark matter (DM) candidate [37,38], it has been quite puzzling that except for a SM-like Higgs boson, no new particles beyond the SM have been so far observed in the LHC experiments near and above the TeV threshold. One plausible scenario for the LHC null search results is that all the colored SUSY particles with QCD strong interactions are rather heavy and thus out of reach [275–280]. The EW particles, although kinematically accessible, may not lead to experimentally tractable signals due to the rather small production rate, the un-characteristic signature and the large SM backgrounds at hadron colliders [278,281–296]. This situation happens quite naturally when the lower-lying EW states are nearly degenerate in mass, and thus the final state products are rather soft and have little missing transverse energy. On the other hand, the future e^+e^- colliders, such as the International Linear Collider (ILC) [87–89], would be capable of covering the search as long as kinematically accessible, because of the well-constrained event topology and the very clean experimental environment.

In this chapter, we set out to study this challenging scenario at an e^+e^- collider in a rather model-independent way, to quantify the observability for the missing particle signal, and to explore the feasibility to determine the missing particle spin and chiral couplings. Within a generic framework of the minimal supersymmetric standard model (MSSM), we focus on three representative cases to study the EW lower-lying states, where the other SUSY particles are assumed to be decoupled. The first scenario, to be called the spin-1/2 Higgsino scenario, is the case where the only accessible SUSY particles are two spin-1/2 Higgsino doublets ($\tilde{H}^+, \tilde{H}^0$). The second scenario, to be called the spin-1/2 wino scenario, is the case

where the only accessible SUSY particles are a spin-1/2 wino triplet $(\tilde{W}^+, \tilde{W}^0, \tilde{W}^-)$. The third scenario, to be called the spin-0 slepton scenario, is the case where the only accessible SUSY particles consist of a spin-0 left-handed slepton doublet $(\tilde{\nu}_\ell, \tilde{\ell}^-)$.

In each scenario, the charged particle and its neutral partner are degenerate in mass before EWSB and their mass splitting originates dominantly from loop-induced EWSB corrections in the Higgsino and wino scenarios, or from the so-called D-term potential after EWSB in the slepton scenario. Due to the near degeneracy it would be very challenging to observe the soft final state particles. Analogous to the mono-jet plus missing energy signature at hadron colliders [297, 298], single energetic photon plus missing energy at e^+e^- colliders is known to be one of the promising search channels for the missing particles [281, 287, 288, 299, 300]. This method was used for counting neutrino families [301–303], as a means to search for heavy neutrinos [304] or (nearly) invisible SUSY particles [305–314], or anomalous gauge couplings [315–317]. We provide systematic and detailed methods not only for determining the spins of the (nearly) invisible particles unambiguously, but also for characterizing each of the three benchmark scenarios through single-photon processes at e^+e^- colliders by exploiting electron and positron beam polarizations. We find that, if kinematically accessible, the spins and coupling strengths of the invisible particles to γ/Z in such single-photon processes can be determined clearly by exploiting the initial electron (and positron) beam polarization and investigating the threshold excitation patterns of the processes.

The remainder of the chapter is organized as follows. We first set up the three benchmark scenarios in the MSSM framework. We lay out their spectra and interactions with the SM particles. We present the mass splitting in each scenario by radiative corrections or by D-term. Section 5.2 is devoted to systematic analyses for the radiative processes involving the pair production and an associated hard photon in e^+e^- collisions with special emphasis on the comparison of the initial-state radiation (ISR) and final-state radiation (FSR) in the charged pair production. We present the dependence of the cross sections on the photon energy and the electron/positron beam polarizations. In Sec. 5.3, we first study the discovery limit of the new invisible particles based on the statistical significance of each mode at a 500 GeV ILC. We then describe systematically how the threshold behavior and the ratios of polarized

cross sections enable us to determine the SUSY particle spin and characterize each scenario unambiguously. We briefly comment on the other alternative methods for characterizing the properties of the scenarios. Finally, we summarize our results and present our conclusions in Sec. 5.4.

5.1 SCENARIOS WITH A DEGENERATE PAIR OF SUSY PARTICLES

To study the nearly degenerate EW states in a relatively model-independent way, we take the MSSM as a generic framework and make the following simple assumptions: only a pair of SUSY color-singlet EW particles is kinematically accessible below the ILC threshold, and the other heavier states are essentially decoupled. This could be realized when the soft SUSY-breaking scalar quark masses and the gluino mass scale M_3 are much heavier than the EW soft SUSY-breaking scales. Specifically, we consider three benchmark scenarios in MSSM, each representing a qualitative different case, as described in detail below.

5.1.1 The spin-1/2 Higgsino ($H_{1/2}$) scenario

The first scenario for a degenerate pair of EW new states, the scenario $H_{1/2}$, is provided by the Higgsino sector with the spin-1/2 SUSY partners of the down- and up-type Higgs bosons in the MSSM. This is realized practically when the Higgsino mass parameter μ of the superpotential term $\mu \hat{H}_d \cdot \hat{H}_u$ mixing the two Higgs superfields is much smaller than all the other SUSY parameters including the gaugino mass parameters, $M_{1,2,3}$ [278,281,283–286,288]. (Without any loss of generality, we assume the parameters, $M_{1,2}$ and μ to be real and positive in the present note.) When the gaugino states as well as the other SUSY states are decoupled without generating any mixing with the Higgsinos, the two SU(2)-doublet Higgsino states $\tilde{H}_d = [\tilde{H}^0_{dL}, \tilde{H}^-_{dL}]$ and $\tilde{H}_u = [\tilde{H}^+_{uL}, \tilde{H}^0_{uL}]$ have maximal mixing. The mass term for the charged and neutral Higgsino states can be cast into the mass term for a degenerate pair of a Dirac chargino and a Dirac neutralino with mass μ as

$$\mu \left(\overline{\tilde{H}^-_{uR}} \tilde{H}^-_{dL} + \overline{\tilde{H}^+_{dR}} \tilde{H}^+_{uL} \right) - \mu \left(\overline{\tilde{H}^0_{uR}} \tilde{H}^0_{dL} + \overline{\tilde{H}^0_{dR}} \tilde{H}^0_{uL} \right) \quad \Rightarrow \quad \mu \, \overline{\chi^-_H} \, \chi^-_H + \mu \, \overline{\chi^0_H} \, \chi^0_H \qquad (5.1)$$

where the Dirac chargino and Dirac neutralino are defined by

$$\chi_H^- \;=\; \tilde{H}_{dL}^- + \tilde{H}_{uR}^- \quad \text{and} \quad \chi_H^0 \;=\; \tilde{H}_{dL}^0 - \tilde{H}_{uR}^0 \tag{5.2}$$

in terms of the current Higgsino states with the charge-conjugated states, $\tilde{H}_{uR}^- = (\tilde{H}_{uL}^+)^c$ and $\tilde{H}_{uR}^0 = (\tilde{H}_{uL}^0)^c$.

As the down- and up-type Higgsinos form a vector-like $\mathrm{SU}(2)_L$ doublet, the interactions of the Dirac chargino χ_H^- and Dirac neutralino χ_H^0 with the electromagnetic (EM) and weak gauge bosons are described by the Lagrangian

$$\begin{aligned}\mathcal{L}_{V\chi\chi}^H = \;& e\,\overline{\chi_H^-}\gamma^\mu\chi_H^-\,A_\mu + e\,\frac{(1/2 - s_W^2)}{c_W s_W}\,\overline{\chi_H^-}\gamma^\mu\chi_H^-\,Z_\mu - \frac{1}{2}\,\frac{e}{c_W s_W}\,\overline{\chi_H^0}\gamma^\mu\chi_H^0\,Z_\mu \\ & - \frac{e}{\sqrt{2}s_W}\left(\overline{\chi_H^0}\gamma^\mu\chi_H^-\,W_\mu^+ + \text{h.c.}\right)\end{aligned} \tag{5.3}$$

where the Lorentz structure of every gauge interaction term is of a pure vector type and its strength is fixed only by the positron electric charge e and weak mixing angle θ_W. In the present note we use the abbreviations $s_W = \sin\theta_W$ and $c_W = \cos\theta_W$ for the sake of convenience.

5.1.2 The spin-1/2 wino ($W_{1/2}$) scenario

The second scenario for a degenerate pair of SUSY states, the $W_{1/2}$ scenario, is provided by the MSSM wino sector with the spin-1/2 partners of the $\mathrm{SU}(2)_L$ gauge bosons. This is realized practically when the $\mathrm{SU}(2)_L$ gaugino mass parameter M_2 is much smaller than the other gaugino mass parameters $M_{1,3}$ and the Higgsino mass parameter μ as well as all the other SUSY parameters [283, 284, 289–293]. In this scenario the mass term of the SU(2)-triplet wino state $\tilde{W} = [\tilde{W}_L^+, \tilde{W}_L^0, \tilde{W}_L^-]$ can be cast into a Dirac mass term for a Dirac chargino and a Majorana mass term for a Majorana neutralino with a common mass M_2 as

$$M_2\,(\overline{\tilde{W}_R^+}\tilde{W}_L^+ + \overline{\tilde{W}_R^0}\tilde{W}_L^0 + \overline{\tilde{W}_R^-}\tilde{W}_L^-) \quad \Rightarrow \quad M_2\,\overline{\chi_W^-}\,\chi_W^- + \frac{1}{2}\,M_2\,\overline{\chi_W^0}\,\chi_W^0 \tag{5.4}$$

by defining a Dirac chargino χ_W^- and a Majorana neutralino χ_W^0 by

$$\chi_W^- = \tilde{W}_L^- + \tilde{W}_R^- \quad \text{and} \quad \chi_W^0 = \tilde{W}_L^0 + \tilde{W}_R^0 \tag{5.5}$$

with the charge-conjugated states $\tilde{W}_R^{\pm} = (\tilde{W}_L^{\mp})^c$ and $\tilde{W}_R^0 = (\tilde{W}_L^0)^c$. Note that by definition the neutralino state is identical to its charge-conjugated anti-particle, i.e. $(\chi_W^0)^c = \chi_W^0$.

In the $W_{1/2}$ scenario, the interactions of the vector-like SU(2)-triplet states with the EM and weak gauge bosons are described by

$$\mathcal{L}^W_{V\chi\chi} = e\,\overline{\chi_W^-}\gamma^\mu\chi_W^-\,A_\mu + e\,\frac{(1-s_W^2)}{c_W s_W}\,\overline{\chi_W^-}\gamma^\mu\chi_W^-\,Z_\mu - \frac{e}{s_W}\left(\overline{\chi_W^0}\gamma^\mu\chi_W^-\,W_\mu^+ + \text{h.c.}\right) \tag{5.6}$$

Again, like the $H_{1/2}$ scenario, the Lorentz structure of every gauge interaction term is of a pure vector type, but the coupling strengths determined uniquely by the weak mixing angle θ_W are characteristically different from those in the $H_{1/2}$ scenario. Note that the Majorana neutralino in the $W_{1/2}$ scenario couples neither to the photon nor to the neutral weak boson Z.

5.1.3 The left-handed slepton (L_0) scenario

The third scenario for a degenerate pair of SUSY states, the L_0 scenario, is provided by the MSSM left-handed slepton sector with the spin-0 partners $\tilde{L} = [\tilde{\nu}_\ell, \tilde{\ell}_L^-]$ of the $\text{SU}(2)_L$-doublet lepton. This is realized practically when the SUSY-breaking slepton mass parameter $\tilde{m}_{\ell_L}$ is much smaller than all the other SUSY parameters. In general, the charged slepton $\tilde{\ell}_L^-$ and the sneutrino $\tilde{\nu}_\ell$ are non-degenerate and split by the so-called D-term potential after EWSB $\Delta m^2 = m^2_{\tilde{\ell}_L^-} - m^2_{\tilde{\nu}_\ell} = -m_Z^2\cos 2\beta\, c_W^2$, vanishing for $\tan\beta = 1$. For the sake of comparison, the charged slepton and neutral sneutrino may be assumed to be degenerate with $\tan\beta = 1$ at the tree level.

In the L_0 scenario, the interactions of the left-handed SU(2)-doublet slepton state with the EM and weak gauge bosons are described by the Lagrangian

$$\begin{aligned}\mathcal{L}^L_{V\tilde{\ell}_L\tilde{\ell}_L} = {} & e\,\tilde{\ell}_L^+\overleftrightarrow{\partial_\mu}\tilde{\ell}_L^-\,A^\mu + e\,\frac{(1/2-s_W^2)}{c_W s_W}\,\tilde{\ell}_L^+\overleftrightarrow{\partial_\mu}\tilde{\ell}_L^-\,Z^\mu - \frac{1}{2}\,\frac{e}{c_W s_W}\,\tilde{\nu}_\ell^*\overleftrightarrow{\partial_\mu}\tilde{\nu}_\ell\,Z^\mu \\ & - \frac{e}{\sqrt{2}s_W}\left(\tilde{\nu}_\ell^*\overleftrightarrow{\partial_\mu}\tilde{\ell}_L^-\,W^{+\mu} + \text{h.c.}\right)\end{aligned} \tag{5.7}$$

where $A\overleftrightarrow{\partial_\mu}B = A\partial_\mu B - (\partial_\mu A)B$. Note that the gauge coupling strengths of the charged slepton and neutral sneutrino are identical to those of the Dirac chargino and Dirac neutralino in the Higgsino case. However, because of their zero spin values, the Lorentz structure of the

gauge interactions are different from that of the chargino and neutralino states. In addition, there exist 4-point contact gauge interactions of left-handed sleptons. The Lagrangian for the $\gamma\gamma\tilde{\ell}_L^-\tilde{\ell}_L^-$ and $\gamma Z\tilde{\ell}_L^-\tilde{\ell}_L^-$ four-point vertices read

$$\mathcal{L}^L_{\gamma Z\tilde{\ell}_L^-\tilde{\ell}_L^-} = e^2\tilde{\ell}_L^+\tilde{\ell}_L^- A_\mu A^\mu + 2e^2\frac{(1/2-s_W^2)}{c_W s_W}\tilde{\ell}_L^+\tilde{\ell}_L^- A_\mu Z^\mu \tag{5.8}$$

Because of these momentum-independent contact terms the charged slepton pair production associated with a hard final-state as well as initial-state photon emission exhibits a S-wave threshold excitation pattern in contrast to the P-wave excitation pattern in the neutral sneutrino pair production only with a hard initial photon emission, as shown later in Sec. 5.2.2.

5.1.4 Feynman rules for a vector boson converting into a particle pair and a photon

Depending on the electric charge and spin of the SUSY EW particle X, the vertex $VX\bar{X}$ for the process $V^*(q) \to X(q_1)\bar{X}(q_2)$ with $V = \gamma, Z$ can be parameterized as

$$\langle X(q_1)\bar{X}(q_2)||\, V^\mu(q)\rangle = ec_X^V \begin{cases} (q_1-q_2)^\mu & \text{for spin-0 chaged sleptons or sneutrinos} \\ \bar{u}(q_1)\gamma^\mu v(q_2) & \text{for spin-1/2 charginos or neutralinos} \end{cases} \tag{5.9}$$

with $q = q_1 + q_2$ and the normalized couplings c_X^V for $(V = \gamma, Z)$ expressed as

$$c^\gamma_{\chi_H^-} = c^\gamma_{\tilde{\ell}_L^-} = 1, \quad c^Z_{\chi_H^-} = c^Z_{\tilde{\ell}_L^-} = \frac{(1/2-s_W^2)}{c_W s_W}, \quad c^Z_{\chi_H^0} = c^Z_{\tilde{\nu}_\ell} = -\frac{1}{2c_W s_W} \tag{5.10}$$

$$c^\gamma_{\chi_W^-} = 1, \quad c^Z_{\chi_W^-} = \frac{c_W}{s_W}, \quad c^Z_{\chi_W^0} = 0 \tag{5.11}$$

in terms of c_W and s_W.

In addition to the standard three-point vertices in Eqs. (5.10) and (5.11), there exists a four-point momentum-independent vertex contributing to the FSR process $V^* \to \gamma\,\tilde{\ell}_L^-\tilde{\ell}_L^+$ in the L_0 scenario:

$$\langle\gamma^\nu\tilde{\ell}_L^+\tilde{\ell}_L^-\,||\,V^\mu\rangle = 2e^2\, d^V_{\tilde{\ell}_L^-} g^{\mu\nu} \tag{5.12}$$

with the normalized couplings $d^{\gamma,Z}_{\tilde{\ell}_L^-}$ identical to $c^{\gamma,Z}_{\tilde{\ell}_L^-}$ given in Eq. (5.10).

5.1.5 Radiatively-induced mass difference

Although in all the three scenarios the charged and neutral SUSY particles are degenerate in mass before EWSB, the gauge symmetry breaking part in the MSSM causes a finite calculable mass splitting through radiative corrections. Moreover, the so-called D-term potential leads to an additional mass splitting between the spin-0 charged slepton and neutral sneutrino in the L_0 scenario unless the two Higgs vacuum expectation values, $v_u = v\cos\beta$ and $v_d = v\sin\beta$, are equal, i.e. $\tan\beta = 1$.

At the leading order the mass splitting stems from one-loop virtual photon and Z-boson exchange corrections to the masses and the wave functions of the chargino and neutralino states in the $H_{1/2}$ or $W_{1/2}$ scenarios [285, 290–296, 318]. The one-loop mass splitting for the on-shell SUSY states is

$$\Delta m_H = m_{\chi_H^\pm} - m_{\chi_H^0} = \frac{\alpha}{4\pi}\mu\left[f(m_Z/\mu) - f(0)\right] \tag{5.13}$$

$$\Delta m_W = m_{\chi_W^\pm} - m_{\chi_W^0} = \frac{\alpha}{4\pi s_W^2} M_2\left[f(m_W/M_2) - c_W^2 f(m_Z/M_2) - s_W^2 f(0)\right] \tag{5.14}$$

respectively, where the loop function $f(a) = 2\int_0^1 dx\,(1+x)\ln\left[x^2 + (1-x)a^2\right]$ and $\alpha = e^2/4\pi$. The asymptotic value of the mass splitting for $\mu, M_2 \gg m_Z$ is $\alpha m_Z/2 \simeq 355$ MeV and $\alpha m_W/2(1+c_W) \simeq 165$ MeV, respectively. (In order for the radiatively induced mass splitting to be dominant, the winos/Higgsinos must be separated from the next-heaviest electroweak states. For the $W_{1/2}$ scenario it suffices that M_1 and μ parameters are of order 1 TeV. In contrast, for the $H_{1/2}$ scenario, the gaugino masses M_1 and M_2 must be above 10 TeV, unless there occur some cancellations between wino and bino contributions [288, 319].)

In the L_0 scenario, the charged slepton is in general non-degenerate with the neutral sneutrino, the $\mathrm{SU}(2)_L$ doublet partner, due to the D-term contribution leading to a mass splitting of $O(m_Z^2/M_s)$ where M_s is a common SUSY-breaking slepton mass parameter, unless $\tan\beta = 1$. Even if they are degenerate with $\tan\beta = 1$ at the tree level, a leading-order mass splitting arises from one-loop corrections with virtual sleptons of same and different flavor and Higgs bosons as well as virtual photon, Z-boson and W-boson diagrams. Nevertheless, as the splitting must vanish without EWSB, it is therefore bounded by a quantity proportional to the EM fine structure constant times the Z-boson mass.

5.2 SINGLE-PHOTON PROCESSES AT e^+e^- COLLIDERS

In the above scenarios, the pair of SUSY states may be produced at the ILC via s-channel γ/Z exchanges. However, as the mass splitting between the charged and neutral states is of the order of a few hundred MeV, the expected signatures at the ILC can vary from soft ($p_T \sim 300$ MeV) decay products through displaced vertices to massive charged tracks. We do not perform any sophisticated analyses for distinguishing the charged modes from the neutral modes in the present work and assume the charged and neutral states in each scenario to be (nearly) degenerate in the following numerical analyses. For more dedicated studies for separating the charged modes from the neutral modes and measuring the mass splitting based on the visible decay products of the charged states, we refer to Refs. [287, 288].

One method to search for production of invisible particles is to identify an associated hard radiated photon in single-photon processes in e^+e^- collisions, $e^+e^- \to \gamma + \not{E}$. In the three $\{H_{1/2}, W_{1/2}, L_0\}$ scenarios, a pair of charged or neutral particles, $X\bar{X}$, are produced through a virtual γ or Z-exchange and accompanied by a hard photon radiation in the single-photon process

$$e^+e^- \to \gamma\, V^* \quad \text{or} \quad V^* \to \gamma\, X\bar{X} \quad \text{with} \quad V = \gamma, Z \tag{5.15}$$

For the neutral $\chi^0_H\chi^0_H$ and $\tilde{\nu}_\ell\tilde{\nu}^*_\ell$ pairs, the photon in the single-photon process (5.15) is radiated only from the initial electron or positron line, but for every charged pair the photon is emitted also from the final charged particle lines as shown in Fig. 5.1. In each process, the ISR and FSR parts are separately EM gauge invariant and develop no interference terms between them (when the Z-boson width is ignored).

The FSR part has been ignored in most of the previous studies on the single-photon processes. In the present analysis we include not only the ISR part but also the FSR part for assessing the validity of the ISR approximation and the influence of the FSR part in characterizing the (nearly) invisible particles through single-photon processes in e^+e^- collisions.

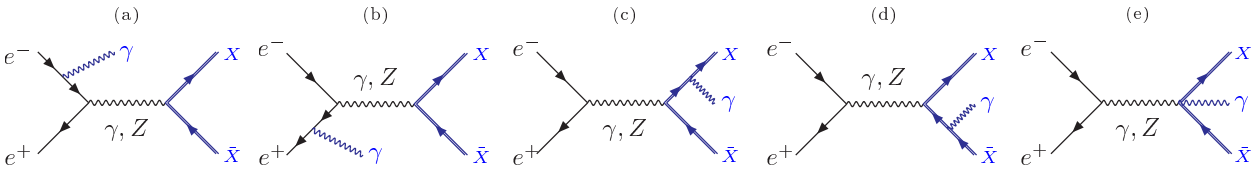

Figure 5.1: Feynman diagrams for the single-photon process $e^+e^- \to \gamma X\bar{X}$ with the charged or neutral particle-antiparticle pair, X and $\bar{X}$. The diagrams (a) and (b) are for the ISR processes with the photons radiated from the initial electron and positron lines with $X = \{\chi^-_{H,W}, \chi^0_H, \tilde{\ell}^-_L, \tilde{\nu}_\ell\}$ and the diagrams (c) and (d) for the FSR processes with the photons emitted from the final-state charged particles with $X = \{\chi^-_{H,W}, \tilde{\ell}^-_L\}$. The diagram (e) involving a four-point coupling is only for a scalar particle $X = \tilde{\ell}^-_L$.

5.2.1 Initial state radiation

We ignore the electron mass except for avoiding collinear singularity. We include the possible $e^\pm$ beam polarizations $P_\pm$ in studying the dependence of the signal process $e^+e^- \to \gamma X\bar{X}$ on the photon energy fraction $x_\gamma = 2E_\gamma/\sqrt{s}$ and the photon scattering angle θ_γ with respect to the e^- momentum direction in the e^+e^- center-of-mass (CM) frame.

The ISR effect can be expressed in a factorized form with a universal Weizsacker-Williams radiator function [320–322] as

$$\frac{d\sigma(e^+e^- \to \gamma X\bar{X})_{\rm ISR}}{dx_\gamma\, d\cos\theta_\gamma} = \mathcal{R}(s; x_\gamma, \cos\theta_\gamma) \times \sigma^{X\bar{X}}(q^2) \tag{5.16}$$

where the ISR radiator function $\mathcal{R}$ can be expressed to a very good approximation as

$$\mathcal{R}(s; x_\gamma, \cos\theta_\gamma) = \frac{\alpha}{\pi}\frac{1}{x_\gamma}\left[\frac{1+(1-x_\gamma)^2}{1+4m_e^2/s - \cos^2\theta_\gamma} - \frac{x_\gamma^2}{2}\right] \tag{5.17}$$

which is nearly independent of the beam energy except for the forward or backward collinear direction. The total cross section of the $X\bar{X}$ pair production in e^+e^- annihilation to be evaluated with the reduced CM energy squared $q^2 = (1-x_\gamma)s$ is given by

$$\sigma^{X\bar{X}}(q^2) = \frac{2\pi\alpha^2}{3q^2}\beta_q \mathcal{P}(X; P_-, P_+; q^2)\, \mathcal{K}(\beta_q) \tag{5.18}$$

with $\beta_q = \sqrt{1-4m_X^2/(1-x_\gamma)s}$, the speed of the particle X in the $X\bar{X}$ CM frame. The polarization-dependent factor $\mathcal{P}$ is defined in terms of the beam polarizations and γ and Z-boson propagators as

$$\begin{aligned}\mathcal{P}(X;P_-,P_+;q^2) = \; & \frac{(1+P_-)(1-P_+)}{4}\left|c_X^\gamma + c_R c_X^Z \frac{q^2}{q^2-m_Z^2}\right|^2 \\ & + \frac{(1-P_-)(1+P_+)}{4}\left|c_X^\gamma + c_L c_X^Z \frac{q^2}{q^2-m_Z^2}\right|^2\end{aligned} \tag{5.19}$$

with $c_L = (1/2 - s_W^2)/c_W s_W$ and $c_R = -s_W/c_W$ and the couplings c_X^γ and c_X^Z given in Eqs. (5.10) and (5.11). The kinematical factor $\mathcal{K}(\beta_q)$ reads

$$\mathcal{K}(\beta_q) = \begin{cases} \beta_q^2 & \text{for spin-0 charged slepton or sneutrino} \\ 2(3-\beta_q^2) & \text{for spin-1/2 chargino or neutralino} \end{cases} \tag{5.20}$$

The range of x_γ is $0 \le x_\gamma \le 1 - 4m_X^2/s$ with its maximal value $x_\gamma^{max} = 1 - 4m_X^2/s$ corresponding to the $X\bar{X}$ production threshold with $\beta_q = 0$. Asymptotically when $\beta_q \to 0$, i.e. $x_\gamma \to 1 - 4m_X^2/s$, the cross section is proportional to β_q^3 for the spin-0 particles, exhibiting a slowly-rising P-wave threshold excitation, but it is proportional to β_q for the spin-1/2 particles, exhibiting a steeply-rising S-wave excitation near the threshold.

5.2.2 Final state radiation

Unlike the ISR effect, the FSR parts of the photon-energy and angular distributions are not universal and have no collinear singular term.

For any charged pair $X\bar{X} = \chi_H^-\chi_H^+,\ \chi_W^-\chi_W^+,\ \tilde{\ell}_L^-\tilde{\ell}_L^+$, the dependence of the FSR part on the FSR photon energy fraction x_γ and the photon scattering angle θ_γ can be decomposed as

$$\begin{aligned}\frac{d\sigma(e^+e^- \to \gamma X\bar{X})_{\rm FSR}}{dx_\gamma\, d\cos\theta_\gamma} = \; & \frac{3}{8}\left[(1+\cos^2\theta_\gamma)\mathcal{F}_1^X(s;x_\gamma) + (1-3\cos^2\theta_\gamma)\mathcal{F}_2^X(s;x_\gamma)\right] \\ & \times \sigma^{X\bar{X}}(s)\end{aligned} \tag{5.21}$$

where the final-state radiator functions $\mathcal{F}_{1,2}^X$ are process-dependent. Explicitly, for the production of a chargino pair with $X = \chi_H^-$ or χ_W^-, the FSR radiator functions are given by

$$\mathcal{F}_1^X(s;x_\gamma) = \frac{\alpha}{\pi}\frac{1}{x_\gamma}\frac{\beta_q}{\beta_s}\left[(1+\beta_s^2-2x_\gamma)L(\beta_q) - 2(1-x_\gamma) + \frac{2x_\gamma^2}{3-\beta_s^2}[L(\beta_q)-1]\right] \quad (5.22)$$

$$\mathcal{F}_2^X(s;x_\gamma) = \frac{\alpha}{\pi}\frac{1}{x_\gamma}\frac{\beta_q}{\beta_s}\frac{2}{3-\beta_s^2}\left[2-2x_\gamma-(1-\beta_s^2)L(\beta_q)\right] \quad (5.23)$$

in terms of x_γ with $\beta_s = \sqrt{1-4m_X^2/s}$, the CM speed of the X in the process $e^+e^- \to X\bar{X}$ with no photon emission [323]. On the other hand, for the production of a charged slepton pair with $X = \tilde{\ell}_L^-$, the FSR radiator functions read

$$\mathcal{F}_1^X(s;x_\gamma) = \frac{\alpha}{\pi}\frac{1}{x_\gamma}\frac{\beta_q}{\beta_s}\left[(1+\beta_s^2-2x_\gamma)L(\beta_q) - 2(1-x_\gamma) + \frac{2x_\gamma^2}{\beta_s^2}\right] \quad (5.24)$$

$$\mathcal{F}_2^X(s;x_\gamma) = \frac{\alpha}{\pi}\frac{1}{x_\gamma}\frac{\beta_q}{\beta_s}\frac{1}{\beta_s^2}\left[(3-\beta_s^2-2x_\gamma)L(\beta_q) - 6(1-x_\gamma)\right] \quad (5.25)$$

with the logarithmic function $L(\beta_q)$ defined by

$$L(\beta_q) = \frac{1}{\beta_q}\ln\left(\frac{1+\beta_q}{1-\beta_q}\right) \quad (5.26)$$

Integrating the distribution over the full range of the photon scattering angle, the normalized FSR-photon energy distribution approaches a well-known universal FSR radiator function in the soft-photon limit with x_γ close to zero:

$$\mathcal{F}_1^X(s;x_\gamma) \to \frac{\alpha}{\pi}\frac{1}{x_\gamma}\left[(1+\beta_s^2)L(\beta_s) - 2\right] \quad \text{as} \quad x_\gamma \to 0 \quad (5.27)$$

independently of the spin of the charged particle emitting the photon [324, 325].

When the photon energy fraction approaches the $X\bar{X}$ threshold, the radiator function $\mathcal{F}_2^X$ goes to zero $\sim \beta_q^3$ for both the spin-0 and spin-1/2 cases. In contrast to this P-wave behavior, the radiator function $\mathcal{F}_1^X$ exhibits a S-wave threshold behavior as

$$\mathcal{F}_1^X(s;x_\gamma) \to \frac{\alpha}{\pi}\beta_q\begin{cases} 2/\beta_s & \text{for spin-0 charged slepton} \\ 2\beta_s/(3-\beta_s^2) & \text{for spin-1/2 chargino} \end{cases} \quad \text{as} \quad x_\gamma \to \beta_s^2 \quad (5.28)$$

not only for the spin-1/2 chargino case but also for the spin-0 charged slepton case. In the charged slepton case, the S-wave excitation of the FSR part is due to the momentum-independent four-point contact terms contributing to the diagram in Fig. 5.1(e).

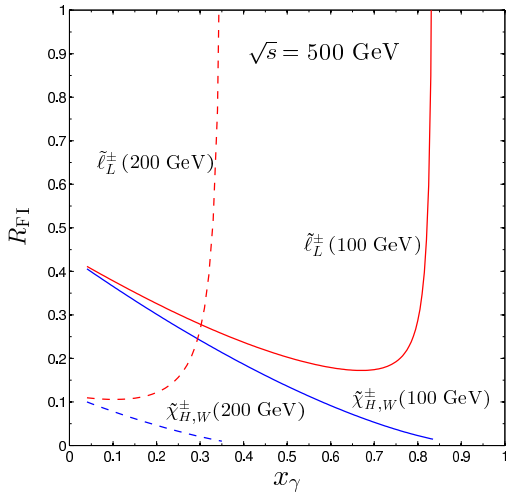

Figure 5.2: Ratio of the FSR to the ISR versus x_γ in the production of a charged pair at a 500 GeV ILC. The solid and dashed lines are for $m_X = 100$ GeV and 200 GeV, respectively. The up-ward (red) and falling (blue) lines are for the spin-0 charged slepton case and the spin-1/2 chargino cases, respectively.

5.2.3 Effects of the ISR and FSR in charged pair production

The FSR part in the photon-associated charged pair production is expected to be much smaller in magnitude than the ISR part as the photon in the FSR part is generated from a charged particle much heavier than the electron. Because of this generally-expected feature, the FSR part has been ignored in most previous analytic and numerical analyses on the single-photon processes. In this subsection, we assess the validity of the ISR approximation critically by exploiting the ratio of the FSR part to the ISR part defined as

$$\mathcal{R}_{\rm FI}(x_\gamma) = \frac{d\sigma(e^+e^- \to \gamma X \bar{X})_{\rm FSR}/dx_\gamma}{d\sigma(e^+e^- \to \gamma X \bar{X})_{\rm ISR}/dx_\gamma}. \tag{5.29}$$

in terms of the x_γ-dependent distributions derived by integrating Eqs.(5.16) and (5.21) over the scattering angle θ_γ, respectively.

Figure 5.2 shows the dependence of the ratio of the FSR part to the ISR part for two mass values, $m_X = 100$ GeV (solid lines) and 200 GeV (dashed lines). The photon scattering angle has been restricted to $10^\circ < \theta_\gamma < 170^\circ$. As the falling (blue) lines indicate, the

FSR part of the chargino pair production cross section is consistently smaller than the corresponding ISR part and it becomes negligible, in particular, near the threshold. As the mass increases, the ratio is even more suppressed. Nevertheless, for more precise mass and coupling measurements it will be more meaningful to include the FSR part in any realistic analyses.

In contrast to the spin-1/2 chargino case, the ratio of the FSR part to the ISR part does not monotonically decrease with increasing x_γ in the slepton scenario. In fact, the ratio blows up near the threshold, as the FSR part decreases in proportion to β_q in S-waves while the ISR part decreases in proportion to β_q^3 in P-waves. Therefore, the FSR contribution qualitatively changes the threshold behavior, although it would be challenging to quantitatively determine the fast-falling distribution at the threshold with limited statistics, as will be discussed in Sec. 5.3.2.

5.3 CHARACTERISTICS OF THE PRODUCTION CROSS SECTIONS

The most severe irreducible background to the signal events under consideration is the standard $e^+e^- \to \gamma\nu\bar{\nu}$ with $\nu = \nu_e, \nu_\mu$ and ν_τ. For the sake of comparison, the unpolarized x_γ distribution for the background is shown (solid line on the top) together with the distributions for different SUSY EW particles with $m_X = 100$ GeV in Fig. 5.3. Throughout this chapter, we will illustrate our results for a 500 GeV ILC.

For $m_X > m_Z/2$, one powerful kinematic cut for reducing the irreducible background reaction $e^+e^- \to \gamma\nu\bar{\nu}$ can be applied to the recoil mass squared $q^2 = (q_1 + q_2)^2 = (p_1 + p_2 - k)^2 = s(1 - x_\gamma)$ which can be very accurately reconstructed by measuring the photon energy fraction x_γ. We evaluate the overall statistical significance N_{SD} for the signal and background by summing over all events not only with the photon energy and angular cuts applied but also with the recoil mass cut $\sqrt{q^2} > 2m_X$. Note that this mass cut eliminates the Z-pole contribution to the $\gamma\nu\bar{\nu}$ background.

Another way of removing the background significantly is to exploit the electron and positron beam polarizations. The t-channel W-exchange diagrams contribute to the back-

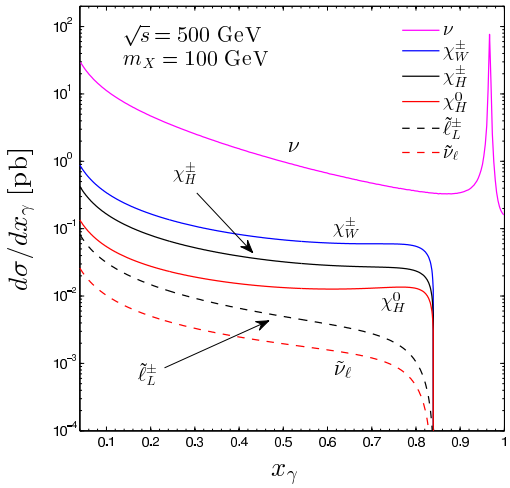

Figure 5.3: Unpolarized x_γ distribution $d\sigma/dx_\gamma$ with $m_X = 100$ GeV at a 500 GeV ILC, for different SUSY EW particles, as well as that of the background process $e^+e^- \to \gamma\nu\bar{\nu}$ (solid line on the top). The photon scattering angle has been restricted to $10^\circ < \theta_\gamma < 170^\circ$.

ground process $e^+e^- \to \gamma\nu_e\bar{\nu}_e$ only for the left-handed electrons so that the background can be significantly reduced by taking the right-handed electron and left-handed positron beams. However, which beam polarization is more efficient for the signal significance is determined also according to the polarization dependence of the signal events.

5.3.1 Statistical significance of signal events

In order to quantify whether an excess of signal photons from the $X\bar{X}$ pair production, $N_S = \mathcal{L}\sigma$ for a given integrated luminosity $\mathcal{L}$, can be measured over the $N_B = \mathcal{L}\sigma_B$ SM background photons from the radiative neutrino production, we define a simple-minded theoretical significance

$$N_{SD} = \frac{N_S}{\sqrt{N_S + N_B}} = \frac{\sigma}{\sqrt{\sigma + \sigma_B}}\sqrt{\mathcal{L}} \tag{5.30}$$

For our simple numerical analysis we require the photon energy to be $E_\gamma > 10$ GeV, corresponding to $x_\gamma > 0.04$ and the photon scattering angle to be $10^\circ < \theta_\gamma < 170^\circ$ so as to

guarantee that the photon will have an accurate momentum measurement. We also assume the CM energy $\sqrt{s} = 500$ GeV and the total integrated luminosity $\mathcal{L} = 0.5\,\mathrm{ab}^{-1}$.

The number of signal events needed for a required N_{SD} depends not only on the beam polarization, but also on m_X, since the recoil mass cut $\sqrt{q^2} = 2m_X$ is applied to the background process. For example, for $m_X = 100$ GeV, the total cross section of the background for $(P_-, P_+) = (-0.8, +0.3)$ is about 6230 fb implying $N_S \sim 8840$ signal events needed for statistical significance $N_{SD} = 5$, while for $(P_-, P_+) = (+0.8, -0.3)$ the cross section is 400 fb and only $N_S \sim 2250$ signal events is enough to reach $N_{SD} = 5$.

Figure 5.4 shows the dependence of the signal significance N_{SD} on the mass m_X. The left panel is for the spin-1/2 chargino or neutralino pair production and the right panel is for the spin-0 slepton pair production. In each panel, the solid lines are for the left-handed electron and right-handed positron beam polarizations with $(P_-, P_+) = (-0.8, +0.3)$ and the dashed lines for the right-handed electron and left-handed positron beam polarization with $(P_-, P_+) = (+0.8, -0.3)$.

The value of the statistical significance N_{SD} is very sensitive to the beam polarizations in the wino-type chargino $\chi^{\pm}_W$ and Higgsino-type neutralino χ^0_H cases. As the red solid and dashed lines in the left panel indicate, the significance for the Higgsino-type neutralino χ^0_H is enhanced with the right-handed/left-handed electron/positron beam polarizations. On the contrary, the significance for the wino-type chargino $\chi^{\pm}_W$ is greatly enhanced with the left-hand/right-handed electron/positron beam polarizations. In both $H_{1/2}$ and $W_{1/2}$ scenarios, the neutralinos as well as charginos can be discovered with large statistical significances up to their mass close to the beam energy $\sqrt{s}/2$.

In contrast, as shown in the right panel of Fig. 5.4 the value of the statistical significance for the charged slepton pair and the sneutrino pair production is so small that the charged slepton and the neutral sneutrino can be discovered only when its mass is less than ~ 100 GeV and 60 GeV, respectively. Higher integrated luminosity would thus be desirable for the scalar state searches.

5.3.2 Spin determination

As indicated by the kinematical factor $\mathcal{K}(\beta_q)$ in Eq. (5.20), the threshold behavior of the production cross section of a neutral pair is distinctly different in the spin-0 and spin-1/2 cases. As the red solid and dashed lines in Fig. 5.5 show, the normalized cross section for a spin-1/2 Higgsino-type Dirac neutralino pair is steeply excited in S-waves at the threshold but the corresponding cross section for a spin-0 sneutrino pair is slowly excited in P-waves. In this neutral pair production case, the spin identification can be made unambiguously through the x_γ distribution pattern near the threshold.

Like the neutral case, the ISR part of the production cross section for a charged pair exhibits a S-wave and P-wave excitation for the spin-1/2 and spin-0 particle, respectively. As pointed out before, the FSR part is steeply excited in S-waves even in the spin-0 case, which could spoil the characteristic spin-0 P-wave threshold behavior for the ISR part. However, as can be checked quantitatively with the relative contribution of the FSR part in Fig. 5.2, the FSR part becomes larger than the ISR only when the photon energy fraction x_γ is extremely close to the threshold value, where both the FSR and ISR parts are already very small due to the suppressed phase-space factor β_q. Therefore, as shown in Fig. 5.5, the spin of the SUSY EW particles can be determined through the excitation pattern of the (normalized) photon energy distributions near the threshold − a sharp S-wave excitation for a spin-1/2 particle and a slow P-wave excitation for a spin-0 particle, only with a negligible contamination of the FSR part even for the charged pair production.

It would be instructive to quantify the statistical significance of the measurement for the energy distributions. Assuming the CM energy $\sqrt{s} = 500$ GeV and the total integrated luminosity $\mathcal{L} = 0.5\,\text{ab}^{-1}$ we examine the signal distributions after the background subtraction, like those in Fig. 5.5. For illustration, we compare the three production scenarios for $H_{1/2}$, $W_{1/2}$ and L_0. In Figs. 5.6, we show predicted shapes of the event distributions versus x_γ by the solid curves, for $m_X = 100$ GeV (upper row) and 60 GeV (lower row), respectively. To be realistic, we also include the statistical error bars as determined by the large number of background events $\sqrt{N_B}$ in the last three bins near the threshold. As noticed earlier, the $L_{1/2}$ scalar signal is not nearly as good as the fermionic states. Thus the spectrum determination

near the threshold is significantly worse as shown in Fig. 5.6(c) and (f). Nevertheless, the difference between the spin-1/2 and spin-0 distributions is unambiguously distinguishable as seen from the figures. The difference becomes more distinctive for lighter states. If future data hint at low cross section scalar signal, it will warrant a dedicated experimental study including soft decay products, which could significantly improve signal-to-background ratio as shown in Ref. [288]. In such a case a definitive confirmation of the scalar nature could be achieved already with moderate luminosities.

5.3.3 Ratio of left-handed and right-handed cross sections

To see the polarization dependence of the signal cross sections, we define the left-right (LR) ratio of the purely right-handed cross section to the purely left-handed cross section:

$$\mathcal{R}_{LR}(X; x_\gamma) = \frac{d\sigma(e^+e^-_R \to \gamma X\bar{X})/dx_\gamma}{d\sigma(e^+e^-_L \to \gamma X\bar{X})/dx_\gamma} \tag{5.31}$$

obtained after applying the photon-angle cut described before. Fig. 5.7 shows the x_γ dependence of the ratio of the right-handed electron cross section to the left-handed electron cross section.

Before discussing the features that the LR ratios exhibit, we note that for $m_X = 100$ GeV the inequality relation $s \geq q^2 \geq 4m_X^2 = 4 \times 10^4$ GeV$^2 \gg m_Z^2$ is satisfied so that the polarization factor $\mathcal{P}$ defined in Eq. (5.19) is nearly constant over the whole x_γ range $[0.05, 0.84]$. In particular, for the neutral pair production with the photon radiated from the initial electron or positron line and with no virtual-photon exchange, the ratio is indeed constant and its value for the SU(2)$_L$ doublet state $X = \chi^0_H, \tilde{\nu}_\ell$ is given by

$$\mathcal{R}_{LR}[X] = \frac{c_R^2}{c_L^2} = \frac{s_W^4}{(1/2 - s_W^2)^2} \simeq 0.648 \quad \text{for} \quad X = \chi^0_D, \tilde{\nu}_\ell \tag{5.32}$$

independently of the spin of the produced particle X for $s_W^2 \simeq 0.223$ given in Ref. [326], as shown in the left frame of Fig. 5.7.

In contrast to the neutral pair production, the LR ratio for each charged pair production exhibits a slight dependence on the photon energy fraction x_γ with a visible variation near the threshold with $x_\gamma = 1 - 4m_X^2/s = 0.84$ (see the lower two lines in the left frame of

Fig. 5.7). The reason is that the cross section for the charged pair production consists not only of the ISR but also of the FSR parts which have different x_γ-dependent radiator functions as well as slightly different x_γ-dependent polarization factors. Note that the initial polarization factor is a function of q^2, i.e. x_γ, while the final polarization factor is constant for a given $\sqrt{s}$. Neglecting the slight variations due to the FSR contributions, the LR ratio $\mathcal{R}_{LR}$ is given to a good approximation by

$$\mathcal{R}_{LR}[X] \simeq \begin{cases} 4s_W^4 \approx 0.199 & \text{for} \quad X = \chi_H^-, \tilde{\ell}_L^- \\ 0 & \text{for} \quad X = \chi_W^- \end{cases} \tag{5.33}$$

The approximately zero ratio $\mathcal{R}_{LR}$ in the wino-type chargino case can be traced to the perfect cancellation between the γ and Z exchange diagrams for the right-handed electron beam polarization, i.e. $1 + c_R\, c^Z_{\chi_W^-} = 1 - (s_W/c_W)(c_W/s_W) = 0$ in the asymptotic limit.

The right frame of Fig. 5.7 shows the LR ratio of the inclusive sum of the charged and neutral pair production cross sections in each scenario. Again this inclusive LR ratio remains almost constant and enables us to distinguish the $W_{1/2}$ scenario from the $H_{1/2}$ and L_0 scenarios.

Figure 5.8 shows the statistical errors of the LR ratio measurements as determined by the background fluctuation $\sqrt{N_B}$, for the three scenarios with two different representative masses $m_X = 100$ GeV (left panel) and 60 GeV (right panel), assuming $\sqrt{s} = 500$ GeV CM energy and $\mathcal{L} = 0.5\,\text{ab}^{-1}$ luminosity with both polarizations $(P_-, P_+) = (\mp 0.8, \pm 0.3)$. It is clear that the $W_{1/2}$ and $H_{1/2}$ scenarios show very distinct value, even after the fluctuation of the background is included. However, similar to the spin determination, it is less impressive to measure the ratio for the $L_{1/2}$ scenario, due to its low significance.

5.3.4 Alternative discrimination methods

While the Higgsino-type neutralino χ_H^0 in the $H_{1/2}$ scenario is a Dirac fermion, the wino-type neutralino χ_W^0 in the $W_{1/2}$ scenario is a Majorana fermion. Unlike the Dirac neutralino the Majorana neutralino χ_W^0 can mediate via a t-channel exchange a typical fermion-number violating process such as the same-sign chargino-pair production process, $W^-W^- \to \chi_W^-\chi_W^-$. The possible e^-e^- collision mode of the ILC experiments enables us to distinguish the $W_{1/2}$

scenario from the $H_{1/2}$ scenario by searching for the same-sign WW fusion process via the process $e^-e^- \to \nu_e\nu_e W^-W^- \to \nu_e\nu_e\chi_W^-\chi_W^-$.

Although the neutral state X^0 of the (nearly) degenerate pair $[X^-, X^0]$ in each scenario is stable, the charged state X^- can decay to X^0 via charged current interactions. For the typical loop-induced mass differences of a few hundred MeV the most important decay modes are $X^- \to X^0\pi^-, X^0e^-\bar{\nu}_e$ and $X^0\mu^-\bar{\nu}_\mu$. The decay products typically have low p_T, but as demonstrated for the proposed International Large Detector (ILD) at the ILC tracking efficiency of 60% can be expected down to p_T values of 200 MeV [89]. On the other hand, the inner layer of the ILD vertex detector would be extended down to the radius of 1.6 cm, therefore offering good prospects of observing X^- tracks, which in this case would have a decay length of $\mathcal{O}(10\,\text{cm})$ or less. The combination of different detection methods based on the massive charged tracks, displaced vertices, and soft decay products will enable us to cover all mass differences. Since relatively low data volumes are expected, no hardware trigger would be needed allowing for search of rare processes. Even in the case when the decays products can be observed, all scenarios analyzed here would lead to the same final state. The angular photon distributions would therefore offer a convenient discrimination method. Finally, angular distributions of the decay products would provide additional information on the spin, but such an analysis is beyond scope of the present study.

5.4 SUMMARY

Given the current null results for SUSY searches at the LHC, we were strongly motivated to consider the situation in which the only accessible SUSY states are EW gauginos, Higgsinos or sleptons. We explored three characteristic scenarios, each of which has a nearly degenerate pair of a charged state and a neutral state with a small mass difference. In the framework of MSSM the three cases can be characterized as (a) two spin-1/2 Higgsino $\text{SU}(2)_L$ doublets, (b) a spin-1/2 wino $\text{SU}(2)_L$ triplet and (c) a spin-0 left-handed slepton $\text{SU}(2)_L$ doublet beyond the SM particle spectrum. We presented the theoretical structures, their interactions with the SM fields and their radiatively-induced mass splitting in Sec. 5.1.

Due to near mass degeneracy, not only the neutral particle but also the charged particle of each pair is not easily detectable in collider experiments. We first presented the analytic expressions for the pair production of an invisible neutral pair involving a hard photon emission, and discussed their general features from the initial state radiation (ISR) and the final state radiation (FSR) in Sec. 5.2. In our numerical studies, we illustrated our results with a 500 GeV ILC. We provided a detailed and systematic analysis with polarized electron and positron polarizations so as to check the detectability of the charged particles as well as neutral particles and how well their properties can be characterized. As discussed in Sec. 5.2.3, the FSR effect in the spin-1/2 charged pair production, compared to the ISR part, decreases monotonically in size from about 40 (10) % for $x_\gamma = 0.04$ and becomes negligible close to the threshold with $x_\gamma = 0.84$ (0.36) for $m_X = 100$ (200) GeV and $\sqrt{s} = 500$ GeV. Therefore, the previous analyses in the literature based on the ISR approximation are rather reliable, especially when the mass m_X is not far from the half of the e^+e^- CM energy $\sqrt{s}$. On the contrary, in the spin-0 charged pair production, the FSR effect becomes larger than the ISR part near the threshold as shown in Fig. 5.2, which might endanger any consequences based simply on the ISR approximation. Nevertheless, we found that, in spite of the FSR contamination, the results based on the ISR approximation are quantitatively very similar to those with both the ISR and FSR parts.

In Sec. 5.3.1, we studied the signal observation with respect to the SM backgrounds. We also demonstrated in Sec. 5.3.2 that the excitation pattern near the threshold can be exploited through the photon energy distribution to determine the spin of the SUSY EW particles unambiguously. The (normalized) photon energy distribution near threshold shows a steeply-rising S-wave excitation for a spin-1/2 pair while a slowly-rising P-wave excitation for a spin-0 pair, even after the contamination from the FSR part is included (see Fig. 5.5). For two representative masses $m_X = 100$ and 60 GeV, we showed, in Fig. 5.6, that the threshold patterns of the $H_{1/2}$ and $W_{1/2}$ scenarios can be determined with a good accuracy at the ILC with the CM energy $\sqrt{s} = 500$ GeV and the total integrated luminosity $\mathcal{L} = 0.5\,\text{ab}^{-1}$, and they are notably distinctive from the $L_{1/2}$ scenario.

Furthermore, the LR ratio of right-handed and left-handed cross sections introduced in Sec. 5.3.3 takes very different values according to the production modes; $\sim s_W^4/(1/2 - s_W^2)^2 \simeq$

0.65 for $X = \chi_D^0$ and $\tilde{\nu}_\ell$; $\sim 4s_W^4 \simeq 0.20$ for $X = \chi_H^-$ and $\tilde{\ell}_L^-$; and ~ 0 for $X = \chi_W^-$. Even after taking the inclusive sum of the charged and neutral modes in each scenario, the LR ratio has a nearly constant value that can be used for distinguishing the $W_{1/2}$ scenario from the others even with statistical error included, as shown in Fig. 5.7 and Fig. 5.8. Therefore, in addition to enhancing the statistical significance sizably, the electron and positron beam polarizations are very powerful in characterizing the production modes. Combining the LR ratio and the threshold excitation pattern, we can identify unambiguously which scenario among the three scenarios is realized. Our analyses are easily generalizable to other collider energies as long as the pair production is kinematically accessible.

Our analytic and numerical results demonstrate clearly the strong physics potential of the ILC in detecting and characterizing the invisible particles, complementary to the very difficult searching environment at the LHC. Further detailed analyses and detector simulations may be needed to reach fully realistic conclusions at the ILC.

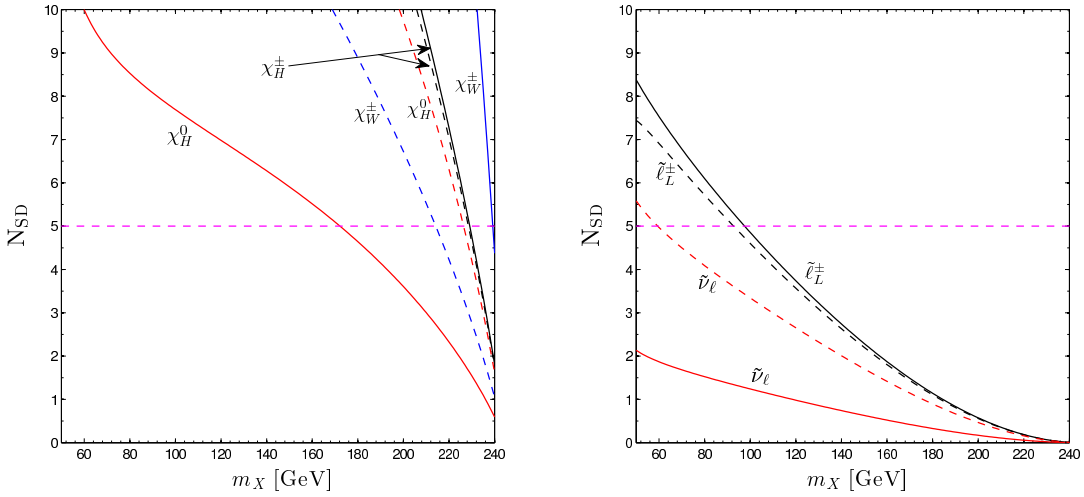

Figure 5.4: Statistical significance N_{SD} versus m_X for $\sqrt{s} = 500$ GeV and the total integrated luminosity $\mathcal{L} = 0.5\,\text{ab}^{-1}$. The left panel is for the spin-1/2 chargino or neutralino pair production and the right panel for the spin-0 slepton pair production. The solid/dashed lines are for the left-handed/right-handed electron and right-handed/left-handed positron beam polarizations with $(P_-, P_+) = (\mp 0.8, \pm 0.3)$, respectively.

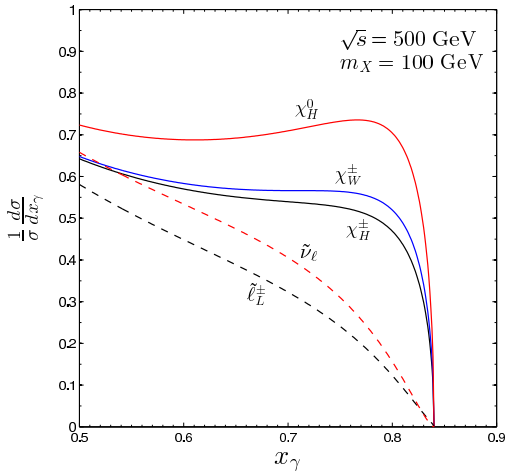

Figure 5.5: Normalized distribution versus the photon energy fraction x_γ with $m_X = 100$ GeV. Effects of both FSR and ISR are included.

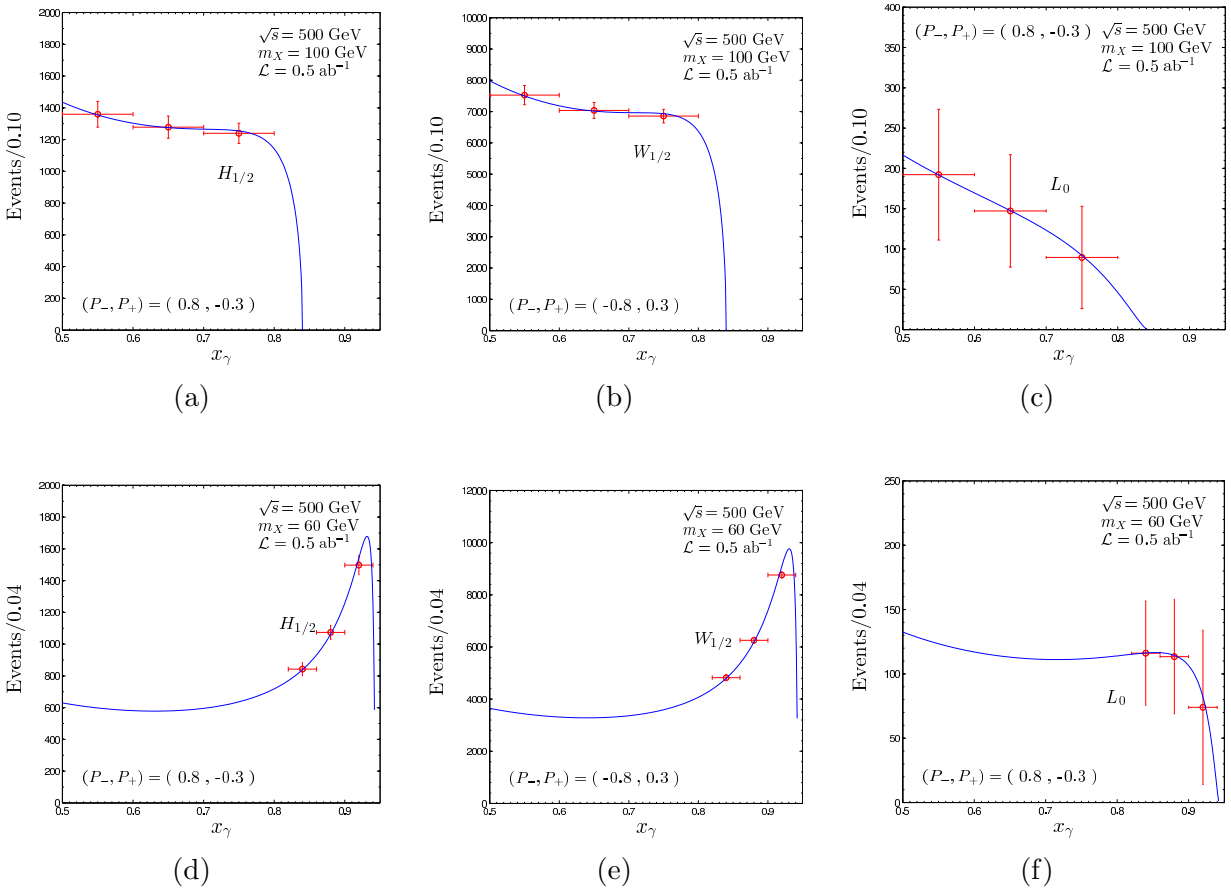

Figure 5.6: Photon energy fraction distribution near the threshold, after the background subtraction, with $m_X = 100$ GeV (first row) and 60 GeV (second row). The statistical error bars correspond to the background fluctuation $\sqrt{N_B}$

.

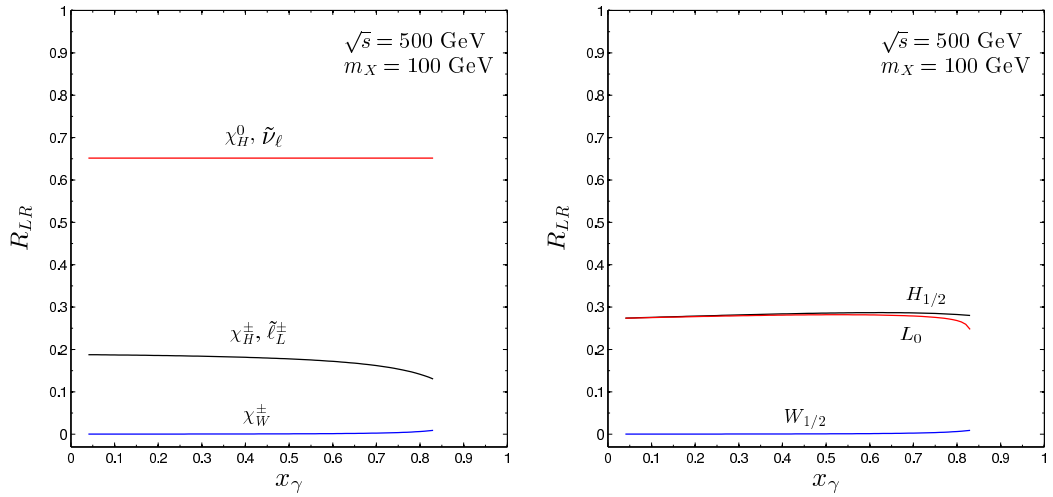

Figure 5.7: Ratio of the purely right-handed electron cross section to the purely left-handed electron cross section versus the photon energy fraction x_γ with $m_X = 100$ GeV. Left panel: individual channels of the pair production. Right panel: inclusive sums of the charged and neutral pair production.

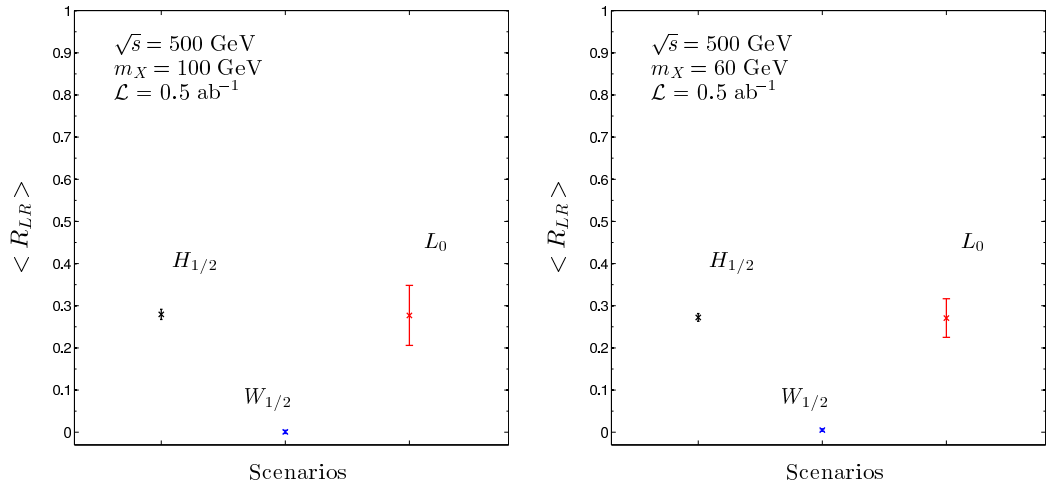

Figure 5.8: Ratio of the purely right-handed electron total cross section to the purely left-handed electron total cross section with $m_X = 100$ GeV (left panel) and 60 GeV (right panel). The statistical error bars correspond to the background fluctuation $\sqrt{N_B}$ that comes from the measurement of the total cross sections with polarizations $(P_-, P_+) = (\mp 0.8, \pm 0.3)$.

6.0 SPIN AND CHIRALITY EFFECTS IN ANTLER-TOPOLOGY PROCESSES AT HIGH ENERGY e^+e^- COLLIDERS

Once any new particle indicating new physics beyond the SM is discovered at the LHC or high energy e^+e^- colliders, one of the first crucial steps is to experimentally determine its spin as well as its mass because spin is one of the canonical characteristics of all particles required for defining a new theoretical framework as a Lorentz-invariant quantum field theory [41].

Many models beyond the SM [24–36] have been proposed and studied not only to resolve several conceptual issues like the gauge hierarchy problem but also to explain the dark matter (DM) composition of the Universe with new stable weakly interacting massive particles [37–39]. For this purpose, a (discrete) symmetry such as R paity in supersymmetric (SUSY) models and Kaluza-Klein (KK) parity in universal extra-dimension (UED) models is generally introduced to guarantee the stability of the particles and thus to explain the DM relic density quantitatively. As a consequence, the new particles can be produced only in pairs at high energy hadron or lepton colliders, leading to challenging signatures with at least two invisible final-state particles.

In chapter, we study the following production-decay

$$e^+e^- \to \mathcal{P}^+\mathcal{P}^- \to (\ell^+\mathcal{D}^0)(\ell^-\bar{\mathcal{D}}^0) \tag{6.1}$$

dubbed antler-topology events [57], which contain the production of an electrically charged pair $\mathcal{P}^+\mathcal{P}^-$ in e^+e^- collisions followed by the two-body decays, $\mathcal{P}^+ \to \ell^+\mathcal{D}^0$ and $\mathcal{P}^- \to \ell^-\bar{\mathcal{D}}^0$, giving rise to a charged lepton pair $\ell^\pm(= e^\pm, \mu^\pm)$ and an invisible pair $\mathcal{D}^0\bar{\mathcal{D}}^0$ (See Fig. 6.1).

The invisible particle $\mathcal{D}^0$ may be charge self-conjugate, i.e. $\bar{\mathcal{D}}^0 = \mathcal{D}^0$. Nevertheless, it is expected to be insubstantial quantitatively whether the particle is self-conjugate or not, unless the width of the parent particle $\mathcal{P}^\pm$ is very large and there exist large chirality mixing

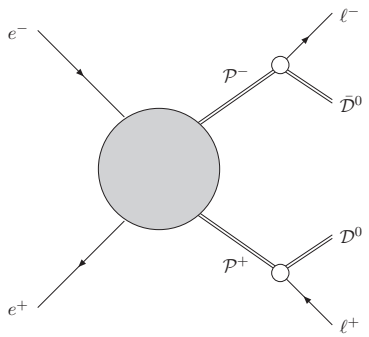

Figure 6.1: The correlated process $e^+e^- \to \mathcal{P}^+\mathcal{P}^- \to (\ell^+\mathcal{D}^0)(\ell^-\bar{\mathcal{D}}^0)$ characterized by the antler-topology diagram. Here, the invisible final-state particle $\mathcal{D}^0$ might be charge self-conjugate, i.e. $(\mathcal{D}^0)^c = \mathcal{D}^0$.

contributions [327]. So, any interference effects due to the charge self-conjugateness of the invisible particle will be ignored in the present work.[1]

If the parent particle $\mathcal{P}^-$ carries an electron number $L_e(\mathcal{P}^-) = +1$ or a muon number $L_\mu(\mathcal{P}^-) = +1$, then the final-state leptons must be e^-e^+ or $\mu^-\mu^+$, respectively, if electron and muon numbers are conserved individually and the invisible particles, $\mathcal{D}^0$ and $\bar{\mathcal{D}}^0$, carry no lepton numbers. On the other hand, if the parent particle carries no lepton number, the final-state leptons can be any of the four combinations, $\{e^-e^+, e^-\mu^+, \mu^-e^+, \mu^-\mu^+\}$, and the invisible particles, $\mathcal{D}^0$ and $\bar{\mathcal{D}}^0$, must carry the same lepton number as $\ell^\mp = e^\mp, \mu^\mp$, respectively.

Once the masses of new particles are determined by (pure) kinematic effects [328], a sequence of techniques increasing in complexity can be applied to determine the spins and chirality properties of particles in the correlated antler-topology process at e^+e^- colliders [329–334]:

(a) Rise of the excitation curve near threshold with polarized electron and positron beams;

(b) Angular distribution of the production process;

[1] An indirect but powerful way of checking the charge self-conjugateness of the particle $\mathcal{D}^0$ is to study the process $e^-e^- \to \mathcal{P}^-\mathcal{P}^-$ to which the self-conjugate particle $\mathcal{D}^0$ can contribute through its t-channel exchange. The e^-e^- mode is under consideration as a satellite mode at the ILC.

(c) Angular distributions of the decays of polarized particles;

(d) Angular correlations between decay products of two particles.

While the first and second steps (a) and (b) are already sufficient in the case with a spin-0 scalar $\mathcal{P}^\pm = S_p^\pm$ as will be demonstrated in detail, the production-decay correlations need to be considered for the case with a spin-1/2 fermion $\mathcal{P}^\pm = F_p^\pm$ and a spin-1 $\mathcal{P}^\pm = V_p^\pm$ to determine the $\mathcal{P}$ spin unambiguously; in principle a proper combination of these complementary techniques enables us to determine the spins of the invisible particles, $\mathcal{D}^0$ and $\bar{\mathcal{D}}^0$, and all the intermediate particles exchanged in s-, t- or u-channel diagrams participating in the production process. For our numerical analysis we follow the standard procedure. We show through detailed simulations how the theoretically predicted distributions can be reconstructed after including initial state QED radiation (ISR), beamstrahlung and width effects as well as typical kinematic cuts.

The chapter is organized as follows. In Sect. 6.1 we describe a general theoretical framework for the spin and chiral effects in antler-topology processes at high energy e^+e^- colliders. In Sect. 6.2 we present the complete amplitudes and polarized cross sections for the production process $e^+e^- \to \mathcal{P}^+\mathcal{P}^-$ in the e^+e^- center-of-mass (c.m.) frame with the general set of couplings listed in Appendix A. The technical framework we have employed is the helicity formalism [335]. Then, we present in Sect. 6.3 the complete helicity amplitudes of the two-body decays $\mathcal{P}^+ \to \ell^+\mathcal{D}^0$ and $\mathcal{P}^- \to \ell^-\bar{\mathcal{D}}^0$ with general couplings given in Appendix A. Sect. 6.4 describes how to obtain the fully-correlated six-dimensional production-decay angular distributions by combining the production helicity amplitudes and the two two-body decay helicity amplitudes and by implementing arbitrary electron and positron polarizations [336–340]. Sect. 6.5, the main part of the present work, is devoted to various observables: the threshold-excitation patterns, the production angle distributions equipped with polarized beams, the lepton decay polar-angle distributions and the lepton angular-correlations of the two two-decay modes. They provide us with powerful tests of the spin and chirality effects in the production-decay correlated process. While all the analytic results are maintained to be general, the numerical analyses are given for the theories with (approximate) electron chirality conservation such as SUSY and UED models and a subsection will be devoted to a brief discussion of the possible influence from electron chirality violation effects. Finally, we sum-

marize our findings and conclude in Sect. 6.6. For completeness, we include three appendices in addition to Appendix A. In Appendix B, we list all of the Wigner d-functions used in the main text [341]. In Appendix C, we describe how to obtain the expression of the production matrix element-squared for arbitrary polarized electron and positron beams. Finally, in Appendix D we give an analytic proof of the presence of a twofold discrete ambiguity in determining the $\mathcal{P}^{\pm}$ momenta in the process $e^+e^- \to \mathcal{P}^+\mathcal{P}^- \to (\ell^+\mathcal{D}^0)(\ell^-\bar{\mathcal{D}}^0)$, even if the masses of the particles, $\mathcal{P}^{\pm}$ and $\mathcal{D}^0$ ($\bar{\mathcal{D}}^0$), are a priori known.

6.1 SETUP FOR MODEL-INDEPENDENT SPIN DETERMINATIONS

Generally, the production part $e^+e^- \to \mathcal{P}^+\mathcal{P}^-$ of the antler-topology process (6.1) can occur through s-, t- and/or u-channel diagrams in renormalizable field theories, as shown in Fig. 6.2. Which types of diagrams are present and/or significant depend crucially on the nature of the new particles, $\mathcal{P}^{\pm}$, $\mathcal{D}^0$ and $\bar{\mathcal{D}}^0$ as well as the SM leptons $\ell^{\pm}$ and on the constraints from the discrete symmetries conserved in the theory.

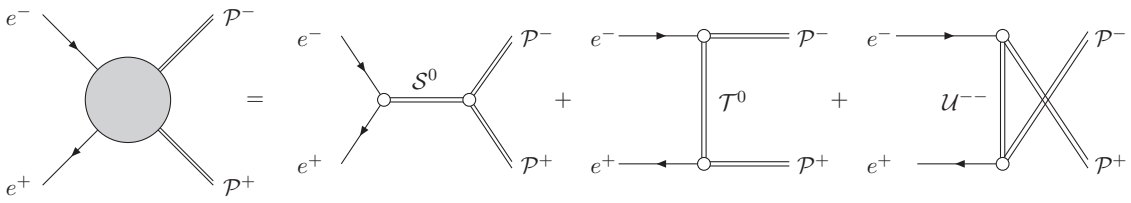

Figure 6.2: New s-channel $\mathcal{S}^0$-exchange diagrams (including the standard γ- and Z-exchange diagrams), new t-channel $\mathcal{T}^0$-exchange diagrams and new u-channel $\mathcal{U}^{--}$-exchange diagrams to the pair-production process $e^+e^- \to \mathcal{P}^+\mathcal{P}^-$.

We assume that the new particles, $\mathcal{P}^{\pm}$, $\mathcal{D}^0$ and $\bar{\mathcal{D}}^0$, are produced on-shell in the antler-topology process (6.1), and they are uncolored under the SM strong-interaction group so that they are not strongly interacting.[2] Motivated mainly by the DM problem, the new particles

[2]In addition, assuming the widths of the new particles to be much smaller than their corresponding

are assumed to be odd under a conserved discrete Z_2-parity symmetry. Therefore, they can only be produced in pairs at high energy hadron and lepton colliders with an initial Z_2-parity even environment such as LHC, ILC, TLEP and CLIC, etc. Furthermore, the invisible particle $\mathcal{D}^0$ participating in the two-body decay $\mathcal{P}^+ \to e^+\mathcal{D}^0$, if the decay mode is present, is included among the particles $\mathcal{T}^0$ exchanged in the t-channel diagram of the production process $e^+e^- \to \mathcal{P}^+\mathcal{P}^-$. This implies that unavoidably at least one of the particles $\mathcal{T}^0$ is lighter than the particle $\mathcal{P}^\pm$ in the antler-topology process with $\ell^\pm = e^\pm$.

As the $\mathcal{P}^-$ as well as the electron e^- is singly electrically-charged, the s- and t-channel processes are mediated by (potentially several) neutral particles, $\mathcal{S}^0$ and $\mathcal{T}^0$, but any u-channel processes must be mediated by (potentially several) doubly-charged particles, $\mathcal{U}^{--}$. In passing, we note that most of the popular extensions of the SM such as supersymmetry (SUSY) and universal extra-dimension (UED) models contain no doubly-charged particles so that there exist only s-channel and/or t-channel exchange diagrams but no u-channel exchange diagrams contributing to the production process $e^+e^- \to \mathcal{P}^+\mathcal{P}^-$. The s-channel scalar-exchange contributions may be practically negligible as well because the electron-chirality violating couplings of any scalar to the electron line are strongly suppressed in proportion to the tiny electron mass in those SUSY and UED models.

Since the on-shell particles, $\mathcal{P}^\pm$, $\mathcal{D}^0$ and $\bar{\mathcal{D}}^0$ as well as the virtual intermediate particles, $\mathcal{S}^0$, $\mathcal{T}^0$ and $\mathcal{U}^{\pm\pm}$, are not directly measured, their spins and couplings as well as masses are not a priori known. The neutral state $\mathcal{S}^0$ can be a spin-0 scalar, S^0_s, or a spin-1 vector boson, V^0_s, including the standard gauge bosons $V^0_s = \gamma, Z$ as well. Each of the other intermediate particles can be a spin-0 scalar, a spin-1/2 fermion or a spin-1 vector boson, assigned in relation to the spin of the particle $\mathcal{P}^\pm$. In any Lorentz-invariant theories, there exist in total twenty ($20 = 2 + 8 + 8 + 2$) different spin assignments for the production-decay correlated antler-topology process (6.1) as

$$\begin{aligned}(J_{\mathcal{P}},J_{\mathcal{D}};J_{\mathcal{S}},J_{\mathcal{T}},J_{\mathcal{U}}) = \Big\{ &\left(0,\tfrac{1}{2};0\oplus 1,\tfrac{1}{2},\tfrac{1}{2}\right),\left(\tfrac{1}{2},0;0\oplus 1,0\oplus 1,0\oplus 1\right), \\ &\left(\tfrac{1}{2},1;0\oplus 1,0\oplus 1,0\oplus 1\right),\left(1,\tfrac{1}{2};0\oplus 1,\tfrac{1}{2},\tfrac{1}{2}\right)\Big\}\end{aligned} \tag{6.2}$$

masses, we neglect their width effects for any analytic expressions, although we consider them in numerical simulations in the present work.

with spins up to 1 and couplings consistent with renormalizable interactions. The symbols used for the particles in our analysis are listed in Table 6.1 along with their charges, spins and Z_2 parities. Generically, the intermediate states, $\mathcal{S}^0$, $\mathcal{T}^0$ and $\mathcal{U}^{--}$ may stand for several different states, although typically the on-shell particle $\mathcal{P}^{\pm}$ or $\mathcal{D}^0$ stands for a single state. Note that, if the parent particle $\mathcal{P}^{\pm}$ turns out to be a spin-0 or spin-1 particle, then the daughter particles, $\mathcal{D}^0$ and $\bar{\mathcal{D}}^0$, and the t- and u-channel intermediate particles $\mathcal{T}^0$ and $\mathcal{U}^{\pm\pm}$ are guaranteed to be spin-1/2 particles.

Particle	Spin			Charge	Z_2 Parity
	0	1/2	1		
ℓ^-		ℓ^-		-1	$+$
$\mathcal{D}^0$	S_d^0	F_d^0	V_d^0	0	$-$
$\mathcal{P}^-$	S_p^-	F_p^-	V_p^-	-1	$-$
$\mathcal{S}^0$	S_s^0	F_s^0	V_s^0	0	$+$
$\mathcal{T}^0$	S_t^0	F_t^0	V_t^0	0	$-$
$\mathcal{U}^{--}$	S_u^{--}	F_u^{--}	V_u^{--}	-2	$-$

Table 6.1: List of symbols used for the particles in our analysis with their electric charges, spins and Z_2 parities. The symbol ℓ^- denotes an electron e^- or a muon μ^-. The last three lines are for the new particles exchanged in the s-, t- and u-channel diagrams including the neutral electroweak gauge bosons, γ and Z, exchanged in the s-channel diagram in the production process, $e^+e^- \to \mathcal{P}^+\mathcal{P}^-$.

Among the elementary particles discovered so far, the electron is the lightest electrically-charged particle in the SM. Its mass $m_e \simeq 0.51\,\text{MeV} \sim 2 \times 10^{-6}\, v$ is much smaller than the vacuum expectation value (vev) $v \simeq 246$ GeV of the SM Higgs field, the weak scale for setting the masses of leptons and quarks, as well as the c.m. energies of future high-energy e^+e^- colliders. Any kinematic effects due to the electron mass are negligible so that the electron will be regarded as a massless particle from the kinematic point of view in the present work. The near masslessness of the electron is related to the approximate chiral

symmetry of the SM. Any new theory beyond the SM should guarantee the experimentally-established smallness of the electron mass. This is a challenge in new theories beyond the SM since they usually involve larger mass scale(s) than the weak scale. One simple and natural protection mechanism is chiral symmetry.[3]

Nevertheless, we do not impose any type of chiral symmetry so as to maintain full generality in our model-independent analysis of spin and chirality effects, emphasising the importance of checking experimentally to what extent the underlying theory possesses chiral symmetry. In each three-point vertex involving a fermion line, i.e. two spin-1/2 fermion states, we allow for an arbitrary linear combination of right-handed and left-handed couplings. Only in our numerical examples will every interaction vertex involving the initial $e^{\pm}$ line and the final-state lepton $\ell^{\pm}$ $(= e^{\pm}, \mu^{\pm})$ be set to be purely chiral, as is nearly valid in typical SUSY and UED models, apart from tiny contaminations proportional to the electron or muon masses generated through the BEH mechanism of EWSB [342–346].

6.2 PAIR PRODUCTION PROCESSES

In this section we present the analytic form of helicity amplitudes for the production process

$$e^-(p_-, \sigma_-) + e^+(p_+, \sigma_+) \to \mathcal{P}^-(q_-, \lambda_-) + \mathcal{P}^+(q_+, \lambda_+) \tag{6.3}$$

with the s-, t- and u-channel contributions as depicted in Fig. 6.2 with the general three-point couplings listed in Appendix A. Here, we discuss only the amplitudes for on-shell $\mathcal{P}$ pair production. The technical framework for our analytic results is the standard helicity formalism [335].

The helicity of a massive particle is not a relativistically invariant quantity. It is invariant only for rotations or boosts along the particle's momentum, as long as the momentum does not change its sign. In the present work, we define the helicities of the $\mathcal{P}^{\pm}$ in the e^+e^- c.m. frame. Helicity amplitudes contain full information on the production process and enable

[3] Other possible solutions for getting a massless fermion naturally is that the fermion is a Nambu-Goldstone fermion, the super-partner of an unbroken gauge boson or the super-partner of a Goldstone boson.

us to take into account polarization of the initial e^+e^- beams in a straightforward way as described in Appendix C.

Generically, ignoring the electron mass, we can cast the helicity amplitude into a compact form composed of two parts - an electron-chirality conserving (ECC) part Q^c and an electron-chirality violating (ECV) part Q^v - as

$$\mathcal{M}[e^-_{\sigma_-}e^+_{\sigma_+} \to \mathcal{P}^-_{\lambda_-}\mathcal{P}^+_{\lambda_+}] = \sqrt{2}e^2\left[\delta_{\sigma_+,-\sigma_-}Q^c_{\sigma_-;\lambda_-,\lambda_+} + \delta_{\sigma_+,\sigma_-}Q^v_{\sigma_-;\lambda_-,\lambda_+}\right] d^{J_0}_{\Delta\sigma,\Delta\lambda}(\theta) \tag{6.4}$$

where $J_0 = \max(|\Delta\sigma|, |\Delta\lambda|)$ with the difference of the $e^\mp$ helicities $\Delta\sigma = J_e(\sigma_- - \sigma_+) = \pm 1, 0$ and that of the $\mathcal{P}^\mp$ helicities $\Delta\lambda = J_\mathcal{P}(\lambda_- - \lambda_+)$. Here, $J_e = 1/2$ and $J_\mathcal{P}$ are the spin of the electron and the particle $\mathcal{P}$, respectively. No helicity indices are needed when the spin of the particle $\mathcal{P}$ is zero, i.e. $J_\mathcal{P} = 0$. After extracting the spin value of the electron and $\mathcal{P}$, $\sigma_\pm$ takes two values of ± 1 while $\lambda_\pm$ takes two values of ± 1 or three values $\pm 1, 0$ for $J_\mathcal{P} = 1/2$ or 1, respectively. Frequently, in the present work we adopt the conventions, $\sigma_{-,+} = \pm$ and $\lambda_{-,+} = \pm, 0$, will be used to denote the sign of the re-scaled helicity values for the sake of notational convenience. The angle θ in Eq. (6.4) denotes the scattering angle of $\mathcal{P}^-$ with respect to the e^- direction in the e^+e^- c.m. frame. The explicit form of the d functions needed here is reproduced in Appendix B.

The polarization-weighted polar-angle differential cross sections of the production process can be cast into the form

$$\begin{aligned}\frac{d\sigma^\mathcal{P}_{\rm pol}}{d\cos\theta} &= \frac{\pi\alpha^2\beta}{4s}\Big[(1 - P^L_- P^L_+)(\mathcal{C}^+_+ + \mathcal{C}^-_-) + (P^L_- - P^L_+)(\mathcal{C}^+_+ - \mathcal{C}^-_-) \\ &\quad + (1 + P^L_- P^L_+)(\mathcal{V}^+_+ + \mathcal{V}^-_-) + (P^L_- + P^L_+)(\mathcal{V}^+_+ - \mathcal{V}^-_-) \\ &\quad + 2P^T_- P^T_+ \cos\delta\,{\rm Re}(\mathcal{V}^-_+) + 2P^T_- P^T_+ \sin\delta\,{\rm Im}(\mathcal{V}^-_+)\Big]\end{aligned} \tag{6.5}$$

with δ the relative opening angle of the electron and positron transverse polarizations and β the speed of pair-produced particles, where $P^{L,T}_\pm$ is the degrees of longitudinal and transverse polarizations and δ is the relative opening angle of the $e^\pm$ transverse polarizations. The ECC

and ECV production tensors $\mathcal{C}$ and $\mathcal{V}$ are defined in terms of the reduced production helicity amplitudes by

$$\mathcal{C}_{\sigma}^{\sigma} = \sum_{\lambda_-,\lambda_+} \left| Q^{c}_{\sigma;\lambda_-,\lambda_+} \right|^2 \left[d^{J_0}_{\sigma,\Delta\lambda}(\theta) \right]^2 \tag{6.6}$$

$$\mathcal{V}_{\sigma}^{\sigma'} = \sum_{\lambda_-,\lambda_+} \left(Q^{v}_{\sigma;\lambda_-,\lambda_+} Q^{v*}_{\sigma';\lambda_-,\lambda_+} \right) \left[d^{J_0}_{0,\Delta\lambda}(\theta) \right]^2 \tag{6.7}$$

with $\sigma, \sigma' = \pm 1$ or simply $\pm$ for notational convenience. (For more detailed derivation of the polarized cross sections, see Appendix C.) The polarized total cross section $\sigma^{\mathcal{P}}_{\rm pol}$ can then be obtained by integrating the differential cross section over the full range of $\cos\theta$.

If all of the coupling coefficients are real and all the particle widths are neglected, the following relations must hold for both the ECC and ECV parts of the production helicity amplitudes:

$$Q^{c}_{\sigma;\lambda_-,\lambda_+} = Q^{c*}_{\sigma;-\lambda_+,-\lambda_-} \quad \text{and} \quad Q^{v}_{\sigma;\lambda_-,\lambda_+} = Q^{v*}_{-\sigma;-\lambda_+,-\lambda_-} \tag{6.8}$$

as a consequence of CPT invariance in the absence of any absorptive parts. Therefore, violation of this relation indicates the presence of re-scattering effects. On the other hand, CP invariance leads to the relation:

$$Q^{c}_{\sigma;\lambda_-,\lambda_+} = Q^{c}_{\sigma;-\lambda_+,-\lambda_-} \quad \text{and} \quad Q^{v}_{\sigma;\lambda_-,\lambda_+} = Q^{v}_{-\sigma;-\lambda_+,-\lambda_-} \tag{6.9}$$

independently of the absorptive parts so that the relation can be directly used as a test of CP conservation. Similarly, it is easy to see that P invariance leads to the relation for both the ECC and ECV amplitudes:

$$Q^{c,v}_{\sigma;\lambda_-,\lambda_+} = Q^{c,v}_{-\sigma;-\lambda_-,-\lambda_+} \tag{6.10}$$

which is violated usually through chiral interactions such as weak interactions in the SM.

Applying the P and CP symmetry relations to the ECC and ECV production tensors, (6.6) and (6.7), we can classify the six polar-angle distributions in Eq. (6.5) according to their P and CP properties as shown in Table 6.2. We find that the two combinations, $\mathcal{C}_+^+ + \mathcal{C}_-^-$ and $\mathcal{V}_+^+ + \mathcal{V}_-^-$, contributing to the unpolarized part are both P- and CP-even whereas the terms, $\mathcal{C}_+^+ - \mathcal{C}_-^-$ and $\mathcal{V}_+^+ - \mathcal{V}_-^-$, linear in the degrees of longitudinal polarization are P-odd

and CP-even. One of the two transverse-polarization dependent parts, $\mathrm{Re}(\mathcal{V}_+^-)$, is both P- and CP-even and the other one, $\mathrm{Im}(\mathcal{V}_+^-)$, is both P- and CP-odd. Unlike the other five distributions, the distribution $\mathrm{Im}(\mathcal{V}_+^-)$ vanishes due to CPT invariance if all the couplings are real.

Polar-angle distributions	P	CP
$\mathcal{C}_+^+ + \mathcal{C}_-^-$	even	even
$\mathcal{C}_+^+ - \mathcal{C}_-^-$	odd	even
$\mathcal{V}_+^+ + \mathcal{V}_-^-$	even	even
$\mathcal{V}_+^+ - \mathcal{V}_-^-$	odd	even
$\mathrm{Re}(\mathcal{V}_+^-)$	even	even
$\mathrm{Im}(\mathcal{V}_+^-)$	odd	odd

Table 6.2: P and CP properties of the production polar-angle distributions separable with initial beam polarizations.

As can be checked with the expression of the last line in Eq. (6.5), the transverse-polarization dependent parts can be non-zero only in the presence of some non-trivial ECV contributions so that they serve as a useful indicator for the ECV parts. If both the electron and positron longitudinal polarizations are available, then we can obtain the ECC and ECV parts of the unpolarized cross section separately. For the degrees $\xi_\pm$ of $e^\pm$ longitudinal

polarization the ECC and ECV parts of the cross section are given by the relations:

$$\begin{aligned}\frac{d\sigma^{\mathcal{P}c}_{\rm unpol}}{d\cos\theta} &= \frac{\pi\alpha^2\beta}{4s}(\mathcal{C}^+_+ + \mathcal{C}^-_-) \\ &= \frac{1}{8\xi_-\xi_+}\left[(1+\xi_-\xi_+)\left(\frac{d\sigma^{\mathcal{P}}_{\uparrow\downarrow}}{d\cos\theta}+\frac{d\sigma^{\mathcal{P}}_{\downarrow\uparrow}}{d\cos\theta}\right)-(1-\xi_-\xi_+)\left(\frac{d\sigma^{\mathcal{P}}_{\uparrow\uparrow}}{d\cos\theta}+\frac{d\sigma^{\mathcal{P}}_{\downarrow\downarrow}}{d\cos\theta}\right)\right]\end{aligned} \tag{6.11}$$

$$\begin{aligned}\frac{d\sigma^{\mathcal{P}v}_{\rm unpol}}{d\cos\theta} &= \frac{\pi\alpha^2\beta}{4s}(\mathcal{V}^+_+ + \mathcal{V}^-_-) \\ &= \frac{1}{8\xi_-\xi_+}\left[(1+\xi_-\xi_+)\left(\frac{d\sigma^{\mathcal{P}}_{\uparrow\uparrow}}{d\cos\theta}+\frac{d\sigma^{\mathcal{P}}_{\downarrow\downarrow}}{d\cos\theta}\right)-(1-\xi_-\xi_+)\left(\frac{d\sigma^{\mathcal{P}}_{\uparrow\downarrow}}{d\cos\theta}+\frac{d\sigma^{\mathcal{P}}_{\downarrow\uparrow}}{d\cos\theta}\right)\right]\end{aligned} \tag{6.12}$$

where the upper arrow ($\uparrow$) or down arrow ($\downarrow$) indicates that the direction of longitudinal polarization is parallel or anti-parallel to the particle momentum with the first and second one for the electron and positron, respectively. Furthermore, we can construct two P-odd LR-asymmetric quantities, of which one is ECC and the other is ECV, as

$$\begin{aligned}\mathcal{A}^{\mathcal{P}c}_{LR} &\equiv \frac{\pi\alpha^2\beta}{4s}(\mathcal{C}^+_+ - \mathcal{C}^-_-) \\ &= \frac{1}{8\,\xi_-\xi_+}\left[(\xi_-+\xi_+)\left(\frac{d\sigma^{\mathcal{P}}_{\uparrow\downarrow}}{d\cos\theta}-\frac{d\sigma^{\mathcal{P}}_{\downarrow\uparrow}}{d\cos\theta}\right)-(\xi_--\xi_+)\left(\frac{d\sigma^{\mathcal{P}}_{\uparrow\uparrow}}{d\cos\theta}-\frac{d\sigma^{\mathcal{P}}_{\downarrow\downarrow}}{d\cos\theta}\right)\right]\end{aligned} \tag{6.13}$$

$$\begin{aligned}\mathcal{A}^{\mathcal{P}v}_{LR} &\equiv \frac{\pi\alpha^2\beta}{4s}(\mathcal{V}^+_+ - \mathcal{V}^-_-) \\ &= \frac{1}{8\,\xi_-\xi_+}\left[(\xi_-+\xi_+)\left(\frac{d\sigma^{\mathcal{P}}_{\uparrow\uparrow}}{d\cos\theta}-\frac{d\sigma^{\mathcal{P}}_{\downarrow\downarrow}}{d\cos\theta}\right)-(\xi_--\xi_+)\left(\frac{d\sigma^{\mathcal{P}}_{\uparrow\downarrow}}{d\cos\theta}-\frac{d\sigma^{\mathcal{P}}_{\downarrow\uparrow}}{d\cos\theta}\right)\right]\end{aligned} \tag{6.14}$$

These observables, $\mathcal{A}^{\mathcal{P}c}_{LR}$ and $\mathcal{A}^{\mathcal{P}v}_{LR}$, are expected to play a crucial role in diagnosing the chiral structure of the ECC and ECV parts of the production process, respectively. Furthermore, Eq. (6.11) and Eq. (6.13) are powerful even when electron chirality invariance is violated. As we will see, they enable us to extract the ECC parts separately so that the analysis of observables discussed in Sect. 6.5 can be adopted without any further elaboration.

6.2.1 Charged spin-0 scalar pair $S_p^+ S_p^-$ production

The production of an electrically charged spin-0 scalar pair $S_p^+ S_p^-$ in e^+e^- collisions

$$e^-(p_-,\sigma_-) + e^+(p_+,\sigma_+) \;\to\; S_p^-(q_-) + S_p^+(q_+) \tag{6.15}$$

is generally mediated by the s-channel exchange of neutral spin-0 S_s^0 and spin-1 V_s^0 (including the standard γ and Z bosons), by the t-channel exchange of neutral spin-1/2 fermions F_t^0, and also by the u-channel exchange of doubly-charged spin-1/2 fermions F_u^{--}. The t- or u-channel diagrams can contribute to the process only when the produced scalar S_p^- has the same electron number as the electron or positron in theories with conserved electron number. (Again, $\sigma_{-,+} = \pm 1$ are twice the electron and positron helicities and the convention $\sigma_{-,+} = \pm$ is used.)

The amplitude of the scalar-pair production process in Eq. (6.15) can be expressed in terms of four generalized ECC and ECV bilinear charges, $Q_\pm^c$ and $Q_\pm^v$, in the e^+e^- c.m. frame as

$$\mathcal{M}\left[\, e^-_{\sigma_-} e^+_{\sigma_+} \;\to\; S_p^- S_p^+ \right] = \sqrt{2} e^2 \left[\delta_{\sigma_+,-\sigma_-}\, Q^c_{\sigma_-} + \delta_{\sigma_+,\sigma_-}\, Q^v_{\sigma_-} \right] \, d^{J_0}_{\Delta\sigma,0}(\theta) \tag{6.16}$$

where $J_0 = |\Delta\sigma|$ with $\Delta\sigma = (\sigma_- - \sigma_+)/2 = \pm 1, 0$ and θ is the scattering polar angle between S_p^- with respect to the e^- direction in the e^+e^- c.m. frame. Explicitly, the ECC and ECV reduced helicity amplitudes are given in terms of all the relevant 3-point couplings listed in Appendix A by

$$Q^c_\pm = \; \beta \left[s^V_{ee\pm} s^{SS}_V D_s(M^2_{V_s}) - |t^{eS}_{F\pm}|^2 D_t(M^2_{F_t}, M^2_{S_p}) + |u^{eS}_{F\pm}|^2 D_u(M^2_{F_u}, M^2_{S_p}) \right] \tag{6.17}$$

$$\begin{aligned} Q^v_\pm = \; & -\frac{1}{\sqrt{2}\gamma} \left[s^S_{ee\pm} s^{SS}_S D_s(M^2_{S_s}) - \frac{M_{F_t}}{M_{S_p}}\, t^{eS}_{F\pm} t^{eS*}_{F\mp}\, D_t(M^2_{F_t}, M^2_{S_p}) \right. \\ & \left. - \frac{M_{F_u}}{M_{S_p}}\, u^{eS}_{F\pm} u^{eS*}_{F\mp}\, D_u(M^2_{F_u}, M^2_{S_p}) \right] \end{aligned} \tag{6.18}$$

in terms of the boost factor $\gamma = \sqrt{s}/2M_{S_p}$ and the re-scaled angle-independent s-channel propagator $D_s(M_a^2)$ and the re-scaled angle-dependent t-channel and u-channel propagators, $D_t(M_a^2, M_b^2)$ and $D_u(M_a^2, M_b^2)$ defined as

$$D_s(M_a^2) = \frac{1}{1 - M_a^2/s + iM_a\Gamma_a/s} \tag{6.19}$$

$$D_{t/u}(M_a^2, M_b^2) = \frac{1}{\Delta_{ab} \mp \beta\cos\theta} \tag{6.20}$$

with $\Delta_{ab} = 1 + 2(M_a^2 - M_b^2)/s$ and $\cos\theta$ in the e^+e^- c.m. frame. All of the propagators are constant, i.e. independent of the polar angle at threshold with $\beta = 0$, i.e. when the scalar pair $S_p^+ S_p^-$ are produced at rest. (The width Γ_a appearing in the s-channel propagator is supposed to be much smaller than M_a and the c.m. energy so that their effects will be ignored in our later numerical analyses.)

Using the explicit form of d functions (see Appendix B), we obtain the polarization-weighted differential cross sections of the production of scalar particles as

$$\begin{aligned}\frac{d\sigma^S_{\rm pol}}{d\cos\theta} = \frac{\pi\alpha^2}{8s}\beta\,\big[&(1 - P_-^L P_+^L)(|Q_+^c|^2 + |Q_-^c|^2)\,\sin^2\theta + (P_-^L - P_+^L)(|Q_+^c|^2 - |Q_-^c|^2)\,\sin^2\theta \\ &+2(1 + P_-^L P_+^L)(|Q_+^v|^2 + |Q_-^v|^2) + 2(P_-^L + P_+^L)(|Q_+^v|^2 - |Q_-^v|^2) \\ &+4P_-^T P_+^T \cos\delta\,{\rm Re}(Q_+^v Q_-^{v*}) + 4P_-^T P_+^T \sin\delta\,{\rm Im}(Q_+^v Q_-^{v*})\big]\end{aligned} \tag{6.21}$$

where $P_\mp^{L,T}$ and δ are the degrees of longitudinal and transverse $e^\mp$ polarizations and the relative opening angle of the $e^\mp$ transverse polarizations. The polarized total cross section $\sigma^S_{\rm pol}$ can be then obtained by integrating the differential cross section over the full range of $\cos\theta$. One noteworthy point is that the transverse-polarization dependent parts on the last line in Eq. (6.21) survive even after the integration if there exist any non-trivial ECV amplitudes.

Inspecting the polarization-weighted differential cross sections in Eq. (6.21), we find the following aspects of the scalar pair production:

- As previously demonstrated in detail for the production of scalar smuon or selectron pairs in SUSY models, the ECC part of the production cross section of an electrically-charged scalar pair in e^+e^- collisions, originated from the $J = 1$ e^+e^- system, has two characteristic features. Firstly, the cross section rises slowly in P-waves near the threshold, i.e. $\sim \beta^3$ as the ECC amplitudes $Q^c_\pm$ are proportional to β. Secondly, as the total spin angular momentum of the final system of two spinless scalar particles is zero, angular momentum conservation generates the $\sin^2\theta$ dependence of the ECC part of the differential cross section, leading to the angular distribution $\sim \sin^2\theta$ near the threshold.

- However, the two salient features of the ECC parts are spoiled by any non-trivial ECV contributions originated from s-channel scalar exchanges or t- and u-channel spin-1/2 fermion exchanges with both left-handed and right-handed couplings. Near the threshold the ECV amplitudes become constant. Therefore, in contrast to the ECC part the ECV part of the total cross section rises sharply in S-waves $\sim \beta$ and the ECV part of the differential cross section is isotropic.

- As mentioned before, even in the presence of both the ECC and ECV contributions, the electron and positron beam polarizations can provide powerful diagnostic handles for differentiating the ECC and ECV parts. On one hand, the presence of the ECV contributions, if not suppressed, can be confirmed by transverse $e^\pm$ polarizations.[4] On the other hand, longitudinal electron and positron polarizations enable us to extract out the ECC parts and to check the chiral structure of the three-point eeS_s, eF_tS_p and eF_uS_p couplings.

- Then, the polar-angle distribution can be used for confirming the presence of t- or u-channel exchanges, as the distribution is peaked near the forward and/or backward directions for the t- and/or u-channel contributions.

- If there exist only s-channel contributions, then the ECC and ECV part of the angular distribution is proportional to $\sin^2\theta$ and to a constant in the scalar-pair production in e^+e^- collisions, respectively.

[4] As is well known, transversely-polarized electron and positron beams can be produced at e^+e^- circular colliders by the guiding magnetic field of storage rings through its coupling to the magnetic moment of electrons and positrons.

To find which of the these aspects are unique to the spin-0 case we need to compare them with the spin-1/2 and spin-1 case.

Asymptotically the ECV amplitudes become vanishing $\sim M_{S_p}^2/s$ and the ECC ones remain finite as can be checked with Eqs. (6.17) and (6.18). As the c.m. energy increases, the ECV contributions diminish and the ECC part of the unpolarized cross section of a scalar-pair production scales as

$$\sigma_{\rm unpol}^{Sc} \;\to\; \frac{\pi\alpha^2}{6s}\left(|s_{ee+}^V s_V^{SS}|^2 + |s_{ee-}^V s_V^{SS}|^2\right) \quad \text{as} \quad s \to \infty \tag{6.22}$$

in the absence of both t- and u-channel contributions, following the simple scaling law $\propto 1/s$, and the cross section scales in the presence of the t-channel and u-channel contributions as

$$\begin{aligned}
\sigma_{\rm unpol}^{Sc} \to\; & \frac{\pi\alpha^2}{4s}\left\{\left[\left(|t_{F+}^{eS}|^2\right)^2 + \left(|t_{F-}^{eS}|^2\right)^2\right]\log\frac{s}{M_{F_t}^2} + \left[\left(|u_{F+}^{eS}|^2\right)^2 + \left(|u_{F-}^{eS}|^2\right)^2\right]\log\frac{s}{M_{F_u}^2}\right\} \\
& \qquad\qquad\qquad\qquad\qquad\qquad\qquad\qquad\qquad\qquad \text{as } s \to \infty \\
\to\; & \frac{\pi\alpha^2}{4s}\left[\left(|t_{F+}^{eS}|^2\right)^2 + \left(|t_{F-}^{eS}|^2\right)^2 + \left(|u_{F+}^{eS}|^2\right)^2 + \left(|u_{F-}^{eS}|^2\right)^2\right]\log\frac{s}{M_{S_p}^2} \\
& \qquad\qquad\qquad\qquad\qquad\qquad\qquad\qquad\qquad\qquad \text{as } s \to \infty
\end{aligned} \tag{6.23}$$

as expected from the near-forward and near-backward enhancements of the t- and u-channel exchanges. (The expression on the last line in Eq. (6.23) is obtained by replacing all the intermediate masses by the scalar mass M_{S_p} as a typical mass scale.) As the ECC part of the $S_p^\pm$-pair production cross section is zero in strict forward and backward direction $\theta = 0, \pi$ due to angular momentum conservation, the cross section remains scale-invariant apart from the logarithmic coefficients.

6.2.2 Charged spin-1/2 fermion pair $F_p^+F_p^-$ production

The analysis presented in Subsect. 6.2.1 for the scalar pair production repeats itself rather closely for new spin-1/2 fermion states, $F_p^\pm$. In addition to the standard γ and Z exchanges, there may exist the s-, t- and u-channel exchanges of new spin-0 scalar states, S_s^0, S_t^0 and S_u^{--}, and new spin-1 vector states, V_s^0, V_t^0 and V_u^{--}. Despite the complicated superposition of scalar and vector interactions, the helicity amplitudes of the production of an electrically-charged fermion pair, $F_p^+F_p^-$, can be decomposed into the ECC and ECV parts as in Eq. (6.4) with $\Delta\sigma = (\sigma_- - \sigma_+)/2 = \pm 1, 0$, $\Delta\lambda = (\lambda_- - \lambda_+)/2 = \pm 1, 0$, and $J_0 = \max(|\Delta\sigma|, |\Delta\lambda|) = 1, 0$. Explicitly, employing the general couplings listed in Appendix A, we obtain for the ECC helicity amplitudes $Q^c_{\sigma_-;\lambda_-,\lambda_+}$ for which $J_0 = 1$:

$$\begin{aligned} Q^c_{\pm;\lambda,\lambda} &= -\frac{1}{2\gamma} s^V_{ee\pm} \left(s^{FF}_{V+} + s^{FF}_{V-}\right) D_s(M^2_{V_s}) \\ &\quad + \frac{1}{2\gamma}\left[|t^{eF}_{S\pm}|^2 D_t(M^2_{S_t}, M^2_{F_p}) - |u^{eF}_{S\pm}|^2 D_u(M^2_{S_u}, M^2_{F_p})\right] \\ &\quad + \frac{1}{2\gamma}\left[\left(2 + \frac{M^2_{F_P}}{M^2_{V_t}}\right)|t^{eF}_{V\pm}|^2 D_t(M^2_{V_t}, M^2_{F_p}) \right. \\ &\quad \left. - \left(2 + \frac{M^2_{F_p}}{M^2_{V_u}}\right)|u^{eF}_{V\pm}|^2 D_u(M^2_{V_u}, M^2_{F_p})\right] \end{aligned} \tag{6.24}$$

for the same $F_p^\mp$ helicities, $\lambda_- = \lambda_+ = \lambda = \pm$, and

$$\begin{aligned} Q^c_{\pm;\lambda,-\lambda} &= -\frac{1}{\sqrt{2}} s^V_{ee\pm}\left[(s^{FF}_{V+} + s^{FF}_{V-}) + \lambda\beta\,(s^{FF}_{V+} - s^{FF}_{V-})\right] D_s(M^2_{V_s}) \\ &\quad + \frac{1}{\sqrt{2}}\left[(1 \mp \lambda\beta)\,|t^{eF}_{S\pm}|^2 D_t(M^2_{S_t}, M^2_{F_p}) - (1 \pm \lambda\beta)\,|u^{eF}_{S\pm}|^2 D_u(M^2_{S_u}, M^2_{F_p})\right] \\ &\quad + \frac{1}{\sqrt{2}}\left[2(1 \pm \lambda\beta) + \frac{M^2_{F_p}}{M^2_{V_t}}(1 \mp \lambda\beta)\right]|t^{eF}_{V\pm}|^2 D_t(M^2_{V_t}, M^2_{F_p}) \\ &\quad - \frac{1}{\sqrt{2}}\left[2(1 \mp \lambda\beta) + \frac{M^2_{F_p}}{M^2_{V_u}}(1 \pm \lambda\beta)\right]|u^{eF}_{V\pm}|^2 D_u(M^2_{V_u}, M^2_{F_p}) \end{aligned} \tag{6.25}$$

for the opposite $F_p^\mp$ helicities, $\lambda_- = -\lambda_+ = \lambda = \pm$ with the boost factors, $\gamma = \sqrt{s}/2M_{F_p}$ and $\beta = \sqrt{1 - 4M^2_{F_p}/s}$. On the other hand, the ECV reduced helicity amplitudes $Q^v_{\sigma_-;\lambda_-,\lambda_+}$

read

$$
\begin{aligned}
Q^{v}_{\pm;\lambda,\lambda} \;=\; & \frac{1}{2\sqrt{2}}\, s^{S}_{ee\pm}\left[\lambda(s^{FF}_{S+}-s^{FF}_{S-})-(s^{FF}_{S+}+s^{FF}_{S-})\,\beta\right] D_s(M^2_{S_s}) \\
& -\frac{1}{2\sqrt{2}}\,(\beta\mp\lambda)\,(1\pm\lambda\cos\theta)\, t^{eF}_{S\pm}t^{eF*}_{S\mp}\, D_t(M^2_{S_t},M^2_{F_p}) \\
& -\frac{1}{2\sqrt{2}}\,(\beta\mp\lambda)\,(1\mp\lambda\cos\theta)\, u^{eF}_{S\pm}u^{eF*}_{S\mp}\, D_u(M^2_{S_u},M^2_{F_p}) \\
& +\frac{1}{\sqrt{2}}\left[2(\beta\pm\lambda)-\frac{M^2_{F_p}}{M^2_{V_t}}(\beta\mp\lambda)(1\pm\lambda\cos\theta)\right] t^{eF}_{V\pm}t^{eF*}_{V\mp}\, D_t(M^2_{V_t},M^2_{F_p}) \\
& +\frac{1}{\sqrt{2}}\left[2(\beta\pm\lambda)-\frac{M^2_{F_p}}{M^2_{V_u}}(\beta\mp\lambda)(1\mp\lambda\cos\theta)\right] u^{eF}_{V\pm}u^{eF*}_{V\mp}\, D_u(M^2_{V_u},M^2_{F_p}) \qquad (6.26)
\end{aligned}
$$

for the same $F_p^{\mp}$ helicities, $\lambda_- = \lambda_+ = \lambda = \pm$, and

$$
\begin{aligned}
Q^{v}_{\pm;\lambda,-\lambda} \;=\; & \frac{1}{2\gamma}\left[t^{eF}_{S\pm}t^{eF*}_{S\mp}\, D_t(M^2_{S_t},M^2_{F_p}) - u^{eF}_{S\pm}u^{eF*}_{S\mp}\, D_u(M^2_{S_u},M^2_{F_p})\right] \\
& +\frac{1}{2\gamma}\left[\frac{M^2_{F_p}}{M^2_{V_t}}\, t^{eF}_{V\pm}t^{eF*}_{V\mp}\, D_t(M^2_{V_t},M^2_{F_p}) - \frac{M^2_{F_p}}{M^2_{V_u}}\, u^{eF}_{V\pm}u^{eF*}_{V\mp}\, D_u(M^2_{V_u},M^2_{F_p})\right] \qquad (6.27)
\end{aligned}
$$

for the opposite $F_p^{\mp}$ helicities, $\lambda_- = -\lambda_+ = \lambda = \pm$. From these ECC and ECV reduced amplitudes, one can get the polarized differential cross section by using Eq. (6.5).

Inspecting the explicit form of the ECC and ECV reduced helicity amplitudes leads to the following features of the amplitudes:

- Near threshold, the ECC reduced amplitudes become independent of the $F_p^{\pm}$ helicities, leading to the relation $Q^{c}_{\pm;\lambda,-\lambda} = \sqrt{2}\, Q^{c}_{\pm;\lambda,\lambda}$. This implies that the ECC part of the unpolarized differential cross section behaves like

$$
\frac{d\sigma^{Fc}_{\rm unpol}}{d\cos\theta} \;\sim\; \left[1+\beta^2\cos^2\theta\right]\,\mathcal{G}(\beta\cos\theta)+\cdots \quad\rightarrow\quad \text{flat near the threshold} \qquad (6.28)
$$

- Because not only the $e^{\pm}$ but also the particle $F_p^{\pm}$ are electrically charged, there exists at least an s-channel γ exchange contribution to the production process with pure vector-current couplings as $s^{\gamma}_{ee\pm} = s^{FF}_{\gamma\pm} = +1$. This contribution generates a non-zero significant amplitude at threshold with $\beta = 0$ as can be proved with Eq. (6.25). Therefore, the rise of the excitation curve of the unpolarized production cross section must be of an S-wave type, i.e. $\sigma^{Fc}_{\rm unpol} \sim \beta$ near the threshold. Note that this threshold pattern is not spoiled by the ECV contributions.

- If there are neither t-channel nor u-channel exchange diagrams, the ECV reduced helicity amplitudes $Q^{v}_{\pm;\lambda,-\lambda}$ are vanishing and all the other non-vanishing ECV reduced amplitudes are constant. Therefore, the ECV part of the polar-angle distribution is isotropic. On the other hand, in this case, the production cross section rises in P-waves or S-waves when the $S_s F_p F_p$ coupling is of a pure scalar type ($s^{FF}_{S+} = s^{FF}_{S-}$) or of a pure pseudoscalar type ($s^{FF}_{S+} = -s^{FF}_{S-}$).
- The ECV ECC t-channel and/or u-channel contributions arise from non-chiral eS_tF_p, eS_uF_p scalar and/or eV_tF_p, eV_uF_p vector couplings. They develop a non-trivial angular dependence near the threshold

$$\frac{d\sigma^{Fv}_{\rm unpol}}{d\cos\theta} \quad \to \quad \left[a_v + b_v \cos^2\theta\right] + \cdots \quad \text{with } a_v > 0 \text{ and } b_v \neq 0 \text{ near the threshold} \tag{6.29}$$

  The sign of the coefficient b_v depends on the relative size of the scalar and vector contributions in the t- and u-channel diagrams.

Compared with the spin-0 case, we can claim that the spin-1/2 case has distinct characteristics in the threshold behavior and the polar-angle distribution.

As the c.m. energy increases, the ECC amplitudes with the same $F^{\pm}_p$ helicities and the ECV amplitudes with the opposite $F^{\pm}_p$ helicities vanish $\sim M^2_{F_p}/s$. However, the ECC amplitudes with the opposite $F^{\pm}_p$ helicities and the ECV amplitudes with the same $F^{\pm}_p$ helicities are finite in the asymptotic high-energy limit as can be checked with Eqs. (6.24), (6.25),(6.26) and (6.27). Therefore, unlike the spin-0 case, both the ECC and ECV parts of the unpolarized cross section of the fermion-pair production scale asymptotically as

$$\sigma^{Fc}_{\rm unpol} \quad \to \quad \frac{\pi\alpha^2}{3s}\left(|s^{V}_{ee+}s^{FF}_{V+}|^2 + |s^{V}_{ee-}s^{FF}_{V-}|^2 + |s^{V}_{ee+}s^{FF}_{V-}|^2 + |s^{V}_{ee-}s^{FF}_{V-}|^2\right) \quad \text{as } s \to \infty \tag{6.30}$$

$$\sigma^{Fv}_{\rm unpol} \quad \to \quad \frac{\pi\alpha^2}{4s}\left(|s^{S}_{ee+}s^{FF}_{S+}|^2 + |s^{S}_{ee-}s^{FF}_{S-}|^2 + |s^{V}_{ee+}s^{FF}_{S-}|^2 + |s^{V}_{ee-}s^{FF}_{S-}|^2\right) \quad \text{as } s \to \infty \tag{6.31}$$

in the absence of both t- and u-channel contributions, following the simple scaling law $\propto 1/s$, and both the ECC and ECV parts of the cross section scale in the presence of the t-channel and u-channel contributions as

$$\sigma^{Fc}_{\rm unpol} \to \pi\alpha^2 \left[\frac{1}{M^2_{V_t}} \left((|t^{eF}_{V+}|^2)^2 + (|t^{eF}_{V-}|^2)^2 \right) + \frac{1}{M^2_{V_u}} \left((|u^{eF}_{V+}|^2)^2 + (|u^{eF}_{V-}|^2)^2 \right) \right] \quad \text{as } s \to \infty \tag{6.32}$$

$$\sigma^{Fv}_{\rm unpol} \to \pi\alpha^2 \left[\frac{M^4_{F_p}}{M^6_{V_t}} |t^{eF}_{V+} t^{eF*}_{V-}|^2 + \frac{M^4_{F_p}}{M^6_{V_u}} |u^{eF}_{V+} u^{eF*}_{V-}|^2 \right] \quad \text{as } s \to \infty \tag{6.33}$$

as expected from the forward and backward enhancements of the t- and u-channel exchanges, which is a remnant of the Rutherford pole damped by the Yukawa mass cut-off in the exchange of heavy particles. The size of the cross section is set by the Compton wave-lengths of the particles exchanged in the t-channel and/or u-channel.

6.2.3 Charged spin-1 vector-boson pair $V_p^+ V_p^-$ production

Similarly to the production of an electrically-charged spin-0 scalar pair, the production of an electrically-charged spin-1 vector-boson pair $V_p^+ V_p^-$ in e^+e^- collisions

$$e^-(p_-, \sigma_-) + e^+(p_+, \sigma_+) \to V_p^-(q_-, \lambda_-) + V_p^+(q_+, \lambda_+) \tag{6.34}$$

is generally mediated by the s-channel exchange of neutral spin-0 particles S^0_s and spin-1 particles V^0_s (including the standard γ and Z bosons), by the t-channel exchange of neutral spin-1/2 fermions F^0_t, and also by the u-channel exchange of doubly-charged spin-1/2 fermions F^{--}_u, if the produced scalar V_p^- has the same lepton number as the positron, when electron number conservation is imposed on the theory. Here, σ_-, σ_+ are twice the electron and positron helicities and $\lambda_-, \lambda_+ = \pm 1, 0$ are the $V_p^\mp$ helicities, respectively.

The amplitude describing the production process in Eq. (6.34) can be expressed in terms of the scattering angle θ between the e^- and V_p^- momentum directions in the e^+e^- c.m. frame as in Eq. (6.4) with $\Delta\sigma = (\sigma_- - \sigma_+)/2 = 0, \pm 1$, $\Delta\lambda = \lambda_- - \lambda_+ = 0, \pm 1, \pm 2$ and

$J_0 = \max(|\Delta\sigma|, |\Delta\lambda|)$. Explicitly, the ECC reduced helicity amplitudes $Q^c_{\sigma_-;\lambda_-,\lambda_+}$ are given by

$$\begin{aligned} Q^c_{\sigma_-;\pm,\pm} =& -\beta s^V_{ee\sigma_-} s^{VV}_V D_s(M^2_{V_s}) + (\beta - \cos\theta)|t^{eV}_{F\sigma_-}|^2 D_t(M^2_{F_t}, M^2_{V_p}) \\ & -(\beta + \cos\theta)|u^{eV}_{F\sigma_-}|^2 D_u(M^2_{F_u}, M^2_{V_p}) \end{aligned} \tag{6.35}$$

$$Q^c_{\sigma_-;0,0} = (2\gamma^2+1)\, Q^c_{\sigma_-;\pm,\pm} + \cos\theta \left[|t^{eV}_{F\sigma_-}|^2 D_t(M^2_{F_t}, M^2_{V_p}) + |u^{eV}_{F\sigma_-}|^2 D_u(M^2_{F_u}, M^2_{V_p})\right] \tag{6.36}$$

$$Q^c_{\sigma_-;\pm,0} = Q^c_{\sigma_-;0,\mp} = 2\gamma\, Q^c_{\sigma_-;\pm,\pm} \pm \frac{\sigma_-}{\gamma}\left[|t^{eV}_{F\sigma_-}|^2 D_t(M^2_{F_t}, M^2_{V_p}) + |u^{eV}_{F\sigma_-}|^2 D_u(M^2_{F_u}, M^2_{V_p})\right] \tag{6.37}$$

$$Q^c_{\sigma_-;\pm,\mp} = -\sqrt{2}\left[|t^{eV}_{F\sigma_-}|^2 D_t(M^2_{F_t}, M^2_{V_p}) + |u^{eV}_{F\sigma_-}|^2 D_u(M^2_{F_u}, M^2_{V_p})\right] \tag{6.38}$$

and the ECV reduced helicity amplitudes by

$$\begin{aligned} Q^v_{\sigma_-;\pm,\pm} =& -\frac{1}{\sqrt{2}\gamma} s^S_{ee\sigma_-} s^{VV}_S D_s(M^2_{S_s}) \\ & + \frac{1}{\sqrt{2}\gamma}\frac{M_{F_t}}{M_{V_p}}(1 \pm \sigma_- \cos\theta)\, t^{eV}_{F\sigma_-} t^{eV*}_{F-\sigma_-} D_t(M^2_{F_t}, M^2_{V_p}) \\ & + \frac{1}{\sqrt{2}\gamma}\frac{M_{F_u}}{M_{V_p}}(1 \mp \sigma_- \cos\theta)\, u^{eV}_{F\sigma_-} u^{eV*}_{F-\sigma_-} D_u(M^2_{F_u}, M^2_{V_p}) \end{aligned} \tag{6.39}$$

for both transversely polarized vector bosons with the same helicity, and

$$\begin{aligned} Q^v_{\sigma_-;0,0} =& \sqrt{2}\gamma(1 - \gamma^{-2}/2)\, s^S_{ee\sigma_-} s^{VV}_S D_s(M^2_{S_s}) \\ & - \sqrt{2}\gamma\frac{M_{F_t}}{M_{V_p}}(1 - \gamma^{-2}/2 - \beta\cos\theta)\, t^{eV}_{F\sigma_-} t^{eV*}_{F-\sigma_-} D_t(M^2_{F_t}, M^2_{V_p}) \\ & - \sqrt{2}\gamma\frac{M_{F_u}}{M_{V_p}}(1 - \gamma^{-2}/2 + \beta\cos\theta)\, u^{eV}_{F\sigma_-} u^{eV*}_{F-\sigma_-} D_u(M^2_{F_u}, M^2_{V_p}) \end{aligned} \tag{6.40}$$

for both longitudinally polarized vector bosons, respectively. For $|\Delta\lambda| = 1$ with one transversely polarized and one longitudinally polarized vector bosons and for $|\Delta\lambda| = 2$, we have

$$\begin{aligned} Q^v_{\sigma_-;\pm,0} = Q^v_{\sigma_-;0,\pm} =& \frac{(\beta \pm \sigma_-)}{\sqrt{2}}\left[\frac{M_{F_t}}{M_{V_p}}\, t^{eV}_{F\sigma_-} t^{eV*}_{F-\sigma_-}\, D_t(M^2_{F_t}, M^2_{V_p})\right. \\ & \left. - \frac{M_{F_u}}{M_{V_p}}\, u^{eV}_{F\sigma_-} u^{eV*}_{F-\sigma_-}\, D_u(M^2_{F_u}, M^2_{V_p})\right] \end{aligned} \tag{6.41}$$

$$Q^v_{\sigma_-;\pm,\mp} = 0 \tag{6.42}$$

2 Here, the boost factors are $\gamma = \sqrt{s}/2M_{V_p}$ and $\beta = \sqrt{1 - 4M_{V_p}^2/s}$. The ECC diagrams with s-channel V_s^0-exchange such as the standard s-channel γ and Z exchange have only a $J = 1$ partial wave because of angular momentum conservation, contributing to only the seven final helicity combinations with $J_0 = 1$. On the other hand, the diagrams with t-channel and u-channel fermion exchanges have all the partial waves with $J \geq J_0$.

In the case with $J_0 = 2$ only the F_t^0 and F_u^{--} exchange diagrams can contribute to this final-state configuration. Moreover, because $|\Delta\lambda| = 2$, the final vector bosons are both transverse $[(\lambda, \bar{\lambda}) = (\pm, \mp)]$. Thus these amplitudes do not have any bad high-energy behavior.

The other seven ECC final helicity combinations give $J_0 = 1$. Five of them have at least one longitudinal V_p, which could give a divergent behavior at high energies. Some parts of the amplitudes $Q^c_{\sigma_-;\pm,0} = Q^c_{\sigma_-;0,\pm}$ and $Q^c_{\sigma_-;0,0}$ are proportional to the ECC amplitude $Q^c_{\sigma_-;\pm,\pm}$ with the proportionality coefficients, γ or γ^2, respectively, as expected from longitudinal $V_p^\pm$ counting. To avoid the bad high-energy behavior, it is necessary to satisfy the two relations[5] among the couplings as provided by gauge symmetry in the SM [347–349]:

$$s^V_{ee\pm} s^{VV}_V = |t^{eV}_{F\pm}|^2 - |u^{eV}_{F\pm}|^2 \tag{6.43}$$

$$s^S_{ee\pm} s^{VV}_S = \frac{M_{F_t}}{M_{V_p}} t^{eV}_{F\pm} t^{eV*}_{F\mp} + \frac{M_{F_u}}{M_{V_p}} u^{eV}_{F\pm} u^{eV*}_{F\mp} \tag{6.44}$$

for each electron helicity $\sigma_- = \pm$, leading to an effective cancellation among the s-channel, t-channel and u-channel contributions so that the ECC amplitudes $Q^c_{\sigma_-;\pm,\pm}$ and $Q^c_{\sigma_-;0,0}$ and the ECV ampltitudes $Q^v_{\sigma_-;0,0}$ vanish asymptotically as the c.m. energy increases.[6]

If the ECC cancellation condition (6.43) for the ECC part is satisfied, the ECC amplitudes $Q^c_{\sigma_-;\pm,0} = Q^c_{\sigma_-;0,\pm}$ for one longitudinal and one transverse V_p pair decrease as γ^{-1} at high energies, while the ECC amplitudes $Q^c_{\sigma_-;\pm,\pm}$ are suppressed by $(1 - \beta) \sim \gamma^{-2}$ since $D_{t/u} \sim (1 \mp \beta \cos\theta)^{-1}$ at high energies. Therefore, only three of the nine ECC helicity combinations, $(+,-), (-,+)$ and $(0,0)$, survive at high energies. On the other hand, if the ECV

[5] If the electron mass is not ignored, additional divergent parts proportional to the mass appear in the ECV parts with longitudinally polarized $V_p^\pm$. They can be cancelled by the s-channel scalar exchanges with their couplings proportional to the electron mass as in the SM.

[6] The cancellation conditions enforce the condition that $s^V_{ee\pm} s^{VV}_V$ are real and $s^S_{ee\pm} s^{VV}_S$ are complex conjugate to each other.

cancellation condition (6.44) is satisfied, the $J_0 = 0$ ECV amplitudes, $Q^v_{\sigma_-;\pm,\pm}$ and $Q^v_{\sigma_-;0,0}$ are suppressed by γ^{-1} while the $J_0 = 1$ ECV amplitudes, $Q^v_{\sigma_-;\pm,0}$ and $Q^v_{\sigma_-;0,\pm}$, survive at high energies.

The three ECC amplitudes surviving at high energies do not contribute to the ECC cross section equally. The $J_0 = 2$ ECC amplitudes with the $(\pm,\mp)$ helicity combinations dominate over the other $(0,0)$ ECC amplitude at high energies because of the t-channel and/or u-channel polar factors $1/(\Delta \mp \beta\cos\theta)$ which peaks at $\cos\theta = \pm 1$ with a $(1-\beta)^{-1} \sim \gamma^2$ enhancement. (In practice the peaks appear below $|\cos\theta| = 1$ because the relevant $d^2_{\sigma_-;\pm 2}$ functions with $|\sigma_-| = 1$ are proportional to $\sin\theta$ and vanish at $|\cos\theta| = 1$.) As there must exist the t-channel and/or u-channel contributions for preserving the good high-energy behavior of the cross section by compensating the s-channel γ, Z contributions for both of the e^+e^- helicity combinations $(\sigma_-,\sigma_+) = (\pm,\mp)$, the ECC unpolarized cross section scales asymptotically as

$$\sigma^{Vc}_{\rm unpol} \;\to\; \frac{4\pi\alpha^2}{s}\left\{\left[(|t^{eV}_{F+}|^2)^2 + (|t^{eV}_{F-}|^2)^2\right]\log\frac{s}{M^2_{F_t}} + \left[(|u^{eV}_{F+}|^2)^2 + (|u^{eV}_{F-}|^2)^2\right]\log\frac{s}{M^2_{F_u}}\right\} \quad \text{as } s \to \infty \tag{6.45}$$

which follows the typical scaling law $\propto 1/s$ apart from the logarithmic parts.

In contrast, the $J_0 = 2$ ECV amplitudes are zero and, with the ECV cancellation condition (6.44), only the $J_0 = 1$ ECV amplitudes $Q^v_{\pm;\pm,0}$ and $Q^v_{\pm;0,\pm}$ survive asymptotically, leading to the form of the ECV cross section:

$$\sigma^{Vv}_{\rm unpol} \;\to\; \frac{2\pi\alpha^2}{s}\left[\frac{M^2_{F_t}}{M^2_{V_p}}|t^{eV}_{F+}t^{eV*}_{F-}|^2\log\frac{s}{M^2_{F_t}} + \frac{M^2_{F_u}}{M^2_{V_p}}|u^{eV}_{F+}u^{eV*}_{F-}|^2\log\frac{s}{M^2_{F_u}}\right] \quad \text{as} \quad s \to \infty \tag{6.46}$$

which follows the scaling law $\propto 1/s$ apart from the logarithmic parts with the mass-squared of the intermediate particles indicating the chiral-flipping phenomena.

At threshold of the spin-1 vector pair production, the total spin becomes equal to the total angular momentum so that it takes only the three values, $J = 0, 1, 2$, because no orbital angular momentum is developed between the final $V^\pm_p$. Among the three possible angular momenta, $J = 0$ is forbidden for the ECC parts because the initial e^+e^- state can have only $J \geq 1$ if the electron mass is neglected. The ECC part of the cross section needs

to have a $J = 2$ contribution from t-channel or u-channel spin-1/2 fermion exchanges or a $J = 1$ contribution from new s-channel spin-1 vector-boson exchanges, partly as a means for erasing the bad high-energy behavior. In the presence of the t- or u-channel contributions as in the SM, the ECC part of the total cross section rises sharply in S-waves near threshold as

$$\sigma^{Vc}_{\rm unpol} \sim \frac{4\pi\alpha^2}{M^2_{V_p}} \left\{ \left[\frac{|t^{eV}_{F_+}|^2}{1+M^2_{F_t}/M^2_{V_p}} + \frac{|u^{eV}_{F_+}|^2}{1+M^2_{F_u}/M^2_{V_p}} \right]^2 + \left[\frac{|t^{eV}_{F_-}|^2}{1+M^2_{F_t}/M^2_{V_p}} + \frac{|u^{eV}_{F_-}|^2}{1+M^2_{F_u}/M^2_{V_p}} \right]^2 \right\} \beta \tag{6.47}$$

while the ECC part of the angular distribution

$$\frac{1}{\sigma^{Vc}_{\rm unpol}} \frac{d\sigma^{Vc}_{\rm unpol}}{d\cos\theta} \sim \frac{1}{2} + O(\beta)\cos\theta \tag{6.48}$$

is essentially flat in the threshold region and the flat behavior is modified linearly in β above the threshold, unless the theory is P-invariant.

If there exist any ECV contributions in the s-, t- and/or u-channel diagrams due to non-chiral couplings, the ECV amplitudes for the spin-1 vector-boson pair production are finite at threshold so that the ECV part of the cross section rises sharply in S-waves near threshold as

$$\sigma^{Vv}_{\rm unpol} \sim \frac{8\pi\alpha^2}{M^2_{V_p}} \left[3\,\mathcal{B}_1 + 2\,\mathcal{B}_2 \right] \beta \tag{6.49}$$

with the non-negative functions defined as $\mathcal{B}_1$ and $\mathcal{B}_2$

$$\mathcal{B}_1 = \left| 2 s^S_{ee+} s^{VV}_S \frac{M^2_{V_p}}{4M^2_{V_p} - M^2_{S_s}} - t^{eV}_{F+} t^{eV*}_{F-} \frac{M_{V_p} M_{F_t}}{M^2_{V_p} + M^2_{F_t}} - u^{eV}_{F+} u^{eV*}_{F-} \frac{M_{V_p} M_{F_u}}{M^2_{V_p} + M^2_{F_u}} \right|^2 \tag{6.50}$$

$$\mathcal{B}_2 = \left| t^{eV}_{F+} t^{eV*}_{F-} \frac{M_{V_p} M_{F_t}}{M^2_{V_p} + M^2_{F_t}} - u^{eV}_{F+} u^{eV*}_{F-} \frac{M_{V_p} M_{F_u}}{M^2_{V_p} + M^2_{F_u}} \right|^2 \tag{6.51}$$

and, similarly to the ECC part, the ECV part of the angular distribution is essentially flat in the threshold region.

Comparing the predictions for the excitations of the spin-1 electrically-charged vector bosons with those of the spin-1/2 electrically-charged fermions leads us to the conclusion that the onset of the excitation curves alone does not discriminate one from the other. Therefore, the analyses of the final-state two-body decay processes and/or production-decay angular correlations are required for discriminating the spin-1 vector bosons from the spin-1/2 fermions.

6.3 TWO-BODY DECAYS

The decay amplitudes $\mathcal{D}_-$ and $\mathcal{D}_+$ of the two-body decays, $\mathcal{P}^- \to \ell^- \bar{\mathcal{D}}^0$ and $\mathcal{P}^+ \to \ell^+ \mathcal{D}^0$, are most simply expressed in the $\mathcal{P}^-$ and $\mathcal{P}^+$ rest frames, respectively. We define each of these frames by a boost of the e^+e^- c.m. frame along the z-axis as shown in Fig. 6.3. In the $\mathcal{P}^\mp$ rest frame, we parameterize the $\ell^\mp$ four-momenta, p_1 and p_3, as

$$p_1^\mu = p_{\ell^-}^\mu = \frac{M_\mathcal{P}^2 - M_\mathcal{D}^2}{2M_\mathcal{P}} (1, \sin\theta_- \cos\phi_-, \sin\theta_- \sin\phi_-, \cos\theta_-) \tag{6.52}$$

$$p_3^\mu = p_{\ell^+}^\mu = \frac{M_\mathcal{P}^2 - M_\mathcal{D}^2}{2M_\mathcal{P}} (1, \sin\theta_+ \cos\phi_+, \sin\theta_+ \sin\phi_+, -\cos\theta_+) \tag{6.53}$$

In this convention of the coordinate systems the angles of the charged lepton are chosen as (θ_-, ϕ_-) in the $\mathcal{P}^-$ decays and $(\pi - \theta_+, \phi_+)$ in the $\mathcal{P}^+$ decays.

It is a straightforward exercise to evaluate the helicity amplitudes of the decays $\mathcal{P}^- \to \ell^- \bar{\mathcal{D}}^0$ and $\mathcal{P}^+ \to \ell^+ \mathcal{D}^0$ with the general couplings listed in Appendix A in the $\mathcal{P}^\mp$ rest frames described before. Generically, when the charged lepton masses are ignored, the decay amplitudes can be written as

$$\mathcal{D}_-[\mathcal{P}^-_{\lambda_-} \to \ell^-_{\sigma_1} \bar{\mathcal{D}}^0_{\sigma_2}] = e\, K_{\mathcal{P}\mathcal{D}}\, D_-[\mathcal{P}^- \to \ell^- \bar{\mathcal{D}}^0]_{\sigma_1\sigma_2}\, d^{J_\mathcal{P}}_{\lambda_-,\sigma_1-\sigma_2}(\theta_-)\, \mathrm{e}^{i(\lambda_- - \sigma_1 + \sigma_2)\,\phi_-} \tag{6.54}$$

$$\mathcal{D}_+[\mathcal{P}^+_{\lambda_+} \to \ell^+_{\sigma_3} \mathcal{D}^0_{\sigma_4}] = e\, K_{\mathcal{P}\mathcal{D}}\, D_+[\mathcal{P}^+ \to \ell^+ \mathcal{D}^0]_{\sigma_3\sigma_4}\, d^{J_\mathcal{P}}_{\lambda_+,\sigma_3-\sigma_4}(\theta_+)\, \mathrm{e}^{-i(\lambda_+ - \sigma_3 + \sigma_4)\,\phi_+} \tag{6.55}$$

with $K_{\mathcal{P}\mathcal{D}} = \sqrt{M_\mathcal{P}^2 - M_\mathcal{D}^2}$ and $\lambda_-(\lambda_+), \sigma_1(\sigma_3)$ and $\sigma_2(\sigma_4)$ the helicities of the particles $\mathcal{P}^-(\mathcal{P}^+), \ell^-(\ell^+)$ and $\bar{\mathcal{D}}^0(\mathcal{D}^0)$. We obtain for all the decay combinations with $\mathcal{P}^\pm = S_p^\pm, F_p^\pm, V_p^\pm$ and $\mathcal{D}^0 = F_d^0, S_d^0, V_d^0$ the reduced decay helicity amplitudes:

$$D_-[S_p^- \to \ell^- \bar{F}_d^0]_{\sigma_1\sigma_2} = \delta_{\sigma_2\sigma_1}\, d^{\ell F}_{S\sigma_1} \tag{6.56}$$

$$D_-[F_p^- \to \ell^-\, \bar{S}_d^0]_{\sigma_1} = d^{\ell S}_{F\sigma_1} \tag{6.57}$$

$$D_-[F_p^- \to \ell^- \bar{V}_d^0]_{\sigma_1\sigma_2} = -\left[\sqrt{2}\,\delta_{\sigma_2\sigma_1} + \delta_{\sigma_2 0}(M_{F_p}/M_{V_d})\right] d^{\ell V}_{F\sigma_1} \tag{6.58}$$

$$D_-[V_p^- \to \ell^- \bar{F}_d^0]_{\sigma_1\sigma_2} = \left[\delta_{\sigma_2\sigma_1}(M_{F_d}/M_{V_p}) + \sqrt{2}\,\delta_{\sigma_2,-\sigma_1}\right] d^{\ell F}_{V\sigma_1} \tag{6.59}$$

and the reduced decay amplitudes for the charge-conjugated decays $\mathcal{P}^+ \to \ell^+ \mathcal{D}^0$ are given by the relation

$$D_+[\mathcal{P}^+ \to \ell^+ \mathcal{D}^0]_{\sigma_3\sigma_4} = \mp D_-[\mathcal{P}^- \to \ell^- \bar{\mathcal{D}}^0]^*_{-\sigma_3,-\sigma_4} \tag{6.60}$$

up to an overall sign. The sign $+$ is for $\mathcal{P}^\pm = V_p^\pm$ and the sign $-$ for $\mathcal{P}^\pm = S_p^\pm, F_p^\pm$.

6.4 FULL ANGULAR-CORRELATIONS OF THE FINAL-STATE LEPTONS

In this section we present the most general angular distribution of the decay products in the correlated production-decay process, following the formalism in Ref. [350]

$$\begin{aligned} e^-(p_-,\sigma_-) + e^+(p_+,\sigma_+) &\to \mathcal{P}^-(q_-,\lambda_-) + \mathcal{P}^+(q_+,\lambda_+) \\ \mathcal{P}^-(q_-,\lambda_-) &\to \ell^-(p_1,\sigma_1) + \bar{\mathcal{D}}^0(p_2,\sigma_2) \\ \mathcal{P}^+(q_+,\lambda_+) &\to \ell^+(p_3,\sigma_3) + \mathcal{D}^0(p_4,\sigma_4) \end{aligned} \tag{6.61}$$

with two visible massless charged leptons $\ell^\pm$ and two invisible neutral particles $\mathcal{D}^0$ and $\bar{\mathcal{D}}^0$ in the final state. Combining the production process and two decay processes, we can extract explicitly the dependence of the correlated cross section on final charged lepton angles as well as the production angles and beam polarizations.

6.4.1 Derivation of the correlated distributions

The fully production-decay correlated amplitudes can be expressed in terms of the production and decay helicity amplitudes as follows:

$$\mathcal{M}(p_-,\sigma_-;p_+,\sigma_+;p_{1,2},\sigma_{1,2};p_{3,4},\sigma_{3,4}) \tag{6.62}$$

$$\begin{aligned} = \; & \Pi_{\mathcal{P}^-}(q_-^2)\,\Pi_{\mathcal{P}^+}(q_+^2) \sum_{\lambda_-,\lambda_+} \mathcal{M}(p_-,\sigma_-;p_+,\sigma_+;q_-,\lambda_-;q_+,\lambda_+) \\ & \times \mathcal{D}_-(q_-,\lambda_-;p_1,\sigma_1;p_2,\sigma_2) \times \mathcal{D}_+(q_+,\lambda_+;p_3,\sigma_3;p_4,\sigma_4) \end{aligned} \tag{6.63}$$

where the Breit-Wigner propagator factors $\Pi_{\mathcal{P}^\pm}$ for the $\mathcal{P}^\pm$ particles are

$$\Pi_{\mathcal{P}^\pm}(q_\pm^2) = (q_\pm^2 - M_{\mathcal{P}}^2 + iM_{\mathcal{P}}\Gamma_{\mathcal{P}})^{-1} \tag{6.64}$$

Here we take the summations over intermediate $\mathcal{P}^\pm$ polarizations in the helicity basis, i.e. helicities, which are most convenient for theoretical considerations.

In the c.m. frame of the colliding e^+e^- beams, we choose the $\mathcal{P}^-$ momentum direction as the z-axis and the $\vec{p}_-(e^-) \times \vec{q}_-(\mathcal{P}^-)$ direction as the y-axis so that the scattering $e^+e^- \to$

$\mathcal{P}^+\mathcal{P}^-$ takes place in the x-z plane (see Fig. 6.3).[7] The production amplitude $\mathcal{M}$ is then a function of the scattering angle θ between e^- and $\mathcal{P}^-$ momentum directions, as explicitly shown in the previous section. The explicit form of the production amplitude and two decay amplitudes in the e^+e^- c.m. frame can be derived by the relations:

$$\begin{aligned}
\mathcal{M}(p_-,\sigma_-;p_+,\sigma_+;q_-,\lambda_-;q_+,\lambda_+) &= \mathcal{M}[e^-_{\sigma_-}e^+_{\sigma_+}\to\mathcal{P}^-_{\lambda_-}\mathcal{P}^+_{\lambda_+}] && (6.65)\\
\mathcal{D}_-(q_-,\lambda_-;p_1,\sigma_1;p_2,\sigma_2) &= \mathcal{D}_-[\mathcal{P}^-_{\lambda_-}\to\ell^-_{\sigma_1}\bar{\mathcal{D}}^0_{\sigma_2}] && (6.66)\\
\mathcal{D}_+(q_+,\lambda_+;p_3,\sigma_3;p_4,\sigma_4) &= \mathcal{D}_+[\mathcal{P}^+_{\lambda_+}\to\ell^+_{\sigma_3}\mathcal{D}^0_{\sigma_4}] && (6.67)
\end{aligned}$$

with the expressions defined in Eq. (6.4) for the production amplitudes and Eqs. (6.54) and (6.55) for the decay amplitudes, respectively.

6.4.2 Polarization-weighted cross sections

Generally, the full correlations of the production and two two-body decay processes can contain maximally $2^4\times(2J_{\mathcal{P}}+1)^4$ independent observables expressed in terms of the e^+e^- c.m. energy $\sqrt{s}$ and six production and decay angles - two angles (θ,φ) for the production process and four angles $(\theta_\pm,\phi_\pm)$ for two decay processes - for arbitrarily-polarized electron and positron beams. (Here, $J_{\mathcal{P}}$ is the spin of the particle $\mathcal{P}^\pm$.) The factor $2^4=16$ comes from the production part and the other $(2J_{\mathcal{P}}+1)^4$ ($=1$, 16 and 81 for $J_{\mathcal{P}}=0,1/2$ and 1) from the production-decay correlations.

The polarization-weighted squared matrix elements can be cast into a decomposed form:

$$\overline{\sum}|\mathcal{M}|^2=\left|\Pi_{\mathcal{P}^-}(q_-^2)\right|^2\left|\Pi_{\mathcal{P}^+}(q_+^2)\right|^2\,\mathcal{P}^{\lambda_-\lambda_+}_{\lambda'_-\lambda'_+}\,\mathcal{D}^{\lambda_-}_{\lambda'_-}\,\overline{\mathcal{D}}^{\lambda_+}_{\lambda'_+} \tag{6.68}$$

with the summation over repeated indices $(\lambda_-,\lambda'_-,\lambda_+,\lambda'_+)$ assumed here and in the following equations. The polarization-weighted production tensor reads

$$\mathcal{P}^{\lambda_-\lambda_+}_{\lambda'_-\lambda'_+}=\sum_{\sigma_-,\sigma'_-}\sum_{\sigma_+,\sigma'_+}P^-_{\sigma_-\sigma'_-}P^+_{\sigma_+\sigma'_+}\,\mathcal{M}[e^-_{\sigma_-}e^+_{\sigma_+}\to\mathcal{P}^-_{\lambda_-}\mathcal{P}^+_{\lambda_+}]\,\mathcal{M}^*[e^-_{\sigma_-}e^+_{\sigma_+}\to\mathcal{P}^-_{\lambda'_-}\mathcal{P}^+_{\lambda'_+}] \tag{6.69}$$

[7] The dependence of the distribution on the production azimuthal-angle φ can be encoded in terms dependent on the transverse beam polarizations as shown in Appendix C.

in terms of the production helicity amplitudes, where the electron and positron polarization tensors $P^{\mp}$ are given in the $(+,-)$ helicity basis by [337]

$$P^{-}_{\sigma_-\sigma'_-} = \frac{1}{2}\begin{pmatrix} 1+P^L_- & P^T_- e^{-i\phi_-} \\ P^T_- e^{i\phi_-} & 1-P^L_- \end{pmatrix} \tag{6.70}$$

$$P^{+}_{\sigma_+\sigma'_+} = \frac{1}{2}\begin{pmatrix} 1+P^L_+ & P^T_+ e^{-i\phi_+} \\ P^T_+ e^{i\phi_+} & 1-P^L_+ \end{pmatrix} \tag{6.71}$$

respectively, where $\phi_- = -\varphi$ and $\phi_+ = -\varphi + \delta$ with the azimuthal angle φ of the $\mathcal{P}^-$ flight direction as measured from the electron transverse polarization direction and δ the relative opening angle of the electron and positron transverse-polarization directions. Details of this calculation for incorporating beam polarizations are given in Appendix C. The decay density matrices with the daughter particle polarizations summed in Eq. (6.68) are given by

$$\mathcal{D}^{\lambda_-}_{\lambda'_-}(\theta_-,\phi_-) = \sum_{\sigma_1,\sigma_2} \mathcal{D}_-[\mathcal{P}^-_{\lambda_-} \to \ell^-_{\sigma_1}\bar{\mathcal{D}}^0_{\sigma_2}]\,\mathcal{D}^*_-[\mathcal{P}^-_{\lambda'_-} \to \ell^-_{\sigma_1}\bar{\mathcal{D}}^0_{\sigma_2}] \tag{6.72}$$

$$\overline{\mathcal{D}}^{\lambda_+}_{\lambda'_+}(\theta_+,\phi_+) = \sum_{\sigma_3,\sigma_4} \mathcal{D}_+[\mathcal{P}^+_{\lambda_+} \to \ell^+_{\sigma_3}\mathcal{D}^0_{\sigma_4}]\,\mathcal{D}^*_+[\mathcal{P}^+_{\lambda'_+} \to \ell^+_{\sigma_3}\mathcal{D}^0_{\sigma_4}] \tag{6.73}$$

After integration over the virtual $\mathcal{P}$ masses squared, q^2_- and q^2_+, the unpolarized differential cross section can be expressed in the narrow width approximation as

$$\frac{d\sigma}{d\cos\theta d\varphi\, d\cos\theta_- d\phi_- d\cos\theta_+ d\phi_+} = \frac{(2J_{\mathcal{P}}+1)^2\beta}{1024\pi^4 s}\,\mathrm{Br}[\mathcal{P}^- \to \ell^-\bar{\mathcal{D}}^0]\,\mathrm{Br}[\mathcal{P}^+ \to \ell^+\mathcal{D}^0] \times \mathcal{P}^{\lambda_-\lambda_+}_{\lambda'_-\lambda'_+}\,\rho^{\lambda_-}_{\lambda'_-}\,\overline{\rho}^{\lambda_+}_{\lambda'_+} \tag{6.74}$$

with $\beta = (1-4M^2_{\mathcal{P}}/s)^{1/2}$. Here, ρ and $\overline{\rho}$ are the normalized decay density matrices defined as

$$\rho^{\lambda_-}_{\lambda'_-} = \frac{\mathcal{D}^{\lambda_-}_{\lambda'_-}}{\mathrm{Tr}(\mathcal{D})} \quad \text{and} \quad \overline{\rho}^{\lambda_+}_{\lambda'_+} = \frac{\overline{\mathcal{D}}^{\lambda_+}_{\lambda'_+}}{\mathrm{Tr}(\overline{\mathcal{D}})} \tag{6.75}$$

satisfying the normalization conditions $\mathrm{Tr}(\rho) = 1$ and $\mathrm{Tr}(\overline{\rho}) = 1$. With this normalization condition the overall constant $\mathcal{K}$ is fixed in terms of the branching fractions $\mathrm{Br}(\mathcal{P}^- \to \ell^-\bar{\mathcal{D}}^0)$

and $\mathrm{Br}(\mathcal{P}^+ \to \ell^+\mathcal{D}^0)$. By integrating over $\mathcal{P}^+$ decays, we obtain the inclusive $\mathcal{P}^- \to \ell^-\bar{\mathcal{D}}^0$ decay distribution

$$\frac{d\sigma}{d\cos\theta d\varphi\, d\cos\theta_- d\phi_-} = \frac{(2J_{\mathcal{P}}+1)\beta}{256\pi^3 s}\,\mathrm{Br}[\mathcal{P}^- \to \ell^-\bar{\mathcal{D}}^0]\;\mathcal{P}^{\lambda_-\lambda_+}_{\lambda'_-\lambda_+}\,\rho^{\lambda_-}_{\lambda'_-} \tag{6.76}$$

and alternatively we obtain the $\mathcal{P}^+ \to \ell^+\mathcal{D}^0$ decay distribution as

$$\frac{d\sigma}{d\cos\theta d\varphi\, d\cos\theta_+ d\phi_+} = \frac{(2J_{\mathcal{P}}+1)\beta}{256\pi^3 s}\,\mathrm{Br}[\mathcal{P}^+ \to \ell^+\mathcal{D}^0]\;\mathcal{P}^{\lambda_-\lambda_+}_{\lambda_-\lambda'_+}\,\bar{\rho}^{\lambda_+}_{\lambda'_+} \tag{6.77}$$

By further integrating out all the decay lepton angles, we simply get the unpolarized differential cross section for the production process $e^+e^- \to \mathcal{P}^+\mathcal{P}^-$:

$$\frac{d\sigma}{d\cos\theta d\varphi} = \frac{\beta}{64\pi^2 s}\,\mathcal{P}^{\lambda_-\lambda_+}_{\lambda_-\lambda_+} \tag{6.78}$$

whose explicit form for the process $e^+e^- \to \mathcal{P}^+\mathcal{P}^-$ can be found in Eq. (6.5). By comparing Eqs. (6.74), (6.76) and (6.77) with Eq. (6.78) we can get the additional information on not only the $\mathcal{P}^+\mathcal{P}^-$ production amplitudes but also the $\mathcal{P}^\pm$ decay amplitudes encoded in decay lepton angular distributions.

6.4.3 Decay density matrices

The explicit form of the normalized decay density matrix for each spin combination of the parent and daughter particles, $\mathcal{P}^-$ and $\bar{\mathcal{D}}^0$, in the decay $\mathcal{P}^- \to \ell^-\bar{\mathcal{D}}^0$ can be derived with the explicit form of each decay amplitude listed in Eqs. (6.56), (6.57), (6.58) and (6.59), respectively. For the spin-0 case with $\mathcal{P}^- = S_p^-$ and $\bar{\mathcal{D}}^0 = F_d^0$, the decay matrix is a single number:

$$\rho[S_p^- \to \ell^-\bar{F}_d^0] = 1 \tag{6.79}$$

generating no production-decay correlations, independently of the chiral structure of the couplings. On the other hand, for the two spin-1/2 cases, the 2×2 decay density matrices read

$$\rho[F_p^- \to \ell^-\bar{S}_d^0] = \frac{1}{2}\begin{pmatrix} 1+\xi_{\rm fs}\cos\theta_- & \xi_{\rm fs}\sin\theta_-\mathrm{e}^{i\phi_-} \\ \xi_{\rm fs}\sin\theta_-\mathrm{e}^{-i\phi_-} & 1-\xi_{\rm fs}\cos\theta_- \end{pmatrix} \quad \text{with} \quad \xi_{\rm fs} = \frac{|d^{\ell S}_{F+}|^2 - |d^{\ell S}_{F-}|^2}{|d^{\ell S}_{F+}|^2 + |d^{\ell S}_{F-}|^2} \tag{6.80}$$

for the spin-0 daughter particle $\bar{S}_d^0$ and

$$\rho[F_p^- \to \ell^- \bar{V}_d^0] = \frac{1}{2}\begin{pmatrix} 1+\xi_{\rm fv}\eta_{\rm fv}\cos\theta_- & \xi_{\rm fv}\eta_{\rm fv}\sin\theta_-\mathrm{e}^{i\phi_-} \\ \xi_{\rm fv}\eta_{\rm fv}\sin\theta_-\mathrm{e}^{-i\phi_-} & 1-\xi_{\rm fv}\eta_{\rm fv}\cos\theta_- \end{pmatrix}$$
$$\text{with} \quad \eta_{\rm fv} = \frac{M_{F_p}^2 - 2M_{V_d}^2}{M_{F_p}^2 + 2M_{V_d}^2} \quad \text{and} \quad \xi_{\rm fv} = \frac{|d_{F+}^{\ell V}|^2 - |d_{F-}^{\ell V}|^2}{|d_{F+}^{\ell V}|^2 + |d_{F-}^{\ell V}|^2} \tag{6.81}$$

for the spin-1 daughter particle $\bar{V}_d^0$, and the 3×3 decay density matrix for the spin-1 parent particle V_p^- reads:

$$\rho[V_p^- \to \ell^- \bar{F}_d^0] = (1-\eta_{\rm vf})\,\mathbb{1}_{3\times 3} + (3\eta_{\rm vf}-2)\,\rho_T + \xi_{\rm vf}\,\eta_{\rm vf}\,\delta_T$$
$$\text{with} \quad \eta_{\rm vf} = \frac{2M_{V_p}^2}{2M_{V_p}^2 + M_{F_d}^2} \quad \text{and} \quad \xi_{\rm vf} = \frac{|d_{V+}^{\ell F}|^2 - |d_{V-}^{\ell F}|^2}{|d_{V+}^{\ell F}|^2 + |d_{V-}^{\ell F}|^2} \tag{6.82}$$

where $\mathbb{1}_{3\times 3}$ is the 3×3 identity matrix, and the normalized matrix ρ_T and the traceless matrix δ_T are given by

$$\rho_T = \frac{1}{4}\begin{pmatrix} 1+c_-^2 & \sqrt{2}c_-s_-\mathrm{e}^{i\phi_-} & s_-^2\mathrm{e}^{2i\phi_-} \\ \sqrt{2}c_-s_-\mathrm{e}^{-i\phi_-} & 2s_-^2 & -\sqrt{2}c_-s_-\mathrm{e}^{i\phi_-} \\ s_-^2\mathrm{e}^{-2i\phi_-} & -\sqrt{2}c_-s_-\mathrm{e}^{-i\phi_-} & 1+c_-^2 \end{pmatrix} \tag{6.83}$$

$$\delta_T = \frac{1}{4}\begin{pmatrix} 2c_- & \sqrt{2}s_-\mathrm{e}^{i\phi_-} & 0 \\ \sqrt{2}s_-\mathrm{e}^{-i\phi_-} & 0 & \sqrt{2}s_-\mathrm{e}^{i\phi_-} \\ 0 & \sqrt{2}s_-\mathrm{e}^{-i\phi_-} & -2c_- \end{pmatrix} \tag{6.84}$$

with the abbreviations $c_- = \cos\theta_-$ and $s_- = \sin\theta_-$.

The density matrices for the charge-conjugated decays $\mathcal{P}^+ \to \ell^+\mathcal{D}^0$ are related to those of the decays $\mathcal{P}^- \to \ell^-\bar{\mathcal{D}}^0$ as follows:

$$\overline{\rho}[\mathcal{P}^+ \to \ell^+\mathcal{D}^0] = \rho[\mathcal{P}^- \to \ell^-\bar{\mathcal{D}}^0]\ (\theta_- \to \theta_+,\ \phi_- \to -\phi_+,\ \xi \to -\xi) \tag{6.85}$$

The two density matrices can be used for describing non-trivial final-state angular correlations between two visible leptons through the connection linked by the production process.

As shown clearly by the expressions in Eqs. (6.80), (6.81) and (6.82), the decay distributions are affected not just by the spins and masses of the particles but also the chiralities of their couplings. We find:

- If the relative chirality ξ_{fs} is zero, i.e. the coupling is either pure vector-like or pure axial-vector-like, the decay density matrix becomes an identity matrix, washing out any correlation in the final-state leptons of the decays $F_p^- \to \ell^- \bar{S}_d^0$ and $F_p^+ \to \ell^+ S_d^0$ completely. On the contrary, if the coupling is purely chiral with $\xi_{\text{fs}} = \pm 1$, the decay distributions provide maximal information on the production-decay correlations.

- In addition to the relative chirality ξ_{fv} there exists a kinematic factor η_{fv} determining the polarization analysis power in the decay $F_p^- \to \ell^- \bar{V}_d^0$. This purely mass-dependent factor vanishes for the special case with $M_{F_p} = \sqrt{2} M_{V_d}$ and takes its maximum value of unity only when $M_{V_d} = 0$, i.e. the spin-1 daughter particle V_d^0 is massless. Nevertheless, if the coupling is purely chiral, then this decay mode with a spin-1 daughter particle can be distinguished from the decay mode with a spin-0 daughter particle by measuring the polarization analysis power; in the latter case its magnitude is 1 and in the former case its magnitude is $\eta_{\text{fv}} < 1$ for $M_{V_d} > 0$.

- In the spin-1 case, if the relative chirality ξ_{vf} is zero, the density matrix becomes an identity matrix only when the parent and daughter particles are degenerate, i.e. $M_{V_p} = M_{F_d}$. However, in this degenerate case, the decay is kinematically forbidden. Therefore, we can conclude that the spin-1 case can be distinguished from the spin-0 and spin-1/2 cases.

Before closing this subsection, we emphasize that, with all these spin- and chirality-dependent characteristics of the decay density matrices, the decay angle correlations of the final-state leptons become trivial unless the parent particles are polarized as will be demonstrated below.

6.5 OBSERVABLES

In the last section, we gave a detailed description of the angular distribution of the final-state lepton-antilepton pairs arising from the decay of the $\mathcal{P}^+\mathcal{P}^-$ pair. Schematically, the 6-fold

differential cross section has the form

$$d\sigma \;\sim\; \sum^{N_{\rm tot}} \mathrm{P}_i(P_-^L, P_+^L; P_-^T, P_+^T, \delta; \theta, \varphi; \sqrt{s})\mathrm{D}_i(\theta_-, \phi_-, \theta_+, \phi_+), \text{ with } N_{\rm tot} = (2J_{\mathcal{P}}+1)^4 \quad (6.86)$$

Here the functions D_i form a linearly independent set consisting of low-energy spherical harmonics, which reflects the decay dynamics. The dynamics of the production process is solely contained in the factors P_i, forming maximally 16 independent terms. These are given essentially by the density matrix of the $\mathcal{P}^+\mathcal{P}^-$ pair and by beam polarizations. The fact that we can in principle measure $16 \times (2J_{\mathcal{P}}+1)^4$ functions shows that it is possible to extract an enormous amount of information on the production and decay mechanism.

However, unless we have a sufficient number of events, it is neither possible nor practical to perform a fit with the large number of all independent angular and/or polarization distributions. Rather it is meaningful to obtain from the experimental data a specific set of observables depending on the c.m. energy, the beam polarizations, the production angles and the decay angular distributions that are efficiently controllable and reconstructible and sensitive to the spin and chirality effects. In the following numerical analysis we restrict ourselves to five conventional kinematic variables — the beam energy $\sqrt{s}$, the production polar angle θ, the two lepton polar angles, θ_- and θ_+, in the decays, $\mathcal{P}^- \to \ell^-\bar{\mathcal{D}}^0$ and $\mathcal{P}^+ \to \ell^+\mathcal{D}^0$, and the cosine of the azimuthal-angle difference ϕ between two decay planes. The impact of beam polarizations on each observable is also diagnosed numerically.

In order to gauge the sensitivities of the observables mentioned in the previous subsection to spin and chirality effects in the antler-topology processes, we investigate their distributions for ten typical spin and chirality assignments as shown with five examples from the MSSM and five examples from the MUED listed in Table 6.3. For the sake of simplicity, when describing the specific examples, we impose electron chirality invariance (which is valid to a very good precision in the popular models MSSM and MUED), forcing us to neglect any s-channel scalar contributions and to set any three-point $e\mathcal{T}\mathcal{P}$ and $\mathcal{P}\ell\mathcal{D}$ vertices with $\ell = e, \mu$ to be purely chiral in the t-channel diagram and the two-body decay diagrams. Furthermore, in the present numerical analysis we do not have any u-channel exchange of doubly-charged particles, for which new higher representations of the SM gauge group have to be introduced in the theories. In any case, note that in principle all the u-channel contributions, if they exist,

can be worked out through the analytic expressions presented in Sect. 6.2. For example, the major difference between a u-channel process and a t-channel process is that the production polar-angle distribution will be backward-peaked instead of forward-peaked, as can be seen from Eq. (6.20).

In general several particles may contribute to the s-channel and/or t-channel diagrams and the mass spectrum of the new particles depends strongly on the mass generation mechanism unique to each model beyond the SM. Nevertheless, expecting no significant loss of generality, we assume in our numerical analysis that only the SM neutral electroweak gauge bosons γ and Z contribute to the s-channel diagram and only one or two particles, named $\mathcal{T}_1^0$ and $\mathcal{T}_2^0$ when two particles are involved, are exchanged in the t-channel diagram. Then, we take the following simplified mass spectrum:

$$M_{\mathcal{P}} = M_{\mathcal{T}_2} = 200\,\text{GeV} \quad \text{and} \quad M_{\mathcal{D}} = M_{\mathcal{T}_1} = 100\,\text{GeV} \tag{6.87}$$

We emphasize that the mass spectrum (6.87) is chosen only as a simple illustrative example in the MSSM and MUED models with different spins but similar final states and so the procedure for spin determination demonstrated in the present work can be explored for any other BSM models as well as within the SM itself. The coupling of the Z boson as well as the photon γ to the new spin-1/2 charged fermion pair $F_p^+ F_p^-$ with $\mathcal{P}^\pm = F_p^\pm$ is taken to be purely vector-like, as this is valid for the first Kaluza-Klein (KK) lepton states in MUED with $F_p^\pm = \ell_{L1/R1}^\pm$ and for the pure charged wino or higgsino states in the MSSM with $F_p^\pm = \tilde{W}^\pm, \tilde{H}$, valid to very good approximation when the mixing between the gaugino and higgsino states due to EWSB is ignored in the MSSM. It is also assumed that the lightest neutralino is a pure bino, $\tilde{B}$, and the second lightest neutralino is a pure wino, $\tilde{W}^0$. In this case, the lightest chargino is almost degenerate with the second lightest neutralino.

Applying all the assumptions mentioned above to the MSSM and MUED processes listed in Table 6.3, we can obtain the full list of non-zero ECC couplings for the processes [27, 351]:

for the s-channel couplings

$$s^{\gamma}_{ee\pm} = s^{\tilde{\ell}_R\tilde{\ell}_R}_{\gamma} = s^{\tilde{\ell}_L\tilde{\ell}_L}_{\gamma} = s^{\ell_{R1}\ell_{R1}}_{\gamma\pm} = s^{\ell_{L1}\ell_{L1}}_{\gamma\pm} = s^{\tilde{W}\tilde{W}}_{\gamma\pm} = s^{W_1W_1}_{\gamma} = 1 \tag{6.88}$$

$$s^{Z}_{ee+} = s^{\tilde{\ell}_R\tilde{\ell}_R}_{Z} = s^{\ell_{R1}\ell_{R1}}_{Z\pm} = -s_W/c_W \tag{6.89}$$

$$s^{Z}_{ee-} = s^{\tilde{\ell}_L\tilde{\ell}_L}_{Z} = s^{\ell_{L1}\ell_{L1}}_{Z\pm} = (1/2 - s^2_W)/c_W s_W \tag{6.90}$$

$$s^{\tilde{W}\tilde{W}}_{Z\pm} = s^{W_1W_1}_{Z} = c_W/s_W \tag{6.91}$$

with $\ell^{\pm} = e^{\pm}, \mu^{\pm}$ and for the t-channel and decay couplings

$$t^{e\tilde{e}_R}_{\tilde{B}+} = d^{\ell\tilde{B}}_{\tilde{\ell}_R-} = -\sqrt{2}/c_W; \quad t^{e\tilde{e}_L}_{\tilde{B}-} = d^{\ell\tilde{B}}_{\tilde{\ell}_L+} = 1/\sqrt{2}c_W; \quad t^{e\tilde{e}_L}_{\tilde{W}-} = 1/\sqrt{2}s_W, \quad t^{e\tilde{W}}_{\tilde{\nu}_e-} = d^{\ell\tilde{\nu}_\ell}_{\tilde{W}+} = -1/s_W \tag{6.92}$$

$$t^{ee_{R1}}_{B_1+} = d^{\ell B_1}_{\ell_{R1}+} = 1/c_W; \quad t^{ee_{L1}}_{B_1-} = d^{\ell B_1}_{\ell_{L1}-} = 1/2c_W; \quad t^{ee_{L1}}_{W_1-} = 1/2s_W; \quad t^{eW_1}_{\nu_{e1}-} = d^{\ell\nu_{\ell 1}}_{W_1-} = -1/\sqrt{2}s_W \tag{6.93}$$

in the MSSM and in the MUED, respectively. All the other couplings are vanishing in the ECC limit.

6.5.1 Kinematics

Before presenting the detailed analytic and numerical analysis of spin and chirality effects on each observable, we first describe how each kinematic observable can be constructed for the antler-topology processes. The measurement of the cross section for $\mathcal{P}^+\mathcal{P}^-$ pair production can be carried out by identifying acoplanar $\ell^+\ell^-$ pairs with respect to the $e^{\pm}$ beam axis accompanied by large missing energy carried by the invisible $\mathcal{D}^0\bar{\mathcal{D}}^0$ pairs.[8]

For very high energy $\sqrt{s} \gg M_{\mathcal{P}}$ the flight direction of the parent particle can be approximated by the flight direction of the daughter particles $\ell^{\pm}$ and the dilution due to the decay kinematics is small. However, at medium e^+e^- energies the dilution increases, and the reconstruction of the $\mathcal{P}^{\pm}$ flight direction provides more accurate results on the angular distribution of the $\mathcal{P}^{\pm}$ pairs. If all particle masses are known, the magnitude of the particle

[8] A detailed proof of the twofold discrete ambiguity in reconstructing the full kinematics of the antler-topology process production is given in Appendix D.

momenta is calculable and the relative orientation of the momentum vectors of $\ell^{\pm}$ and $\mathcal{P}^{\pm}$ is fixed by the two-body decay kinematics:

$$M_{\mathcal{P}}^2 - M_{\mathcal{D}}^2 = \sqrt{s}E_{\ell^{\pm}}\left(1 - \beta\,\hat{n}_{\mathcal{P}^{\pm}} \cdot \hat{n}_{\pm}\right) = \sqrt{s}\,E_{\ell^{\pm}}\left(1 - \beta\cos\alpha_{\pm}\right) \tag{6.94}$$

where the unit vector $\hat{n}_{\mathcal{P}^{\pm}}$ stands for the $\mathcal{P}^{\pm}$ momentum direction, the unit vectors $\hat{n}_{\pm}$ for the $\ell^{\pm}$ flight directions and the angles $\alpha_{\pm}$ for the opening angles between the visible $\ell^{\pm}$ tracks and the parent $\mathcal{P}^{\pm}$ momentum directions in the e^+e^- c.m frame. The angles $\alpha_{\pm}$ can be reconstructed event by event by measuring the lepton energies in the laboratory frame, i.e. the e^+e^- c.m. frame and they define two cones about the ℓ^+ and ℓ^- axes intersecting in two lines — the true $\mathcal{P}^{\pm}$ flight direction and a false direction. Thus the $\mathcal{P}^{\pm}$ flight direction can be reconstructed up to a two-fold discrete ambiguity.

In contrast to the production angle, the decay polar angles $\theta_{\pm}$ in the $\mathcal{P}^{\pm}$ rest frames can be unambiguously determined event by event independently of the reconstruction of the $\mathcal{P}^{\pm}$ direction by the relation:

$$\cos\theta_{\pm} = \frac{1}{\beta}\left(\frac{E_{\ell^{\pm}}}{E^*_{\ell^{\pm}}} - 1\right) \quad \text{with} \quad E^*_{\ell^{\pm}} = \frac{M_{\mathcal{P}}^2 - M_{\mathcal{D}}^2}{2M_{\mathcal{P}}} \tag{6.95}$$

where $E^*_{\ell^{\pm}}$ is the fixed $\ell^{\pm}$ energy in the $\mathcal{P}^{\pm}$ rest frame. Therefore, any decay polar-angle correlations between two leptons in the correlated process can be reconstructed event by event by measuring the lepton energies in the laboratory frame.

Another angular variable, which is reconstructible event by event in the antler-topology processes, is the cosine of the difference $\phi = \phi_+ - \phi_-$ of the azimuthal angles of two leptons with respect to the production plane. Explicitly, it is related to the opening angle of two visible leptons and two polar angles $\alpha_{\pm}$ in the laboratory frame as

$$\cos\phi = \cos(\phi_+ - \phi_-) = \frac{\hat{n}_+ \cdot \hat{n}_- + \cos\alpha_+\cos\alpha_-}{\sin\alpha_+\sin\alpha_-} \tag{6.96}$$

Note that the $\cos 2\phi$ distribution also can be measured unambiguously as $\cos 2\phi = 2\cos^2\phi - 1$.[9] In contrast, the sign of the sine of the angular difference of two azimuthal angles is

[9] Actually, $\cos(n\theta)$ with any non-zero integer n is a polynomial of $\cos\phi$.

not uniquely determined because of the intrinsic two-fold discrete ambiguity in the determination of the $\mathcal{P}^{\pm}$ flight direction, although its magnitude is determined. (For details, see Appendix D.)

There exist many other types of angular distributions which provide us with additional information on the spin and chirality effects. Nevertheless, while postponing the complete analysis based on the full set of energy and angular distributions, we will study the four kinematic observables $\{\sqrt{s},\, \theta,\, \theta_{-},\, \cos\phi\}$ supplemented with beam polarizations.

6.5.2 Beam energy dependence and threshold excitation pattern

As described through a detailed analytical investigation before, the excitation curve of the production cross section near threshold in the ECC scenario exhibits its characteristic pattern according to the spin of the produced particle $\mathcal{P}^{\pm}$ and the chiral patterns of the couplings among the on-shell particles and any intermediate particles exchanged in the s-, t- and/or u-channel diagrams.[10]

The production cross section of a spin-0 scalar pair as in the scenario $A_{L/R}$ of the L- or R-smuon pair production and the scenario $B_{L/R}$ of the L- or R-selectron pair production shows a characteristic slow P-wave threshold excitation, i.e. $\sigma \sim \beta^3$, despite the t-channel neutral bino and/or wino contributions to the selectron pair production. In contrast, the production cross section of a spin-1/2 fermion pair as in the scenarios $C_{L/R}$ and $D_{L/R}$ for the L- or R-handed first KK-muon and KK-electron pair production and as in the scenario E_L of a wino pair production always exhibits a sharp S-wave threshold excitation, i.e. $\sigma \sim \beta$, (due to the unavoidable pure-vector coupling of a photon to the e^+e^- and $F_p^+F_p^-$). The excitation pattern in the scenario F_L for the first KK W-boson pair production is characterized dominantly by the presence of the t-channel contributions, which should be present for preventing the cross section from developing a bad high energy behavior as the s-channel γ and Z contributions cannot cancel each other at high energies simultaneously for left- and right-chiral couplings. Note that the polarized cross section with perfect right-handed electron polarization does not

[10] Very close to the threshold the excitation curves may be distorted due to particle widths and Coulomb attraction between two oppositely charged particles. However, the effects are insubstantial for small widths so that they are ignored in the present work.

have the t-channel spin-1/2 ν_{e1} contribution but only the s-channel γ and Z contributions leading to complete asymptotic cancellation. In this case, the cross section exhibits a slow P-wave behavior as in the scalar case. Otherwise, the cross section contains the non-zero t-channel ν_{e1} contribution with the $J_0 = 2$ amplitude finite at threshold so that the cross section rises in a sharp S-wave near threshold. These threshold patterns are summarized in Table 6.4.

Based on the mass spectrum in Eq. (6.87) and the explicit form of the couplings listed in Eqs. (6.88), (6.89), (6.90), and (6.91) and Eqs. (6.92) and (6.93), we show in Figs. 6.5 the energy dependence of total cross sections, with the threshold excitation curves embedded, for spin-0 scalar bosons indexed with $A_{L/R}$ and $B_{L/R}$, for spin-1/2 fermions indexed with $C_{L/R}$, $D_{L/R}$ and E_L, and for spin-1 vector bosons indexed with F_L. Here, the electron and positron beams are assumed to be unpolarized, except for Figs. 6.5(d) and (h). In contrast to Figs. 6.5(d), the plot in Figs. 6.5(h) clearly shows that the cross section with purely right-handed electron and purely left-handed positron beams killing the t-channel contributions while keeping only the s-channel spin-1 vector-boson contributions exhibits a slow P-wave rise in the excitation curve. We note in passing that it will be crucial to control beam polarization to very good precision in extracting out the right-handed part as the right-handed cross section is more than one thousand times smaller than the left-handed cross section.

To summarize. The threshold energy scan of the polarized cross sections of the pair production process $e^+e^- \to \mathcal{P}^+\mathcal{P}^-$ can be very powerful in identifying the spin of the new charged particles $\mathcal{P}^\pm$. However, we note that this method may not be fully powerful enough for encompassing the most general scenario including the case with simultaneous left-/right-chiral t- and/or u-channel contributions and the case with neither of them.

6.5.3 Polar-angle distribution in the production process

As pointed out before and described in detail in Appendix D, there exists a twofold discrete ambiguity in constructing the production polar angle θ. For very high energy $\sqrt{s} \gg M_{\mathcal{P}}$ the flight direction of the parent particle $\mathcal{P}^\pm$ can be approximated by the flight direction

of daughter particle $\ell^{\pm}$ and the dilution due to the decay kinematics is small. However, at medium energies the dilution increases and so the reconstruction of the $\mathcal{P}^{\pm}$ flight direction provides more accurate results on the angular distribution of the $\mathcal{P}^{\pm}$ pairs.

Analytically, the angle $\theta_{\rm ft}$ between the false and the true axis is related to the azimuthal angle ϕ between two decay planes and to the boosts $\gamma_{\pm} = \gamma(\cos\theta_{\pm} + \beta)$ of the leptons $\ell^{\pm}$ in the laboratory frame as

$$\cos\theta_{\rm ft} = 1 - \frac{2\sin^2\phi}{\gamma_+^2 + \gamma_-^2 + 2\gamma_+\gamma_-\cos\phi + \sin^2\phi} \tag{6.97}$$

For high energies the maximum opening angle reduces effectively to $\theta_{\rm ft} \leq O(1/\gamma)$ and approaches zero asymptotically when the two axes coincide. Quite generally, as a result of the Jacobian root singularity in the relation between $\cos\theta_{\rm ft}$ and ϕ, the false solutions tend to accumulate slightly near the true axis for all energies [330].

Experimentally, the absolute orientation in space is operationally obtained by rotating the two $\mathcal{P}^{\pm}$ vectors around the $\ell^{\pm}$ axes against each other until they are aligned back to back in opposite directions. The flattened false-axis distribution can be extracted on the basis of Monte Carlo simulations. Figs. 6.6 shows the normalized production polar-angle distributions for the polarization-weighted differential cross sections, $(1/\sigma_{L/R})\, d\sigma_{L/R}/d\cos\theta$, of the ten processes listed in Table 6.3. The plots in Figs. 6.6(a) and (b) are for the scalar-pair production processes, $A_{L/R}$ for smuon pairs and $B_{L/R}$ for selectron pairs and the plots in Figs. 6.6(c), (e), (f) and (g) are for the five fermion-pair production processes, E_L for a wino pair, $C_{L/R}$ for the first KK-muon pairs and $D_{L/R}$ for the first KK-electron pairs, respectively, while the two plots in Figs. 6.6(d) and (h) are for a vector-boson-pair production process, F_L, for the first KK-W pair.

- From Figs. 6.6(a) and (b), we find that the cross sections vanish in the forward and back directions with $\cos\theta = \pm 1$ due to the overall angular factor proportional to $\sin^2\theta$, independently of the presence of t-channel contributions. If the t-channel fermion contributions are absent ($A_{L/R}$) or killed by beam polarization (B_R), the polar-angle distribution is forward and backward symmetric and simply $\sim \sin^2\theta$.

- In contrast, the polar-angle distributions for spin-1/2 particles exhibit very distinct angular patterns. If the t-channel contributions are absent, as shown in Figs. 6.6(c), or killed by right-handed electron and left-handed positron beam polarizations, as in Figs. 6.6(g), the differential cross sections having only the s-channel vector-boson contributions with pure vector-type couplings in the three cases have a typical angular distribution $1 + \kappa_{1/2} \cos^2\theta$ with $\kappa_{1/2} = \beta^2/(2-\beta^2) = 0$ at threshold and 1 at asymptotic high energies, leading to the characteristic distribution $1 + \cos^2\theta$, reflecting the equal contributions of the dominant $(\lambda_-, \lambda_+) = (\pm, \mp)$ amplitudes. Once the t-channel contributions are included, the angular distribution is severely distorted. Nevertheless, as shown in Figs. 6.6(c) and (f), the cross sections are peaked at the forward direction.
- Figs. 6.6(d) and (h) show the angular distributions for spin-1 first KK W-boson pair production (F_L). If the t-channel contribution is absent as in Figs. 6.6(h), the differential cross section has only s-channel spin-1 vector-boson contributions with pure vector-type couplings (F_L) so that the $(\pm\mp)$ amplitudes with $J_0 = 2$ are zero and the $(0,0)$ amplitudes become dominant. As a result, the polar-angle distributions exhibit a characteristic energy-independent polar-angle distribution $\sim 1 - \kappa_1 \cos^2\theta$ with the energy-dependent coefficient $\kappa_1 = 3/19$ at threshold and 1 at asymptotically high energies, leading to the simple $\sin^2\theta$ distribution identical to the spin-0 case. This asymptotic behavior is a consequence of the so-called Goldstone boson equivalence theorem [348].

To summarize. The characteristic patterns of the polarized ECC polar-angle distributions can be powerful in determining the spin of $\mathcal{P}^\pm$. Evidently it is crucial to have the (longitudinal) polarization of electron and positron beams for the spin determination through the angular distribution. However, we note that the polar-angle distributions alone may not be powerful enough for covering the more general scenarios.

6.5.4 Single lepton polar-angle distributions in the decays

If the parent particle $\mathcal{P}^\pm$ is a spin-0 scalar boson $S_p^\pm$, there is no production-decay angular correlation at all so that the (normalized) lepton polar-angle distribution is flat, independently of any chirality assignments to the couplings for the production and decay processes

as well as of any initial beam polarizations, i.e.

$$\frac{d\sigma^S\left[S_p^- \to \ell^- \bar{F}_d^0\right]}{d\cos\theta d\cos\theta_-} = \frac{d\sigma^S}{d\cos\theta}\cdot\frac{1}{2} \quad \Rightarrow \quad \frac{1}{\mathcal{C}_{\rm sf}}\frac{d\mathcal{C}_{\rm sf}}{d\cos\theta_-} = \frac{1}{2} \tag{6.98}$$

The linear relation in Eq. (6.95) between the polar angle $\theta_\pm$ and the ℓ^- energy $E_{\ell^\pm}$ indicates that the lepton energy distribution is flat with the energy between $E_{\rm min} = E^*_{\ell^\pm}(1-\beta)$ and $E_{\rm max} = E^*_{\ell^\pm}(1+\beta)$ with $\beta = \sqrt{1-4M^2_{\mathcal{P}}/s}$.

When the parent particle $\mathcal{P}^\pm$ is a spin-1/2 fermion $F_p^\pm$, then we can directly determine the differential or total cross section for fixed $F_p^\pm$ helicities by measuring the polar angle distribution of the $F_p^\pm$ decay products. Depending on the spin of the invisible particle $\mathcal{D}^0 = S_d^0, V_d^0$ and the chirality assignments to the $F_pS_d\ell$ and $F_pV_d\ell$ couplings, the normalized and correlated polar-angle distributions can be expressed as

$$\frac{d\sigma^F[F_p^- \to \ell^-\bar{S}_d^0]}{d\cos\theta\, d\cos\theta_-} = \frac{d\sigma^F}{d\cos\theta}\cdot\frac{1}{2}\left[1+\xi_{\rm fs}\,\mathbb{P}_F\,\cos\theta_-\right] \quad \Rightarrow \quad \frac{1}{\mathcal{C}_{\rm fs}}\frac{d\mathcal{C}_{\rm fs}}{d\cos\theta_-} = \frac{1}{2}\left[1+\xi_{\rm fs}\,\langle\mathbb{P}_F\rangle\,\cos\theta_-\right] \tag{6.99}$$

$$\frac{d\sigma^F[F_p^- \to \ell^-\bar{V}_d^0]}{d\cos\theta\, d\cos\theta_-} = \frac{d\sigma}{d\cos\theta}\cdot\frac{1}{2}\left[1+\xi_{\rm fv}\eta_{\rm fv}\,\mathbb{P}_F\,\cos\theta_-\right] \Rightarrow \frac{1}{\mathcal{C}_{\rm fv}}\frac{d\mathcal{C}_{\rm fv}}{d\cos\theta_-} = \frac{1}{2}\left[1+\xi_{\rm fv}\eta_{\rm fv}\langle\mathbb{P}_F\rangle\cos\theta_-\right] \tag{6.100}$$

where two relative chiralities $\xi_{\rm fs}$ and $\xi_{\rm fv}$ and one dilution factor $\eta_{\rm fv}$ are defined by

$$\xi_{\rm fs} = \frac{|d^{\ell S}_{F+}|^2 - |d^{\ell S}_{F-}|^2}{|d^{\ell S}_{F+}|^2 + |d^{\ell S}_{F-}|^2} \tag{6.101}$$

$$\xi_{\rm fv} = \frac{|d^{\ell V}_{F+}|^2 - |d^{\ell V}_{F-}|^2}{|d^{\ell V}_{F+}|^2 + |d^{\ell V}_{F-}|^2} \tag{6.102}$$

$$\eta_{\rm fv} = \frac{M^2_{F_p} - 2M^2_{V_d}}{M^2_{F_p} + 2M^2_{V_d}} \tag{6.103}$$

in terms of the chiral coupling coefficients (which are introduced in Appendix A) and the masses M_{F_p} and M_{V_d}, and the differential cross section and the polar-angle dependent polarization observable are defined by

$$\frac{d\sigma^F}{d\cos\theta} = \frac{d\sigma^F(\lambda_- = +)}{d\cos\theta} + \frac{d\sigma^F(\lambda_- = -)}{d\cos\theta} \tag{6.104}$$

$$\mathbb{P}_F = \left[\frac{d\sigma^F(\lambda_- = +)}{d\cos\theta} - \frac{d\sigma^F(\lambda_- = -)}{d\cos\theta}\right] \Big/ \frac{d\sigma^F}{d\cos\theta} \tag{6.105}$$

respectively. The average of the polarization observable over the production angle θ are given by

$$\langle \mathbb{P}_F \rangle = \frac{1}{\sigma^F} \int_{-1}^{1} \mathbb{P}_F \frac{d\sigma^F}{d\cos\theta} \, d\cos\theta = \left(\mathbb{p}_{++}^{++} + \mathbb{p}_{+-}^{+-} \right) - \left(\mathbb{p}_{-+}^{-+} + \mathbb{p}_{--}^{--} \right) \tag{6.106}$$

satisfying the inequality condition $|\langle \mathbb{P}_F \rangle| \leq 1$ in terms of the normalized production tensor $\mathbb{p}$ defined as an integral over the production polar and azimuthal angles θ and φ as

$$\mathbb{p}_{\lambda'_- \lambda'_+}^{\lambda_- \lambda_+} = \int \mathcal{P}_{\lambda'_- \lambda'_+}^{\lambda_- \lambda_+} \, d\cos\theta \, d\varphi \Big/ \int \left(\sum_{\kappa_-, \kappa_+} \mathcal{P}_{\kappa_- \kappa_+}^{\kappa_- \kappa_+} \right) d\cos\theta \, d\varphi \tag{6.107}$$

with the production tensor $\mathcal{P}$'s. The production tensor $\mathbb{p}$ satisfies the normalization condition $\sum_{\lambda_-, \lambda_+} \mathbb{p}_{\lambda_- \lambda_+}^{\lambda_- \lambda_+} = 1$.

Any non-trivial ℓ^- polar-angle distribution can exist only when the parent particle $F_p^\pm$ state has a non-zero degree of longitudinal polarization $\mathbb{P}_F$ which may be generated by some parity-violating interactions or by electron (and positron) beam polarizations. At the same time, the relative chiralities, $\xi_{\rm fs}$ and $\xi_{\rm fv}$, and the polarization dilution factor $\eta_{\rm fv}$ should not be zero.

It is evident from Eqs. (6.99) and (6.100) that the single polar-angle distributions are isotropic as in the scalar case if the relative chiralities, $\xi_{\rm fs}$ and $\xi_{\rm fv}$, are zero, i.e. the couplings for the decays, $F_p^- \to \ell^- \bar{S}_d^0$ and $F_p^- \to \ell^- \bar{V}_d^0$, are pure scalar-type and pure vector-type. In the latter decay mode, not only the relative chirality but also the dilution factor $\eta_{\rm fv}$ must not be zero, i.e, $M_{F_p} \neq \sqrt{2} M_{V_d}$. Furthermore, as mentioned before, the P-odd polarization observable $\langle \mathbb{P}_F \rangle$ needs to be non-zero in both of the decay modes, for any non-trivial single decay polar-angle distributions.

Before presenting the single decay polar-angle distributions at a fixed c.m. energy $\sqrt{s} = 500$ GeV, we investigate the energy and polarization dependence of the P-odd polarization observable $\langle \mathbb{P}_F \rangle$ in the $C_{L/R}$, $D_{L/R}$ and E_L scenarios of spin-1/2 particles.

- Firstly, we note that the polarization observable is identically zero, independently of beam polarization, in the $C_{L/R}$ scenario for the production of a first KK-muon pair $\mu_1^+ \mu_1^-$, because the coupling of the Z as well as γ to the first KK muon pair in the s-channel exchange diagram is of a pure vector-type, generating no P-violating effects,

so that the single decay polar-angle distribution is isotropic as in the spin-0 scalar-pair production. Therefore, the single decay polar-angle distribution cannot be exploited for distinguishing the spin-1/2 case of a first KK muon pair from the spin-0 case of a smuon pair.

- In contrast, as the production of a first KK electron pair occurs through the t-channel spin-1 vector-boson contributions with pure left-chiral (D_L) or right-chiral (D_R) $ee_1V_t^0$ couplings with the first KK vector boson $V_t^0 = B_1$, W_1^0 as well as the s-channel γ and Z-boson contributions with pure vector couplings with $F_p^\pm$, the P-odd polarization observable depends strongly on the c.m. energy and beam polarizations. As the c.m. energy increases, the t-channel contributions with maximally P-violating couplings become dominant rapidly due to the exchange of spin-1 neutral vector bosons B_1 and W_1^0 so that the P-odd observable approaches its maximum value of unity in magnitude in the D_L (D_R) scenario for left-handed (right-handed) electron and right-handed (left-handed) positron polarizations. In the former and latter cases (D_L and D_R), the observable is negative and positive, respectively. On the other hand, for the opposite combination of beam polarizations the observable is zero because the t-channel contributions are killed. These features are clearly demonstrated in Figs. 6.7(a) and (d).

- In the charged wino case (E_L), the t-channel diagram is mediated by a spin-0 electron sneutrino $\tilde{\nu}_e$, killing the amplitude effectively in the forward direction due to chirality flipping. As a result, the P-odd observable decreases in size as the c.m. energy increases. Moreover, as the $e\tilde{\nu}_e\tilde{W}$ coupling is purely left-chiral, the P-odd observable is zero for right-handed electron and left-handed positron polarizations. These features can be verified with the plots in Figs. 6.7(b) and (e).

It is necessary to compare these features of the spin-1/2 $F_p^\pm$ cases to those for the spin-1 $V_p^\pm$ cases.

When the parent particle $\mathcal{P}^\pm$ is a spin-1 vector boson $V_p^\pm$, the correlated polar-angle distributions and the normalized lepton polar-angle distribution are given in terms of the

$V_p^{\pm}$ helicity-dependent production cross sections by

$$\frac{d\sigma^V[V_p^- \to \ell^- \bar{F}_d^0]}{d\cos\theta\, d\cos\theta_-} = \frac{d\sigma^V}{d\cos\theta} \cdot \frac{1}{2}\left[1 + \frac{3}{2}\,\xi_{\rm vf}\,\eta_{\rm vf}\,\mathbb{P}_V\,\cos\theta_- + \frac{1}{2}(3\eta_{\rm vf} - 2)\,\mathbb{Q}_V\,\frac{(3\cos^2\theta_- - 1)}{2}\right] \tag{6.108}$$

$$\frac{1}{\mathcal{C}_{\rm vf}}\frac{d\mathcal{C}_{\rm vf}}{d\cos\theta_-} = \frac{1}{2}\left[1 + \frac{3}{2}\,\xi_{\rm vf}\,\eta_{\rm vf}\,\langle\mathbb{P}_V\rangle\,\cos\theta_- + \frac{1}{2}(3\eta_{\rm vf} - 2)\,\langle\mathbb{Q}_V\rangle\,\frac{(3\cos^2\theta_- - 1)}{2}\right] \tag{6.109}$$

with a relative chirality $\xi_{\rm vf}$ and a dilution factor $\eta_{\rm vf}$ defined by

$$\xi_{\rm vf} = \frac{|d_{F+}^{\ell V}|^2 - |d_{F-}^{\ell V}|^2}{|d_{F+}^{\ell V}|^2 + |d_{F-}^{\ell V}|^2} \tag{6.110}$$

$$\eta_{\rm vf} = \frac{2M_{V_p}^2}{2M_{V_p}^2 + M_{F_d}^2} \tag{6.111}$$

with its minimum value of $\eta_{\rm vf}^{\rm min} = 2/3$ for $M_{V_p} = M_{F_d}$, where the differential cross section and two polarization observables $\mathbb{P}_V$ and $\mathbb{Q}_V$ are defined by

$$\frac{d\sigma^V}{d\cos\theta} = \frac{d\sigma^V(\lambda_- = +)}{d\cos\theta} + \frac{d\sigma^V(\lambda_- = -)}{d\cos\theta} + \frac{d\sigma^V(\lambda_- = 0)}{d\cos\theta} \tag{6.112}$$

$$\mathbb{P}_V = \left[\frac{d\sigma^V(\lambda_- = +)}{d\cos\theta} - \frac{d\sigma^V(\lambda_- = -)}{d\cos\theta}\right] \Big/ \frac{d\sigma^V}{d\cos\theta} \tag{6.113}$$

$$\mathbb{Q}_V = \left[\frac{d\sigma^V(\lambda_- = +)}{d\cos\theta} + \frac{d\sigma^V(\lambda_- = -)}{d\cos\theta} - 2\frac{d\sigma^V(\lambda_- = 0)}{d\cos\theta}\right] \Big/ \frac{d\sigma^V}{d\cos\theta} \tag{6.114}$$

and the averages of two polarization observables over the polar-angle distribution are given by

$$\langle\mathbb{P}_V\rangle = \frac{1}{\sigma}\int_{-1}^{1}\mathbb{P}_V\frac{d\sigma^V}{d\cos\theta}\,d\cos\theta = \left(\mathbb{p}_{++}^{++} + \mathbb{p}_{+0}^{+0} + \mathbb{p}_{+-}^{+-}\right) - \left(\mathbb{p}_{-+}^{-+} + \mathbb{p}_{-0}^{-0} + \mathbb{p}_{--}^{--}\right) \tag{6.115}$$

$$\langle\mathbb{Q}_V\rangle = \frac{1}{\sigma}\int_{-1}^{1}\mathbb{Q}_V\frac{d\sigma^V}{d\cos\theta}\,d\cos\theta = \left(\mathbb{p}_{++}^{++} + \mathbb{p}_{+0}^{+0} + \mathbb{p}_{+-}^{+-}\right) + \left(\mathbb{p}_{-+}^{-+} + \mathbb{p}_{-0}^{-0} + \mathbb{p}_{--}^{--}\right) - 2\left(\mathbb{p}_{0+}^{0+} + \mathbb{p}_{00}^{00} + \mathbb{p}_{0-}^{0-}\right) \tag{6.116}$$

satisfying the inequality conditions $|\langle\mathbb{P}_V\rangle| \leq 1$ and $|\langle\mathbb{Q}_V\rangle| \leq 2$ in terms of the 3×3 normalized production tensor matrix $\mathbb{p}$ defined similarly to the equation (6.107).

Clearly, only if the vector boson V_p^- is unpolarized, i.e. the production cross section for each V_p^- is identical with $d\sigma^V(\lambda_- = +) = d\sigma^V(\lambda_- = -) = d\sigma^V(\lambda_- = 0)$, will the decay polar-angle distribution be isotropic. Note that, even if there are no parity-violating effects,

i.e. $d\sigma^V(\lambda_- = +) = d\sigma^V(\lambda_- = -)$, in the production process, there can exist a non-trivial lepton polar-angle distribution proportional to $3\cos^2\theta_- - 1$, unless the averaged degree of longitudinal polarization $P_L(V_p^-) = \sigma^V(\lambda_- = 0)/\sigma^V$ of the particle V_p^- is identical to 1/3. These properties are demonstrated by the plots in Figs. 6.7(c) and (f) for the production of a charged first KK W-boson pair with s-channel γ, Z exchanges with pure vector-type couplings and t-channel spin-1/2 first KK neutrino exchange with a pure left-chiral coupling. Firstly, as the right-handed electron and left-handed positron polarizations kill the t-channel contributions, the P-odd observable $\langle \mathbb{P}_V \rangle$ is vanishing so that there is no term linear in $\cos\theta_-$. Even in this case the P-even polarization observable $\langle \mathbb{Q}_V \rangle$ survives and increases in size as the c.m. energy increases as shown in Figs. 6.7(f). Secondly, for the left-handed electron and right-handed positron polarizations, the P-violating t-channel contribution survives and both the P-even and P-odd observables increase in size as the c.m. energy increases as shown in Figs. 6.7(c).

Figure 6.8 shows the normalized single decay polar-angle distributions for a spin-1/2 negatively charged first KK muon $\mu^-_{1L/1R}$ ($C_{L/R}$) and first KK electron $e^-_{1L/1R}$ ($D_{L/R}$), for a spin-1/2 negatively charged wino $\tilde{W}^-$ (E_L) and for a spin-1 negatively charged first KK W-boson W_1^- (F_L), pair produced with its anti-particle in e^+e^- collisions at a fixed c.m. energy of 500 GeV.

- As shown in Figs. 6.8(a) and (e), the distribution for the μ_1^- decay is flat because the couplings of both γ and Z to the $\mu_1^+\mu_1^-$ pair are pure vector-type, preserving parity (P).
- Similarly the flat distributions appear for the left-handed (right-handed) KK electron with right-handed (left-handed) electron and left-handed (right-handed) positron polarizations as shown by a (blue) dashed line in Figs. 6.8(b) and a (red) solid line in Figs. 6.8(f), as in both cases the P-violating t-channel contributions are killed. The same flat distribution in the $\tilde{W}$ decay occurs for right-handed electron and left-handed positron beams, killing the t-channel sneutrino contribution, as shown in Figs. 6.8(g).
- There exist non-trivial decay polar-angle distributions with a positive slope in the $e^-_{1L/1R}$ decay for left-handed/right-handed electron and right-handed/left-handed positron beams as shown by the red solid line in Figs. 6.8(b) and by the blue dashed line in Figs. 6.8(f). This is due to the fact that both the P-odd polarization observable $\langle \mathbb{P}_F \rangle$ and the relative

chirality factor $\xi_{\rm fv}$ is negative and positive for the e^-_{1L} and e^-_{1R} decay, respectively, so that the product of two quantities is positive in both cases. In contrast, in the E_L case with left-handed electron and right-handed positron beams, the P-odd polarization observable is positive but the relative chirality $\xi_{\rm fs}$ is negative so that the slope determined by the product of two quantities is negative as shown in Figs. 6.8(c).

- Finally, in the F_L case for a spin-1 negatively charged first KK W-boson W_1^- decay, the lines are clearly curved instead of being straight, as shown in Figs. 6.8(d) and (h). In particular, even though the coupling of γ and Z to a $W_1^\pm$ pair is P-conserving so that the P-odd observable $\langle \mathbb{P}_V \rangle$ vanishes for right-handed electron and left-handed positron beams, the single decay polar-angle distribution takes a non-trivial quadratic curve shape due to non-vanishing P-even polarization observable $\langle \mathbb{Q}_V \rangle$.

To summarize. It is necessary to have P-violating decays for any non-trivial single decay polar-angle distribution. Moreover, in the spin-1/2 case, the production process must have P-violating contributions due to the presence of P-violating interactions which can be greatly enhanced by initial beam polarizations. In the spin-1 case, in addition to the P-odd polarization observable, there can exist a P-even polarization observable leading to non-trivial decay polar-angle distribution, the shape of which is quadratic in $\cos\theta_\mp$.

6.5.5 Angular correlations of two charged leptons

As can be checked with Eqs. (6.99) and (6.100), the lepton polar-angle distribution of the process $e^-e^+ \to F_p^- F_p^+$ followed by the decay $F_p^- \to \ell^- S_d^0$ or $\ell^- V_d^0$ is isotropic if the integration of the polarization observable $\mathbb{P}_F$ over the polar-angle θ is vanishing as in the KK muon-pair production due to the pure vector coupling of the photon and Z boson to the KK muon pair. Therefore, a single lepton angle distribution cannot be exploited to distinguish the spin-1/2 case from the spin-0 case. In this situation, we can exploit the angular correlations of two charged leptons.

6.5.5.1 Polar-angle correlations As the spin-1 case can usually be distinguished from the spin-0 and spin-1/2 cases through the coefficient proportional to $(3\cos^2\theta_- - 1)$ even when

either the P-odd observable $\langle \mathbb{P}_F \rangle$ or the P-odd relative chirality is vanishing. On the contrary, in the spin-1/2 case there can exist a non-trivial single lepton polar-angle distribution only when both the P-odd coefficients and the P-odd integral are non-vanishing. Otherwise, the spin-1/2 case cannot be distinguished from the spin-0 case by the single lepton angular distribution. In this P-invariant case, we can consider the polar-angle correlation of two final leptons, which is a P-even quantity. In general, the polar-angle correlation in the spin-1/2 case can be decomposed into four parts as

$$\begin{aligned}\frac{1}{\mathcal{C}_D}\frac{d\mathcal{C}_D}{d\cos\theta_- d\cos\theta_+} = & \frac{1}{4}\left\{1+\xi_D\eta_D\left[(\cos\theta_-+\cos\theta_+)\,\Theta_{F1}+(\cos\theta_--\cos\theta_+)\,\Theta_{F2}\right]\right. \\ & \left.+\xi_D^2\eta_D^2\,\cos\theta_-\cos\theta_+\,\Theta_{F3}\right\}\end{aligned} \tag{6.117}$$

with $\xi_D = \xi_{\rm fs}, \xi_{\rm fv}$ and $\eta_D = 1, \eta_{\rm fv}$ for the decay modes, $F_p^- \to \ell^- S_d^0, \ell^- V_d^0$, respectively. Here, the P-odd coefficients, $\Theta_{F1,F2}$, and the P-even coefficient Θ_{F3}, which are in general dependent on the e^+e^- c.m. energy and beam polarizations, are given by

$$\Theta_{F1} = \mathbb{p}_{++}^{++} - \mathbb{p}_{--}^{--} \tag{6.118}$$

$$\Theta_{F2} = \mathbb{p}_{+-}^{+-} - \mathbb{p}_{-+}^{-+} \tag{6.119}$$

$$\Theta_{F3} = \left(\mathbb{p}_{+-}^{+-} + \mathbb{p}_{-+}^{-+}\right) - \left(\mathbb{p}_{++}^{++} + \mathbb{p}_{--}^{--}\right) \tag{6.120}$$

We note in passing that the P-odd quantity $\langle \mathbb{P}_F \rangle$ appearing in the single lepton polar-angle θ_- distributions is identical to the sum $\Theta_{F1} + \Theta_{F2}$. An identical relation is valid also for the P-odd quantity $\langle \mathbb{P}_V \rangle$ in the spin-1 case.

As indicated in the previous subsection, the P-odd quantities $\Theta_{F1,F2}$ are vanishing[11] in the production of a first KK-muon $\mu_{1L/1R}^{\pm}$ pair, because the coupling of the spin-1 vector bosons γ, Z to the first KK-muon pair is of a pure vector type. However, the coefficient Θ_{F3} defining the P-conserving decay polar-angle correlation in Eq. (6.117) is P-even so that this quantity does not have to be vanishing even in the P-conserving case. As shown numerically by the (red) solid lines in Figs. 6.9(a) and (d), the P-even coefficient Θ_{F3} increases in size as the c.m. energy increases. As a consequence, it is evident that the spin-1/2 $\mu_1^{\pm}$ case can be distinguished from the spin-0 $\tilde{\mu}_{L/R}^{\pm}$ case through the non-trivial polar-angle correlation,

[11] The quantity Θ_{F1} vanishes in the absence of any absorptive parts as a consequence of CPT invariance.

which can be significant for pure right-chiral or left-chiral decays with $\xi_{\rm fv} = \pm 1$ and a sizable dilution factor $\eta_{\rm fv}$. We note in passing that the P-even coefficients in the other spin-1/2 cases ($D_{L/R}$ and E_L) in Figs. 6.9(b), (e), (c)and (f) are also increasing in size with the c.m. energy and already sizable at the c.m. energy of 500 GeV.

6.5.5.2 Azimuthal-angle correlations In this subsection, we study the fully-correlated azimuthal-angle distributions in the production of a $\mathcal{P}^+\mathcal{P}^-$ pair in e^+e^- collisions and both of their sequential two-body decays $\mathcal{P}^- \to \ell^-\bar{\mathcal{D}}^0$ and $\mathcal{P}^+ \to \ell^+\mathcal{D}^0$. The azimuthal-angle difference $\phi = \phi_- - \phi_+$ under consideration is the angle between the two decay planes, which is invariant under any Lorentz boost along the $\mathcal{P}^\pm$ flight direction. These distributions develop through quantum interference between the different helicity states in a coherent sum, indicating that the effect is diluted as the e^+e^- c.m. energy increases. By extracting this angular dependence, we can determine which helicity states contribute to the sum, and thus we can extract useful information on the spin of the pair-produced particles in a model-independent way [332].

The general form of the azimuthal-angle correlation for the production and decays of a spin J particle pair is

$$\frac{1}{\mathcal{C}}\frac{d\mathcal{C}}{d\phi} = \frac{1}{2\pi}\left[1 + \mathbb{A}_1\cos(\phi) + \cdots + \mathbb{A}_{2J}\cos(2J\phi)\right] \tag{6.121}$$

We emphasize that the expression is still valid even in a CP-noninvariant theory as all the sine terms are washed out by taking the average over two possible production azimuthal angles, which is unavoidable due to a twofold ambiguity in reconstructing the $\mathcal{P}^\pm$ momentum directions as shown in Eq. (D.18) in Appendix D. Each coefficient $\mathbb{A}_i$ (i = 1-2J) can be worked out from the standard rules of constructing matrix elements, as explicitly described below for the spin-1/2 and spin-1 cases.

Evidently, the correlated azimuthal-angle distribution for a spin-0 scalar-pair production process is flat due to the absence of any production-decay spin correlations. In contrast, the azimuthal-angle distribution for the spin-1/2 fermion-pair production process is given by

$$\frac{1}{\mathcal{C}_D}\frac{d\mathcal{C}_D}{d\phi} = \frac{1}{2\pi}\left[1 - \xi_D^2\eta_D^2\,\Phi_F\cos\phi\right] \tag{6.122}$$

in terms of a C-even and P-even quantity Φ_F defined as

$$\Phi_F = \frac{\pi^2}{16}\,\mathrm{Re}(\mathbb{p}_{--}^{++} + \mathbb{p}_{++}^{--}) \tag{6.123}$$

with $\xi_D = \xi_{\rm fs}, \xi_{\rm fv}$ and $\eta_D = 1, \eta_{\rm fv}$ for $\mathcal{D}^0 = S_d^0$ and V_d^0, respectively, and the super/sub-scripts $\pm$ for the helicities $\pm 1/2$ of the spin-1/2 fermion $F_p^\pm$. On the other hand, the correlated azimuthal-angle distribution for a spin-1 vector boson pair $V_p^+ V_p^-$ consists of three parts as

$$\frac{1}{\mathcal{C}_{\rm vf}}\frac{d\mathcal{C}_{\rm vf}}{d\phi} = \frac{1}{2\pi}\left[1 - \xi_{\rm vf}^2\eta_{\rm vf}^2\,\Phi_{V1}\,\cos\phi + (3\eta_{\rm vf} - 2)^2\,\Phi_{V2}\,\cos(2\phi)\right] \tag{6.124}$$

in terms of two C-even and P-even quantities Φ_{V1} and Φ_{V2} defined as[12]

$$\Phi_{V1} = \frac{9\pi^2}{64}\,\mathrm{Re}(\mathbb{p}_{00}^{++} + \mathbb{p}_{--}^{00} + \mathbb{p}_{0-}^{+0} + \mathbb{p}_{-0}^{0+}) \tag{6.125}$$

$$\Phi_{V2} = \frac{1}{4}\,\mathrm{Re}(\mathbb{p}_{--}^{++} + \mathbb{p}_{++}^{--}) \tag{6.126}$$

where the super/sub-scripts $\pm, 0$ stand for the helicities, $\pm 1, 0$ of the spin-1 vector bosons $\mathcal{P}^\pm$. We note that the two-body decays do not suppress the $\cos\phi$ terms, while the highest $\cos(2\phi)$ mode may be suppressed if the polarization analyzing power $\eta_{\rm vf}$ is 2/3, satisfied only when the parent and daughter particles, $V_p^\pm$ and F_d^0, are nearly degenerate.

Conceptually, any azimuthal-angle correlation, which is a pure quantum-mechanical effect, requires non-trivial interference among helicity amplitudes with different helicity assignments as indicated by Eqs. (6.123), (6.125) and (6.126) and so they tend to diminish as the c.m. energy increases, as demonstrated numerically in Figs. 6.10.

- Numerically, the quantity Φ_F takes a value roughly between 0.1 and 0.2 at $\sqrt{s} = 500\,\mathrm{GeV}$ and sensitive to initial beam polarization for the processes with chiral t-channel contributions ($D_{L/R}$ and E_L) as shown in Figs. 6.10(b), (c), (f) and (g), while it is independent of beam polarization in the production for a charged first KK muon pair $\mu_{1L/1R}^\pm$ ($C_{L/R}$) with no t-channel contributions as shown in Figs. 6.10(a) and (d).

[12] As the coefficients Φ_F and $\Phi_{V1,V2}$ are C-even, no identification of the electric charges of two leptons is required for reconstructing the azimuthal-angle correlations.

- One noteworthy aspect in the spin-1 case (F_L) is that the quantity Φ_{V2} is too small (less than 2 %) in magnitude to distinguish the spin-1 $W_1^\pm$ state from the spin-1/2 states, $\mu_1^\pm$, $e_1^\pm$ or $\tilde{W}^\pm$ as shown in Figs. 6.10(d) and (h). This strong suppression in the spin-1 $W_1^\pm$ case is due to the cancellation of the corresponding production helicity amplitudes ($\sim M^2_{W_1^\pm}/E^2_{\rm cm}$) that is forced by the relations satisfied for saving the tree-level unitarity.
- On the other hand, the coefficient Φ_{V1} in the $\cos\phi$ term is sufficiently large so that this correlation can be exploited for distinguishing the spin-1 case at least from the spin-0 case as indicated by the solid lines in Figs. 6.10(d) and (h).

To summarize. The fully-correlated azimuthal-angle correlations encoding quantum interference between different helicity final states can provide a supplementary but not complete method for spin measurements.

Based on the mass spectrum (6.87) leading to the dilution factor $\eta_{\rm fv} = 1/3$ (obtained by substituting these masses into Eq. (6.103)) while $\eta_{\rm fs} = 1$, we show in Figs. 6.11 the fully-correlated azimuthal-angle distributions for a spin-1/2 charged first KK muon and electron ($C_{L/R}$ and $D_{L/R}$), for a spin-1/2 charged wino (E_L) and for a spin-1 charged first KK W-boson (F_L). The plots in the upper (lower) frames are for left-handed (right-handed) electron and right-handed (left-handed) positron beams, respectively.

- In the first KK muon and electron cases ($C_{L/R}$ and $D_{L/R}$), the azimuthal-angle correlations are too small to be distinguished from the flat distribution in the spin-0 case as shown in Figs. 6.11(a), (b), (e) and (f). This tiny correlation is owing to the fact that we have a small coefficient Φ_F but also a small dilution factor $\eta^2_{\rm fv} = 1/9$, which can be much larger for a small mass ratio of the parent and daughter particles.
- In contrast the spin-1/2 charged wino case (E_L) shows a rather distinct azimuthal-angle correlation as the dilution factor $\eta_{\rm fs} = 1$ independently of particle masses, as shown in Figs. 6.11(c) and (g).
- In the spin-1 case the dilution factor is $\eta_{\rm vf} = 8/9$ and the coefficient Φ_{V1} in the $\cos\phi$ term is between 0.4 and 0.6 in magnitude while the coefficient Φ_{V2} is extremely tiny. As a consequence, the azimuthal-angle correlation exhibits a distinct distribution proportional to $1 + \alpha_1 \cos\phi + \alpha_2 \cos 2\phi$ with $\alpha_1 \sim 0.25$ and $\alpha_2 \sim 0$, as shown in Figs. 6.11(d) and (h).

To summarize. We have shown for the mass spectrum (6.87) that the spin-1/2 KK muons and electrons cannot be so easily distinguished from the spin-0 smuons and selectrons through the azimuthal-angle correlation. In contrast, the spin-1/2 charged wino case and the spin-1 KK W-boson case can be distinguished from the spin-0 cases. However, it turned out to be difficult to establish the spin-1 nature of the KK W-boson due to the strong suppression of the $\cos 2\phi$ mode, requiring other methods such as the decay polar-angle distributions.

6.5.6 Effects of ISR, beamstrahlung, particle widths and kinematic cuts

In this subsection for a more realistic investigation we study the impact on the various kinematic observables by initial state radiation (ISR) [352], beamstrahlung [353] and finite width of the particle $\mathcal{P}^\pm$ as well as typical kinematic cuts in an e^+e^- collider environment. We use FeynRules [354–356] to implement all the vertices and propagators into the format of CalcHEP [357]. Then, we perform extensive simulations for the spin and chirality assignments listed in Table 6.3.

The kinematic cuts taken in the present numerical analysis are

$$|\cos\theta_\ell| < 0.9962 \quad \text{and} \quad E_\ell > 10\,\text{GeV} \tag{6.127}$$

to ensure detection, where θ_ℓ and E_ℓ are the polar angle and the energy of the lepton in the laboratory frame, and

$$\not{p}_T > 10\,\text{GeV} \tag{6.128}$$

to remove the background from $e^+e^- \to e^+e^-\ell^+\ell^-$ where the final e^+e^- pair is missed. The $\mathcal{P}$ total width $\Gamma_\mathcal{P}$ is calculated to be the sum of the partial widths of the two decays $\mathcal{P}^- \to \ell^-\bar{\mathcal{D}}^0$ with $\ell = e$ and/or μ, for a simple analysis of the impact of the width. ISR and Beamstrahlung effects at ILC are calculated with CalcHEP using parameters in Table 6.5 [358].

Rather than listing all the scenarios studied in the previous subsections, we present our simulation results for only a few typical scenarios selected for each observable. Figs. 6.12 shows the excitation curve of the production of a spin-0 charged R-selectron pair $\tilde{e}_R^\pm$ (B_R), a spin-1/2 charged R-type first KK-electron pair $\tilde{e}_R^\pm$ (D_R), a spin-1/2 charged wino pair $\tilde{W}^\pm$

(E_L) or a spin-1 charged first KK W-boson pair $W_1^\pm$ (F_L) close to threshold after the ISR, beamstrahlung and width effects as well as the kinematic cuts in Eqs. (6.127) and (6.128) are included. The statistical errors correspond to $\mathcal{L} = 10\,\text{fb}^{-1}$ per point. Except for Figs. 6.12(c) and (f), the initial electron and positron beams are taken to be unpolarized. The plot of the upper (lower) right frame is for left-handed (right-handed) electron and right-handed (left-handed) positron beams.

- The production cross section can take a finite value even below threshold as the particle can be produced virtually with a mass smaller than its on-shell mass due to its non-zero width, as indicated by the tail extended toward the lower energy region in each frame. Adjusting the width effect, it is evident that for unpolarized beams the spin-0 scalar production process (B_R) exhibits a slow P-wave excitation shown in Figs. 6.12(a) while the spin-1/2 fermion production processes (D_R and E_L) and the spin-1 vector-boson production process (F_L) show a sharp S-wave excitation, as in Figs. 6.12(b), (c), (d) and (e).
- In the spin-1 case, if the t-channel contribution is killed by complete right-handed electron and left-handed positron polarizations, the cross section rises in slow P waves near threshold in Figs. 6.12(f). Nevertheless, the number of events is very small so that it is expected to be quite difficult to confirm this P-wave pattern quantitatively.
- The threshold behavior is not affected so much by ISR and beamstrahlung effects.

To recapitulate. The spin-0 case can be clearly distinguished from the spin-1/2 and spin-1 cases in the specific scenarios through the threshold scan method, although a new method is required for distinguishing the spin-1 case from the spin-1/2 cases and even from the spin-0 case in the general case, as emphasized before.

As shown before, there exists a two-fold discrete ambiguity in determining the $\mathcal{P}^\pm$ momentum in the antler-topology event. Therefore, we show in Figs. 6.13 the polar-angle distributions with the contribution of false solution included for the production of a spin-0 charged R-type smuon/selectron pair $\tilde{e}_R^\pm/\tilde{e}_R^\pm$ (A_R/B_R), a spin-1/2 charged R-type first KK-muon/KK-electron pair $\mu_1^\pm/e_1^\pm$ (C_R/D_R), a spin-1/2 charged wino pair $\tilde{W}^\pm$ (E_L) or a spin-1 charged first KK W-boson pair $W_1^\pm$ (F_L), including ISR, beamstrahlung and width effects

as well as the kinematic cuts in Eqs. (6.127) and (6.128). Except for Figs. 6.13(d) and (h), the initial electron and positron beams are assumed to be unpolarized. The plot of the upper (lower) right-most frame is for left-handed (right-handed) electron and right-handed (left-handed) positron beams. For the simulation we simply take a fixed number of events $N_{\rm ev} = 10^4$ at the c.m. energy of 500 GeV.

- The $\sin^2\theta$ law for the production of spin-0 particles (for R-type smuons (A_R) and R-type selectrons (B_R) close to threshold) is a unique signal for the spin-0 character. This feature can be confirmed in Figs. 6.13(a) and (b) after the false distribution following the true distribution with a little dilution are extracted out from the sum of the true and false solutions.

- However, the polar-angle distributions in the spin-1/2 and spin-1 cases have so much more involved patterns that it is not straightforward to distinguish the spin-1 case from the spin-1/2 case, unless beam polarizations are exploited.

- In the spin-1 case (F_L) the polar-angle distribution is quite different for each combination of the electron and positron longitudinal polarizations as shown in Figs. 6.13(d) and (h). In particular, the true polar-angle distribution in Figs. 6.13(h) with right-handed electron and left-handed positron polarizations is characteristically different from that for the spin-1/2 first KK muon case (C_R) shown in Figs. 6.13(e).

We note that the curve of the false solution is sensitively related not only to the curve of the true solution but also to the chiral structure of the decay processes as clearly shown by the shaded area in Figs. 6.13(h). This is because the direction of the false solution depends not only on the the direction of the true solution but also on the flight directions of the two leptons, whose distributions are strongly chirality-dependent. Numerically we have confirmed that the curve with a negative slope is due to the pure left-chiral $eW_1\nu_1$ coupling involved in the decay $W_1^- \to \ell^-\bar{\nu}_\ell$. As in the excitation curves, the polar-angle distributions turn out to be not much distorted by the ISR and beamstrahlung effects.

Then, let us consider the single decay polar-angle distributions in the combined process of the $\mathcal{P}^\pm$ pair production followed by the decay of a negatively-charged particle $\mathcal{P}^- \to \ell^-\bar{\mathcal{D}}^0$ and the decay azimuthal-angle correlations in the antler-topology process in the four

scenarios, B_R for a spin-0 charged R-type selectron pair $\tilde{e}^{\pm}_R$, D_R for a spin-1/2 charged R-type first KK-electron pair $e^{\pm}_{1R}$, E_L for a spin-1/2 chargino wino pair $\tilde{W}^{\pm}$ and F_L for a spin-1 first KK W-boson pair $W^{\pm}_1$. The initial electron and positron beams are taken to be unpolarized.

The upper frames of Figs. 6.14 show the single decay polar-angle distributions after including the ISR, beamstrahlung and width effects as well as the kinematic cuts in Eqs. (6.127) and (6.128) in the four different scenarios (B_R, D_R, E_L and F_L). For the hypothetical case that no QED radiation degrades the nominal production energy, since the ratios of the right-handed cross section with $(P^L_-, P^L_+) = (1, -1)$ over the left-handed one with $(P^L_-, P^L_+) = (-1, +1)$ for scenario B_R, D_R, E_L and F_L are 27.4, 99.8, 4.51×10^{-4} and 2.89×10^{-4} respectively, the distribution should be flat in the scenario B_R, linear with a positive slope in the scenario D_R, linear with a negative slope in the scenario E_L and quadratic in a downward curved shape in the scenario F_L for unpolarized beams, as worked out from the plots in Figs. 6.8. However, in the more realistic situation that ISR and beamstrahlung decrease the $\mathcal{P}^+\mathcal{P}^-$ production energy, the angular distribution is no longer linear in the spin-0 and spin-1/2 cases and no longer curved downward in the spin-1 case, as shown in the upper frames of Figs. 6.14. Considerable depletions are observed at $\cos\theta_- \to \pm 1$ when the constraint on $E_{\mathcal{P}^\pm}$ tends to be most largely invalidated. However, we note that, since both the ISR spectrum [352] and the beamstrahlung spectrum [353] can be calculated theoretically and measured precisely, the ISR and beamstrahlung effects can be unfolded from the data, for instance, by applying a bin-by-bin correction or a matrix inversion procedure, although we will not perform the unfolding procedure in the present, rather simple numerical analysis.

The lower frames of Figs. 6.14 show the full azimuthal-angle correlations in the same set of four scenarios as in the single decay polar-angle distributions. Firstly, it turns out that the ISR, beamstrahlung and width as well as the kinematic cuts do not spoil the azimuthal-angle correlation patterns. The distribution is indeed flat in the angle ϕ in the scenario B_R for a spin-0 selectron pair and nearly flat in the scenario D_R as expected from Figs. 6.14 (e) and (f). The curves in the spin-1/2 charged wino case (E_L) and the spin-1 first KK W-boson case (F_L) are consistent with the simple $\cos\phi$ distribution, as shown in Figs. 6.14(g) and (h). (We fold the range of the angle ϕ into $[0, \pi]$ with respect to the line with $\phi = \pi$ for the numerical simulation, as ϕ is calculated from $\cos\phi$ which can be determined unambiguously.) We note

once more that the coefficient of the $\cos 2\phi$ mode is strongly suppressed due to the relations for restoring tree-level unitarity.

6.5.7 Influence from ECV interactions

Every numerical analysis performed so far is based on the assumption that electron chirality is preserved (to very good approximation). Although the approximation is valid in the SM with its EW gauge symmetry spontaneously breaking through the BEH mechanism, it may be invalid in the models with additional scalar bosons and with mass generation by different mechanisms. Evidently the ECV terms are already constrained by various low-energy physical quantities. However, the complete analysis of those constraints is very much involved and beyond the scope of the present work. Therefore, before closing this lengthy section, we comment briefly on the possible influence of the ECV terms on the spin determination rather qualitatively, if they are not so strongly suppressed.

As the analytic expressions of production and two-body helicity amplitudes listed in Sects. 6.2 and 6.3 indicate, the ECV effects in the production process $e^+e^- \to \mathcal{P}^+\mathcal{P}^-$ are generated when a spin-0 scalar S_s^0 couples both to the e^+e^- pair and also when the $\mathcal{P}^+\mathcal{P}^-$ pair and/or the t/u-channel trilinear vertices involving an electron are non-chiral, i.e. have both left-handed and right-handed couplings while the ECV effects in the decay processes are generated by non-chiral decay trilinear $\mathcal{P}\ell\mathcal{D}$ vertices.

In the ECV case, the electron and positron helicities are identical, $\sigma_- = \sigma_+$ and they form a $J_0 = 0$ initial two-body state. Therefore, the production polar-angle distribution is isotropic at threshold and the threshold excitation is in a sharp S wave except when a spin-1/2 $F_p^+F_p^-$ pair is produced only through an s-channel pseudoscalar exchange ($s_{S+}^{FF} = -s_{S-}^{FF}$). As a result, the characteristic patterns of threshold excitation and polar-angle distribution in the ECC case can be spoiled in the presence of the ECV contributions.

If the decay vertices are non-chiral, the relative chirality is not maximal in magnitude any more, i.e. $|\xi| < 1$, reducing the production-decay correlation even for the spin-1/2 and spin-1 cases. In the extreme situation with zero relative chirality, there exist no non-trivial decay angular distributions for determining whether the spin of the parent particle $\mathcal{P}$ is 0

or 1/2. In contrast to the spin-1/2 case, there exists a decay-angle distribution independent of the relative chirality in the spin-1 case. Even though the effectiveness of this distribution is reduced by a dilution factor, the spin-1 case can be distinguished from the spin-0 and spin-1/2 cases through the chirality-independent decay-angle correlations [334].

6.6 SUMMARY AND CONCLUSIONS

In this chapter, we have made a systematic study of kinematic observables connected with the antler-topology process $e^+e^- \to \mathcal{P}^+\mathcal{P}^- \to \ell^+\ell^-\mathcal{D}^0\bar{\mathcal{D}}^0$ which could serve as model-independent tests for determining the spins of the charged particles $\mathcal{P}^\pm$ and the invisible neutral particles $\mathcal{D}^0$ and $\bar{\mathcal{D}}^0$ as well as the intermediate virtual particles participating in the production process.

It is evident from our analysis that the model-independent determination of the spin quantum numbers of new particles is a complex task even at e^+e^- colliders with clean and fixed initial-state environments and beam polarizations. The degree of complexity depend crucially on the chiral structures as well as kinematic features of the particles. Not only threshold excitation and angular distributions controlled through initial beam polarizations in pair production but also angular correlations in particle decays provide powerful methods for experimental spin measurements.

The predictions for the threshold excitation and the polar-angle distributions in the production processes, separated into the ECC and ECV parts when the electron is assumed to be massless, are summarized in Table 6.6.

In any theory with conserved chiral symmetry guaranteeing the electron mass to be zero before EWSB such as MSSM and MUED, the ECV parts are connected with the extremely tiny electron mass so that their contributions are negligible for high energy processes. In this ECC case, as shown in the chirality conserving part of Table 6.6, the $\sin^2\theta$ law for the production of a spin-0 scalar pair (close to threshold) is a unique signal of the spin-0 character. While the observation of the $\sin^2\theta$ polar-angle distribution is sufficient for scalar particles, the P-wave β^3 onset of the excitation curve is necessary but not a sufficient condition for the

spin-0 character. Nevertheless, we have found that combining the two distributions and using initial beam polarizations to separately diagnose four e^+e^- helicity combinations enable us not only to determine the $\mathcal{P}$ spin unambiguously but also to get crucial information on the spins of intermediate particles and the chiral structure of the couplings in the ECC case.

If there exist any non-negligible ECV contributions, then the patterns of both threshold excitation and production angle distribution may be qualitatively different from those in the ECC case, as shown in the chirality violating part of Table 6.6. However, one can always use Eq. (6.11) and Eq. (6.13) to extract the ECC part of pair production, as there exists at least a contribution from an s-channel photon, to get spin information from threshold excitation and production angle distribution of the ECC part.

Combining the production and decay processes in the antler-topology process, it is possible to construct several correlated observables for a spin-1/2 or spin-1 particle pair $\mathcal{P}^{\pm}$. Evidently there is no production-decay correlation for a spin-0 $\mathcal{P}$, which is a characteristic feature for the spin-0 case. The sensitivities to the $\mathcal{P}$ spin depend strongly on the chiral structure reflected in the production and decay helicity amplitudes and the degrees of initial and final beam polarizations. If the couplings for the decays are pure chiral and the high degree of beam polarizations are available, then the decay polar-angle distributions are very powerful for determining the $\mathcal{P}$ spin as the relative chiralities serving as the polarization analysis powers are maximal. The azimuthal-angle distribution for the difference ϕ between the azimuthal angles of two decay planes also provides a supplementary method for determining the $\mathcal{P}$ spin, although this quantum-interference effect diminishes as the c.m. energy increases.

If the decay vertices are not pure chiral, the sensitivities of the kinematic observables to the particle spins are reduced. In the extreme cases of P-conserving pure vector or axial vector couplings, we do not have any production-decay correlations in the spin-1/2 case. Even in this case, there exists a non-trivial P-even observable in the $\cos 2\phi$ mode in the spin-1 case. However, we have found that the coefficient determined by the production process $e^+e^- \to V_p^+V_p^-$ is strongly suppressed when the specific relations among couplings are satisfied for saving tree-level unitarity at high energies. As a result, it may be very difficult in those extreme cases to determine the spins of the particle involved in the antler-topology

process.

To conclude. It is a very complex task to determine the spins of new particles in a model-independent way in a general theory beyond the SM. Nevertheless, we have found that, if electron chirality invariance is valid to very good approximation, the spin of the new particles taking part in the antler-topology process can be determined in a model-independent way through various energy- and angle-dependent observables at e^+e^- colliders with polarized beams. Any non-chiral contributions, which are expected to be insignificant as in many popular models beyond the SM, render the model-independent spin determination more difficult. However we can still use beam polarizations to extract the chirality-conserving pieces to get useful information on the spins of new particles based on various approaches described in the present work. After all, a high energy e^+e^- collider with polarized beams is a powerful machine for diagnosing not only the spin but also the chirality structure of new particles, if they are kinematically available.

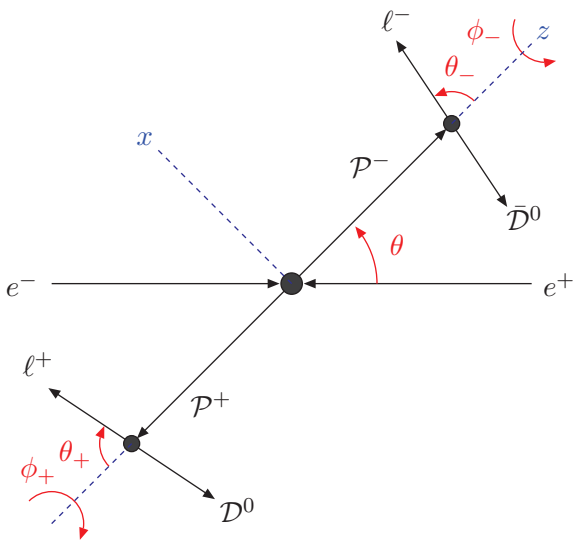

Figure 6.3: The coordinate system in the colliding e^+e^- c.m. frame. The y-axis is chosen along the $\vec{p}_-(e^-) \times \vec{q}_-(\mathcal{P}^-)$ direction and it is pointing towards the observer. The coordinate systems in the $\mathcal{P}^-$ and $\mathcal{P}^+$ rest frames are obtained from it by boosts along the z-axis. The angles $\theta_\pm$ and $\phi_\pm$ are the polar and azimuthal angles of the lepton $\ell^\pm$ associated with the two-body decay of the $\mathcal{P}^\pm$ particles in their respective rest frames.

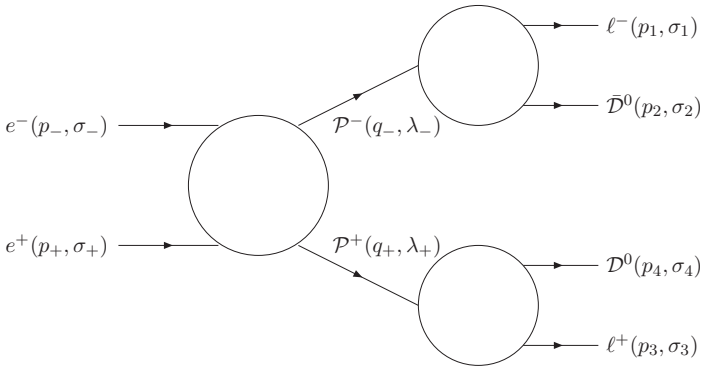

Figure 6.4: A schematic view of the process $e^+e^- \to \mathcal{P}^+\mathcal{P}^- \to (\ell^+\mathcal{D}^0)(\ell^-\bar{\mathcal{D}}^0)$. Shown in the parentheses are the four-momenta and re-scaled helicities of the corresponding particles.

Index	$[J_{\mathcal{P}}, J_{\mathcal{D}}]$	Chirality	Antler-topology process	s-channel $[J_{\mathcal{S}^0}]$	t-channel $[J_{\mathcal{T}^0}]$	Model
$A_{L/R}$	$[0, 1/2]$	L/R	$e^+e^- \to \tilde{\mu}^+_{L/R}\tilde{\mu}^-_{L/R} \to (\mu^+\tilde{B})(\mu^-\tilde{B})$	$\gamma, Z \quad [J=1]$	$-$	MSSM
$B_{L/R}$	$[0, 1/2]$	L/R	$e^+e^- \to \tilde{e}^+_{L/R}\tilde{e}^-_{L/R} \to (e^+\tilde{B})(e^-\tilde{B})$	$\gamma, Z \quad [J=1]$	$\tilde{B}, \tilde{W}^0 \quad [J=1/2]$	MSSM
$C_{L/R}$	$[1/2, 1]$	L/R	$e^+e^- \to \mu^+_{L1/R1}\mu^-_{L1/R1} \to (\mu^+B_1)(\mu^-B_1)$	$\gamma, Z \quad [J=1]$	$-$	MUED
$D_{L/R}$	$[1/2, 1]$	L/R	$e^+e^- \to e^+_{L1/R1}e^-_{L1/R1} \to (e^+B_1)(e^-B_1)$	$\gamma, Z \quad [J=1]$	$B_1, W_1^0 \quad [J=1]$	MUED
E_L	$[1/2, 0]$	L	$e^+e^- \to \tilde{W}^+\tilde{W}^- \to (\ell^+\tilde{\nu}_\ell)(\ell^-\tilde{\nu}^*_\ell)$	$\gamma, Z \quad [J=1]$	$\tilde{\nu}_e \quad [J=0]$	MSSM
F_L	$[1, 1/2]$	L	$e^+e^- \to W_1^+W_1^- \to (\ell^+\nu_{\ell 1})(\ell^-\bar{\nu}_{\ell 1})$	$\gamma, Z \quad [J=1]$	$\nu_{e1} \quad [J=1/2]$	MUED

Table 6.3: Ten examples for the antler-topology processes - five in MSSM and five in MUED. Every ECV effect due to EWSB in these models is small so that the $e\mathcal{T}\mathcal{P}$ and $\mathcal{P}\ell\mathcal{D}$ couplings are purely chiral to very good approximation. The first index is introduced to specify each spin and chirality assignment. The chirality index, R or L, in the third column stands for the chiral structure of the $e^-\mathcal{T}^0\mathcal{P}^-$ vertex and the $\mathcal{P}^-\ell^-\bar{\mathcal{D}}^0$ vertex. We note that the chirality of each t-channel coupling is identical to the chirality of the vertex describing the decay $\mathcal{P}^- \to \ell^-\bar{\mathcal{D}}^0$ in every scenario.

Spin $J_{\mathcal{P}}$	Polarized cross section	Threshold excitation	Model
0	$\sigma_{L/R}[e^+e^- \to \tilde{\ell}_R^+\tilde{\ell}_R^-]$	β^3	MSSM
	$\sigma_{L/R}[e^+e^- \to \tilde{\ell}_L^+\tilde{\ell}_L^-]$	β^3	MSSM
1/2	$\sigma_{L/R}[e^+e^- \to \ell_{R1}^+\ell_{R1}^-]$	β	MUED
	$\sigma_{L/R}[e^+e^- \to \ell_{L1}^+\ell_{L1}^-]$	β	MUED
	$\sigma_{L/R}[e^+e^- \to \tilde{W}^+\tilde{W}^-]$	β	MSSM
1	$\sigma_L[e^+e^- \to W_1^+W_1^-]$	β	MUED
	$\sigma_R[e^+e^- \to W_1^+W_1^-]$	β^3	MUED

Table 6.4: Threshold excitation of the polarization-weighted total cross sections for the ten MSSM and MUED processes with $\ell = e, \mu$. $\beta = (1-4M_{\mathcal{P}}^2/s)^{1/2}$ is the speed of the particle $\mathcal{P}$ in the e^+e^- c.m. frame. $\sigma_{L/R}$ stands for the polarization-weighted cross section with perfect left-handed or right-handed electron beam polarization.

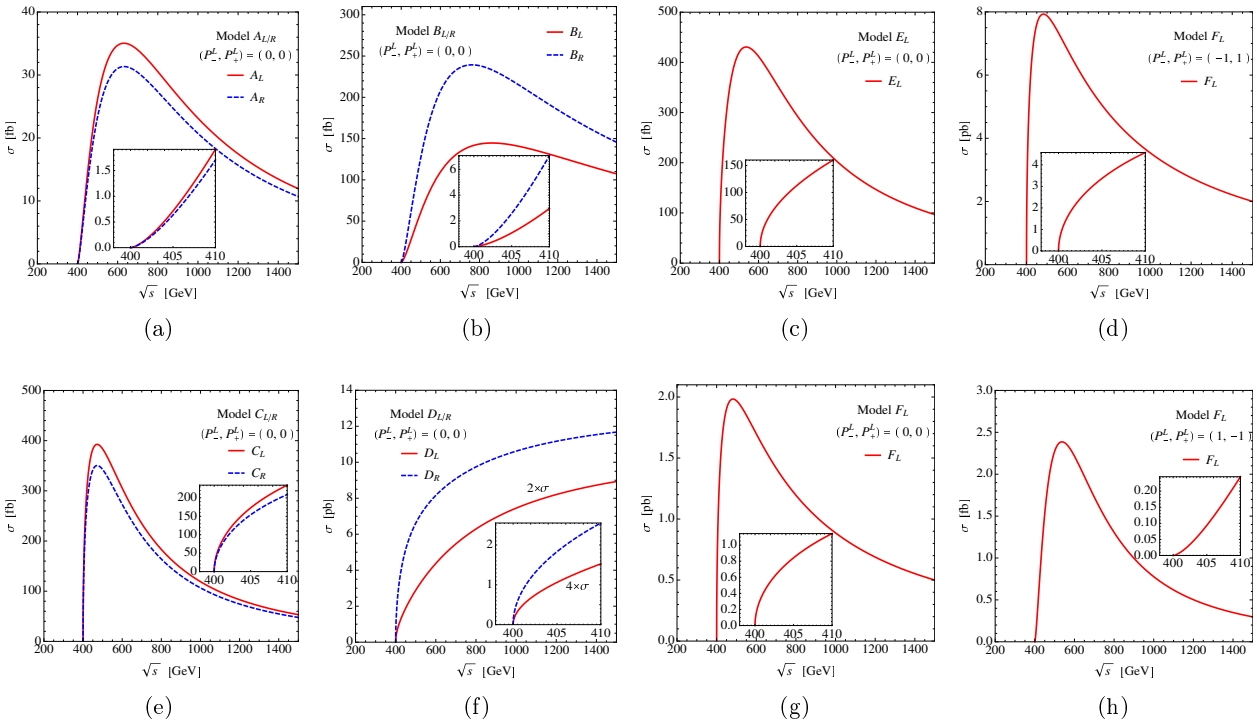

Figure 6.5: Energy dependence of the total cross sections with the threshold excitation curves embedded for spin-0 scalar bosons ($A_{L/R}$ and $B_{L/R}$), spin-1/2 fermions ($C_{L/R}, D_{L/R}$ and E_L) and spin-1 vector bosons (F_L). The electron and positron beams are set to be unpolarized, except for the frames, (d) and (h); the upper (lower) frame is for purely left (right) polarized electron and purely right (left) polarized positron beams.

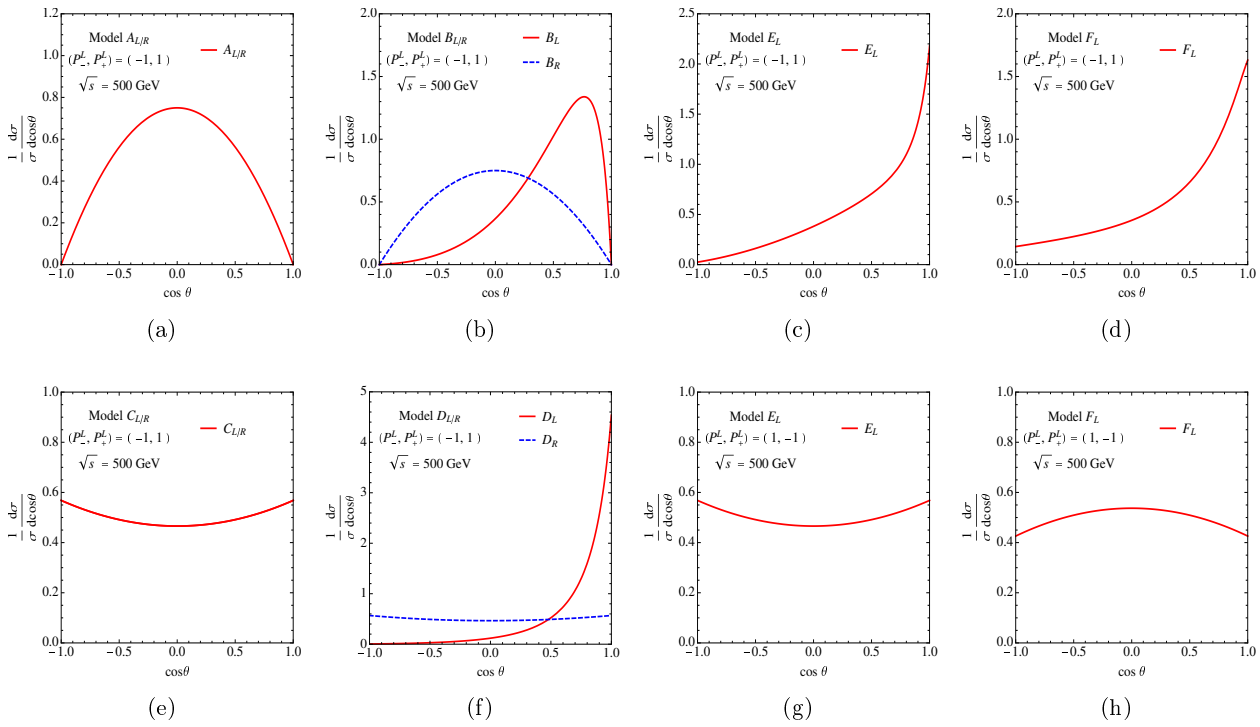

Figure 6.6: Production polar-angle distributions for the spin-0 scalar bosons indexed with $A_{L/R}$ and $B_{L/R}$, for the spin-1/2 fermions indexed with $C_{L/R}$, $D_{L/R}$ and E_L, and for the spin-1 vector bosons indexed with F_L in the MSSM and MUED models. The c.m. energy $\sqrt{s}$ is set to be 500 GeV.

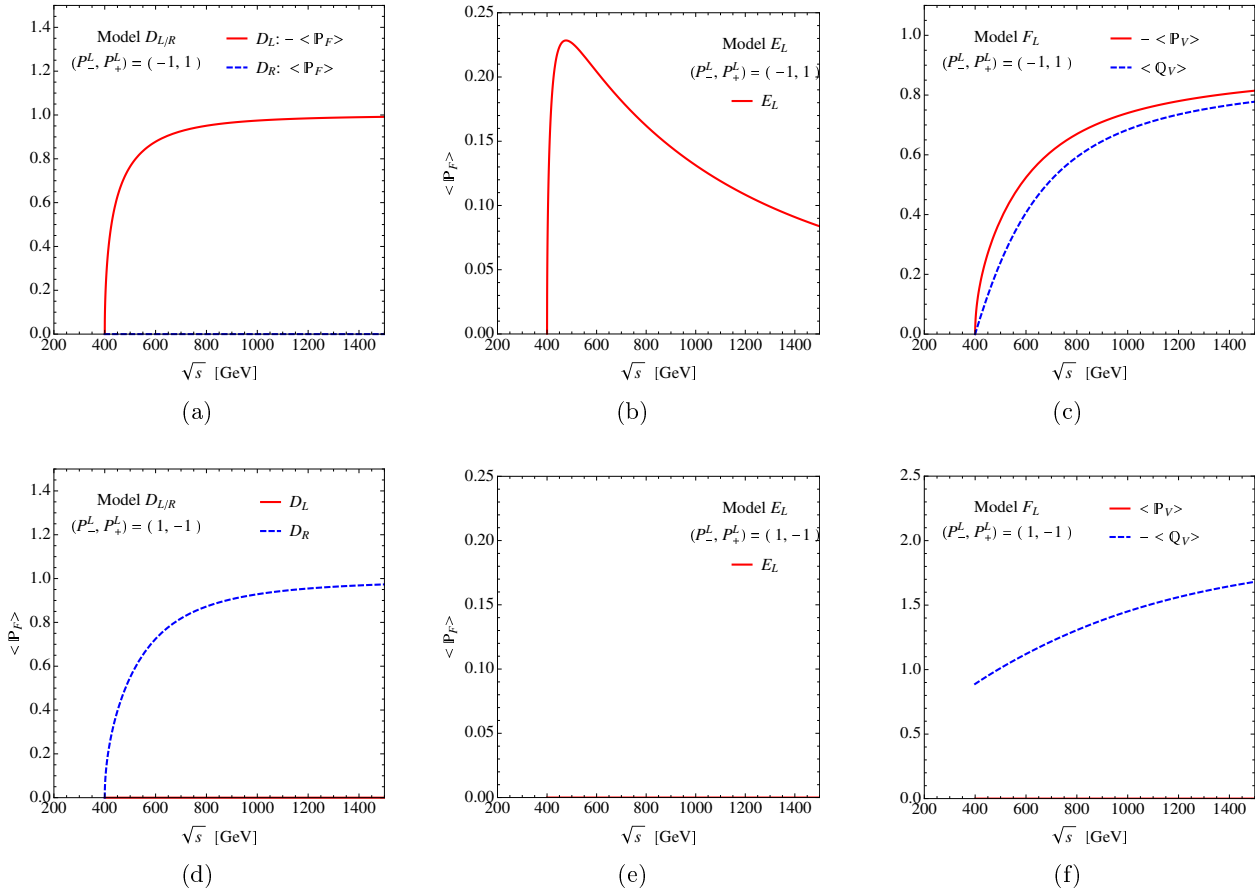

Figure 6.7: Energy dependence of the coefficients $\langle \mathbb{P}_{F,V} \rangle$ and $\langle \mathbb{Q}_V \rangle$ for a first KK electron ($D_{L/R}$), for a spin-1/2 charged wino (E_L), and for a spin-1 charged first KK W-boson (F_L). The upper (lower) frames are for left-handed (right-handed) electron and right-handed (left-handed) positron beams, respectively.

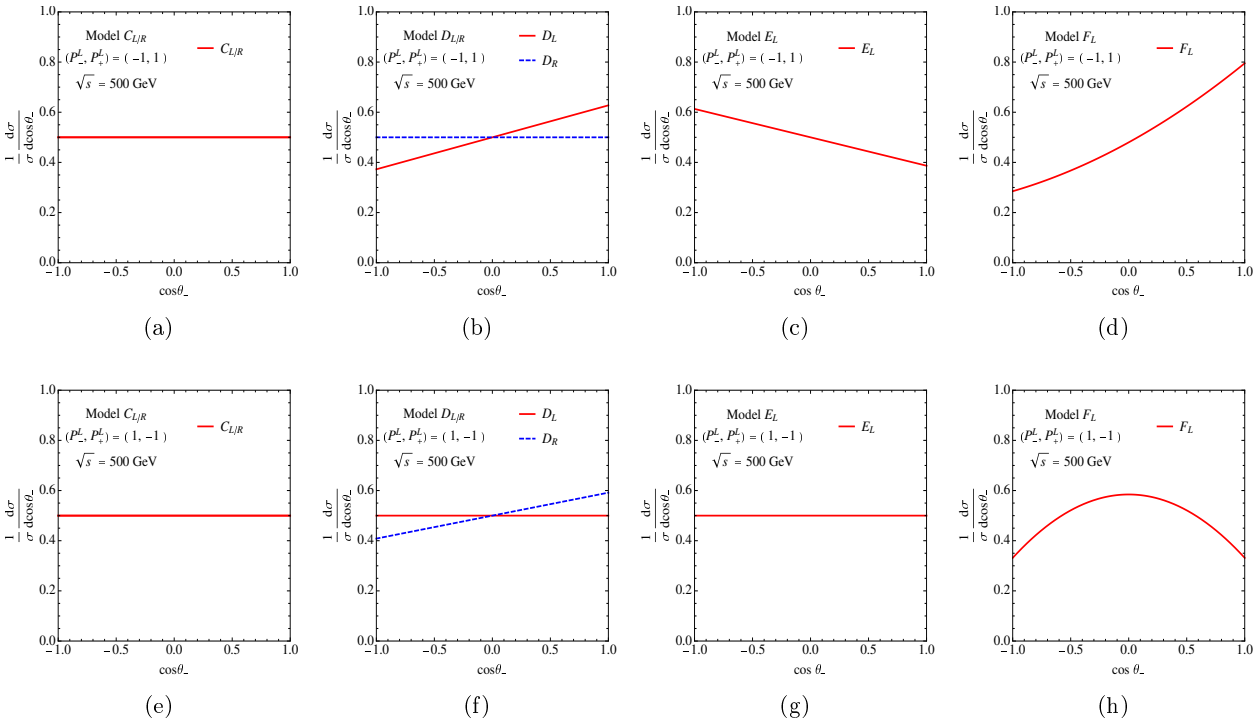

Figure 6.8: Normalized single decay polar-angle distributions for a spin-1/2 charged first KK muon $\mu^-_{1L/1R}$ ($C_{L/R}$) and first KK electron $e^-_{1L/1R}$ ($D_{L/R}$), for a spin-1/2 charged wino $\tilde{W}^-$ (E_L) and for a spin-1 charged first KK W-boson W^-_1 (F_L), pair produced with its anti-particle in e^+e^- collisions at a fixed c.m. energy of 500 GeV. The upper (lower) frames are for left-handed (right-handed) electron and right-handed (left-handed) positron beams.

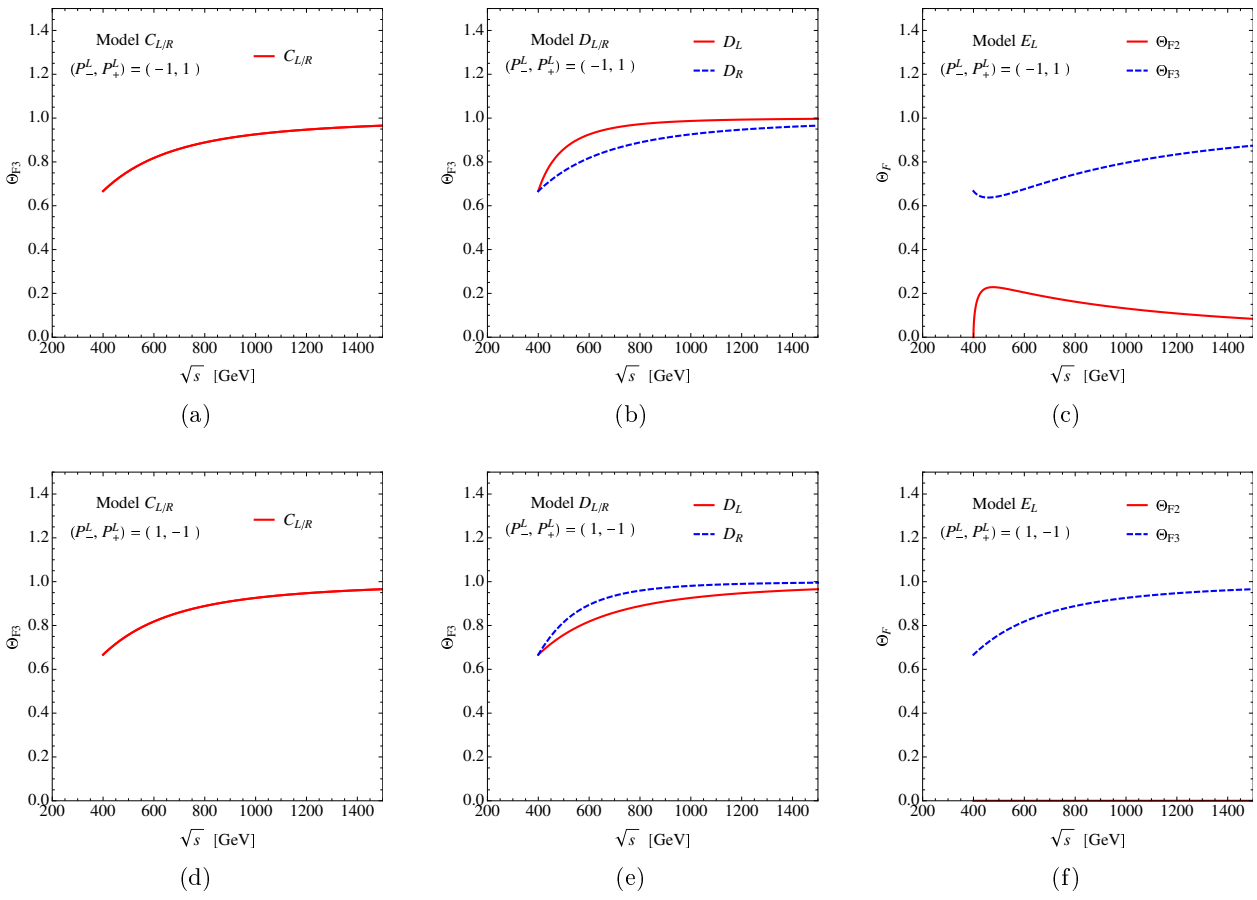

Figure 6.9: Energy dependence of the coefficients Θ_{F2} and/or Θ_{F3} of the correlated decay polar-angle distributions for a spin-1/2 charged first KK-muon ($C_{L/R}$) and first KK-electron ($D_{L/R}$) and for a spin-1/2 charged wino (E_L). The lines in the upper (lower) frames are for left-handed (right-handed) electron and right-handed (left-handed) positron beams, respectively.

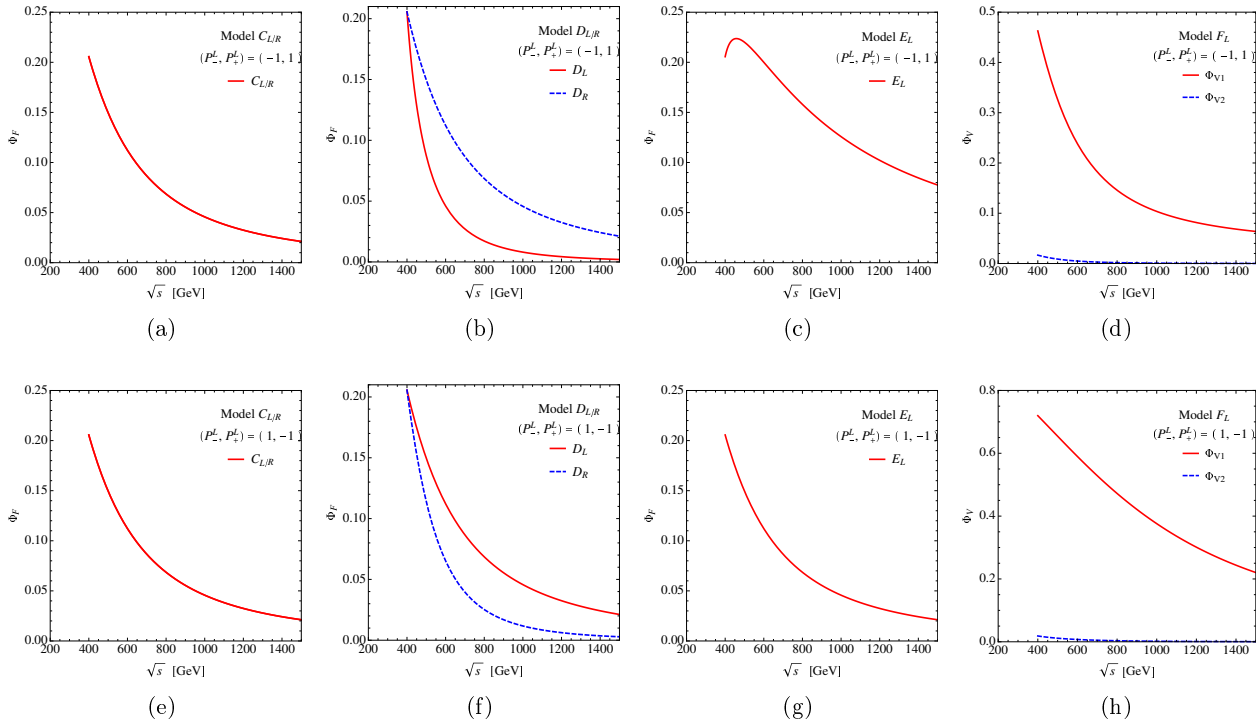

Figure 6.10: Energy dependence of the coefficients Φ_F and $\Phi_{V1,V2}$ for correlated decay azimuthal-angle distributions for a spin-1/2 charged first KK-muon pair $\mu^{\pm}_{1L/1R}$ $(C_{L/R})$ and first KK-electron pair $e^{\pm}_{1L/1R}$ $(D_{L/R})$, for a spin-1/2 charged wino pair $\tilde{W}^{\pm}$ (E_L) and for a spin-1 charged first KK-W $W_1^{\pm}$ (F_L). The lines in the upper (lower) frames are for left-handed (right-handed) electron and right-handed (left-handed) positron beams, respectively.

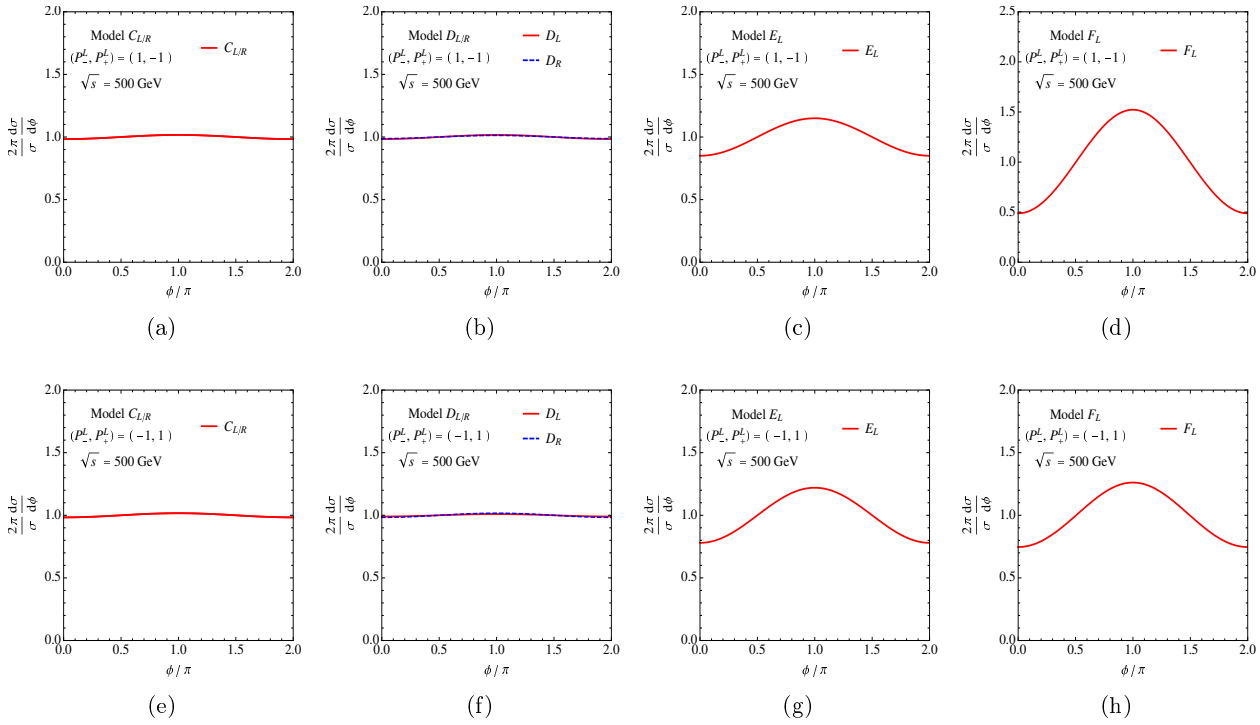

Figure 6.11: Correlated azimuthal-angle distributions for a spin-1/2 charged first KK-muon and KK-electron ($C_{L/R}$ and $D_{L/R}$), for a spin-1/2 charged wino (E_L) and for a spin-1 charged first KK-W (F_L). The upper (lower) frames are for left-handed (right-handed) electron and right-handed (left-handed) positron beams.

Collider	$E_{\rm cm}$ ($\sqrt{s}$) [GeV]	N [10^{10}]	σ_x [nm]	σ_y [nm]	σ_z [μm]
ILC	500	2	640	5.7	300

Table 6.5: Key parameters of the initial beams at the ILC used in our numerical analysis. Here N is the number of particles per bunch, $\sigma_{x,y}$ are the RMS beam sizes at the interaction point, and σ_z is the RMS bunch length.

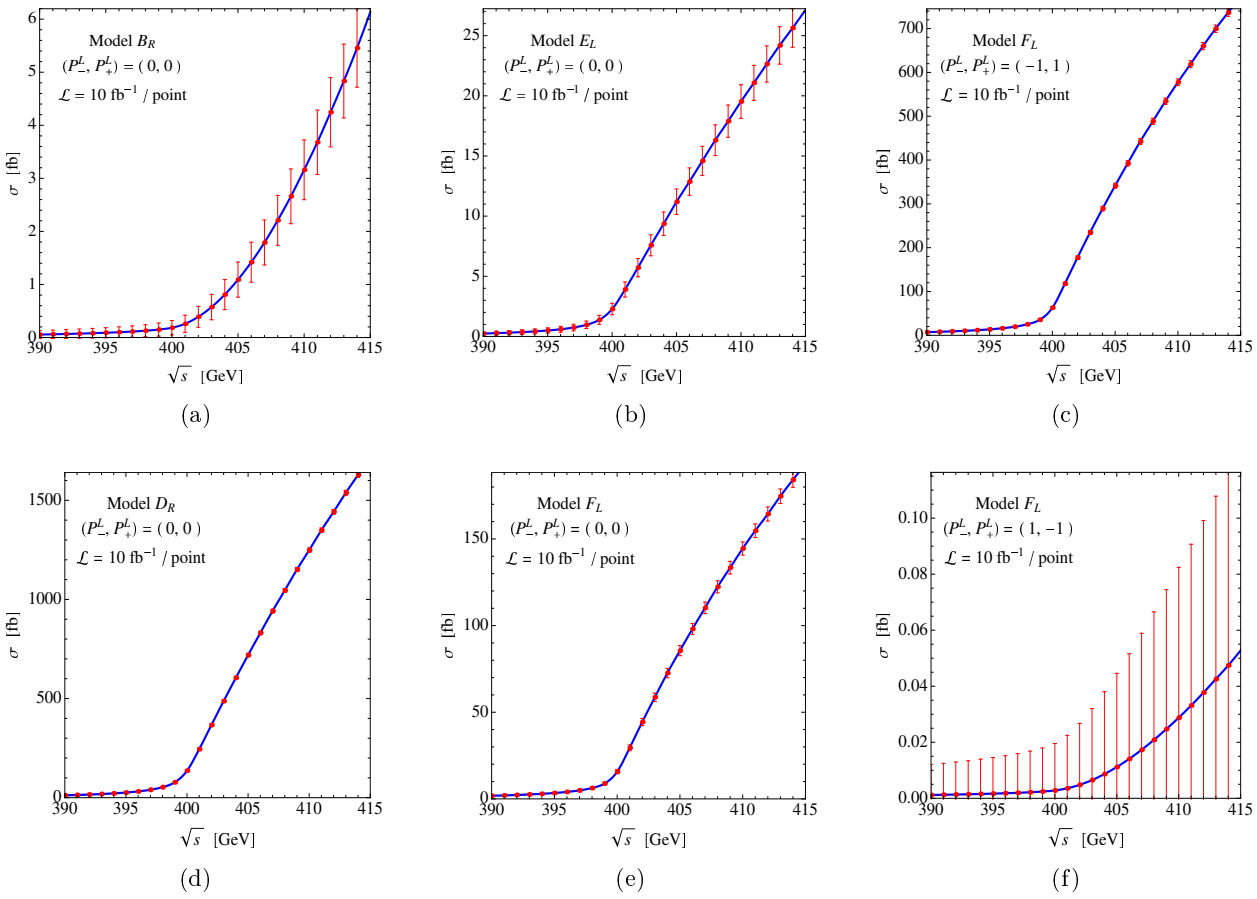

Figure 6.12: Excitation curve of the cross section close to threshold for the production of a spin-0 charged R-selectron pair $\tilde{e}^{\pm}_R$ (B_R), a spin-1/2 charged R-type first KK-electron pair $\tilde{e}^{\pm}_R$ (D_R), a spin-1/2 charged wino pair $\tilde{W}^{\pm}$ (E_L) or a spin-1 charged first KK-W pair $W^{\pm}_1$ (F_L) close to threshold including ISR, beamstrahlung and width effects as well as the kinematic cuts in Eqs. (6.127) and (6.128); the statistical errors correspond to $\mathcal{L} = 10\,\mathrm{fb}^{-1}$ per point. The initial beams are set to be unpolarized in the frames, (a), (b), (d) and (e), while the electron (positron) beams are purely left-handed (right-handed) and purely right-handed (left-handed) in the frames, (c) and (f).

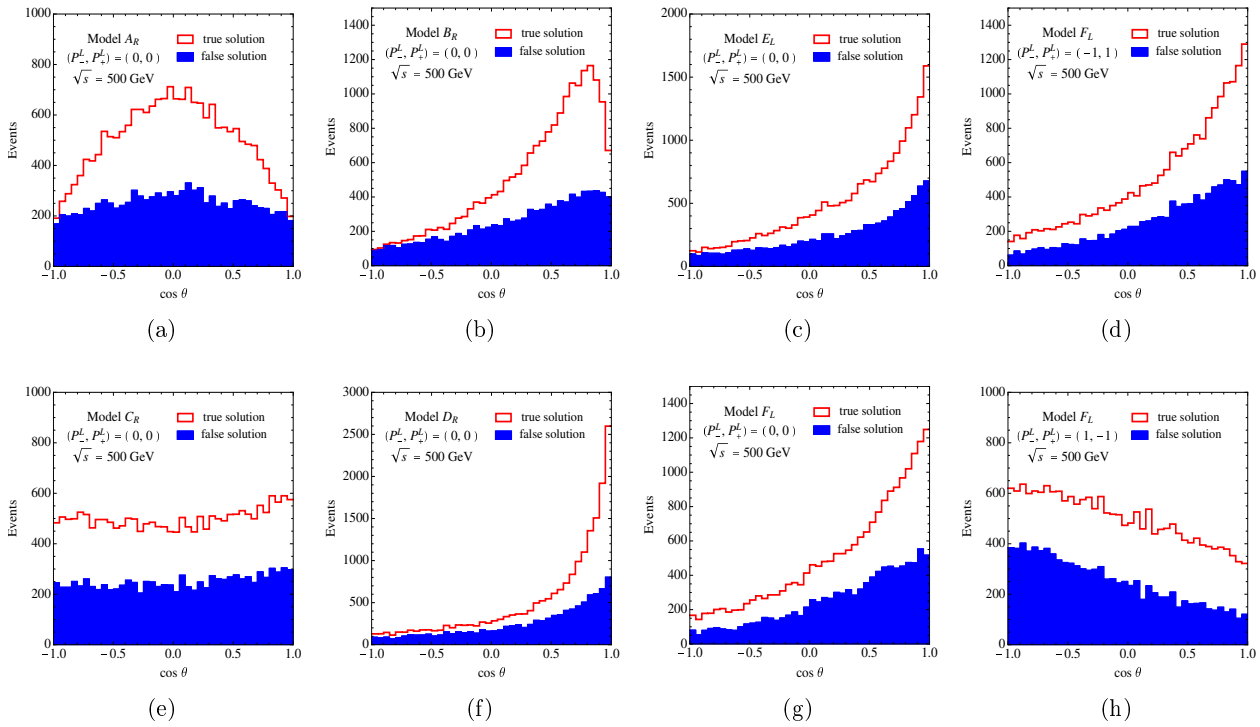

Figure 6.13: The polar-angle distributions with the contribution of false solution for the production of a spin-0 charged R-type smuon/selectron pair $\tilde{e}_R^{\pm}/\tilde{e}_R^{\pm}$ (A_R/B_R), a spin-1/2 charged R-type first KK-muon/KK-electron pair $\mu_1^{\pm}/e_1^{\pm}$ (C_R/D_R), a spin-1/2 charged wino pair $\tilde{W}^{\pm}$ (E_L) or a spin-1 charged first KK-W pair $W_1^{\pm}$ (F_L), including ISR, beamstrahlung and width effects. Except for the frames, (d) and (e), the initial electron and positron beams are set to be unpolarized. The frames, (d) and (h), are for left-handed (right-handed) and right-handed (left-handed) electron (positron) beams, respectively. The simulation for the polar-angle distribution is based on a fixed number of events $N_{\rm ev} = 10^4$ at the c.m. energy of 500 GeV.

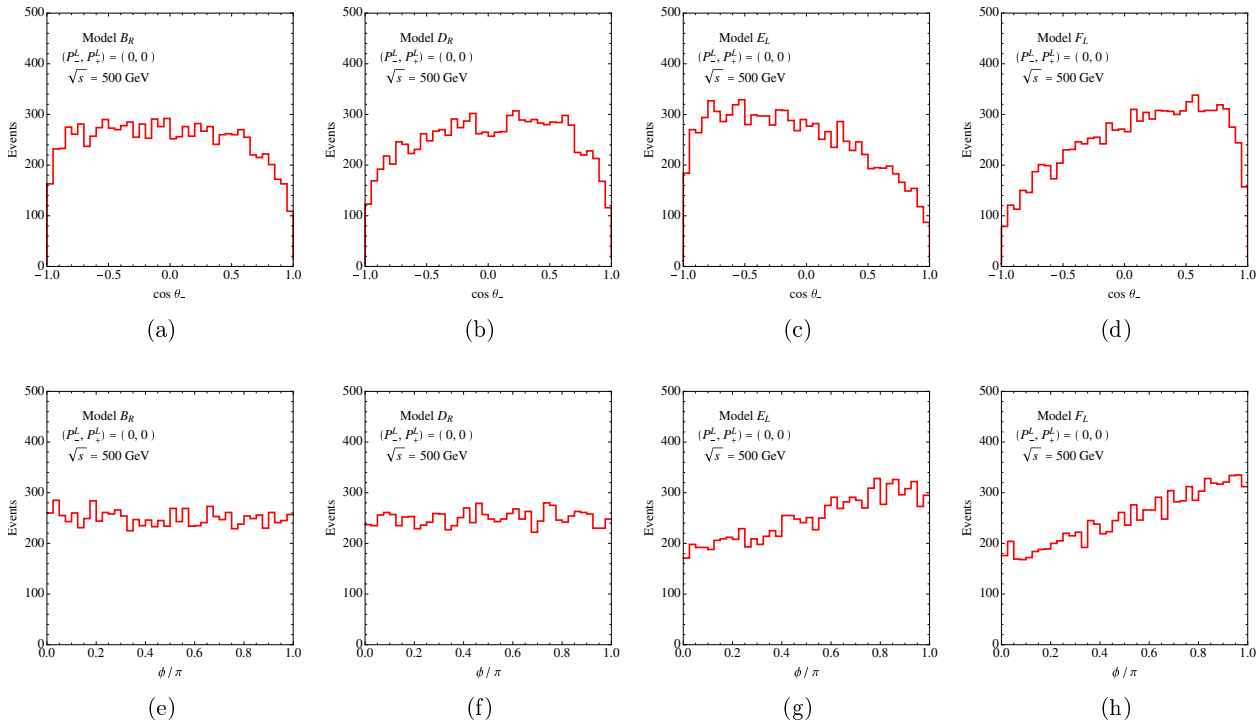

Figure 6.14: The upper frames are for the single decay polar-angle distribution for the combination of the production of a charged pair $\mathcal{P}^-\mathcal{P}^-$ and the sequential decay of the negatively-charged particle $\mathcal{P}^- \to \ell^-\bar{\mathcal{D}}^0$ and the lower frames are for the full azimuthal-angle correlations in the antler-topology process. For these distributions, we consider the production of a spin-0 charged R-type selectron pair $\tilde{e}^\pm_R$ (B_R), a spin-1/2 charged R-type first KK-electron pair $e^\pm_{1R}$ (D_R), a spin-1/2 charged wino pair $\tilde{W}^\pm$ (E_L) or a spin-1 charged first KK-W pair $W^\pm_1$ (F_L), including ISR, beamstrahlung and width effects as well as the kinematic cuts in Eqs. (6.127) and (6.128). The initial electron and positron beams are assumed to be unpolarized. The simulation for each of the decay polar-angle distributions and azimuthal-angle correlations is based on a fixed number of events $N_{\rm ev} = 10^4$ at the c.m. energy of $\sqrt{s} = 500\,\text{GeV}$.

e^+e^- chiralities	Spin $J_{\mathcal{P}}$	t or u contributions	Threshold excitation	Production polar-angle distribution
chirality conserving	0	N	β^3	$\sin^2\theta$
		Y	β^3	$\sin^2\theta$ at threshold
	1/2	N	β	$1+\kappa_{1/2}\cos^2\theta$
		Y	β	isotropic at threshold
	1	N	β^3	$1-\kappa_1\cos^2\theta$
		Y	β	isotropic at threshold
chirality violating	0	N	β	isotropic
		Y	β	isotropic at threshold
	1/2	N	β^3/β [S/P]	isotropic
		Y	β	isotropic at threshold
	1	N	β	isotropic
		Y	β	isotropic at threshold

Table 6.6: The threshold behavior and the polar-angle distribution of the ECC and ECV parts of the production process $e^+e^- \to \mathcal{P}^+\mathcal{P}^-$, with [S/P] standing for pure scalar-type or pseudoscalar-type couplings, respectively. Here, the energy-dependent coefficients, $\kappa_{1/2}$ and κ_1, take 0 and 3/19 at threshold and they approach 1 asymptotically at high energies, respectively.

7.0 CONCLUSIONS

To conclude, we summarize the key results of the many studies discussed in previous chapters, detailed features of the each analysis can be found in the corresponding sections.

In Chapter 2, we revisit the radiative decays of the Higgs boson to a fermion pair $h \to f\bar{f}\gamma$ where f denotes a fermion in the Standard Model (SM). We include the chirality-flipping diagrams via the Yukawa couplings at the order $\mathcal{O}(y_f^2\alpha)$, the chirality-conserving contributions via the top-quark loops of the order $\mathcal{O}(y_t^2\alpha^3)$, and the electroweak loops at the order $\mathcal{O}(\alpha^4)$. The QED correction is about $Q_f^2 \times \mathcal{O}(1\%)$ and contributes to the running of fermion masses at a similar level, which should be taken into account for future precision Higgs physics. The chirality-conserving electroweak-loop processes are interesting from the observational point of view. First, the branching fraction of the radiative decay $h \to \mu^+\mu^-\gamma$ is about a half of that of $h \to \mu^+\mu^-$, and that of $h \to e^+e^-\gamma$ is more than four orders of magnitude larger than that of $h \to e^+e^-$, both of which reach about 10^{-4}. The branching fraction of $h \to \tau^+\tau^-\gamma$ is of the order 10^{-3}. All the leptonic radiative decays are potentially observable at the LHC Run 2 or the HL-LHC. The kinematic distributions for the photon energy or the fermion pair invariant mass provide non-ambiguous discrimination for the underlying mechanisms of the Higgs radiative decay. We also study the process $h \to c\bar{c}\gamma$ and evaluate the observability at the LHC. We find it potentially comparable to the other related studies and better than the $h \to J/\psi\ \gamma$ channel in constraining the charm-Yukawa coupling.

In Chapter 3, we examine the feasibility of a Higgs-charm Yukawa coupling measurement in the $h \to c\bar{c}\gamma$ channel at the HL-LHC, by proposing an optimal triggering strategy and simulating realistic detector effects. The existence of an additional photon in the final state may help for the signal identification and background suppression. Adopting a refined trig-

gering strategy and utilizing basic machine learning, we find that a coupling limit of about 8 times the SM value may be reached with 2σ sensitivity after the High Luminosity LHC (HL-LHC). Our result is comparable and complementary to other projections for direct and indirect probes of $h \to c\bar{c}$ at the HL-LHC. Without a significant change in detector capabilities, there would be no significant improvement for this search from higher energy hadron colliders.

In Chapter 4, we studied collider probes of two representative scenarios for electroweak DM, namely an wino-like $\mathrm{SU(2)_L}$ triplet and a Higgsino-like $\mathrm{SU(2)_L}$ doublet at three at three different future hadron colliders: the high-luminosity HL-LHC, the proposed 27-TeV LHC upgrade (HE-LHC) and the 100-TeV FCC-hh/SppC. Future runs of the 14-TeV LHC are projected to probe masses of around 300 GeV for DM belonging to an SU(2) doublet (Higgsino-like), and 900 GeV for SU(2) triplet (wino-like). We examine how far this mass reach can be extended at the proposed 27-TeV high-energy upgrade of the LHC (HE-LHC), and compare the results to the case for a 100-TeV hadron collider. Following a detector setup similar to that of the ATLAS tracking system for the Run-2 LHC upgrade, with a new Insertable B-Layer (IBL), a disappearing charged track analysis at the HE-LHC can probe Higgsino-like (wino-like) DM mass of up to 600 GeV (2.1 TeV) at the 95% C.L. The monojet and missing transverse momentum search, on the otherhand, has a weaker reach of 490 GeV (700 GeV) at 95% C.L. for the Higgsino-like (wino-like) states. The mass range accessible in the collider searches can be complementary to the indirect detection probes using gamma rays from dwarf-spheroidal galaxies.

In Chapter 5, we explore the scenarios where the only accessible new states at the electroweak scale consist of a pair of color-singlet electroweak particles, whose masses are degenerate at the tree level and split only by electroweak symmetry breaking at the loop level. For the sake of illustration, we consider a supersymmetric model and study the following three representative cases with the lower-lying states as (a) two spin-1/2 Higgsino $\mathrm{SU(2)}_L$ doublets, (b) a spin-1/2 wino $\mathrm{SU(2)}_L$ triplet and (c) a spin-0 left-handed slepton $\mathrm{SU(2)}_L$ doublet. Due to the mass-degeneracy, those lower-lying electroweak states are difficult to observe at the LHC and rather challenging to detect at the e^+e^- collider as well. We exploit the pair production in association with a hard photon radiation in high energy e^+e^- collisions. If

kinematically accessible, such single-photon processes at e^+e^- colliders with polarized beams enable us to characterize each scenario by measuring the energy of the associated hard photon, and to determine the spin of the nearly invisible particles unambiguously through the threshold behavior in the photon energy distribution.

In Chapter 6, we perform a model-independent investigation of spin and chirality correlation effects in the antler-topology processes $e^+e^- \to \mathcal{P}^+\mathcal{P}^- \to (\ell^+\mathcal{D}^0)(\ell^-\bar{\mathcal{D}}^0)$ at high energy e^+e^- colliders with polarized beams. Generally the production process $e^+e^- \to \mathcal{P}^+\mathcal{P}^-$ can occur not only through the s-channel exchange of vector bosons, $\mathcal{V}^0$, including the neutral Standard Model (SM) gauge bosons, γ and Z, but also through the s- and t-channel exchanges of new neutral states, $\mathcal{S}^0$ and $\mathcal{T}^0$, and the u-channel exchange of new doubly-charged states, $\mathcal{U}^{--}$. The general set of (non-chiral) three-point couplings of the new particles and leptons allowed in a renormalizable quantum field theory is considered. The general spin and chirality analysis is based on the threshold behavior of the excitation curves for $\mathcal{P}^+\mathcal{P}^-$ pair production in e^+e^- collisions with longitudinal and transverse polarized beams, the angular distributions in the production process and also the production-decay angular correlations. In the first step, we present the observables in the helicity formalism. Subsequently, we show how a set of observables can be designed for determining the spins and chiral structures of the new particles without any model assumptions. Finally, taking into account a typical set of approximately chiral invariant scenarios, we demonstrate how the spin and chirality effects can be probed experimentally at a high energy e^+e^- collider.

APPENDIX A

FEYNMAN RULES FOR $e^+e^- \to \mathcal{P}^+\mathcal{P}^- \to (\ell^+\mathcal{D}^0)(\ell^-\bar{\mathcal{D}}^0)$

The initial $e^+e^-\mathcal{S}_s^0$ and final $\mathcal{S}_s^0\mathcal{P}^+\mathcal{P}^-$ currents for the s-channel $\mathcal{S}_s^0$ exchange diagram contributing to the process $e^+e^- \to \mathcal{P}^+\mathcal{P}^-$ with $\mathcal{S}_s^0 = S_s^0$ or V_s^0 and $\mathcal{P}^- = S_p^-, F_p^-$ or V_p^- can be parameterized in the following generic form:

$$J_{ee}^{S} \equiv \langle S_s^0 \| e^-(p_-)e^+(p_+)\rangle = e\,\bar{v}(p_+)\,[s_{ee+}^{S}P_+ + s_{ee-}^{S}P_-]\,u(p_-) \tag{A.1}$$

$$J_{ee}^{V\mu} \equiv \langle V_s^0 \| e^-(p_-)e^+(p_+)\rangle^\mu = e\,\bar{v}(p_+)\,[\gamma^\mu\,(s_{ee+}^{V}P_+ + s_{ee-}^{V}P_-)]\,u(p_-) \tag{A.2}$$

$$J_{S}^{SS} \equiv \langle S_p^-(q_-)S_p^+(q_+) \| S_s^0\rangle = 2eM_{S_p}\,s_S^{SS} \tag{A.3}$$

$$J_{V\mu}^{SS} \equiv \langle S_p^-(q_-)S_p^+(q_+) \| V_s^0\rangle_\mu = e\,s_V^{SS}\,(q_- - q_+)_\mu \tag{A.4}$$

$$J_{S}^{FF} \equiv \langle F_p^-(q_-)F_p^+(q_+) \| S_s^0\rangle = e\,\bar{u}(q_-)\,[s_{S+}^{FF}P_+ + s_{S-}^{FF}P_-]\,v(q_+) \tag{A.5}$$

$$J_{V\mu}^{FF} \equiv \langle F_p^-(q_-)F_p^+(q_+) \| V_s^0\rangle_\mu = e\,\bar{u}(q_-)\,[\gamma^\mu(s_{V+}^{FF}P_+ + s_{V-}^{FF}P_-)]\,v(q_+) \tag{A.6}$$

$$J_{S}^{VV} \equiv \langle V_p^-(q_-)V_p^+(q_+) \| S_s^0\rangle = 2eM_{V_p}\,s_S^{VV}\,\epsilon_-^*(q_-)\cdot\epsilon_+^*(q_+) \tag{A.7}$$

$$\begin{aligned} J_{V\mu}^{VV} \equiv \langle V_p^-(q_-)V_p^+(q_+) \| V_s^0\rangle_\mu = -e\,s_V^{VV}\,\big[&(q_- - q_+)^\mu \epsilon_-^*(q_-)\cdot\epsilon_+^*(q_+) \\ &+2q_+\cdot\epsilon_-^*(q_-)\epsilon_+^{*\mu}(q_+) - 2q_-\cdot\epsilon_+^*(q_+)\epsilon_-^{*\mu}(q_-)\big] \end{aligned} \tag{A.8}$$

with the chiral projection operators $P_\pm = \frac{1}{2}(1\pm\gamma_5)$. In the last expression for the triple-vector vertex, the on-shell conditions $q_-\cdot\epsilon_-^*(q_-) = q_+\cdot\epsilon_+^*(q_+) = 0$ are imposed.

The $e\mathcal{P}\mathcal{T}$ interaction vertices $T_{\mathcal{T}}^{e\mathcal{P}}$ for the t-channel neutral $\mathcal{T}^0$-exchange diagrams in the production process $e^+e^- \to \mathcal{P}^+\mathcal{P}^-$ with $\mathcal{P}^\pm = S_p^\pm, F_p^\pm$ or $V_p^\pm$ and $\mathcal{T}^0 = S_t^0, F_t^0, V_t^0$ can be

parameterized as follows:

$$T_F^{eS} \equiv \langle S_p^- | F_t^0 | e^- \rangle = e\,(t_{F+}^{eS}\,P_+ + t_{F-}^{eS}\,P_-) \tag{A.9}$$

$$T_S^{eF} \equiv \langle F_p^- | S_t^0 | e^- \rangle = e\,(t_{S+}^{eF}\,P_+ + t_{S-}^{eF}\,P_-) \tag{A.10}$$

$$T_{V\mu}^{eF} \equiv \langle F_p^- | V_t^0 | e^- \rangle_\mu = e\,\gamma_\mu\,(t_{V+}^{eF}\,P_+ + t_{V-}^{eF}\,P_-) \tag{A.11}$$

$$T_{F\mu}^{eV} \equiv \langle V_p^- | F_t^0 | e^- \rangle_\mu = e\,\gamma_\mu\,(t_{F+}^{eV}\,P_+ + t_{F-}^{eV}\,P_-) \tag{A.12}$$

and the $e\mathcal{P}\mathcal{U}$ interaction vertices $U_{\mathcal{U}}^{e\mathcal{P}}$ for the u-channel doubly-charged $\mathcal{U}^{--}$-exchange diagrams can be parameterized as follows:

$$U_F^{eS} \equiv \langle S_p^+ | F_u^{--} | e^- \rangle = e\,(u_{F+}^{eS}\,P_+ + u_{F-}^{eS}\,P_-) \tag{A.13}$$

$$U_S^{eF} \equiv \langle F_p^+ | S_t^{--} | e^- \rangle = e\,(u_{S+}^{eF}\,P_+ + u_{S-}^{eF}\,P_-) \tag{A.14}$$

$$U_{V\mu}^{eF} \equiv \langle F_p^+ | V_t^{--} | e^- \rangle_\mu = e\,\gamma_\mu\,(u_{V+}^{eF}\,P_+ + u_{V-}^{eF}\,P_-) \tag{A.15}$$

$$U_{F\mu}^{eV} \equiv \langle V_p^+ | F_t^{--} | e^- \rangle_\mu = e\,\gamma_\mu\,(u_{F+}^{eV}\,P_+ + u_{F-}^{eV}\,P_-) \tag{A.16}$$

We note that in the present work, negatively-charged (positively-charged) states are treated as particles (anti-particles), respectively.

The amplitudes for the two-body decay $\mathcal{P}^-(q_-) \to \ell^-(p_1)\bar{\mathcal{D}}^0(p_2)$ and its charge-conjugated process with $\mathcal{P}^- = S_p^-, F_p^-$ or V_p^- and $\bar{\mathcal{D}}^0 = \bar{S}_d^0, \bar{F}_d^0$ or $\bar{V}_d^0$ can be parameterized in general as follows:

$$D_S^{\ell F} \equiv \langle \ell^- \bar{F}_d^0 \| S_p^- \rangle = e\,\bar{u}(p_1)[d_{S+}^{\ell F} P_+ + d_{S-}^{\ell F} P_-]\,v(p_2) \tag{A.17}$$

$$D_F^{\ell S} \equiv \langle \ell^- \bar{S}_d^0 \| F_p^- \rangle = e\,\bar{u}(p_1)[d_{F+}^{\ell S} P_+ + d_{F-}^{\ell S} P_-]\,u(q_-) \tag{A.18}$$

$$D_F^{\ell V} \equiv \langle \ell^- \bar{V}_d^0 \| F_p^- \rangle = e\,\epsilon^{\mu *}(p_2)\bar{u}(p_1)\gamma_\mu\,[d_{F+}^{\ell V} P_+ + d_{F-}^{\ell V} P_-]\,u(q_-) \tag{A.19}$$

$$D_V^{\ell F} \equiv \langle \ell^- \bar{F}_d^0 \| V_p^- \rangle = e\,\bar{u}(p_1)\gamma_\mu\,[d_{V+}^{\ell F} P_+ + d_{V-}^{\ell F} P_-]\,v(p_2)\,\epsilon_-^\mu(q_-) \tag{A.20}$$

where ℓ^- stands for e^- or μ^-, which are treated as massless particles in in our phenomenological spin and chirality analysis at high energy e^+e^- colliders.

APPENDIX B

EXPLICIT FORM OF THE d FUNCTIONS

The explicit form of the Wigner d-functions, $d^{J_0}_{\Delta\sigma,\Delta\lambda}$ with $J_0 = \max(|\Delta\sigma|, |\Delta\lambda|)$, needed in the present work is reproduced below [341].

The single d function with $J_0 = 0$ is constant with $d^0_{0,0} = 1$. The d functions with $J_0 = 1$ appearing both in the production and decay processes are given by

$$\begin{aligned}
d^1_{1,1} &= d^1_{-1,-1} = \frac{1}{2}(1 + \cos\theta) \\
d^1_{1,-1} &= d^1_{-1,1} = \frac{1}{2}(1 - \cos\theta) \\
d^1_{1,0} &= -d^1_{-1,0} = -\sqrt{\frac{1}{2}}\sin\theta \\
d^1_{0,1} &= -d^1_{0,-1} = \sqrt{\frac{1}{2}}\sin\theta \\
d^1_{0,0} &= \cos\theta;
\end{aligned} \tag{B.1}$$

and those with $J_0 = 2$ appearing in the amplitudes for the production of a vector-boson pair due to t-channel fermion exchange in e^+e^- collisions read

$$\begin{aligned}
d^2_{1,2} &= -d^2_{-1,-2} = \frac{1}{2}(1 + \cos\theta)\sin\theta \\
d^2_{1,-2} &= -d^2_{-1,2} = -\frac{1}{2}(1 - \cos\theta)\sin\theta
\end{aligned} \tag{B.2}$$

The d functions with $J_0 = 1/2$ appear only in the decay processes and they are given by

$$\begin{aligned}
d^{1/2}_{1/2,1/2} &= d^{1/2}_{-1/2,-1/2} = \cos\frac{\theta}{2} \\
d^{1/2}_{1/2,-1/2} &= -d^{1/2}_{-1/2,1/2} = -\sin\frac{\theta}{2};
\end{aligned} \tag{B.3}$$

We note that the convention of Rose is adopted for the d function.

APPENDIX C

ARBITRARY POLARIZED BEAMS

The expression for the matrix element-squared for arbitrary polarized beams is obtained as follows [336, 337]. We denote the transverse polarization directions $\hat{s}_\pm$ of the $e^\pm$ beams as

$$\hat{s}_\pm = (\cos\varphi_\pm, \sin\varphi_\pm, 0) \tag{C.1}$$

where the azimuthal angles in the x-y plane are measured from the x-axis defined by the outgoing $\mathcal{P}^-$ transverse momentum in the production process $e^+e^- \to \mathcal{P}^+\mathcal{P}^-$. We can then express the $e^\pm$ spin vectors as

$$s^\mu_\pm = P^T_\pm\,(0, \hat{s}_\pm) + P^L_\pm\,(|\vec{p}_\pm|,\, E_\pm\hat{p}_\pm)/m_e \tag{C.2}$$

The beam polarizations are limited by $0 \le P^T_\pm \le \sqrt{1-(P^L_\pm)^2}$ with $-1 \le P^L_\pm \le 1$. Purely left-handed $e^\pm$ beams give $P^L_\pm = -1$ and purely right-handed $e^\pm$ beams give $P^L_\pm = +1$. While natural transverse polarization of the e^+e^- circular storage ring colliders gives $\varphi_+ = \varphi_- + \pi$, arbitrary polarized beams are expected to be available at e^+e^- linear colliders.

We can now obtain the matrix element-squared for the production process $e^+e^- \to \mathcal{P}^+\mathcal{P}^-$ combined with the subsequential $\mathcal{P}^\pm$ decays with arbitrary polarized e^+e^- beams summed over the $\mathcal{P}^\pm$ polarizations and final-state polarizations, by choosing the transverse spin directions as

$$\varphi_- = -\varphi \quad \text{and} \quad \varphi_+ = -\varphi + \delta \tag{C.3}$$

where φ is the azimuthal angle of the $\mathcal{P}^-$ as measured from the electron transverse momentum direction, and δ is the relative opening angle of the electron and positron transverse polarizations. Introducing the abbreviated notation $\mathcal{T}(\sigma_-,\sigma_+)$ for the correlated production-decay helicity amplitude with the implicit assumption that the (averaged) summation over the intermediate- and final-state polarizations will be done, we find for the polarization-weighted distribution

$$\begin{aligned}
\Sigma_{\rm pol}^{\mathcal{P}} &= \sum_{\sigma_-,\sigma'_-}\sum_{\sigma_+,\sigma'_+} P^-_{\sigma_-\sigma'_-} P^+_{\sigma_+\sigma'_+}\,\mathcal{T}(\sigma_-,\sigma_+)\,\mathcal{T}^*(\sigma'_-,\sigma'_+) \\
&= \tfrac{1}{4}\,[(1-P_-^LP_+^L)(Q_{+-}^{+-}+Q_{-+}^{-+})+(P_-^L-P_+^L)(Q_{+-}^{+-}-Q_{-+}^{-+}) \\
&\quad +(1+P_-^LP_+^L)(Q_{++}^{++}+Q_{--}^{--})+(P_-^L+P_+^L)(Q_{++}^{++}-Q_{--}^{--}) \\
&\quad +2P_-^TP_+^T\cos(2\varphi-\delta)\,{\rm Re}(Q_{-+}^{+-})+2P_-^TP_+^T\sin(2\varphi-\delta)\,{\rm Im}(Q_{-+}^{+-}) \\
&\quad +2P_-^TP_+^T\cos\delta\,{\rm Re}(Q_{--}^{++})-2P_-^TP_+^T\sin\delta\,{\rm Im}(Q_{--}^{++}) \\
&\quad +2P_-^T(1-P_+^L)\cos\varphi\,{\rm Re}(Q_{--}^{+-})+2P_-^T(1+P_+^L)\cos\varphi\,{\rm Re}(Q_{-+}^{++}) \\
&\quad +2(1+P_-^L)P_+^T\cos(\varphi-\delta)\,{\rm Re}(Q_{++}^{+-})+2(1-P_-^L)P_+^T\cos(\varphi-\delta)\,{\rm Re}(Q_{-+}^{--}) \\
&\quad +2P_-^T(1-P_+^L)\sin\varphi\,{\rm Im}(Q_{--}^{+-})+2P_-^T(1+P_+^L)\sin\varphi\,{\rm Im}(Q_{-+}^{++}) \\
&\quad +2(1+P_-^L)P_+^T\sin(\varphi-\delta)\,{\rm Im}(Q_{++}^{+-})+2(1-P_-^L)P_+^T\sin(\varphi-\delta)\,{\rm Im}(Q_{-+}^{--})] \qquad \text{(C.4)}
\end{aligned}$$

where the electron and positron polarization matrices $P^{\mp}$ and the tensor $Q^{\sigma'_-\sigma'_+}_{\sigma_-\sigma_+}$ are given by

$$P^{\mp}_{\sigma_\mp\sigma'_\mp} = \frac{1}{2}\begin{pmatrix} 1+P_\mp^L & P_\mp^T e^{-i\phi_\mp} \\ P_\mp^T e^{i\phi_\mp} & 1-P_\mp^L \end{pmatrix} \qquad \text{(C.5)}$$

$$Q^{\sigma'_-\sigma'_+}_{\sigma_-\sigma_+} = \mathcal{T}(\sigma_-,\sigma_+)\mathcal{T}^*(\sigma'_-,\sigma'_+) \qquad \text{(C.6)}$$

with the summation over the intermediate and final-state polarizations implicitly assumed when the elements of the tensor Q are evaluated. Taking the average of the polarization-weighted distribution (C.4) over the azimuthal angle φ, we obtain

$$\begin{aligned}
\overline{\Sigma}_{\rm pol}^{\mathcal{P}} &\equiv \int_0^{2\pi}\frac{d\varphi}{2\pi}\,\Sigma_{\rm pol} \\
&= \tfrac{1}{4}\,[(1-P_-^LP_+^L)(Q_{+-}^{+-}+Q_{-+}^{-+})+(P_-^L-P_+^L)(Q_{+-}^{+-}-Q_{-+}^{-+}) \\
&\quad +(1+P_-^LP_+^L)(Q_{++}^{++}+Q_{--}^{--})+(P_-^L+P_+^L)(Q_{++}^{++}-Q_{--}^{--}) \\
&\quad +2P_-^TP_+^T\cos\delta\,{\rm Re}(Q_{--}^{++})-2P_-^TP_+^T\sin\delta\,{\rm Im}(Q_{--}^{++})] \qquad \text{(C.7)}
\end{aligned}$$

The last two terms are the only effect of transverse polarization to the azimuthally integrated cross section.

APPENDIX D

KINEMATICS OF THE ANTLER-TOPOLOGY PROCESS

When the particles, $\mathcal{D}^0$ and $\bar{\mathcal{D}}^0$, escape detection in the correlated production-decay antler-topology process $e^+e^- \to \mathcal{P}^+\mathcal{P}^- \to (\ell^+\mathcal{D}^0)(\ell^-\bar{\mathcal{D}}^0)$ this process is observed experimentally as

$$e^- + e^+ \to \ell^- + \ell^+ + \text{missing energy-momentum} \tag{D.1}$$

where the final lepton pair $\ell^-\ell^+$ can be either one of e^-e^+ or $\mu^-\mu^+$, if each lepton number is strictly preserved in the underlying theory.

As will be explicitly shown below, if the masses, $M_{\mathcal{P}}$ and $M_{\mathcal{D}}$, of the on-shell particles, $\mathcal{P}^\pm$ and $\mathcal{D}^0$ are a priori known, the unobserved $\mathcal{D}^0$ and $\bar{\mathcal{D}}^0$ momenta can be determined from the observed lepton momenta up to a twofold discrete ambiguity, in the limit where the $\mathcal{P}$ width and photon radiation are neglected. In general, the kinematics of the process is determined by six angles, two for the scattering, and two each for the $\mathcal{P}$ decays. Since we observe the two three-momenta of two leptons, we have in general sufficient kinematic relations for fixing the whole configuration. A twofold discrete ambiguity occurs, however, because the solution involves a quadratic equation.

As the $\mathcal{P}^\mp$ energy is fixed to be half of the beam energy, i.e. $E_{\mathcal{P}} = \sqrt{s}/2$ in the e^+e^- c.m. frame, the boost factor γ linking the c.m. frame to each of the $\mathcal{P}^\pm$ rest frames is

$$\gamma = \frac{\sqrt{s}}{2M_{\mathcal{P}}} \quad \text{and} \quad \beta = \sqrt{1 - \frac{4M_{\mathcal{P}}^2}{s}} \tag{D.2}$$

with the boost speed $\beta = \sqrt{1 - 1/\gamma^2}$. In addition, the energies of the invisible particles in the two-body decays, $\mathcal{P}^- \to \ell^- \bar{\mathcal{D}}^0$ and $\mathcal{P}^+ \to \ell^+ \mathcal{D}^0$, are uniquely determined by measuring the lepton energies due to energy conservation:

$$E_2 = \frac{\sqrt{s}}{2} - E_1 \quad \text{and} \quad E_4 = \frac{\sqrt{s}}{2} - E_3 \tag{D.3}$$

with $E_1 = E_{\ell^-}$ and $E_3 = E_{\ell^+}$ in the laboratory frame.

As the particles, $\mathcal{D}^0$ and $\bar{\mathcal{D}}^0$, with an identical mass $M_{\mathcal{D}}$, are involved in the two charge-conjugate two-body decays, the energies of the two leptons $\ell^\pm$ are identical in the $\mathcal{P}^\pm$ rest frame:

$$E^*_\ell = \frac{M^2_{\mathcal{P}} - M^2_{\mathcal{D}}}{2M_{\mathcal{P}}} \tag{D.4}$$

Then, we can determine the decay lepton polar-angle $\theta_\pm$ in each of the $\mathcal{P}$ rest frame with respect to the $\mathcal{P}^\pm$ momentum direction depicted in Fig. 6.1 uniquely event by event by measuring the lepton energy $E_{\ell^\pm}$ in the laboratory frame through the relation

$$\cos\theta_\pm = \frac{1}{\beta}\left(\frac{4M^2_{\mathcal{P}}}{M^2_{\mathcal{P}} - M^2_{\mathcal{D}}}\frac{E_{\ell^\pm}}{\sqrt{s}} - 1\right) \tag{D.5}$$

when the lepton mass is ignored. Furthermore, the relative orientation of the momentum vector of $\ell^\pm$ and $\mathcal{P}^\pm$ is fixed by the two-body decay kinematics:

$$\cos\alpha_\pm = \frac{1}{\beta}\left(1 - \frac{M^2_{\mathcal{P}} - M^2_{\mathcal{D}}}{\sqrt{s}E_{\ell^\pm}}\right) \tag{D.6}$$

where the angles $\alpha_\pm$ are the opening angles between the visible $\ell^\pm$ tracks and the parent $\mathcal{P}^\pm$ momentum directions.

In order to prove the existence of a twofold discrete ambiguity in determining the production angle θ, it is sufficient to solve for the $\mathcal{P}^-$ momentum direction denoted by a unit vector $\hat{n}_{\mathcal{P}} \equiv \hat{q}_- = -\hat{q}_+$. Let us assume, for the moment, that the two lepton three-momentum directions, denoted by $\hat{n}_\pm$, are not parallel. Then we can expand the unit vector $\hat{n}_{\mathcal{P}}$ in terms of the unit vectors $\hat{n}_\pm$

$$\hat{n}_{\mathcal{P}} = a\hat{n}_- + b\hat{n}_+ + c(\hat{n}_- \times \hat{n}_+) \tag{D.7}$$

As shown in Eq. (D.6), the projections of the unit vector along the lepton momentum directions $\hat{n}_\pm$ satisfy

$$\hat{n}_- \cdot \hat{n}_\mathcal{P} = \cos\alpha_- \tag{D.8}$$

$$\hat{n}_+ \cdot \hat{n}_\mathcal{P} = -\cos\alpha_+ \tag{D.9}$$

These two relations constrain $\hat{n}_\mathcal{P}$ to lie on a line in three-dimensional space. They give

$$\begin{aligned} a + b(\hat{n}_- \cdot \hat{n}_+) &= \quad \cos\alpha_- \\ a(\hat{n}_- \cdot \hat{n}_+) + b &= -\cos\alpha_+ \end{aligned} \tag{D.10}$$

which can be explicitly solved:

$$\begin{pmatrix} a \\ b \end{pmatrix} = \frac{1}{(\hat{n}_- \times \hat{n}_+)^2} \begin{pmatrix} 1 & -\hat{n}_- \cdot \hat{n}_+ \\ -\hat{n}_- \cdot \hat{n}_+ & 1 \end{pmatrix} \begin{pmatrix} \cos\alpha_- \\ -\cos\alpha_+ \end{pmatrix} \tag{D.11}$$

The remaining variable is determined by the condition that the vector $\hat{n}_\mathcal{P}$ is a unit vector, i.e. $\hat{n}_\mathcal{P}^2 = 1$:

$$c^2 = \frac{(\hat{n}_- \times \hat{n}_+)^2 - (\cos\alpha_- \hat{n}_- + \cos\alpha_+ \hat{n}_+)^2}{(\hat{n}_- \times \hat{n}_+)^4} \tag{D.12}$$

The sign of c cannot be determined. This explicitly shows the twofold discrete ambiguity mentioned before. The inequality $c^2 \geq 0$ is expected to be violated only by finite $\mathcal{P}$-width effects and by radiative corrections, and hence may serve as a test of the $\mathcal{P}$-pair signal. Introducing the vector $\vec{a} = \cos\alpha_- \hat{n}_- + \cos\alpha_+ \hat{n}_+$, we can rewrite the unit vector $\hat{n}_\mathcal{P}$ as

$$\hat{n}_\mathcal{P} = \frac{1}{(\hat{n}_- \times \hat{n}_+)^2} \left[(\hat{n}_- \cdot \vec{a})\, \hat{n}_- - (\hat{n}_+ \cdot \vec{a})\, \hat{n}_+ \pm \sqrt{(\hat{n}_- \times \hat{n}_+)^2 - \vec{a}^2}\ (\hat{n}_- \times \hat{n}_+) \right] \tag{D.13}$$

determined up to a sign ambiguity.

In the exceptional case where the two lepton momenta are parallel, we obtain a one-parameter family of solution for which the azimuthal angle between two decay planes is left undetermined.

Let us now consider the azimuthal-angle correlations of the decay kinematics. In the coordinate system with the z-axis along the $\mathcal{P}$-momentum direction, the unit vectors denoting the $\ell^{\mp}$ four-momentum directions can be expressed as follows:

$$\vec{n}_- = E_{\ell^-} \left(\sin\alpha_- \cos\phi_-, \sin\alpha_- \sin\phi_-, \cos\alpha_-\right) \tag{D.14}$$

$$\vec{n}_+ = \left(\sin\alpha_+ \cos\phi_+, \sin\alpha_+ \cos\phi_+, -\cos\alpha_+\right). \tag{D.15}$$

Taking the scalar product between the unit vectors:

$$\hat{n}_- \cdot \hat{n}_+ = \sin\alpha_- \sin\alpha_+ \left(\cos\phi_- \cos\phi_+ + \sin\phi_- \sin\phi_+\right) - \cos\alpha_- \cos\alpha_+ \tag{D.16}$$

and noting that $\cos\phi_+ \cos\phi_- + \sin\phi_+ \sin\phi_- = \cos(\phi_+ - \phi_-)$, we can check that the cosine of the difference $\phi = \phi_+ - \phi_-$ of two azimuthal angles

$$\cos\phi = \frac{\hat{n}_- \cdot \hat{n}_+ + \cos\alpha_- \cos\alpha_+}{\sin\alpha_- \sin\alpha_+} \tag{D.17}$$

can be determined uniquely event by event in the correlated antler-topology process. However, we cannot determine the sign of $\sin\phi$, of which the expression

$$\sin\phi = \frac{(\hat{n}_- \times \hat{n}_+) \cdot \hat{n}_{\mathcal{P}}}{\sin\alpha_- \sin\alpha_+} = \pm \frac{\sqrt{(\hat{n}_- \times \hat{n}_+)^2 - \vec{a}^2}}{\sin\alpha_- \sin\alpha_+} \tag{D.18}$$

has a sign ambiguity due to the twofold ambiguity in determining the momentum direction $\hat{n}_{\mathcal{P}}$.

BIBLIOGRAPHY

[1] Georges Aad et al. Observation of a new particle in the search for the Standard Model Higgs boson with the ATLAS detector at the LHC. *Phys. Lett.*, B716:1–29, 2012.

[2] Serguei Chatrchyan et al. Observation of a new boson at a mass of 125 GeV with the CMS experiment at the LHC. *Phys. Lett.*, B716:30–61, 2012.

[3] Georges Aad et al. Measurements of the Higgs boson production and decay rates and constraints on its couplings from a combined ATLAS and CMS analysis of the LHC pp collision data at $\sqrt{s} = 7$ and 8 TeV. *JHEP*, 08:045, 2016.

[4] M. Aaboud et al. Observation of Higgs boson production in association with a top quark pair at the LHC with the ATLAS detector. *Phys. Lett.*, B784:173–191, 2018.

[5] Albert M Sirunyan et al. Observation of $t\bar{t}H$ production. *Phys. Rev. Lett.*, 120(23):231801, 2018.

[6] Morad Aaboud et al. Observation of $H \to b\bar{b}$ decays and VH production with the ATLAS detector. *Phys. Lett.*, B786:59–86, 2018.

[7] A. M. Sirunyan et al. Observation of Higgs boson decay to bottom quarks. *Phys. Rev. Lett.*, 121(12):121801, 2018.

[8] Morad Aaboud et al. Cross-section measurements of the Higgs boson decaying into a pair of τ-leptons in proton-proton collisions at $\sqrt{s} = 13$ TeV with the ATLAS detector. 2018.

[9] Albert M Sirunyan et al. Observation of the Higgs boson decay to a pair of τ leptons with the CMS detector. *Phys. Lett.*, B779:283–316, 2018.

[10] Projections for measurements of Higgs boson signal strengths and coupling parameters with the ATLAS detector at a HL-LHC. Technical Report ATL-PHYS-PUB-2014-016, CERN, Geneva, Oct 2014.

[11] Albert M Sirunyan et al. Inclusive search for a highly boosted Higgs boson decaying to a bottom quark-antiquark pair. *Phys. Rev. Lett.*, 120(7):071802, 2018.

[12] Search for boosted resonances decaying to two b-quarks and produced in association with a jet at $\sqrt{s} = 13$ TeV with the ATLAS detector. Technical Report ATLAS-CONF-2018-052, CERN, Geneva, Nov 2018.

[13] G. C. Branco, P. M. Ferreira, L. Lavoura, M. N. Rebelo, Marc Sher, and Joao P. Silva. Theory and phenomenology of two-Higgs-doublet models. *Phys. Rept.*, 516:1–102, 2012.

[14] Tao Han and Bob McElrath. h to $\mu^+\mu^-$ via gluon fusion at the LHC. *Phys. Lett.*, B528:81–85, 2002.

[15] Tilman Plehn and David L. Rainwater. Higgs Decays to Muons in Weak Boson Fusion. *Phys. Lett.*, B520:108–114, 2001.

[16] Morad Aaboud et al. Search for the dimuon decay of the Higgs boson in pp collisions at $\sqrt{s} = 13$ TeV with the ATLAS detector. *Phys. Rev. Lett.*, 119(5):051802, 2017.

[17] Albert M. Sirunyan et al. Search for the Higgs boson decaying to two muons in proton-proton collisions at $\sqrt{s} = 13$ TeV. *Submitted to: Phys. Rev. Lett.*, 2018.

[18] Prospects for the measurement of the rare Higgs boson decay $H \to \mu\mu$ with 3000 fb^{-1} of pp collisions collected at $\sqrt{s} = 14$ TeV by the ATLAS experiment. Technical Report ATL-PHYS-PUB-2018-006, CERN, Geneva, May 2018.

[19] A. M. Sirunyan et al. Identification of heavy-flavour jets with the CMS detector in pp collisions at 13 TeV. *JINST*, 13(05):P05011, 2018.

[20] Performance and Calibration of the JetFitterCharm Algorithm for c-Jet Identification. Technical Report ATL-PHYS-PUB-2015-001, CERN, Geneva, Jan 2015.

[21] M. Aaboud et al. Search for the Decay of the Higgs Boson to Charm Quarks with the ATLAS Experiment. *Phys. Rev. Lett.*, 120(21):211802, 2018.

[22] J. Duarte-Campderros, G. Perez, M. Schlaffer, and A. Soffer. Probing the strange Higgs coupling at lepton colliders using light-jet flavor tagging. 2018.

[23] Y. Nakai, D. Shih, and S. Thomas. Deep Learning Strange Jets. *https://indico.cern.ch/event/745718/contributions/3174401/attachments/1753217/2841520/StrangeTagV5.pdf*, 2018.

[24] J. Wess and B. Zumino. Supergauge Transformations in Four-Dimensions. *Nucl. Phys.*, B70:39–50, 1974. [,24(1974)].

[25] Hans Peter Nilles. Supersymmetry, Supergravity and Particle Physics. *Phys. Rept.*, 110:1–162, 1984.

[26] Howard E. Haber and Gordon L. Kane. The Search for Supersymmetry: Probing Physics Beyond the Standard Model. *Phys. Rept.*, 117:75–263, 1985.

[27] D. J. H. Chung, L. L. Everett, G. L. Kane, S. F. King, Joseph D. Lykken, and Lian-Tao Wang. The Soft supersymmetry breaking Lagrangian: Theory and applications. *Phys. Rept.*, 407:1–203, 2005.

[28] Marvin Weinstein. CONSERVED CURRENTS, THEIR COMMUTATORS AND THE SYMMETRY STRUCTURE OF RENORMALIZABLE THEORIES OF ELECTROMAGNETIC, WEAK AND STRONG INTERACTIONS. *Phys. Rev.*, D8:2511, 1973.

[29] Steven Weinberg. Implications of Dynamical Symmetry Breaking. *Phys. Rev.*, D13:974–996, 1976. [Addendum: Phys. Rev.D19,1277(1979)].

[30] Leonard Susskind. Dynamics of Spontaneous Symmetry Breaking in the Weinberg-Salam Theory. *Phys. Rev.*, D20:2619–2625, 1979.

[31] Nima Arkani-Hamed, Savas Dimopoulos, and G. R. Dvali. Phenomenology, astrophysics and cosmology of theories with submillimeter dimensions and TeV scale quantum gravity. *Phys. Rev.*, D59:086004, 1999.

[32] Lisa Randall and Raman Sundrum. A Large mass hierarchy from a small extra dimension. *Phys. Rev. Lett.*, 83:3370–3373, 1999.

[33] Thomas Appelquist, Hsin-Chia Cheng, and Bogdan A. Dobrescu. Bounds on universal extra dimensions. *Phys. Rev.*, D64:035002, 2001.

[34] Nima Arkani-Hamed, Andrew G. Cohen, and Howard Georgi. Electroweak symmetry breaking from dimensional deconstruction. *Phys. Lett.*, B513:232–240, 2001.

[35] Csaba Csaki, Christophe Grojean, Hitoshi Murayama, Luigi Pilo, and John Terning. Gauge theories on an interval: Unitarity without a Higgs. *Phys. Rev.*, D69:055006, 2004.

[36] Csaba Csaki, Christophe Grojean, Luigi Pilo, and John Terning. Towards a realistic model of Higgsless electroweak symmetry breaking. *Phys. Rev. Lett.*, 92:101802, 2004.

[37] K. Griest and M. Kamionkowski. Supersymmetric dark matter. *Phys. Rept.*, 333:167–182, 2000.

[38] Gianfranco Bertone, Dan Hooper, and Joseph Silk. Particle dark matter: Evidence, candidates and constraints. *Phys. Rept.*, 405:279–390, 2005.

[39] P. A. R. Ade et al. Planck 2013 results. XVI. Cosmological parameters. *Astron. Astrophys.*, 571:A16, 2014.

[40] Gerard Jungman, Marc Kamionkowski, and Kim Griest. Supersymmetric dark matter. *Phys. Rept.*, 267:195–373, 1996.

[41] Eugene P. Wigner. On Unitary Representations of the Inhomogeneous Lorentz Group. *Annals Math.*, 40:149–204, 1939. [Reprint: Nucl. Phys. Proc. Suppl.6,9(1989)].

[42] C. G. Lester and D. J. Summers. Measuring masses of semiinvisibly decaying particles pair produced at hadron colliders. *Phys. Lett.*, B463:99–103, 1999.

[43] Alan Barr, Christopher Lester, and P. Stephens. m(T2): The Truth behind the glamour. *J. Phys.*, G29:2343–2363, 2003.

[44] Won Sang Cho, Kiwoon Choi, Yeong Gyun Kim, and Chan Beom Park. Gluino Stransverse Mass. *Phys. Rev. Lett.*, 100:171801, 2008.

[45] Alan J. Barr, Ben Gripaios, and Christopher G. Lester. Weighing Wimps with Kinks at Colliders: Invisible Particle Mass Measurements from Endpoints. *JHEP*, 02:014, 2008.

[46] Won Sang Cho, Kiwoon Choi, Yeong Gyun Kim, and Chan Beom Park. Measuring superparticle masses at hadron collider using the transverse mass kink. *JHEP*, 02:035, 2008.

[47] Daniel R. Tovey. On measuring the masses of pair-produced semi-invisibly decaying particles at hadron colliders. *JHEP*, 04:034, 2008.

[48] Hsin-Chia Cheng and Zhenyu Han. Minimal Kinematic Constraints and m(T2). *JHEP*, 12:063, 2008.

[49] Alan J. Barr, Ben Gripaios, and Christopher G. Lester. Transverse masses and kinematic constraints: from the boundary to the crease. *JHEP*, 11:096, 2009.

[50] Konstantin T. Matchev and Myeonghun Park. A General method for determining the masses of semi-invisibly decaying particles at hadron colliders. *Phys. Rev. Lett.*, 107:061801, 2011.

[51] Giacomo Polesello and Daniel R. Tovey. Supersymmetric particle mass measurement with the boost-corrected contransverse mass. *JHEP*, 03:030, 2010.

[52] Partha Konar, Kyoungchul Kong, Konstantin T. Matchev, and Myeonghun Park. Superpartner Mass Measurement Technique using 1D Orthogonal Decompositions of the Cambridge Transverse Mass Variable M_{T2}. *Phys. Rev. Lett.*, 105:051802, 2010.

[53] Timothy Cohen, Eric Kuflik, and Kathryn M. Zurek. Extracting the Dark Matter Mass from Single Stage Cascade Decays at the LHC. *JHEP*, 11:008, 2010.

[54] Johan Alwall, Ayres Freitas, and Olivier Mattelaer. Measuring Sparticles with the Matrix Element. *AIP Conf. Proc.*, 1200(1):442–445, 2010.

[55] Pierre Artoisenet, Vincent Lemaitre, Fabio Maltoni, and Olivier Mattelaer. Automation of the matrix element reweighting method. *JHEP*, 12:068, 2010.

[56] J. Alwall, A. Freitas, and O. Mattelaer. The Matrix Element Method and QCD Radiation. *Phys. Rev.*, D83:074010, 2011.

[57] Tao Han, Ian-Woo Kim, and Jeonghyeon Song. Kinematic Cusps: Determining the Missing Particle Mass at Colliders. *Phys. Lett.*, B693:575–579, 2010.

[58] Tao Han, Ian-Woo Kim, and Jeonghyeon Song. Kinematic Cusps With Two Missing Particles I: Antler Decay Topology. *Phys. Rev.*, D87(3):035003, 2013.

[59] Tao Han, Ian-Woo Kim, and Jeonghyeon Song. Kinematic Cusps with Two Missing Particles II: Cascade Decay Topology. *Phys. Rev.*, D87(3):035004, 2013.

[60] Abhaya Kumar Swain and Partha Konar. Constrained $\sqrt{\hat{S}_{min}}$ and reconstructing with semi-invisible production at hadron colliders. *JHEP*, 03:142, 2015.

[61] A. J. Barr. Determining the spin of supersymmetric particles at the LHC using lepton charge asymmetry. *Phys. Lett.*, B596:205–212, 2004.

[62] Jennifer M. Smillie and Bryan R. Webber. Distinguishing spins in supersymmetric and universal extra dimension models at the large hadron collider. *JHEP*, 10:069, 2005.

[63] AseshKrishna Datta, Kyoungchul Kong, and Konstantin T. Matchev. Discrimination of supersymmetry and universal extra dimensions at hadron colliders. *Phys. Rev.*, D72:096006, 2005. [Erratum: Phys. Rev.D72,119901(2005)].

[64] A. J. Barr. Measuring slepton spin at the LHC. *JHEP*, 02:042, 2006.

[65] Patrick Meade and Matthew Reece. Top partners at the LHC: Spin and mass measurement. *Phys. Rev.*, D74:015010, 2006.

[66] Alexandre Alves, Oscar Eboli, and Tilman Plehn. It's a gluino. *Phys. Rev.*, D74:095010, 2006.

[67] Christiana Athanasiou, Christopher G. Lester, Jennifer M. Smillie, and Bryan R. Webber. Distinguishing Spins in Decay Chains at the Large Hadron Collider. *JHEP*, 08:055, 2006.

[68] Lian-Tao Wang and Itay Yavin. Spin measurements in cascade decays at the LHC. *JHEP*, 04:032, 2007.

[69] Jennifer M. Smillie. Spin correlations in decay chains involving W bosons. *Eur. Phys. J.*, C51:933–943, 2007.

[70] S. Y. Choi, Kaoru Hagiwara, Y. G. Kim, K. Mawatari, and P. M. Zerwas. tau polarization in SUSY cascade secays. *Phys. Lett.*, B648:207–212, 2007.

[71] Can Kilic, Lian-Tao Wang, and Itay Yavin. On the existence of angular correlations in decays with heavy matter partners. *JHEP*, 05:052, 2007.

[72] Alexandre Alves and Oscar Eboli. Unravelling the sbottom spin at the CERN LHC. *Phys. Rev.*, D75:115013, 2007.

[73] Csaba Csaki, Johannes Heinonen, and Maxim Perelstein. Testing gluino spin with three-body decays. *JHEP*, 10:107, 2007.

[74] Lian-Tao Wang and Itay Yavin. A Review of Spin Determination at the LHC. *Int. J. Mod. Phys.*, A23:4647–4668, 2008. [,205(2008)].

[75] Michael Burns, Kyoungchul Kong, Konstantin T. Matchev, and Myeonghun Park. A General Method for Model-Independent Measurements of Particle Spins, Couplings and Mixing Angles in Cascade Decays with Missing Energy at Hadron Colliders. *JHEP*, 10:081, 2008.

[76] Won Sang Cho, Kiwoon Choi, Yeong Gyun Kim, and Chan Beom Park. M(T2)-assisted on-shell reconstruction of missing momenta and its application to spin measurement at the LHC. *Phys. Rev.*, D79:031701, 2009.

[77] Oram Gedalia, Seung J. Lee, and Gilad Perez. Spin Determination via Third Generation Cascade Decays. *Phys. Rev.*, D80:035012, 2009.

[78] Wolfgang Ehrenfeld, Ayres Freitas, Ananda Landwehr, and Daniel Wyler. Distinguishing spins in decay chains with photons at the Large Hadron Collider. *JHEP*, 07:056, 2009.

[79] Lisa Edelhauser, Werner Porod, and Ritesh K. Singh. Spin Discrimination in Three-Body Decays. *JHEP*, 08:053, 2010.

[80] Dean Horton. Reconstructing events with missing transverse momentum at the LHC and its application to spin measurement. 2010.

[81] Hsin-Chia Cheng, Zhenyu Han, Ian-Woo Kim, and Lian-Tao Wang. Missing Momentum Reconstruction and Spin Measurements at Hadron Colliders. *JHEP*, 11:122, 2010.

[82] Matthew R. Buckley and Michael J. Ramsey-Musolf. Diagnosing Spin at the LHC via Vector Boson Fusion. *JHEP*, 09:094, 2011.

[83] Chien-Yi Chen and A. Freitas. General analysis of signals with two leptons and missing energy at the Large Hadron Collider. *JHEP*, 02:002, 2011.

[84] Chien-Yi Chen and A. Freitas. General analysis of decay chains with three-body decays involving missing energy. *JHEP*, 01:124, 2012.

[85] Mihoko M. Nojiri and Jing Shu. Two jets and missing E_T signature to determine the spins of the new particles. *JHEP*, 06:047, 2011.

[86] Gudrid Moortgat-Pick, Krzysztof Rolbiecki, and Jamie Tattersall. Early spin determination at the LHC? *Phys. Lett.*, B699:158–163, 2011.

[87] Ties Behnke, James E. Brau, Brian Foster, Juan Fuster, Mike Harrison, James McEwan Paterson, Michael Peskin, Marcel Stanitzki, Nicholas Walker, and Hitoshi Yamamoto.

The International Linear Collider Technical Design Report - Volume 1: Executive Summary. 2013.

[88] Howard Baer, Tim Barklow, Keisuke Fujii, Yuanning Gao, Andre Hoang, Shinya Kanemura, Jenny List, Heather E. Logan, Andrei Nomerotski, Maxim Perelstein, et al. The International Linear Collider Technical Design Report - Volume 2: Physics. 2013.

[89] Halina Abramowicz et al. The International Linear Collider Technical Design Report - Volume 4: Detectors. 2013.

[90] M. Koratzinos, A. P. Blondel, R. Aleksan, P. Janot, F. Zimmermann, J. R. Ellis, and M. Zanetti. TLEP, first step in a long-term vision for HEP. In *Snowmass 2013: Lepton Collider Workshop Cambridge, MA, USA, April 10-11, 2013*, 2013.

[91] M. Bicer et al. First Look at the Physics Case of TLEP. *JHEP*, 01:164, 2014.

[92] E. Accomando et al. Physics at the CLIC multi-TeV linear collider. In *Proceedings, 11th International Conference on Hadron spectroscopy (Hadron 2005): Rio de Janeiro, Brazil, August 21-26, 2005*, 2004.

[93] Lucie Linssen, Akiya Miyamoto, Marcel Stanitzki, and Harry Weerts. Physics and Detectors at CLIC: CLIC Conceptual Design Report. 2012.

[94] Seong Youl Choi, Neil D. Christensen, Daniel Salmon, and Xing Wang. Spin and chirality effects in antler-topology processes at high energy e^+e^- colliders. *Eur. Phys. J.*, C75(10):481, 2015.

[95] Seong Youl Choi, Tao Han, Jan Kalinowski, Krzysztof Rolbiecki, and Xing Wang. Characterizing invisible electroweak particles through single-photon processes at high energy e^+e^- colliders. *Phys. Rev.*, D92(9):095006, 2015.

[96] Tao Han and Xing Wang. Radiative Decays of the Higgs Boson to a Pair of Fermions. *JHEP*, 10:036, 2017.

[97] Tao Han, Satyanarayan Mukhopadhyay, and Xing Wang. Electroweak Dark Matter at Future Hadron Colliders. *Phys. Rev.*, D98(3):035026, 2018.

[98] Tao Han, Hongkai Liu, Satyanarayan Mukhopadhyay, and Xing Wang. Dark Matter Blind Spots at One-Loop. *JHEP*, 03:080, 2019.

[99] Tao Han, Benjamin Nachman, and Xing Wang. Charm-quark Yukawa Coupling in $h \to c\bar{c}\gamma$ at LHC. *Phys. Lett.*, B793:90–96, 2019.

[100] Ali Abbasabadi, David Bowser-Chao, Duane A. Dicus, and Wayne W. Repko. Radiative Higgs boson decays H $\to$ fermion anti-fermion gamma. *Phys. Rev.*, D55:5647–5656, 1997.

[101] Cong-Sheng Li, Cong-Feng Qiao, and Shou-Hua Zhu. Radiative Higgs boson decays H $\to$ f anti-f gamma beyond the standard model. *Phys. Rev.*, D57:6928–6933, 1998.

[102] Abdesslam Arhrib, Rachid Benbrik, and Tzu-Chiang Yuan. Associated Production of Higgs at Linear Collider in the Inert Higgs Doublet Model. *Eur. Phys. J.*, C74:2892, 2014.

[103] Song Lin Hu, Ning Liu, Jie Ren, and Lei Wu. Revisiting Associated Production of 125 GeV Higgs Boson with a Photon at a Higgs Factory. *J. Phys.*, G41(12):125004, 2014.

[104] Genevieve Belanger, Vincent Bizouard, and Guillaume Chalons. Boosting Higgs boson decays into gamma and a Z in the NMSSM. *Phys. Rev.*, D89(9):095023, 2014.

[105] Abdelhak Djouadi. The Anatomy of electro-weak symmetry breaking. I: The Higgs boson in the standard model. *Phys. Rept.*, 457:1–216, 2008.

[106] P. A. Baikov, K. G. Chetyrkin, and Johann H. Kuhn. Scalar correlator at O(α_s^4), Higgs decay into b-quarks and bounds on the light quark masses. *Phys. Rev. Lett.*, 96:012003, 2006.

[107] Joshua Davies, Matthias Steinhauser, and David Wellmann. Completing the hadronic Higgs boson decay at order α_s^4. 2017.

[108] E. Braaten and J. P. Leveille. Higgs Boson Decay and the Running Mass. *Phys. Rev.*, D22:715, 1980.

[109] N. Sakai. Perturbative QCD Corrections to the Hadronic Decay Width of the Higgs Boson. *Phys. Rev.*, D22:2220, 1980.

[110] Takeo Inami and Takahiro Kubota. Renormalization Group Estimate of the Hadronic Decay Width of the Higgs Boson. *Nucl. Phys.*, B179:171–188, 1981.

[111] S. G. Gorishnii, A. L. Kataev, and S. A. Larin. The Width of Higgs Boson Decay Into Hadrons: Three Loop Corrections of Strong Interactions. *Sov. J. Nucl. Phys.*, 40:329–334, 1984. [Yad. Fiz.40,517(1984)].

[112] Manuel Drees and Ken-ichi Hikasa. NOTE ON QCD CORRECTIONS TO HADRONIC HIGGS DECAY. *Phys. Lett.*, B240:455, 1990. [Erratum: Phys. Lett.B262,497(1991)].

[113] A. L. Kataev. The Order O (alpha alpha-s) and O (alpha**2) corrections to the decay width of the neutral Higgs boson to the anti-b b pair. *JETP Lett.*, 66:327–330, 1997.

[114] K. G. Chetyrkin. Quark mass anomalous dimension to O (alpha-s**4). *Phys. Lett.*, B404:161–165, 1997.

[115] J. A. M. Vermaseren, S. A. Larin, and T. van Ritbergen. The four loop quark mass anomalous dimension and the invariant quark mass. *Phys. Lett.*, B405:327–333, 1997.

[116] D. de Florian et al. Handbook of LHC Higgs Cross Sections: 4. Deciphering the Nature of the Higgs Sector. 2016.

[117] Bernd A. Kniehl. Higgs phenomenology at one loop in the standard model. *Phys. Rept.*, 240:211–300, 1994.

[118] Luminita Mihaila, Barbara Schmidt, and Matthias Steinhauser. $\Gamma(H \to b\bar{b})$ to order $\alpha\alpha_s$. *Phys. Lett.*, B751:442–447, 2015.

[119] K. G. Chetyrkin, Bernd A. Kniehl, and M. Steinhauser. Three loop O (alpha-s**2 G(F) M(t)**2) corrections to hadronic Higgs decays. *Nucl. Phys.*, B490:19–39, 1997.

[120] K. G. Chetyrkin, Bernd A. Kniehl, and M. Steinhauser. Virtual top quark effects on the H —¿ b anti-b decay at next-to-leading order in QCD. *Phys. Rev. Lett.*, 78:594–597, 1997.

[121] Michael E. Peskin. Estimation of LHC and ILC Capabilities for Precision Higgs Boson Coupling Measurements. In *Proceedings, Community Summer Study 2013: Snowmass on the Mississippi (CSS2013): Minneapolis, MN, USA, July 29-August 6, 2013*, 2013.

[122] Ali Abbasabadi, David Bowser-Chao, Duane A. Dicus, and Wayne W. Repko. Higgs photon associated production at $e\bar{e}$ colliders. *Phys. Rev.*, D52:3919–3928, 1995.

[123] Thomas Hahn. Generating Feynman diagrams and amplitudes with FeynArts 3. *Comput. Phys. Commun.*, 140:418–431, 2001.

[124] R. Mertig, M. Bohm, and Ansgar Denner. FEYN CALC: Computer algebraic calculation of Feynman amplitudes. *Comput. Phys. Commun.*, 64:345–359, 1991.

[125] G. Passarino and M. J. G. Veltman. One Loop Corrections for e^+e^- Annihilation Into $\mu^+\mu^-$ in the Weinberg Model. *Nucl. Phys.*, B160:151–207, 1979.

[126] T. Hahn and M. Perez-Victoria. Automatized one loop calculations in four-dimensions and D-dimensions. *Comput. Phys. Commun.*, 118:153–165, 1999.

[127] T. Hahn. CUBA: A Library for multidimensional numerical integration. *Comput. Phys. Commun.*, 168:78–95, 2005.

[128] Ali Abbasabadi and Wayne W. Repko. Higgs boson decay to muon anti-muon gamma. *Phys. Rev.*, D62:054025, 2000.

[129] James S. Gainer, Wai-Yee Keung, Ian Low, and Pedro Schwaller. Looking for a light Higgs boson in the $Z\gamma \to \ell\ell\gamma$ channel. *Phys. Rev.*, D86:033010, 2012.

[130] Long-Bin Chen, Cong-Feng Qiao, and Rui-Lin Zhu. Reconstructing the 125 GeV SM Higgs Boson Through $\ell\bar{\ell}\gamma$. *Phys. Lett.*, B726:306–311, 2013.

[131] Giampiero Passarino. Higgs Boson Production and Decay: Dalitz Sector. *Phys. Lett.*, B727:424–431, 2013.

[132] Yi Sun, Hao-Ran Chang, and Dao-Neng Gao. Higgs decays to $\gamma\ell^+\ell^-$ in the standard model. *JHEP*, 05:061, 2013.

[133] Alexander Yu. Korchin and Vladimir A. Kovalchuk. Angular distribution and forward–backward asymmetry of the Higgs-boson decay to photon and lepton pair. *Eur. Phys. J.*, C74(11):3141, 2014.

[134] Georges Aad et al. Search for Higgs boson decays to a photon and a Z boson in pp collisions at $\sqrt{s}$=7 and 8 TeV with the ATLAS detector. *Phys. Lett.*, B732:8–27, 2014.

[135] Serguei Chatrchyan et al. Search for a Higgs boson decaying into a Z and a photon in pp collisions at sqrt(s) = 7 and 8 TeV. *Phys. Lett.*, B726:587–609, 2013.

[136] Vardan Khachatryan et al. Search for a Higgs boson decaying into $\gamma^*\gamma \to \ell\ell\gamma$ with low dilepton mass in pp collisions at $\sqrt{s} = 8$ TeV. *Phys. Lett.*, B753:341–362, 2016.

[137] Charalampos Anastasiou, Claude Duhr, Falko Dulat, Elisabetta Furlan, Thomas Gehrmann, Franz Herzog, Achilleas Lazopoulos, and Bernhard Mistlberger. High precision determination of the gluon fusion Higgs boson cross-section at the LHC. *JHEP*, 05:058, 2016.

[138] J. Alwall, R. Frederix, S. Frixione, V. Hirschi, F. Maltoni, O. Mattelaer, H. S. Shao, T. Stelzer, P. Torrielli, and M. Zaro. The automated computation of tree-level and next-to-leading order differential cross sections, and their matching to parton shower simulations. *JHEP*, 07:079, 2014.

[139] Massimiliano Grazzini, Stefan Kallweit, Dirk Rathlev, and Alessandro Torre. $Z\gamma$ production at hadron colliders in NNLO QCD. *Phys. Lett.*, B731:204–207, 2014.

[140] John M. Campbell, R. Keith Ellis, Ye Li, and Ciaran Williams. Predictions for diphoton production at the LHC through NNLO in QCD. *JHEP*, 07:148, 2016.

[141] Projections for measurements of Higgs boson cross sections, branching ratios and coupling parameters with the ATLAS detector at a HL-LHC. Technical Report ATL-PHYS-PUB-2013-014, CERN, Geneva, Oct 2013.

[142] Projected Performance of an Upgraded CMS Detector at the LHC and HL-LHC: Contribution to the Snowmass Process. In *Proceedings, Community Summer Study 2013: Snowmass on the Mississippi (CSS2013): Minneapolis, MN, USA, July 29-August 6, 2013*, 2013.

[143] Geoffrey T. Bodwin, Frank Petriello, Stoyan Stoynev, and Mayda Velasco. Higgs boson decays to quarkonia and the $H\bar{c}c$ coupling. *Phys. Rev.*, D88(5):053003, 2013.

[144] Geoffrey T. Bodwin, Hee Sok Chung, June-Haak Ee, Jungil Lee, and Frank Petriello. Relativistic corrections to Higgs boson decays to quarkonia. *Phys. Rev.*, D90(11):113010, 2014.

[145] Matthias König and Matthias Neubert. Exclusive Radiative Higgs Decays as Probes of Light-Quark Yukawa Couplings. *JHEP*, 08:012, 2015.

[146] Geoffrey T. Bodwin, Hee Sok Chung, June-Haak Ee, and Jungil Lee. A new approach to the resummation of logarithms in Higgs-boson decays to a vector quarkonium plus a photon. *Phys. Rev.*, D95(5):054018, 2017.

[147] Georges Aad et al. Search for Higgs and Z Boson Decays to $J/\psi\gamma$ and $\Upsilon(nS)\gamma$ with the ATLAS Detector. *Phys. Rev. Lett.*, 114(12):121801, 2015.

[148] Gilad Perez, Yotam Soreq, Emmanuel Stamou, and Kohsaku Tobioka. Constraining the charm Yukawa and Higgs-quark coupling universality. *Phys. Rev.*, D92(3):033016, 2015.

[149] Search for the Standard Model Higgs and Z Boson decays to $J/\psi\,\gamma$: HL-LHC projections. Technical Report ATL-PHYS-PUB-2015-043, CERN, Geneva, Sep 2015.

[150] Georges Aad et al. Evidence for the Higgs-boson Yukawa coupling to tau leptons with the ATLAS detector. *JHEP*, 04:117, 2015.

[151] Serguei Chatrchyan et al. Evidence for the 125 GeV Higgs boson decaying to a pair of τ leptons. *JHEP*, 05:104, 2014.

[152] Iftah Galon, Arvind Rajaraman, and Tim M. P. Tait. $H \to \tau^+\tau^-\gamma$ as a probe of the τ magnetic dipole moment. *JHEP*, 12:111, 2016.

[153] Gian F. Giudice and Oleg Lebedev. Higgs-dependent Yukawa couplings. *Phys. Lett.*, B665:79–85, 2008.

[154] Martin Bauer, Marcela Carena, and Katrin Gemmler. Flavor from the Electroweak Scale. *JHEP*, 11:016, 2015.

[155] Roni Harnik, Joachim Kopp, and Jure Zupan. Flavor Violating Higgs Decays. *JHEP*, 03:026, 2013.

[156] Cédric Delaunay, Christophe Grojean, and Gilad Perez. Modified Higgs Physics from Composite Light Flavors. *JHEP*, 09:090, 2013.

[157] Cédric Delaunay, Thomas Flacke, J. Gonzalez-Fraile, Seung J. Lee, Giuliano Panico, and Gilad Perez. Light Non-degenerate Composite Partners at the LHC. *JHEP*, 02:055, 2014.

[158] Monika Blanke, Gian F. Giudice, Paride Paradisi, Gilad Perez, and Jure Zupan. Flavoured Naturalness. *JHEP*, 06:022, 2013.

[159] Alexander L. Kagan, Gilad Perez, Tomer Volansky, and Jure Zupan. General Minimal Flavor Violation. *Phys. Rev.*, D80:076002, 2009.

[160] Avital Dery, Aielet Efrati, Gudrun Hiller, Yonit Hochberg, and Yosef Nir. Higgs couplings to fermions: 2HDM with MFV. *JHEP*, 08:006, 2013.

[161] Leandro Da Rold, Cedric Delaunay, Christophe Grojean, and Gilad Perez. Up Asymmetries From Exhilarated Composite Flavor Structures. *JHEP*, 02:149, 2013.

[162] Avital Dery, Aielet Efrati, Yosef Nir, Yotam Soreq, and Vasja Susič. Model building for flavor changing Higgs couplings. *Phys. Rev.*, D90:115022, 2014.

[163] Fady Bishara, Joachim Brod, Patipan Uttayarat, and Jure Zupan. Nonstandard Yukawa Couplings and Higgs Portal Dark Matter. *JHEP*, 01:010, 2016.

[164] Cédric Delaunay, Tobias Golling, Gilad Perez, and Yotam Soreq. Enhanced Higgs boson coupling to charm pairs. *Phys. Rev.*, D89(3):033014, 2014.

[165] Yaofu Zhou. Constraining the Higgs boson coupling to light quarks in the HZZ final states. *Phys. Rev.*, D93(1):013019, 2016.

[166] Gilad Perez, Yotam Soreq, Emmanuel Stamou, and Kohsaku Tobioka. Prospects for measuring the Higgs boson coupling to light quarks. *Phys. Rev.*, D93(1):013001, 2016.

[167] Ilaria Brivio, Florian Goertz, and Gino Isidori. Probing the Charm Quark Yukawa Coupling in Higgs+Charm Production. *Phys. Rev. Lett.*, 115(21):211801, 2015.

[168] Fady Bishara, Ulrich Haisch, Pier Francesco Monni, and Emanuele Re. Constraining Light-Quark Yukawa Couplings from Higgs Distributions. 2016.

[169] Felix Yu. Phenomenology of Enhanced Light Quark Yukawa Couplings and the $W^{\pm}h$ Charge Asymmetry. *JHEP*, 02:083, 2017.

[170] Linda M. Carpenter, Tao Han, Khalida Hendricks, Zhuoni Qian, and Ning Zhou. Higgs Boson Decay to Light Jets at the LHC. *Phys. Rev.*, D95(5):053003, 2017.

[171] b-jet tagging calibration on c-jets containing D^{*+} mesons. 2012.

[172] The ATLAS collaboration. Calibration of the performance of b-tagging for c and light-flavour jets in the 2012 ATLAS data. 2014.

[173] Expected photon performance in the ATLAS experiment. Technical Report ATL-PHYS-PUB-2011-007, CERN, Geneva, Apr 2011.

[174] S. Catani, M. Fontannaz, J. P. Guillet, and E. Pilon. Cross-section of isolated prompt photons in hadron hadron collisions. *JHEP*, 05:028, 2002.

[175] Georges Aad et al. Search for the $b\bar{b}$ decay of the Standard Model Higgs boson in associated $(W/Z)H$ production with the ATLAS detector. *JHEP*, 01:069, 2015.

[176] Serguei Chatrchyan et al. Search for the standard model Higgs boson produced in association with a W or a Z boson and decaying to bottom quarks. *Phys. Rev.*, D89(1):012003, 2014.

[177] Prospects for $H \to c\bar{c}$ using Charm Tagging with the ATLAS Experiment at the HL-LHC. Technical Report ATL-PHYS-PUB-2018-016, CERN, Geneva, Aug 2018.

[178] Morad Aaboud et al. Searches for exclusive Higgs and Z boson decays into $J/\psi\gamma$, $\psi(2S)\gamma$, and $\Upsilon(nS)\gamma$ at $\sqrt{s} = 13$ TeV with the ATLAS detector. *Phys. Lett.*, B786:134–155, 2018.

[179] Yotam Soreq, Hua Xing Zhu, and Jure Zupan. Light quark Yukawa couplings from Higgs kinematics. *JHEP*, 12:045, 2016.

[180] Jonathan Cohen, Shaouly Bar-Shalom, Gad Eilam, and Amarjit Soni. Light-quarks Yukawa couplings and new physics in exclusive high- p_T Higgs boson+jet and Higgs boson + b -jet events. *Phys. Rev.*, D97(5):055014, 2018.

[181] The ATLAS collaboration. Constituent-level pile-up mitigation techniques in ATLAS. 2017.

[182] Peter Berta, Martin Spousta, David W. Miller, and Rupert Leitner. Particle-level pileup subtraction for jets and jet shapes. *JHEP*, 06:092, 2014.

[183] Daniele Bertolini, Philip Harris, Matthew Low, and Nhan Tran. Pileup Per Particle Identification. *JHEP*, 10:059, 2014.

[184] David Krohn, Matthew D. Schwartz, Matthew Low, and Lian-Tao Wang. Jet Cleansing: Pileup Removal at High Luminosity. *Phys. Rev.*, D90(6):065020, 2014.

[185] Matteo Cacciari, Gavin P. Salam, and Gregory Soyez. SoftKiller, a particle-level pileup removal method. *Eur. Phys. J.*, C75(2):59, 2015.

[186] Matteo Cacciari and Gavin P. Salam. Pileup subtraction using jet areas. *Phys. Lett.*, B659:119–126, 2008.

[187] CMS Collaboration. Pileup Jet Identification. 2013.

[188] Morad Aaboud et al. Identification and rejection of pile-up jets at high pseudorapidity with the ATLAS detector. *Eur. Phys. J.*, C77(9):580, 2017. [Erratum: Eur. Phys. J.C77,no.10,712(2017)].

[189] Georges Aad et al. Performance of pile-up mitigation techniques for jets in pp collisions at $\sqrt{s} = 8$ TeV using the ATLAS detector. *Eur. Phys. J.*, C76(11):581, 2016.

[190] J. Martinez et al. Pileup mitigation at the Large Hadron Collider with Graph Neural Networks. 2018.

[191] ATLAS Collaboration. Technical Design Report for the Phase-II Upgrade of the ATLAS TDAQ System. Technical Report CERN-LHCC-2017-020. ATLAS-TDR-029, CERN, Geneva, Sep 2017.

[192] CMS Collaboration. The Phase-2 Upgrade of the CMS L1 Trigger Interim Technical Design Report. Technical Report CERN-LHCC-2017-013. CMS-TDR-017, CERN, Geneva, Sep 2017. This is the CMS Interim TDR devoted to the upgrade of the CMS L1 trigger in view of the HL-LHC running, as approved by the LHCC.

[193] Michelangelo L. Mangano, Mauro Moretti, Fulvio Piccinini, Roberto Pittau, and Antonio D. Polosa. ALPGEN, a generator for hard multiparton processes in hadronic collisions. *JHEP*, 07:001, 2003.

[194] Torbjorn Sjostrand, Stephen Mrenna, and Peter Z. Skands. PYTHIA 6.4 Physics and Manual. *JHEP*, 05:026, 2006.

[195] J. de Favereau, C. Delaere, P. Demin, A. Giammanco, V. Lematre, A. Mertens, and M. Selvaggi. DELPHES 3, A modular framework for fast simulation of a generic collider experiment. *JHEP*, 02:057, 2014.

[196] Morad Aaboud et al. Performance of the ATLAS Trigger System in 2015. *Eur. Phys. J.*, C77(5):317, 2017.

[197] CMS Collaboration. The Phase-2 Upgrade of the CMS Tracker. Technical Report CERN-LHCC-2017-009. CMS-TDR-014, CERN, Geneva, Jun 2017.

[198] CMS Collaboration. The Phase-2 Upgrade of the CMS DAQ Interim Technical Design Report. Technical Report CERN-LHCC-2017-014. CMS-TDR-018, CERN, Geneva, Sep 2017. This is the CMS Interim TDR devoted to the upgrade of the CMS DAQ in view of the HL-LHC running, as approved by the LHCC.

[199] CMS Collaboration. TECHNICAL PROPOSAL FOR A MIP TIMING DETECTOR IN THE CMS EXPERIMENT PHASE 2 UPGRADE. Technical Report CERN-LHCC-2017-027. LHCC-P-009, CERN, Geneva, Dec 2017. This document describes a MIP timing detector for the Phase-2 upgrade of the CMS experiment, in view of HL-LHC running.

[200] ATLAS Collaboration. Expression of Interest: A High-Granularity Timing Detector for ATLAS Phase-2 Upgrade. Technical Report ATL-COM-LARG-2017-049, CERN, Geneva, Oct 2017.

[201] ATLAS Collaboration. Technical Design Report for the ATLAS Inner Tracker Strip Detector. Technical Report CERN-LHCC-2017-005. ATLAS-TDR-025, CERN, Geneva, Apr 2017.

[202] ATLAS Collaboration. Technical Design Report for the ATLAS Inner Tracker Pixel Detector. Technical Report CERN-LHCC-2017-021. ATLAS-TDR-030, CERN, Geneva, Sep 2017.

[203] A. M. Sirunyan3 et al. Particle-flow reconstruction and global event description with the CMS detector. *JINST*, 12(10):P10003, 2017.

[204] Morad Aaboud et al. Jet reconstruction and performance using particle flow with the ATLAS Detector. *Eur. Phys. J.*, C77(7):466, 2017.

[205] ATLAS Collaboration. Expected performance for an upgraded ATLAS detector at High-Luminosity LHC. Technical Report ATL-PHYS-PUB-2016-026, CERN, Geneva, Oct 2016.

[206] ATLAS Collaboration. Optimisation and performance studies of the ATLAS b-tagging algorithms for the 2017-18 LHC run. Technical Report ATL-PHYS-PUB-2017-013, CERN, Geneva, Jul 2017.

[207] CMS Collaboration. CMS Phase II Upgrade Scope Document. Technical Report CERN-LHCC-2015-019. LHCC-G-165, CERN, Geneva, Sep 2015.

[208] ATLAS Collaboration. ATLAS Phase-II Upgrade Scoping Document. Technical Report CERN-LHCC-2015-020. LHCC-G-166, CERN, Geneva, Sep 2015.

[209] G. Apollinari, O. Brüning, T. Nakamoto, and Lucio Rossi. High Luminosity Large Hadron Collider HL-LHC. *CERN Yellow Report*, (5):1–19, 2015.

[210] Alexander L. Read. Presentation of search results: The CL(s) technique. *J. Phys.*, G28:2693–2704, 2002. [,11(2002)].

[211] Tianqi Chen and Carlos Guestrin. Xgboost. *Proceedings of the 22nd ACM SIGKDD International Conference on Knowledge Discovery and Data Mining - KDD '16*, 2016.

[212] Gilles Louppe, Michael Kagan, and Kyle Cranmer. Learning to Pivot with Adversarial Networks. 2016.

[213] Chase Shimmin, Peter Sadowski, Pierre Baldi, Edison Weik, Daniel Whiteson, Edward Goul, and Andreas Søgaard. Decorrelated Jet Substructure Tagging using Adversarial Neural Networks. *Phys. Rev.*, D96(7):074034, 2017.

[214] J. A. Aguilar-Saavedra, Jack H. Collins, and Rashmish K. Mishra. A generic anti-QCD jet tagger. *JHEP*, 11:163, 2017.

[215] Justin Stevens and Mike Williams. uBoost: A boosting method for producing uniform selection efficiencies from multivariate classifiers. *JINST*, 8:P12013, 2013.

[216] James Dolen, Philip Harris, Simone Marzani, Salvatore Rappoccio, and Nhan Tran. Thinking outside the ROCs: Designing Decorrelated Taggers (DDT) for jet substructure. *JHEP*, 05:156, 2016.

[217] Ian Moult, Benjamin Nachman, and Duff Neill. Convolved Substructure: Analytically Decorrelating Jet Substructure Observables. *JHEP*, 05:002, 2018.

[218] ATLAS Collaboration. Performance of mass-decorrelated jet substructure observables for hadronic two-body decay tagging in ATLAS. Technical Report ATL-PHYS-PUB-2018-014, CERN, Geneva, Jul 2018.

[219] J.L. Abelleira et al. High-Energy LHC design. *Journal of Physics: Conference Series*, 1067(2):022009, 2018.

[220] Marco Cirelli, Nicolao Fornengo, and Alessandro Strumia. Minimal dark matter. *Nucl. Phys.*, B753:178–194, 2006.

[221] Marco Cirelli, Alessandro Strumia, and Matteo Tamburini. Cosmology and Astrophysics of Minimal Dark Matter. *Nucl. Phys.*, B787:152–175, 2007.

[222] Benjamin W. Lee and Steven Weinberg. Cosmological Lower Bound on Heavy Neutrino Masses. *Phys. Rev. Lett.*, 39:165–168, 1977. [,183(1977)].

[223] H. Goldberg. Constraint on the Photino Mass from Cosmology. *Phys. Rev. Lett.*, 50:1419, 1983. [,219(1983)].

[224] Gary Steigman, Basudeb Dasgupta, and John F. Beacom. Precise Relic WIMP Abundance and its Impact on Searches for Dark Matter Annihilation. *Phys. Rev.*, D86:023506, 2012.

[225] Kim Griest and David Seckel. Three exceptions in the calculation of relic abundances. *Phys. Rev.*, D43:3191–3203, 1991.

[226] Paolo Gondolo and Graciela Gelmini. Cosmic abundances of stable particles: Improved analysis. *Nucl. Phys.*, B360:145–179, 1991.

[227] Joakim Edsjo and Paolo Gondolo. Neutralino relic density including coannihilations. *Phys. Rev.*, D56:1879–1894, 1997.

[228] N. Arkani-Hamed, A. Delgado, and G. F. Giudice. The Well-tempered neutralino. *Nucl. Phys.*, B741:108–130, 2006.

[229] Junji Hisano, Shigeki Matsumoto, and Mihoko M. Nojiri. Explosive dark matter annihilation. *Phys. Rev. Lett.*, 92:031303, 2004.

[230] Junji Hisano, Shigeki. Matsumoto, Mihoko M. Nojiri, and Osamu Saito. Non-perturbative effect on dark matter annihilation and gamma ray signature from galactic center. *Phys. Rev.*, D71:063528, 2005.

[231] Junji Hisano, Shigeki Matsumoto, Minoru Nagai, Osamu Saito, and Masato Senami. Non-perturbative effect on thermal relic abundance of dark matter. *Phys. Lett.*, B646:34–38, 2007.

[232] Satoshi Mizuta and Masahiro Yamaguchi. Coannihilation effects and relic abundance of Higgsino dominant LSP(s). *Phys. Lett.*, B298:120–126, 1993.

[233] Takeo Moroi and Lisa Randall. Wino cold dark matter from anomaly mediated SUSY breaking. *Nucl. Phys.*, B570:455–472, 2000.

[234] Tao Han and Ralf Hempfling. Messenger sneutrinos as cold dark matter. *Phys. Lett.*, B415:161–169, 1997.

[235] David Tucker-Smith and Neal Weiner. Inelastic dark matter. *Phys. Rev.*, D64:043502, 2001.

[236] Junji Hisano, Koji Ishiwata, and Natsumi Nagata. A complete calculation for direct detection of Wino dark matter. *Phys. Lett.*, B690:311–315, 2010.

[237] Junji Hisano, Koji Ishiwata, Natsumi Nagata, and Tomohiro Takesako. Direct Detection of Electroweak-Interacting Dark Matter. *JHEP*, 07:005, 2011.

[238] Junji Hisano, Koji Ishiwata, and Natsumi Nagata. Direct Search of Dark Matter in High-Scale Supersymmetry. *Phys. Rev.*, D87:035020, 2013.

[239] Junji Hisano, Koji Ishiwata, and Natsumi Nagata. QCD Effects on Direct Detection of Wino Dark Matter. *JHEP*, 06:097, 2015.

[240] Richard J. Hill and Mikhail P. Solon. Universal behavior in the scattering of heavy, weakly interacting dark matter on nuclear targets. *Phys. Lett.*, B707:539–545, 2012.

[241] Richard J. Hill and Mikhail P. Solon. WIMP-nucleon scattering with heavy WIMP effective theory. *Phys. Rev. Lett.*, 112:211602, 2014.

[242] Biplob Bhattacherjee, Masahiro Ibe, Koji Ichikawa, Shigeki Matsumoto, and Kohei Nishiyama. Wino Dark Matter and Future dSph Observations. *JHEP*, 07:080, 2014.

[243] Shigeki Matsumoto. Unexplored regions of WIMP. *PoS*, KMI2017:033, 2017.

[244] Rebecca Krall and Matthew Reece. Last Electroweak WIMP Standing: Pseudo-Dirac Higgsino Status and Compact Stars as Future Probes. *Chin. Phys.*, C42(4):043105, 2018.

[245] The ATLAS collaboration. Search for charginos nearly mass-degenerate with the lightest neutralino based on a disappearing-track signature in pp collisions at $\sqrt{s} = 8$ TeV with the ATLAS detector. 2013.

[246] Morad Aaboud et al. Search for long-lived charginos based on a disappearing-track signature in pp collisions at $\sqrt{s} = 13$ TeV with the ATLAS detector. *JHEP*, 06:022, 2018.

[247] Search for direct pair production of higgsinos by the reinterpretation of the disappearing track analysis with 36.1 fb^{-1} of $\sqrt{s} = 13$ TeV data collected with the ATLAS experiment. Technical Report ATL-PHYS-PUB-2017-019, CERN, Geneva, Dec 2017.

[248] V. Khachatryan et al. Search for disappearing tracks in proton-proton collisions at $\sqrt{s} = 8$ TeV. *JHEP*, 01:096, 2015.

[249] Albert M Sirunyan et al. Search for disappearing tracks as a signature of new long-lived particles in proton-proton collisions at $\sqrt{s} = 13$ TeV. *JHEP*, 08:016, 2018.

[250] Matthew Low and Lian-Tao Wang. Neutralino dark matter at 14 TeV and 100 TeV. *JHEP*, 08:161, 2014.

[251] Marco Cirelli, Filippo Sala, and Marco Taoso. Wino-like Minimal Dark Matter and future colliders. *JHEP*, 10:033, 2014. [Erratum: JHEP01,041(2015)].

[252] Rakhi Mahbubani, Pedro Schwaller, and Jose Zurita. Closing the window for compressed Dark Sectors with disappearing charged tracks. *JHEP*, 06:119, 2017. [Erratum: JHEP10,061(2017)].

[253] Hajime Fukuda, Natsumi Nagata, Hidetoshi Otono, and Satoshi Shirai. Higgsino Dark Matter or Not: Role of Disappearing Track Searches at the LHC and Future Colliders. *Phys. Lett.*, B781:306–311, 2018.

[254] Talk presented by Michaell Benedikt and Oct. 2017. Frank Zimmermann at the `HL-LHC/HE-LHC Physics Workshop`, CERN.

[255] Nima Arkani-Hamed, Tao Han, Michelangelo Mangano, and Lian-Tao Wang. Physics opportunities of a 100 TeV protonproton collider. *Phys. Rept.*, 652:1–49, 2016.

[256] T. Golling et al. Physics at a 100 TeV pp collider: beyond the Standard Model phenomena. *CERN Yellow Report*, (3):441–634, 2017.

[257] R. Contino et al. Physics at a 100 TeV pp collider: Higgs and EW symmetry breaking studies. *CERN Yellow Report*, (3):255–440, 2017.

[258] Muhammd Ahmad et al. CEPC-SPPC Preliminary Conceptual Design Report. 1. Physics and Detector. 2015.

[259] M. Capeans, G. Darbo, K. Einsweiler, M. Elsing, T. Flick, M. Garcia-Sciveres, C. Gemme, H. Pernegger, O. Rohne, and R. Vuillermet. ATLAS Insertable B-Layer Technical Design Report. 2010.

[260] Masahiro Ibe, Shigeki Matsumoto, and Ryosuke Sato. Mass Splitting between Charged and Neutral Winos at Two-Loop Level. *Phys. Lett.*, B721:252–260, 2013.

[261] David Curtin, Kaustubh Deshpande, Oliver Fischer, and JosÃ© Zurita. New Physics Opportunities for Long-Lived Particles at Electron-Proton Colliders. *JHEP*, 07:024, 2018.

[262] Johan Alwall, Michel Herquet, Fabio Maltoni, Olivier Mattelaer, and Tim Stelzer. MadGraph 5 : Going Beyond. *JHEP*, 06:128, 2011.

[263] S. Ovyn, X. Rouby, and V. Lemaitre. DELPHES, a framework for fast simulation of a generic collider experiment. 2009.

[264] J. Pumplin, D. R. Stump, J. Huston, H. L. Lai, Pavel M. Nadolsky, and W. K. Tung. New generation of parton distributions with uncertainties from global QCD analysis. *JHEP*, 07:012, 2002.

[265] M. R. Whalley, D. Bourilkov, and R. C. Group. The Les Houches accord PDFs (LHAPDF) and LHAGLUE. In *HERA and the LHC: A Workshop on the implications of HERA for LHC physics. Proceedings, Part B*, pages 575–581, 2005.

[266] Matteo Cacciari, Gavin P. Salam, and Gregory Soyez. The anti-k_t jet clustering algorithm. *JHEP*, 04:063, 2008.

[267] Matteo Cacciari, Gavin P. Salam, and Gregory Soyez. FastJet User Manual. *Eur. Phys. J.*, C72:1896, 2012.

[268] Matteo Cacciari and Gavin P. Salam. Dispelling the N^3 myth for the k_t jet-finder. *Phys. Lett.*, B641:57–61, 2006.

[269] Patrick J. Fox and Ciaran Williams. Next-to-Leading Order Predictions for Dark Matter Production at Hadron Colliders. *Phys. Rev.*, D87(5):054030, 2013.

[270] Stefan Kallweit, Jonas M. Lindert, Philipp Maierhofer, Stefano Pozzorini, and Marek Schnherr. NLO QCD+EW predictions for V + jets including off-shell vector-boson decays and multijet merging. *JHEP*, 04:021, 2016.

[271] Search for new physics in monojet events in pp collisions at sqrt(s)= 8 TeV. Technical Report CMS-PAS-EXO-12-048, CERN, Geneva, 2013.

[272] J. M. Lindert et al. Precise predictions for $V+$ jets dark matter backgrounds. *Eur. Phys. J.*, C77(12):829, 2017.

[273] Morad Aaboud et al. Search for dark matter and other new phenomena in events with an energetic jet and large missing transverse momentum using the ATLAS detector. *JHEP*, 01:126, 2018.

[274] Dan Hooper. Is the CMB Telling Us that Dark Matter is Weaker than Weakly Interacting? *Phys. Rev.*, D88:083519, 2013.

[275] N. Arkani-Hamed, S. Dimopoulos, G. F. Giudice, and A. Romanino. Aspects of split supersymmetry. *Nucl. Phys.*, B709:3–46, 2005.

[276] G. F. Giudice and A. Romanino. Split supersymmetry. *Nucl. Phys.*, B699:65–89, 2004. [Erratum: Nucl. Phys.B706,487(2005)].

[277] James D. Wells. PeV-scale supersymmetry. *Phys. Rev.*, D71:015013, 2005.

[278] Howard Baer, Vernon Barger, Peisi Huang, and Xerxes Tata. Natural Supersymmetry: LHC, dark matter and ILC searches. *JHEP*, 05:109, 2012.

[279] Michele Papucci, Joshua T. Ruderman, and Andreas Weiler. Natural SUSY Endures. *JHEP*, 09:035, 2012.

[280] Sunghoon Jung and James D. Wells. Gaugino physics of split supersymmetry spectra at the LHC and future proton colliders. *Phys. Rev.*, D89(7):075004, 2014.

[281] C. H. Chen, Manuel Drees, and J. F. Gunion. Searching for invisible and almost invisible particles at e+ e- colliders. *Phys. Rev. Lett.*, 76:2002–2005, 1996.

[282] C. H. Chen, Manuel Drees, and J. F. Gunion. A Nonstandard string / SUSY scenario and its phenomenological implications. *Phys. Rev.*, D55:330–347, 1997. [Erratum: Phys. Rev.D60,039901(1999)].

[283] Gian F. Giudice, Tao Han, Kai Wang, and Lian-Tao Wang. Nearly Degenerate Gauginos and Dark Matter at the LHC. *Phys. Rev.*, D81:115011, 2010.

[284] Tao Han, Sanjay Padhi, and Shufang Su. Electroweakinos in the Light of the Higgs Boson. *Phys. Rev.*, D88(11):115010, 2013.

[285] Kingman Cheung, Cheng-Wei Chiang, and Jeonghyeon Song. A Minimal supersymmetric scenario with only mu at the weak scale. *JHEP*, 04:047, 2006.

[286] Howard Baer, Vernon Barger, and Peisi Huang. Hidden SUSY at the LHC: the light higgsino-world scenario and the role of a lepton collider. *JHEP*, 11:031, 2011.

[287] C. Hensel. *Search for nearly mass degenerate charginos and neutralinos in e+ e- collisions.* PhD thesis, Hamburg U., 2002.

[288] Mikael Berggren, Felix Brmmer, Jenny List, Gudrid Moortgat-Pick, Tania Robens, Krzysztof Rolbiecki, and Hale Sert. Tackling light higgsinos at the ILC. *Eur. Phys. J.*, C73(12):2660, 2013.

[289] Hsin-Chia Cheng, Bogdan A. Dobrescu, and Konstantin T. Matchev. Generic and chiral extensions of the supersymmetric standard model. *Nucl. Phys.*, B543:47–72, 1999.

[290] Tony Gherghetta, Gian F. Giudice, and James D. Wells. Phenomenological consequences of supersymmetry with anomaly induced masses. *Nucl. Phys.*, B559:27–47, 1999.

[291] Kingman Cheung and Cheng-Wei Chiang. Splitting split supersymmetry. *Phys. Rev.*, D71:095003, 2005.

[292] Jonathan L. Feng, Takeo Moroi, Lisa Randall, Matthew Strassler, and Shu-fang Su. Discovering supersymmetry at the Tevatron in wino LSP scenarios. *Phys. Rev. Lett.*, 83:1731–1734, 1999.

[293] M. Ibe, Takeo Moroi, and T. T. Yanagida. Possible Signals of Wino LSP at the Large Hadron Collider. *Phys. Lett.*, B644:355–360, 2007.

[294] Savas Dimopoulos, Nikolaos Tetradis, Rahim Esmailzadeh, and Lawrence J. Hall. TeV Dark Matter. *Nucl. Phys.*, B349:714–726, 1991. [Erratum: Nucl. Phys.B357,308(1991)].

[295] Scott D. Thomas and James D. Wells. Phenomenology of Massive Vectorlike Doublet Leptons. *Phys. Rev. Lett.*, 81:34–37, 1998.

[296] Marc Sher. Charged leptons with nanosecond lifetimes. *Phys. Rev.*, D52:3136–3138, 1995.

[297] Serguei Chatrchyan et al. Search for dark matter and large extra dimensions in monojet events in pp collisions at $\sqrt{s} = 7$ TeV. *JHEP*, 09:094, 2012.

[298] Georges Aad et al. Search for dark matter candidates and large extra dimensions in events with a jet and missing transverse momentum with the ATLAS detector. *JHEP*, 04:075, 2013.

[299] Andreas Birkedal, Konstantin Matchev, and Maxim Perelstein. Dark matter at colliders: A Model independent approach. *Phys. Rev.*, D70:077701, 2004.

[300] Herbert Dreiner, Moritz Huck, Michael Krmer, Daniel Schmeier, and Jamie Tattersall. Illuminating Dark Matter at the ILC. *Phys. Rev.*, D87(7):075015, 2013.

[301] Ernest Ma and Jon Okada. How Many Neutrinos? *Phys. Rev. Lett.*, 41:287, 1978. [Erratum: Phys. Rev. Lett.41,1759(1978)].

[302] K. J. F. Gaemers, R. Gastmans, and F. M. Renard. Neutrino Counting in e+ e- Collisions. *Phys. Rev.*, D19:1605, 1979.

[303] G. Barbiellini, Burton Richter, and J. Siegrist. Radiative Z0 Production: A Method for Neutrino Counting in e+ e- Collisions. *Phys. Lett.*, 106B:414–418, 1981.

[304] Daniele Fargion, Maxim Yu. Khlopov, Rostisslav V. Konoplich, and R. Mignani. On the possibility of searching for heavy neutrinos at accelerators. *Phys. Rev.*, D54:4684–4686, 1996.

[305] K. Grassie and P. N. Pandita. Production of Photinos in $e^+e^- \to \gamma$ Photino Photino. *Phys. Rev.*, D30:22, 1984.

[306] Pierre Fayet. Lower Limit on the Mass of a Light Gravitino from e+ e- Annihilation Experiments. *Phys. Lett.*, B175:471–477, 1986.

[307] Duane A. Dicus, S. Nandi, and Jeffrey Woodside. A New source of single photons from Z0 decay. *Phys. Lett.*, B258:231–235, 1991.

[308] Jorge L. Lopez, Dimitri V. Nanopoulos, and A. Zichichi. Supersymmetric photonic signals at LEP. *Phys. Rev. Lett.*, 77:5168–5171, 1996.

[309] S. Y. Choi, J. S. Shim, H. S. Song, J. Song, and C. Yu. Single-photon events in e+ e- collisions. *Phys. Rev.*, D60:013007, 1999.

[310] Herbi K. Dreiner, Olaf Kittel, and Ulrich Langenfeld. Discovery potential of radiative neutralino production at the ILC. *Phys. Rev.*, D74:115010, 2006.

[311] Rahul Basu, P. N. Pandita, and Chandradew Sharma. Radiative neutralino production in low energy supersymmetric models. *Phys. Rev.*, D77:115009, 2008.

[312] Christoph Bartels, Mikael Berggren, and Jenny List. Characterising WIMPs at a future e^+e^- Linear Collider. *Eur. Phys. J.*, C72:2213, 2012.

[313] Partha Konar, Kyoungchul Kong, Konstantin T. Matchev, and Maxim Perelstein. Shedding Light on the Dark Sector with Direct WIMP Production. *New J. Phys.*, 11:105004, 2009.

[314] P. N. Pandita and Monalisa Patra. Beam polarization effects in the radiative production of lightest neutralinos in e^+e^- collisions in supersymmetric grand unified models. *Phys. Rev.*, D88:055018, 2013.

[315] G. V. Borisov, V. N. Larin, and F. F. Tikhonin. Testing the $(W\gamma W)$ Vertex in the Process $e^+e^- \to$ Neutrino Anti-neutrino γ. *Z. Phys.*, C41:287–292, 1988.

[316] K. J. Abraham, J. Kalinowski, and P. Sciepko. New probes of anomalous W W gamma couplings at future e+ e- linacs. *Phys. Lett.*, B339:136–140, 1994.

[317] Debajyoti Choudhury, Jan Kalinowski, and Anna Kulesza. CP violating anomalous $WW\gamma$ couplings in e^+e^- collisions. *Phys. Lett.*, B457:193–201, 1999.

[318] Damien M. Pierce, Jonathan A. Bagger, Konstantin T. Matchev, and Ren-jie Zhang. Precision corrections in the minimal supersymmetric standard model. *Nucl. Phys.*, B491:3–67, 1997.

[319] Graham D. Kribs, Adam Martin, and Tuhin S. Roy. Supersymmetry with a Chargino NLSP and Gravitino LSP. *JHEP*, 01:023, 2009.

[320] O. Nicrosini and L. Trentadue. Transverse Degrees of Freedom in QED Evolution. *Phys. Lett.*, B231:487–491, 1989.

[321] G. Montagna, O. Nicrosini, F. Piccinini, and L. Trentadue. Invisible events with radiative photons at LEP. *Nucl. Phys.*, B452:161–172, 1995.

[322] Frits A. Berends and R. Kleiss. Initial State Radiation at LEP Energies and the Corrections to Higgs Boson Production. *Nucl. Phys.*, B260:32–60, 1985.

[323] Yuri L. Dokshitzer, Valery A. Khoze, and W. James Stirling. Gluon radiation and energy losses in top quark production. *Nucl. Phys.*, B428:3–18, 1994.

[324] F. E. Low. Bremsstrahlung of very low-energy quanta in elementary particle collisions. *Phys. Rev.*, 110:974–977, 1958.

[325] T. H. Burnett and Norman M. Kroll. Extension of the low soft photon theorem. *Phys. Rev. Lett.*, 20:86, 1968.

[326] K. A. Olive et al. Review of Particle Physics. *Chin. Phys.*, C38:090001, 2014.

[327] Kaoru Hagiwara, Kentarou Mawatari, David Rainwater, and Tim Stelzer. Correlated decays of pair-produced scalar taus. *Phys. Rev.*, D73:075010, 2006.

[328] Neil D. Christensen, Tao Han, Zhuoni Qian, Josh Sayre, Jeonghyeon Song, and Stefanus. Determining the Dark Matter Particle Mass through Antler Topology Processes at Lepton Colliders. *Phys. Rev.*, D90:114029, 2014.

[329] Marco Battaglia, AseshKrishna Datta, Albert De Roeck, Kyoungchul Kong, and Konstantin T. Matchev. Contrasting supersymmetry and universal extra dimensions at the clic multi-TeV e+ e- collider. *JHEP*, 07:033, 2005.

[330] S. Y. Choi, Kaoru Hagiwara, H. U. Martyn, K. Mawatari, and P. M. Zerwas. Spin Analysis of Supersymmetric Particles. *Eur. Phys. J.*, C51:753–774, 2007.

[331] Matthew R. Buckley, Hitoshi Murayama, William Klemm, and Vikram Rentala. Discriminating spin through quantum interference. *Phys. Rev.*, D78:014028, 2008.

[332] Matthew R. Buckley, Seong Youl Choi, Kentarou Mawatari, and Hitoshi Murayama. Determining Spin through Quantum Azimuthal-Angle Correlations. *Phys. Lett.*, B672:275–279, 2009.

[333] Fawzi Boudjema and Ritesh K. Singh. A Model independent spin analysis of fundamental particles using azimuthal asymmetries. *JHEP*, 07:028, 2009.

[334] Neil D. Christensen and Daniel Salmon. New method for the spin determination of dark matter. *Phys. Rev.*, D90(1):014025, 2014.

[335] M. Jacob and G. C. Wick. On the general theory of collisions for particles with spin. *Annals Phys.*, 7:404–428, 1959. [Annals Phys.281,774(2000)].

[336] Ken-ichi Hikasa. Transverse Polarization Effects in e^+e^- Collisions: The Role of Chiral Symmetry. *Phys. Rev.*, D33:3203, 1986.

[337] Kaoru Hagiwara and D. Zeppenfeld. Helicity Amplitudes for Heavy Lepton Production in e+ e- Annihilation. *Nucl. Phys.*, B274:1–32, 1986.

[338] G. Moortgat-Pick et al. The Role of polarized positrons and electrons in revealing fundamental interactions at the linear collider. *Phys. Rept.*, 460:131–243, 2008.

[339] S. Y. Choi, M. Drees, and J. Song. Neutralino production and decay at an e+ e- linear collider with transversely polarized beams. *JHEP*, 09:064, 2006.

[340] B. Ananthanarayan and Saurabh D. Rindani. Two-particle kinematic distributions from new physics at an electron-positron collider with polarized beams. *Eur. Phys. J.*, C56:171–179, 2008.

[341] M.E. Rose. *Elementary Theory of Angular Momentum*. Dover books on physics and chemistry. Dover, 1995.

[342] F. Englert and R. Brout. Broken Symmetry and the Mass of Gauge Vector Mesons. *Phys. Rev. Lett.*, 13:321–323, 1964. [,157(1964)].

[343] Peter W. Higgs. Broken symmetries, massless particles and gauge fields. *Phys. Lett.*, 12:132–133, 1964.

[344] Peter W. Higgs. Broken Symmetries and the Masses of Gauge Bosons. *Phys. Rev. Lett.*, 13:508–509, 1964. [,160(1964)].

[345] Peter W. Higgs. Spontaneous Symmetry Breakdown without Massless Bosons. *Phys. Rev.*, 145:1156–1163, 1966.

[346] T. W. B. Kibble. Symmetry breaking in nonAbelian gauge theories. *Phys. Rev.*, 155:1554–1561, 1967. [,165(1967)].

[347] John M. Cornwall, David N. Levin, and George Tiktopoulos. Uniqueness of spontaneously broken gauge theories. *Phys. Rev. Lett.*, 30:1268–1270, 1973. [Erratum: Phys. Rev. Lett.31,572(1973)].

[348] John M. Cornwall, David N. Levin, and George Tiktopoulos. Derivation of Gauge Invariance from High-Energy Unitarity Bounds on the s Matrix. *Phys. Rev.*, D10:1145, 1974. [Erratum: Phys. Rev.D11,972(1975)].

[349] C. H. Llewellyn Smith. High-Energy Behavior and Gauge Symmetry. *Phys. Lett.*, 46B:233–236, 1973.

[350] Kaoru Hagiwara, R. D. Peccei, D. Zeppenfeld, and K. Hikasa. Probing the Weak Boson Sector in $e^+e^- \to W^+W^-$. *Nucl. Phys.*, B282:253–307, 1987.

[351] AseshKrishna Datta, Kyoungchul Kong, and Konstantin T. Matchev. Minimal Universal Extra Dimensions in CalcHEP/CompHEP. *New J. Phys.*, 12:075017, 2010.

[352] Maciej Skrzypek and Stanislaw Jadach. Exact and approximate solutions for the electron nonsinglet structure function in QED. *Z. Phys.*, C49:577–584, 1991.

[353] Pisin Chen. Differential luminosity under multi - photon beamstrahlung. *Phys. Rev.*, D46:1186–1191, 1992.

[354] Neil D. Christensen and Claude Duhr. FeynRules - Feynman rules made easy. *Comput. Phys. Commun.*, 180:1614–1641, 2009.

[355] Neil D. Christensen, Priscila de Aquino, Celine Degrande, Claude Duhr, Benjamin Fuks, Michel Herquet, Fabio Maltoni, and Steffen Schumann. A Comprehensive approach to new physics simulations. *Eur. Phys. J.*, C71:1541, 2011.

[356] Adam Alloul, Neil D. Christensen, Cline Degrande, Claude Duhr, and Benjamin Fuks. FeynRules 2.0 - A complete toolbox for tree-level phenomenology. *Comput. Phys. Commun.*, 185:2250–2300, 2014.

[357] Alexander Belyaev, Neil D. Christensen, and Alexander Pukhov. CalcHEP 3.4 for collider physics within and beyond the Standard Model. *Comput. Phys. Commun.*, 184:1729–1769, 2013.

[358] Gerald Aarons et al. ILC Reference Design Report Volume 3 - Accelerator. 2007.